

RADIO OCCULTATION OF SATURN'S RINGS WITH THE
CASSINI SPACECRAFT: RING MICROSTRUCTURE INFERRED
FROM NEAR-FORWARD RADIO WAVE SCATTERING

A DISSERTATION
SUBMITTED TO THE DEPARTMENT OF ELECTRICAL
ENGINEERING
AND THE COMMITTEE ON GRADUATE STUDIES
OF STANFORD UNIVERSITY
IN PARTIAL FULFILLMENT OF THE REQUIREMENTS
FOR THE DEGREE OF
DOCTOR OF PHILOSOPHY

Fraser Stuart Thomson

July 2010

© 2010 by Fraser Stuart Thomson. All Rights Reserved.

Re-distributed by Stanford University under license with the author.



This work is licensed under a Creative Commons Attribution-Noncommercial 3.0 United States License.

<http://creativecommons.org/licenses/by-nc/3.0/us/>

This dissertation is online at: <http://purl.stanford.edu/pb657pg3502>

I certify that I have read this dissertation and that, in my opinion, it is fully adequate in scope and quality as a dissertation for the degree of Doctor of Philosophy.

Howard Zebker, Primary Adviser

I certify that I have read this dissertation and that, in my opinion, it is fully adequate in scope and quality as a dissertation for the degree of Doctor of Philosophy.

Per Enge

I certify that I have read this dissertation and that, in my opinion, it is fully adequate in scope and quality as a dissertation for the degree of Doctor of Philosophy.

Essam Marouf

Approved for the Stanford University Committee on Graduate Studies.

Patricia J. Gumpert, Vice Provost Graduate Education

This signature page was generated electronically upon submission of this dissertation in electronic format. An original signed hard copy of the signature page is on file in University Archives.

Abstract

The Cassini spacecraft is a robotic probe sent from Earth to orbit and explore the planet Saturn, its moons, and its expansive ring system. Between May 3 and August 2 of 2005, we undertook a series of radio occultation experiments, during which the Cassini spacecraft operated in conjunction with the NASA Deep Space Network (DSN) to probe the rings at three distinct radio wavelengths.

During our occultation experiments, Cassini flies behind the rings of Saturn as viewed from Earth and transmits coherent radio signals at wavelengths of 13 cm, 3.6 cm, and 0.94 cm, in the radio bands known as S, X, and Ka, respectively. These signals pass through the rings and are received and recorded on Earth at the large antenna complexes of the DSN. At each of the three transmitted frequency channels, the received signal comprises two components, i) a direct (coherent) component, which is the transmitted sinusoid, attenuated and phase shifted by the average effect of its interaction with the interceding ring material, and ii) a scattered (incoherent) signal component, comprising energy that is forward-scattered towards the receiver from all of the ring particles illuminated by the transmitting antenna's beam. The time- and spatially-averaged diffraction signature of ring microstructure—which forms when individual ring particles organize into large clusters or groups under the influence of collisional and self-gravitational forces—is superimposed on the scattered signal.

Coherent radio waves transmitted by the Cassini spacecraft are diffracted at various locations in Ring A and B and indicate the presence of fine-scale structure showing periodic variation in optical depth, which we refer to as periodic microstructure (PM). We interpret the observed spectral signature using simple diffraction grating models, yielding estimates of the structural period $\lambda_{\text{gr}} \approx 100\text{--}250$ meters. In particular, two

regions in Ring A at radial locations $123.05\text{--}123.4 \times 10^3$ km and $123.6\text{--}124.6 \times 10^3$ km yield average estimates of $\bar{\lambda}_{\text{gr}}=163^{+6}_{-6}$ meters and $\bar{\lambda}_{\text{gr}}=217^{+8}_{-8}$ meters, respectively. Three regions in Ring B at radial locations $92.1\text{--}92.6 \times 10^3$ km, $99.0\text{--}104.5 \times 10^3$ km, and $110.0\text{--}115.0 \times 10^3$ km yield average estimates of $\bar{\lambda}_{\text{gr}}=115^{+20}_{-15}$, 146^{+14}_{-14} , and 250^{+150}_{-75} meters, respectively. In all regions, the structure appears to be azimuthally symmetric with mean orientation angles ranging between $-2.8^\circ \leq \bar{\phi}_{\text{gr}} \leq 1.5^\circ$.

Prior to Cassini, axisymmetric periodic microstructure was predicted by fluid dynamical theory and by the results of dynamical simulations of the rings, but was not observed experimentally. Our observations are the first to directly observe PM in the rings, and to report estimates of its structural period and orientation in five distinct regions across Rings A and B.

Acknowledgements

I would like to extend my heartfelt thanks to Howard Zebker for taking over from Len Tyler as my primary advisor in early 2008. Without his support, it is unlikely that I would have completed this degree program. I will always be in his debt for his acts of kindness and support.

Sincere thanks are due to Essam Marouf, who always made the effort to find time in his busy schedule for my many questions. Essam has been a model of patience, diligence, and excellence during our years of collaboration, and his steady provision of guidance, tutelage, and financial support has made this work possible. His ethics and commitment to excellence in his work form an ideal that all scientists should aspire to, and which many on the Cassini radio science team depend on and are indebted to. One of the most memorable moments in my life is being at JPL during the first planned Cassini radio occultation experiment, and watching how excited Essam and Dick French were as we all watched the spectrum of the received signal varying in real time, as the experiment revealed hints of ring structure. Throughout my years at Stanford, it has been a great privilege and joy for me to observe Essam's passion for the rings firsthand.

Thanks also to Per Enge for serving as my third reader, for serving on my oral defense committee, and for teaching me about orbital mechanics and GPS. He is an excellent professor and a friend to many students, myself included.

I extend many thanks to my teacher and friend Ivan Linscott, who always has time to discuss new ideas and old ones, and for being such a generous friend to many students over the years. Thanks also to Antony Fraser-Smith for stepping in to save the day on several occasions, for serving on my defense committee, and for being such

a great guy in general.

Special thanks go to Len Tyler for all of his time, energy, and support, and for being a mentor to me for several years prior to his semi-retirement. Len is a polymath, and memories of times when I have glimpsed his brilliance will always bring a smile to my face. On those rare occasions when Len did not know the answer, his honest and free willingness to admit gaps in his knowledge provide an inspirational lesson to us all; there is no better way to get started solving a problem than to admit what is known and what is not known. Len's insistent attention to detail has taught me to choose my words more carefully, and has made me a better technical writer. As Len would say, a key goal in writing is to minimize the impedance mismatch between the writer and their audience. I hope I have done that here.

A very special thanks to Sami Asmar of NASA's Jet Propulsion Laboratory, for being a friend and a great boss during my all-too-brief work terms at the lab. I would be honored to work with him or for him again, anytime and anywhere. I would also like to thank Christopher Chyba, my friend and mentor, and one of the kindest and smartest people I've ever known. The nine months that we collaborated before I chose to join Cassini was the most exciting and fulfilling period of time that I spent at Stanford.

Lots of love and thanks to my parents, who provided access to all of the opportunities that anyone could ever ask for in life. I would not be writing this without them. There are many other people who, either knowingly or unknowingly, helped to make this dissertation possible. To the anonymous, I offer my thanks also.

I dedicate this dissertation to my wife Katherine and to my son Kaiden (b. June 7, 2009), for showing me how simple life really is, and for being a constant reminder of what is truly important.

This work was supported by the NASA Cassini Project through JPL Contract No. 1214216. The support is gratefully acknowledged.

Contents

Abstract	v
Acknowledgements	vii
1 Introduction and Historical Review	11
1.1 The Discovery of Saturn’s Rings	12
1.2 Occultation Studies of Saturn’s Rings: A Brief History	20
1.3 Contents and Contributions of this Dissertation	22
2 Saturn Ring Structure and Dynamics	27
2.1 Ring Macrostructure	33
2.1.1 Gaps and Ring Boundaries	34
2.1.2 Spiral Density and Bending Waves	38
2.2 Ring Microstructure	40
2.2.1 Gravitational Wakes	40
2.2.2 Periodic Microstructure	42
2.3 Models of Ring Microstructure	44
2.4 Summary	47
3 EM Scattering and Diffraction from Ring Particle Clusters	49
3.1 Introduction	50
3.2 Theoretical Background	53
3.2.1 Coherent Scattering from a Sphere: Mie Theory	56
3.2.2 Multi-Particle Scattering Using Mie Theory	60

3.2.3	Diffraction from an Amplitude Screen	64
3.2.4	Mie and Diffraction Theory: Some Practical Considerations	66
3.3	Simulation Results	68
3.3.1	Scattering from a Single Sphere	70
3.3.2	Scattering from Two and Three Spheres	71
3.3.3	Scattering from Ten Spheres	77
3.4	Discussion	83
3.5	Amplitude Screen Model Results for Thick, Homogeneous Rings	86
3.5.1	An Analytic Solution for Forward Scattering	87
3.5.2	Comparison with the Amplitude Screen Model	89
3.6	Summary	95
4	The Cassini Radio Occultation Experiment	97
4.1	Techniques, Observables, and Properties of the Received Signal	98
4.1.1	Transmitted and Received Signals	98
4.1.2	Trajectory Design and Doppler Contours	101
4.1.3	Observables	105
4.2	Detection of Microstructure in the Rings	111
4.2.1	Diffraction from Ring Microstructure	111
4.2.2	Evidence of Ring Microstructure	113
4.3	Cassini Ring Occultation Observations, May–August 2005	119
4.3.1	Details of the REV 7–12 Observations	120
4.4	Summary	130
5	Fitting Microstructure Models to Radio Occultation Data	131
5.1	Overview of the Method	131
5.2	Microstructure Modeling Techniques	134
5.2.1	Microstructure Simulations using the Amplitude Screen Method	134
5.2.2	Microstructure Modeling using Analytic Methods	142
5.3	Comparing Model Behavior with Radio Occultation Measurements	146
5.3.1	General Approach	147
5.3.2	Periodic Microstructure	157

5.4	Least-Squares Fitting of Model Parameters to the Data	158
5.4.1	Fitting Models of Periodic Microstructure	159
5.4.2	Other Models	163
5.5	Summary	163
6	Periodic Microstructure in Saturn's Rings	165
6.1	A Survey of Periodic Microstructure in Saturn's Rings	166
6.2	Estimates of Physical Parameters λ_{gr} and ϕ_{gr}	173
6.3	Optical Depth Variation within Features A123.2 and A124.1	184
6.4	Discussion	184
6.4.1	Concurrent Microstructure	184
6.4.2	The Onset of Viscous Overstability	185
6.4.3	Optical Depth Characteristics of PM Regions	188
6.5	Summary	192
7	Summary and Conclusions	195
7.1	General Results	195
7.2	Assumptions and Limitations	196
7.3	Contributions	198
7.4	Future Work	198
A	Radio Occultation Studies of Planetary Rings	201
A.1	Optical Depth Profiles	201
A.1.1	Circular Rings	203
A.1.2	Elliptical Rings	205
A.1.3	Resolution Limitations in the Reconstruction Process	206
A.1.4	Profiling Ring Optical Depth	209
A.2	Particle Size Distributions	211
A.2.1	Suprameter-Sized Particles	212
A.2.2	Submeter-Sized Particles	215
A.2.3	Surface Mass Density and Ring Thickness	216
A.3	Summary	217

B	Cassini 2005 Radio Occultation Timelines	219
C	Historically Important Articles on Saturn's Rings	231
C.1	Christiaan Huygens' article on Saturn's Ring	231
C.2	Cassini's Paper on his Eponymous Division	237
D	Limitations on the Use of the Power-Law form of $S_y(f)$ to Compute Allan Variance	241
D.1	Abstract	241
D.2	Introduction	242
D.3	Exact and Approximate Solutions for $\sigma_y^2(\tau)$	243
D.3.1	Evaluation of the f^{-2} -term	243
D.3.2	Evaluation of the f^{-1} -term	244
D.3.3	Evaluation of the f^0 -term	245
D.3.4	Evaluation of the f^1 -term	246
D.3.5	Evaluation of the f^2 -term	247
D.4	Results and Conclusions	247
E	Radon and Abel Transform Equivalence in Atmospheric Radio Oc- cultation	253
E.1	Abstract	253
E.2	Introduction	254
E.3	Atmospheric Radio Occultation	254
E.4	Applicability of the Abel Transform in Radio Occultation	256
E.5	The Radon Transform	257
E.6	Radon and Abel Transform Equivalence for Radio Occultation	258
E.7	Discussion and Conclusion	260
E.8	Derivation of Eq. (E.4)	261

List of Tables

1.1	Key Milestones in the Study of Saturn's Rings	18
2.1	Properties of Saturn's Ring System	32
3.1	Summary of Two-Sphere Scattering Investigations ($x = 40$)	76
3.2	Summary of Three-Sphere Scattering Investigations ($x = 40$)	77
3.3	Summary of Ten-Sphere Scattering Investigations (Monodistribution, $x = 40$)	79
3.4	Summary of Ten-Sphere Scattering Investigations (Uniform Distribu- tion, $40 \leq x \leq 80$)	83
4.1	Summary of Geometric Occultation Parameters	125
6.1	Summary of PM Features in the Rings	175
D.1	One Percent Convergence Conditions for the Exact Solution and the Approximate Solution to Each Term in the Power-Law Formulation of Allan Variance	249

List of Figures

1.1	Sketch of Saturn as seen by Galileo in 1610	12
1.2	Sketch of Saturn as seen by Galileo in 1616	13
1.3	Early Drawings of Saturn published by Christiaan Huygens in <i>Systema Saturnium</i> (1659)	14
1.4	Huygens' Thick Disc Conceptualization of Saturn's Rings	15
1.5	Cassini's Sketch of Cassini Division (1676)	16
1.6	Diagram of the Rings and Moons of the Giant Planets	19
2.1	Structure of Saturn's Rings	29
2.2	Saturn's Main Rings and Ring F	30
2.3	Particle Size Distributions in Saturn's Cassini Division and Ring A	31
2.4	Keeler Gap with Daphnis	35
2.5	Gaps, Density and Bending Waves in Ring A	36
2.6	Propeller Features in Saturn's Rings	37
2.7	Density and Bending Waves	39
2.8	Gravitational Wakes	41
2.9	Periodic Microstructure	43
2.10	Artist's Rendition of Fine-Scale Ring Structure	43
2.11	A Survey of Ring Microstructure	45
2.12	Models of Ring Microstructure	46
3.1	Construction of the Diffraction Screen	54
3.2	Comparison of Mie Theory and Diffraction Theory: Single Sphere	72
3.3	Geometry Definition for Two and Three Sphere Scattering Models	73

3.4	Comparison of Mie Theory and Diffraction Theory: Two Spheres . . .	75
3.5	Comparison of Mie Theory and Diffraction Theory: Three Spheres . . .	78
3.6	Comparison of Mie Theory and Diffraction Theory: Ten Identical Spheres	80
3.7	Comparison of Mie Theoretic Solutions for Lossy vs. Lossless Spheres	81
3.8	Comparison of Mie Theory and Diffraction Theory: Ten Spheres Sam- pled from a Uniform Size Distribution	82
3.9	Ten Spheres and their Diffraction Pattern	84
3.10	Amplitude Screen Models of Homogeneous, MPT Rings	90
3.11	Comparison of the Amplitude Screen Method with the Theory of <i>Marouf</i> <i>et al.</i> [1982]	92
4.1	Ring Occultation Geometry	99
4.2	Occultation Geometry and Doppler Contours	102
4.3	Ring Occultation Signal Properties	107
4.4	Doppler Signature of a Gap in the Rings	109
4.5	Diffraction from Microstructure in Saturn's Rings	115
4.6	Doppler Signature of Periodic Microstructure in the Rings	117
4.7	DSN Complex Locations	119
4.8	Ring Longitude of Occultation Tracks, May–August 2005	121
4.9	Distance from Cassini to the Ring Piercing Point (RPP) during the REV 7, 8, 10, and 12 Observations	123
4.10	REV 7 Observation Timing and Geometry	126
4.11	REV 8 Observation Timing and Geometry	127
4.12	REV 10 Observation Timing and Geometry	128
4.13	REV 12 Observation Timing and Geometry	129
5.1	Comparison of Scattering from Homogeneous MPT and Packed Mono- layer Models of Planetary Rings	136
5.2	Diffraction Signature of Gravitational Wakes	138
5.3	Amplitude Screen Model of Gravitational Wakes or Periodic Microstruc- ture	139
5.4	Sinusoidal Transmittance Amplitude Screen Model	140

5.5	Properties of a Sinusoidal Diffraction Grating	144
5.6	Diffraction Grating and the Cassini Observation Geometry	145
5.7	Constructing Amplitude Screens from Models of Ring Microstructure	148
5.8	Diffraction and Doppler Geometry in the Ring Plane	151
5.9	Determining the Magnitude $\overline{U}(\beta_{x_i}, \beta_{y_j})$ and Doppler Frequency f_{D_p} of Signals Received from Point P in the Ring Plane	152
5.10	Synthesis of $I_s(f_D)$ from Models of Ring Microstructure	154
5.11	Sinusoidal Transmittance Model of PM and its Associated Diffraction Pattern	158
5.12	Diffraction Grating Model of Periodic Microstructure	159
5.13	Estimating the First-Order Diffraction Lobes of PM	161
6.1	A Survey of Periodic Microstructure in Rings A and B	168
6.2	Constancy of PM in the Rings over Multiple Observations	170
6.3	PM Features A123.2 and A124.1 are Evident in S-, X-, and Ka-band Spectrograms	171
6.4	Power Spectra of Periodic Microstructure in Saturn's rings	172
6.5	Estimates of the Structural Period λ_{gr} and Orientation ϕ_{gr} of Periodic Microstructure Detected in Saturn's Rings	177
6.6	Fine-Scale Optical Depth Variation τ_{fs} , Features A123.2 and A124.1	182
6.7	Optical Depth and Spectrograms of Periodic Microstructure Detected with the Cassini Radio Occultation Experiment	189
7.1	Composite View of Saturn and the Rings	200
B.1	Cassini REV 7 Radio Occultation Timeline	220
B.2	Cassini REV 8 Radio Occultation Timeline	221
B.3	Cassini REV 10 Ingress Radio Occultation Timeline	222
B.4	Cassini REV 10 Egress Radio Occultation Timeline	223
B.5	Cassini REV 12 Ingress Radio Occultation Timeline	224
B.6	Cassini REV 12 Egress Radio Occultation Timeline	225
B.7	Cassini REV 7 Elevation Angle at DSN Receiving Stations	226

B.8	Cassini REV 8 Elevation Angle at DSN Receiving Stations	227
B.9	Cassini REV 10 Elevation Angle at DSN Receiving Stations	228
B.10	Cassini REV 12 Elevation Angle at DSN Receiving Stations	229
D.1	Characteristic Physical Noise Processes in Frequency Standards . . .	250
D.2	Ratio of the Exact Solution to the Approximate Solution, f^{-2} term .	250
D.3	Ratio of the Exact Solution to the Approximate Solution, f^{-1} term .	251
D.4	Ratio of the Exact Solution to the Approximate Solution, f^0 term . .	251
D.5	Ratio of the Exact Solution of the f^1 term to the Solution Commonly Given in the Literature	252
D.6	Ratio of the Exact Solution to the Approximate Solution, f^2 term . .	252
E.1	Geometry of Radio Occultation Measurements	264
E.2	Geometry for Derivation of Differential Bending Angle $d\psi$ and Path Integral Element dl	265
E.3	Radon Transform Geometry	266

List of Symbols

β	Scattering angle of the rings relative to the Cassini-Earth line-of-sight; also, a parameter used to define the onset of viscous overstability
Δf	Spatial frequency resolution
ΔR	Spatial resolution of ring optical depth measurements after windowing
ΔR_W	Spatial resolution of ring optical depth measurements, un-windowed, with a reconstruction filter of length W
$\Delta x, \Delta y$	Amplitude screen pixel size in x and y
$\Delta_i(\theta)$	Intensity pattern difference between Mie and diffraction theory for the i^{th} simulated case
ϵ	Electromagnetic permittivity
ϵ_n	Coefficient of restitution, inter-particle collisions
$\Gamma(\vec{r}_o, \overline{P})$	Sum of squares expression that we minimize using a Levenberg-Marquardt algorithm, thereby fitting models of ring microstructure to the Cassini data
\hat{T}	Diffracted received signal from rings of transmittance T
\hat{u}_{gr}	Microstructure orientation vector
\hat{u}_{E}	Unit vector pointing from Cassini to where Earth will be when it receives radio signals transmitted by Cassini

\hat{u}_p	Unit vector pointing from Cassini to the point P in the ring plane
$\hat{X} = \hat{T} + \hat{n}$	Diffracted ring transmittance \hat{T} with additive noise \hat{n}
$\kappa(r)$	Epicyclic (radial) orbital frequency
λ	Wavelength of transmitted radio signal
λ_{gr}	Structural period of microstructure
λ_w	Local wavelength of spiral bending or density waves
μ	Electromagnetic permeability
$\mu(r)$	Natural vertical oscillation frequency
$\mu_o = \sin B$	Geometric factor related to the ring opening angle B
ν	Kinematic shear viscosity
Ω	Angular velocity
ω	Angular frequency of radio wave signal
$\Omega(\vec{r})$	Locus of points of constant angular scattering frequency $\omega_o + f_D/(2\pi)$ in the ring plane
ω_f	Forcing frequency of gravitational perturbations causing bending/density waves
$\overline{\Delta}(\theta)$	Mean difference between Mie and diffraction theory over all simulated cases of a particular configuration
\overline{P}	Parameter vector that we optimize using the Levenberg-Marquardt least-squares algorithm. For periodic microstructure, $\overline{P} = [\lambda_{\text{gr}} \ \phi_{\text{gr}}]$
$\Phi(\theta)$	Phase function (<i>i.e.</i> , Fraunhofer diffraction pattern)
ϕ_{gr}	Microstructure orientation angle

$\psi(r_o, \phi_o; r, \phi)$	Generalized phase function
ψ, ψ_{mn}	Generating function, satisfying the scalar Helmholtz equation
ρ_s	Mean density of Saturn ($\rho_s = 687 \text{ kg m}^{-3}$)
σ_ρ	Surface mass density
σ_{gr}	Standard deviation of the width of normally-distributed particle clusters used to model gravitational wakes or periodic microstructure
$\sigma_d(\beta, \vec{r})$	Differential scattering cross section of the rings per unit surface area
$\sigma_\Delta(\theta)$	Standard deviation of $\overline{\Delta}(\theta)$
$\sigma_{d1}(\beta)$	Equivalent single-scattering cross section of the rings
τ	Normal optical depth
τ_{fs}	Fine-scale optical depth
$\tau_q = \frac{\tau}{\sin B}$	Oblique optical depth
τ_{th}	Threshold optical depth
θ	Boresight angle
θ_d	Diffraction angle of the first-order lobes of periodic microstructure
\vec{B}	Magnetic induction (Tesla)
\vec{D}	Electric displacement (Coulombs·m ⁻²)
\vec{E}	Electric field strength (Volts·m ⁻¹)
$\vec{E}_{\text{inc}}, \vec{H}_{\text{inc}}$	Electric and magnetic field components of an incident plane wave
\vec{E}_s, \vec{H}_s	Scattered electric and magnetic fields
\vec{H}	Magnetic field (Amperes·m ⁻¹)

\vec{J}	Current density vector (Amperes·m ⁻²)
$\vec{k} = \frac{2\pi}{\lambda}\hat{u}_E$	Wave vector of signals transmitted by Cassini
$\vec{N}_{mn}^{(1)}, \vec{M}_{mn}^{(1)}$	Vector spherical wave functions (Bessel j_n basis)
$\vec{N}_{mn}^{(3)}, \vec{M}_{mn}^{(3)}$	Vector spherical wave functions (Bessel $h_n^{(1)}$ and $h_n^{(2)}$ basis)
\vec{r}	Radial vector from Saturn's center of mass to a point (r, ϕ) in the ring plane
\vec{r}_{co}	Vector connecting Cassini to the ring piercing point
\vec{R}_c	Radial vector from Saturn's center to the Cassini spacecraft
\vec{r}_o	Radial vector connecting Saturn's center of mass to the ring piercing point (RPP)
\vec{r}_p	Radial vector connecting Cassini to a ring particle at location P in the ring plane
\vec{S}_1, \vec{S}_2	Locations in the ring plane where the first-order diffraction lobes of periodic microstructure originate
\vec{v}_{gr}	Apparent velocity of microstructure in the ring plane
\vec{v}_p	Velocity of a particular ring particle located at point P in the rings
\vec{v}_s	Velocity of the Cassini spacecraft
\tilde{w}	Averaged single particle albedo
a	Semi-major axis of an ellipse; radius of ring particle; radius of the Cassini high-gain antenna (HGA)
a_n^j, b_n^j	Scattering coefficients of a single, isolated sphere
a_{mn}^j, b_{mn}^j	Scattering coefficients for an aggregate of spheres

A_p	Total projected area of all ring particles within an amplitude screen
B	Ring opening angle
c	Velocity dispersion of ring particles
C_{ext}	Extinction coefficient
e	Orbital eccentricity
F	Fresnel scale
$F(f; \overline{P}_i)$	Gaussian function used to fit the first-order diffraction lobes of periodic microstructure
f_D	Doppler shift of forward-scattered radio signals relative to the transmit frequency
f_{vol}	Volume packing fraction
f_U, f_V	Spatial frequencies in u and v
$f_{\sigma i+}, f_{\sigma i-}$	Detected frequency f_{mi} plus/minus one standard deviation
f_{mi}	Detected center frequency of the i^{th} diffraction lobe
G	Gain pattern of the Cassini high-gain antenna
$I(u, v), I(\tau_q, \theta)$	Intensity of diffracted field
$I_s(f_D), I_s(\beta_x, \beta_y)$	Intensity of the synthesized received signal spectrum
$I_{11}(\theta), I_{22}(\theta)$	Polarized scattered signal intensity
$k = \frac{2\pi}{\lambda}$	Wavenumber
L	Number of spheres in an aggregate
M_s	Mass of Saturn ($M_s = 5.69 \times 10^{26}$ kg)

m_θ	Azimuthal symmetry number
m_r	Radial symmetry number
m_z	Vertical symmetry number
$N(a)$	Cumulative distribution of particles of radius $\leq a$, contained within a unit-area column
$n(a)$	Number density of ring particles of radius a
$n(r)$	Azimuthal orbital frequency
N_p	Total number of ring particles contained in a vignette of the rings
Q_{ext}	Extinction efficiency
R_s	Mean equatorial radius of Saturn ($R_s = 60,268$ km)
r_h	Hill radius
r_L	Origin of a Lindblad resonance in the rings
r_v	Origin of a vertical resonance in the rings
$S(\omega, t)$	Power spectral density of radio wave signals forward-scattered from the rings
T	Complex transmittance of the rings
T_r	Thickness of the rings
$U(\beta_s, \beta_y)$	Scalar diffracted field (angular frequency domain)
$U(u, v)$	Scalar diffracted field (spatial frequency domain)
$U(x, y)$	Scalar amplitude screen
$x = \frac{2\pi a}{\lambda}$	Electrical size parameter of a sphere of radius a
G	Universal Gravitational Constant ($G = 6.67428 \times 10^{-11} \text{ m}^3\text{kg}^{-1}\text{s}^{-2}$)

Glossary

DMP Disable Monopulse.

DSN Deep Space Network.

Egress The final phase of an occultation experiment, where the signal source (*e.g.*, Cassini) reappears from behind the planet/moon, as seen from the receiver, and passes behind any objects under study (atmosphere, ionosphere, rings) to an unobstructed line-of-sight view.

EM Electromagnetic.

EMP Enable Monopulse.

ERT Earth Receive Time.

FFT Fast Fourier Transform.

FNL Finite Number of Layers.

HGA High-Gain Antenna.

ILR Inner Lindblad Resonance.

Ingress The initial phase of an occultation experiment, where the signal source (*e.g.*, Cassini) moves from an unobstructed line-of-sight view, passes behind any objects under study (rings, ionosphere, atmosphere), and disappears behind the planet/moon.

IVR Inner Vertical Resonance.

JPL Jet Propulsion Laboratory.

LHCP Left-Hand Circular Polarization.

LMB Live Movable Block.

Macrostructure Large scale variations in ring optical depth, on length scales of kilometers or more.

Microstructure A fine-scale organization of ring particles into groups or structures, on length scales of tens or hundreds of meters.

MP Monopulse.

MPT Many Particles Thick.

NASA National Aeronautics and Space Administration.

OLR Outer Lindblad Resonance.

OVR Outer Vertical Resonance.

PM Periodic Microstructure.

PT Pacific Time.

RHCP Right-Hand Circular Polarization.

RPP Ring Piercing Point, the point where the line-of-sight ray between Cassini and Earth (*i.e.*, along \hat{u}_E) intercepts the ring plane.

RSS Radio Science Subsystem.

SNR Signal-to-Noise Ratio.

TWNC Two-Way Non-Coherent.

USO Ultra-Stable Oscillator.

UTC Universal Time, Coordinated.

VO Viscous Overstability; Viscously Overstable.

Chapter 1

Introduction and Historical Review

July of 2010 marks the 400th anniversary of Galileo’s discovery of Saturn’s rings, an event made possible by the invention of the modern telescope. During and since Galileo’s time, technological advances have led to improved telescopes, as well as other new instruments and observational techniques. These advances have in turn played key roles in the chain of scientific discoveries that connect the current state of our knowledge to that night in July of 1610.

The Cassini-Huygens mission is the first robotic probe to orbit Saturn, and represents the latest major advance in Saturn exploration tools and techniques. Inserted into Saturn orbit in July of 2004, the Cassini spacecraft carries onboard a complement of 12 scientific instruments designed to study Saturn, its moons, and its impressive ring system. These instruments measure many aspects of the rings with an unprecedented level of fidelity, and are accumulating a cache of observational data that will be studied by scientists for many years after the Cassini mission is completed.

In this dissertation, we seek to explain evidence of fine-scale ring structure that we have detected using the Cassini radio occultation experiment. To place our work in the proper context, we begin our report with a brief history of the major Saturn ring discoveries, starting with Galileo’s first observations of the rings 400 years ago.

1.1 The Discovery of Saturn’s Rings

In 1608, the first practical telescope was invented by Hans Lippershey (1570–1619) in the Netherlands, who used a convex main lens and a concave eyepiece lens to construct an instrument capable of 3x magnification. In the following year, Galileo Galilei (1564–1642) of Pisa built his first telescope, based on imprecise

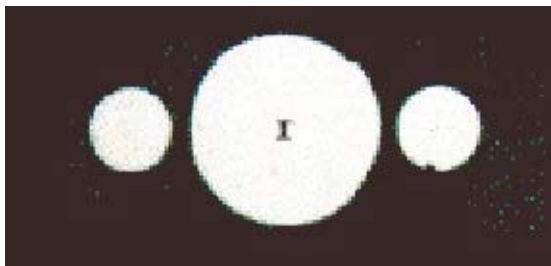


Figure 1.1: Sketch of Saturn as seen by Galileo in 1610.

descriptions of the Dutch design. His first model was also capable of 3x magnification, but soon he had improved the instrument to achieve a magnification of 32x [Alexander, 1962]. Using this instrument, Galileo became the first person to observe planetary rings when he viewed the planet Saturn from Padua, Italy in July of 1610. On the 30th of July, Galileo informed his patrons of his discovery in a letter written to Belesario Vinta, the secretary of the Grand Duke of Tuscany,

“...This is that the star Saturn is not a single star, but is a composite of three, which almost touch each other, never change or move relative to each other, and are arranged in a row along the zodiac, the middle one being three times larger than the lateral ones, and they are situated in this form: oOo.” [van Helden, 1974].

Not wanting to alert other researchers to the discovery, but at the same time wishing to establish a precedent for the observation, he sent his fellow scientists the following message,

“s m a i s m r m i l m e p o e t a l e u m i b u n e n u g t t a u i r a s”

an anagram for *Altissimum planetam tergeminum observavi*, or “I have observed the highest planet [Saturn] tri-form.” The power of the telescope used by Galileo in the summer of 1610 was not sufficient to resolve Saturn’s rings, as evident from his description above, and from his sketch of the 1610 observations presented in Figure 1.1.

Galileo continued to observe Saturn from July 1610 through May 1612. After taking a break of several months, he observed Saturn again in December of 1612, only to find that the companions described in his 1610 letter had disappeared, “I do not know what to say in a case so surprising, so unlooked for, and so novel”, he said of the 1612 vanishing [Burns, 1999]. He was actually observing the rings edge-on. Galileo predicted that the appendages would return, but during the summer of 1616, he was confronted by yet another configuration in the ever-changing ‘star’, Figure 1.2. The odd protrusions he observed in 1616, extending out from either side of the planet, became known as *ansae* or ‘handles’.

Between 1610 and 1656, many astronomers made observations of Saturn, producing sketches and advancing theories to explain what they saw. Johannes Hevelius (1611-1689) published his lavishly-illustrated *Selenographia* in 1647, and in his 1656 publication, *Dissertatio de natura Saturni facie*, claimed that Saturn was an ellipsoid with two ap-

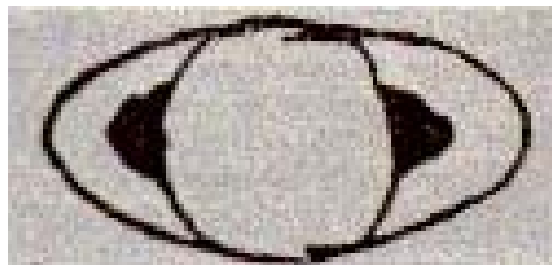


Figure 1.2: Sketch of Saturn as seen by Galileo in 1616, after the rings had ‘returned’.

pendages physically attached to the planet. Francesco Fontana (1580–1656) also saw Saturn with handles as early as 1638, though he did not publish his work until the release of *Novae coelestium terrestriumque rerum observationes* in 1646. Pierre Gassendi (1592–1655) made detailed observations of Saturn, beginning in 1633 and continuing until his death in 1655, cataloging all of the changes in Saturn’s appearance in an effort to discover how they occurred [van Helden, 1974]. Gassendi described his observations in his 1649 publication *Animadversiones*, but the sketches he made of his observations were not published until his posthumous 1658 work, *Opera omnia*. Giovanni Riccioli (1598–1671) published a complete, illustrated almanac of Saturn’s various observed configurations since 1610 in his 1651 book *Almagestum novum*.

The correct interpretation of Saturn’s *ansae* was finally discerned by Christaan Huygens (1629–1695) in February of 1656—interestingly, at a time when the rings as seen from Earth were edge-on and not visible to telescopes of the day. Huygens

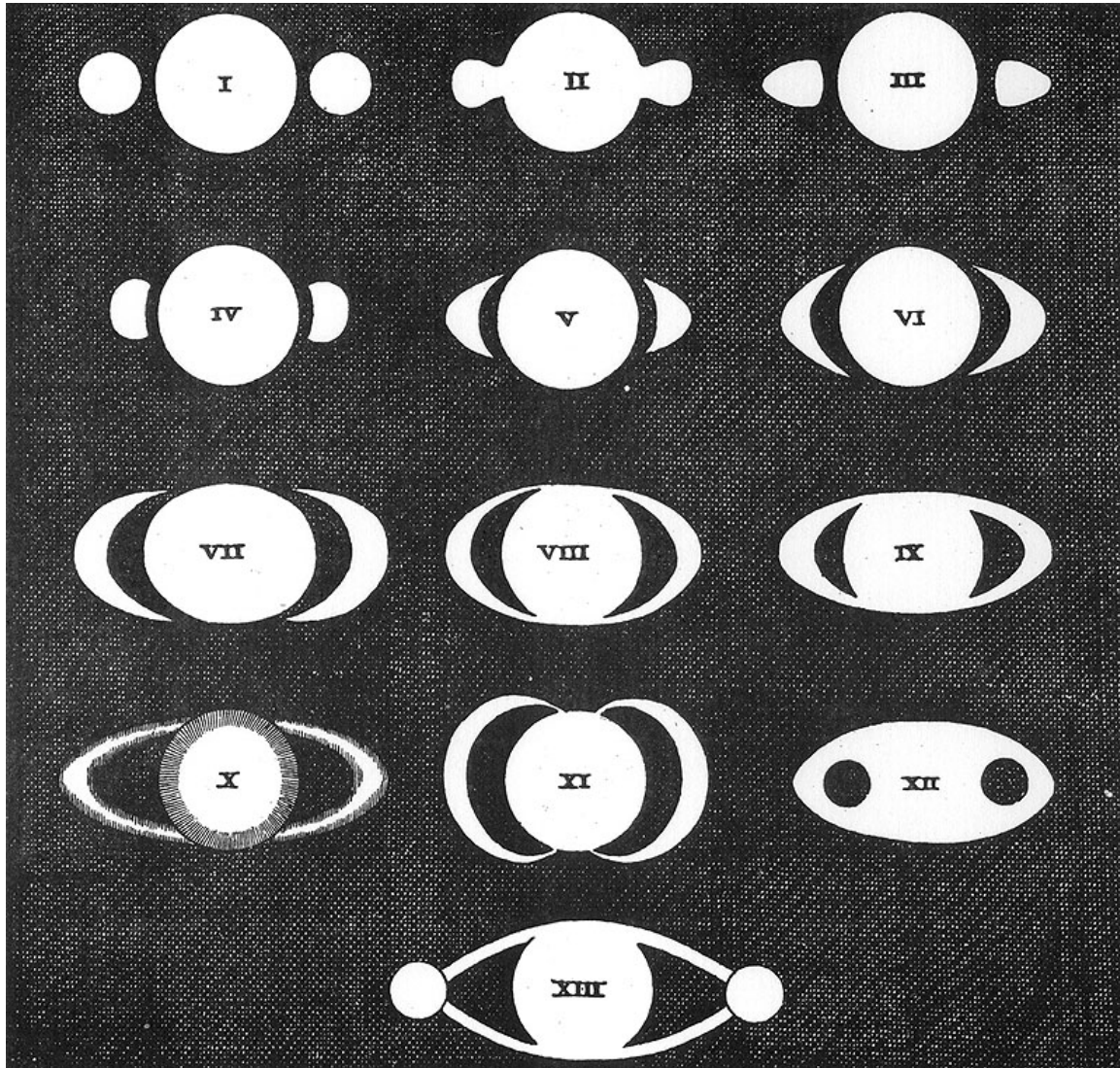


Figure 1.3: Early drawings of Saturn published by Christiaan Huygens in *Systema Saturnium* (1659), showing the observations of Saturn by other astronomers, and their conceptions of the rings. **I** is a copy of Galileo's sketch of his 1610 observation. Remaining sketches are attributed to the observations or theories of **II** Scheiner (1614); **III** Riccioli (1641-43); **IV–VII** Hevelius (1642-47); **VIII–IX** Riccioli (1648-50); **X** Divini (1646-48); **XI** Fontana (1636); **XII** Gassendi (1646); **XIII** Fontana and others (1644-45).

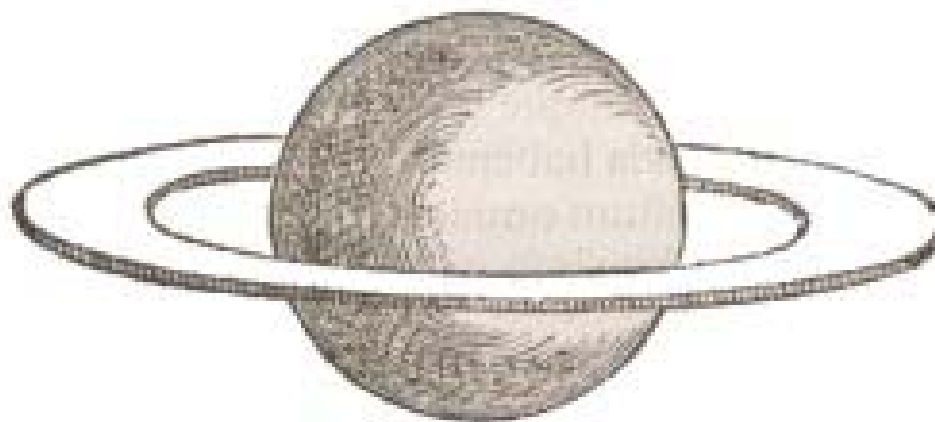


Figure 1.4: Huygens' thick disc conceptualization of Saturn's rings. From *Systema Saturnium* (1659).

may have been predisposed to think in terms of a planar solution to the problem that was the appearance of Saturn's rings, in part due to his association with Rene Descartes (1596–1650), and due to his belief in Descartes' vortex theory [Greenberg and Brahic, 1984]. Descartes, a frequent house guest of Huygens' father, had proposed in 1644 that the universe was filled with contiguous discs of rotating matter—his vortex theory—in part, as a mechanical explanation of the observed orbital motion of satellites. The concept of gravity was unknown at this time, since Isaac Newton (1643–1727) did not publish his theory of universal gravitation until the release of *Principia* in 1687.

In 1656, Huygens published a brief paper, *De Saturni luna observatio nova*, announcing his discovery of the moon that would become known as Titan, and stating that he had found an explanation for the ansae of Saturn. Like Galileo, Huygens chose to disguise his discovery in the form of an anagram,

“a a a a a a c c c c c d e e e e h i i i i i l l l l m m n n n n n n n n
o o o o p p q r r s t t t t t u u u u u”

The anagram translates as *Annulo cingitur, tenui, plano, nusquam cohaerente, ad eclipticam inclinato*, or “It is surrounded by a thin flat ring, nowhere touching, and inclined to the ecliptic”. Huygens finally published his ring theory in *Systema Saturnium* (1659).



Figure 1.5: Sketch drawn by Cassini in 1676, showing the eponymous Cassini Division.

Although the ring concept was generally accepted by 1670, there was still much debate over the composition. Huygens believed the rings to be a solid annulus. Others believed the rings were composed of liquid, or of moonlets or small satellites. The solid disc theory was dealt a blow by the discovery in 1676 of a gap in the rings by Giovanni Cassini (1625–1712), who also believed that the rings were composed of many small satellites. Despite this, William Herschel (1738–1822) suggested in 1791 that the rings were actually composed of two solid annuli [*van Helden*, 1984]. Given his stature within the astronomical community, Herschel’s support revitalized the solid-disc(s) theory. A few years earlier, in 1787, Pierre Simon de Laplace (1749–1827) concluded that the rings were composed of a large number of narrow, solid rings, whose center of mass did not coincide with their geometric centers. In 1785 he had proved that a solid disc would be unstable, but conjectured (though could not prove) that a solid disc could be stable if its mass was distributed unevenly [*Mahon*, 2003].

In 1848, Edouard Roche (1820–1883) speculated that rings could be comprised of the debris of ‘fluid’ satellites that have been torn apart by tidal forces. But the final blow for the solid disc theorists was dealt by James Clerk Maxwell (1831–1879), who addressed the problem of “The Motion of Saturn’s Rings”, which had been set as the Adams Prize in 1857. Maxwell proved that a solid ring was not stable, except in a configuration where 80% of the ring’s mass was concentrated on the outer edge; a result which did not match either intuition or observation. Next, he proved that the

only plausible, stable configuration of the rings is as a multitude of independently orbiting satellites. Maxwell won the 1857 Adams prize (he was the only entry), and his results were published in 1859.

By the time of Maxwell, observations had revealed features within Saturn's rings, the cause of which had remained unexplained. Daniel Kirkwood (1814–1895) put forward a theory to explain the source of observed ring features in 1866, when he pointed out that a particle in the Cassini Division is in 3:1 orbital resonance with Saturn's moon Enceladus. He went on to show (in 1872) that the positions of the Cassini Division and the Enke Gap are associated with orbital resonances of the four interior moons; Mimas, Enceladus, Tethys and Dione [Alexander, 1962], although the exact nature of the Enke Gap was still in question at the time. The first person to clearly view the Enke Gap was James Keeler (1857–1900) in 1888. In 1895, Keeler became the first person to obtain spectrographic images of Saturn's rings, which showed definitively that the orbital speed of the rings decreases with distance from Saturn's center. This was the first measurement to provide observational evidence in support of Maxwell's 1857 proof [Keeler, 1895].

More than 350 years after Galileo's 1610 observations, Saturn was thought to be the only planet in our solar system to have a ring system. Then in 1977, rings were detected at Uranus during a stellar occultation of the star SAO 158687 [Elliot *et al.*, 1977]. Two years later in 1979, Voyager 1 detected faint rings around Jupiter [Smith *et al.*, 1979]. And in 1981, Neptune's "ring arcs" were observed during another stellar occultation, though originally misinterpreted as being due to a chance occultation by a new satellite [Reitsema *et al.*, 1982; Nicholson *et al.*, 1990]. In a matter of a few short years, ring systems went from being unique to Saturn, to being a common feature of the gas giants in our solar system. Each planet has fundamentally different ring systems (see Figure 1.6), the reason for which is still a matter of scientific debate [Burns, 1999].

Table 1.1: Key milestones in the study of Saturn’s rings

Date	Event
1543	Copernicus proposes that the Earth and other planets orbit the Sun
1608	The modern telescope is invented
1609	Kepler publishes the first two of his three laws of motion in <i>Astronomia Nova</i>
1610	Galileo observes the rings of Saturn
1612	Galileo observes the rings’ disappearance
1616	The rings appear as handles, or ‘ansae’
1656	Huygens correctly describes the rings as an annulus
1657	Pendulum clock is invented
1659	Huygens publishes <i>Systema Saturnium</i>
1660	The Royal Society is founded in London
1676	Cassini observes his eponymous division
1687	Newton publishes <i>Principia</i>
1787	Laplace proposes many thin solid ring theory
1791	Herschel supports two solid ring theory
1821	Faraday invents the electric motor
1826	The internal combustion engine is invented
1857	Maxwell proves the rings must be composed of particles
1859	Darwin’s <i>On the Origin of Species</i> is published
1872	Kirkwood proves that observed ring features are caused by resonances with moons
1873	Maxwell’s <i>A Treatise on Electricity and Magnetism</i> is published
1895	Keeler verifies Maxwell’s many-particle theory experimentally
1902	First trans-atlantic radio transmission (Marconi)
1903	First powered flight of an airplane (Wright brothers)
1967	Ring E is discovered
1970	Spectroscopic observations reveal that the rings are composed primarily of water ice
1978	The existence of density waves in the rings is proposed by Goldreich and Tremaine
1979	Ring F is discovered by the Pioneer spacecraft imaging team
1980	Voyager 1 performs the first radio occultation of Saturn’s rings
1980	Ring D is discovered
1981	Lissauer proposes that moonlets are embedded within Saturn’s ring system
1990	The Hubble Space Telescope is deployed to Earth orbit by the Space Shuttle (STS-31)
1997	The Cassini/Huygens spacecraft is launched from Cape Canaveral
2004	Cassini/Huygens is inserted into Saturn orbit

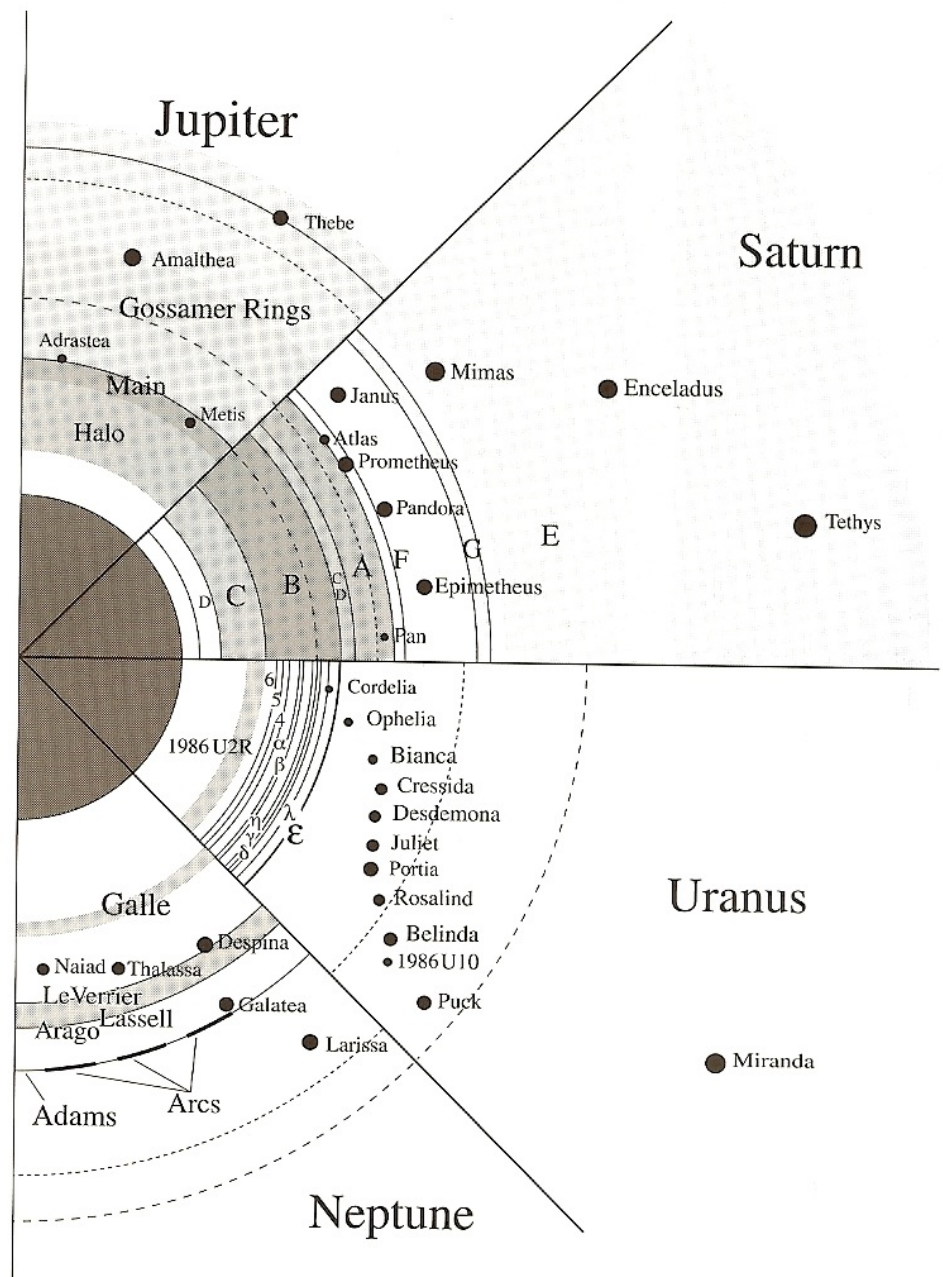


Figure 1.6: Diagram of the rings and moons of the four gas giants in our solar system. Adapted from *de Pater and Lissauer* [2001], who in turn credit J.A. Burns, D.P. Hamilton, and M.R. Showalter.

1.2 Occultation Studies of Saturn’s Rings: A Brief History

Much of what is known about the radial structure in Saturn’s rings has been derived from occultation experiments. Occultation experiments are made when the line-of-sight path between a transmitter and a receiver intercept or ‘occult’ an object under study, be that an atmosphere or a planetary ring system. In the case of stellar occultation, the transmitter is a star, and the receiver is an instrument that collects radiant stellar energy over a particular range of wavelengths in the star’s electromagnetic spectrum. In the case of radio occultation, the transmitter and the receiver are radio instruments designed and built to the specifications required to conduct the experiment.

The primary measurement of occultation experiments is the apparent opacity, or optical depth τ , of the rings to electromagnetic waves of a particular wavelength. If the rings are illuminated with an incident electromagnetic wave of intensity I_o , and the intensity just behind the rings is I , the oblique optical depth τ_q is defined as,

$$\tau_q = -\ln(I/I_o) \quad (1.1)$$

Normal optical depth τ is related to the oblique optical depth by,

$$\tau = \mu_o \tau_q \quad (1.2)$$

where $\mu_o = \sin B$ is the sine of the ring opening angle B , which is the angle that the wave vector \vec{k} of the incident light makes with the ring plane (*i.e.*, if $B = 90^\circ$ then \vec{k} is normal to the plane of the rings). Methods for estimating optical depth from radio occultation measurements are discussed in detail in Appendix A.1. A detailed description of the geometry of the Cassini radio occultation experiments is provided in Chapter 4.

Stellar occultations conducted using the Voyager spacecraft’s ultraviolet spectrometer (UVS) [Sandel *et al.*, 1982; Holberg *et al.*, 1982] and photopolarimeter subsystem (PPS) [Esposito *et al.*, 1983, 1987] observed the occultation of the star δ Sco (located

in the constellation Scorpius) at 0.11- and 0.27- μm wavelengths, respectively, providing optical depth profiles of the rings with sampling resolutions of 0.1 and 3.2 km, respectively. Ground-based observations of the ring occultation of the star 28 Sgr were used by *Nicholson et al.* [2000] to derive optical depth profiles at 0.9, 2.1, 3.3, and 3.9 μm wavelengths, and were used in conjunction with the PPS δ Sco occultation result to estimate the number distribution of particles of radii ranging from 0.3–20 meters [*French and Nicholson*, 2000]. More recently, the visual and infrared mapping spectrometer (VIMS) and the ultraviolet imaging spectrograph (UVIS) instruments onboard NASA's Cassini spacecraft are currently being used to conduct multiple stellar occultations of the Saturnian rings, yielding a dataset that is now being gathered and analyzed (*e.g.*, *Nicholson et al.* [2007]; *Colwell and Esposito* [2007]).

Radio occultation in particular has proven to be a valuable experimental method for probing planetary rings. The technique was first applied to rings during the Voyager 1 flyby of Jupiter on March 5, 1979. Although that particular experiment was unable to detect Jupiter's tenuous rings, the non-detection allowed scientists to establish bounds on the optical depth and particle sizes [*Tyler et al.*, 1981]. The Jovian encounter was followed by the great successes of Voyager 1's flyby encounter with Saturn in 1980, and Voyager 2's flyby of Uranus in 1986.

At Saturn, Voyager 1's radio science subsystem (RSS) simultaneously probed the rings at 3.6- and 13-cm wavelengths, yielding diffraction-corrected optical depth profiles with resolutions approaching 200 meters in regions of Ring C, and with 400-meter resolution over the full extent of the rings [*Tyler et al.*, 1983; *Marouf et al.*, 1986]. Estimates of ring particle size distributions, local ring thickness, and the degree of particle crowding derive from the radio occultation data, for assumed many particles thick (MPT) ring models [*Marouf et al.*, 1982, 1983] and for thin finite number of layers (FNL) ring models [*Zebker and Tyler*, 1984; *Zebker et al.*, 1985]. We describe these models in greater detail in Appendix A.

At Uranus, the large ring opening angle of $B = 81.5^\circ$ facilitated a high signal-to-noise ratio (SNR) radio occultation of the rings. All nine of the rings that were known prior to Voyager were detected in the radio data. The high SNR of these measurements made it possible to reconstruct the optical depth profiles of the rings

at resolutions as fine as 50 meters [Tyler *et al.*, 1986; Gresh *et al.*, 1989].

An attempt was made to observe Neptune’s rings with Voyager 2 in 1989, but this was not successful. Neptune’s rings form incomplete arcs of material, and the spacecraft trajectory did not allow for an occultation measurement of any of these arcs.

The first extensive radio occultation study of a ring system using an orbiting spacecraft is currently underway at Saturn using the RSS onboard NASA’s Cassini spacecraft. In contrast to the hyperbolic flyby trajectories of Voyager, Cassini is an orbiter dedicated to the observation of Saturn, its moons, and its rings. Cassini was inserted into orbit around Saturn on July 1, 2004, and its nominal mission (July 2004 - August 2008) consisted of 75 orbits, during which 20 radio occultations of the rings were performed over a range of observational geometries. Four of these 20 occultations comprise both ingress and egress observations, while the remaining 16 occultations are single-sided (either ingress or egress), for a total of 24 distinct observations. An extended Cassini mission plan was approved by NASA, consisting of a further 60 orbits which took place between July 2008 and July 2010. In February of 2010, NASA announced its plans to extend funding and support for the Cassini mission until 2017.

1.3 Contents and Contributions of this Dissertation

This dissertation focusses on the work done between early 2004 and June of 2008 to estimate the fine-scale structure of Saturn’s rings. Contributions made outside of this area have been included as appendices, as described at the end of this chapter.

We present here a forward-theoretic modeling approach which we use to produce estimates of the key physical dimensions of small-scale microstructure in Saturn’s rings, at length scales of one to several hundreds of meters. We define microstructure as an anisotropic distribution of ring particles to form clusters or groupings that constitute discernible patterns. In particular, we focus on highly periodic, axisymmetric

oscillations in the number density of ring particles that we refer to as periodic microstructure (PM). We have discovered five distinct regions of the rings that contain periodic microstructure by analyzing radio signals forward-scattered by the rings at 0.94- and 3.6-cm wavelengths. These data were collected during four Saturn ring occultations of the Cassini spacecraft, occurring between May and August, 2005. Our findings were first reported informally at a rings working group meeting in Whitefish, Montana in August of 2006. We subsequently reported our results formally [*Thomson et al.*, 2006a, 2007].

Chapter 2 contains an overview of Saturn’s ring structure. Features exist in the rings on many length scales, which we break down into two basic groupings—macrostructure and microstructure. Macrostructure comprises features that exist on length scales of tens to thousands of kilometers in the rings; some examples include spiral waves and gaps. We discuss the physical mechanisms that lead to the formation of both macrostructure and microstructure in the chapter. Key examples of microstructure include the PM described above, as well as gravitational wakes. We discuss models of ring microstructure, which are revisited in later chapters as we explain our analysis technique.

In Chapter 3, we prove that diffraction theory (DT) can be used in place of electromagnetic (EM) theory to estimate the far-field radiation pattern produced when radio waves forward-scatterer from aggregates of ring particles. Synthesis of these radiation patterns is a key step in the technique we have developed to estimate the physical dimensions of ring microstructure. The ability to use diffraction theory to this end is a crucial and enabling result, since the the computational requirements of a full EM solution are prohibitive for our application. We conclude the chapter with a final test of our DT method, comparing its results against a known analytic solution for diffraction from homogeneously-distributed thick rings, and showing excellent agreement between the two.

In Chapter 4 we describe the Cassini radio occultation experiment, including the properties of the transmitted and received signal, and the geometry of the specific set of observations used in our data analysis.

Building on ideas and information presented in Chapters 3 and 4, in Chapter 5

we define the set of tools and procedures we used to extract estimates of the physical dimensions of PM from Cassini signals.

In Chapter 6, we present experimental evidence for the presence of PM in the rings. We apply the techniques described in Chapter 5 to our data, reporting estimates of the location, structural period, and orientation of these PM features. We compute estimates using two different model types to represent PM, and show consistent results. We briefly review a phenomenon known as viscous overstability, and examine its potential to explain the presence of PM in some regions of the rings.

Chapter 7 contains a summary of the key findings presented in this dissertation, along with a discussion of some important open questions and some suggestions for future work.

A summary of the major contributions of this work are:

1. We uncovered five distinct locations in Saturn’s rings A and B exhibiting highly periodic, fine-scale variation in the ring optical depth. The physical period of these variations range between 100–250 meters [*Thomson et al.*, 2007].
2. An exhaustive study, comparing the results of a multiple scattering formulation of Mie theory against the results of scalar diffraction theory. The study, which examined 2-, 3-, and 10-sphere clusters of particles, shows that diffraction theory accurately predicts the far-field scattering pattern of particle aggregates, as long as the region of interest is limited to electrically large particles scattering in the near-forward direction [*Thomson and Marouf*, 2009].
3. Derivation of the exact solution for the five-term power-law expression of Allan variance, showing that the exact solution and the well-known approximate solution converge very quickly; *i.e.*, the approximate form is sufficient and satisfied by most imaginable measurement conditions [*Thomson et al.*, 2005]. An adaptation of this paper is included as Appendix D.
4. Demonstration of the equivalence of the Radon and Abel Transforms, as they are applied in atmospheric radio occultation [*Thomson and Tyler*, 2007]. An adaptation of this paper is included as Appendix E.

In this dissertation, we attempt to conform to the variable naming conventions established *a priori* in the literature to the greatest extent possible. This inevitably leads to some overlap in the use of variables, since the work contained herein spans several fields—electromagnetics, optics, remote sensing, and planetary science. We explicitly describe variable assignments throughout the dissertation to minimize potential confusion. The reader is referred to the List of Symbols provided in the preface material for a complete list of all symbol assignments used in this dissertation.

h

Chapter 2

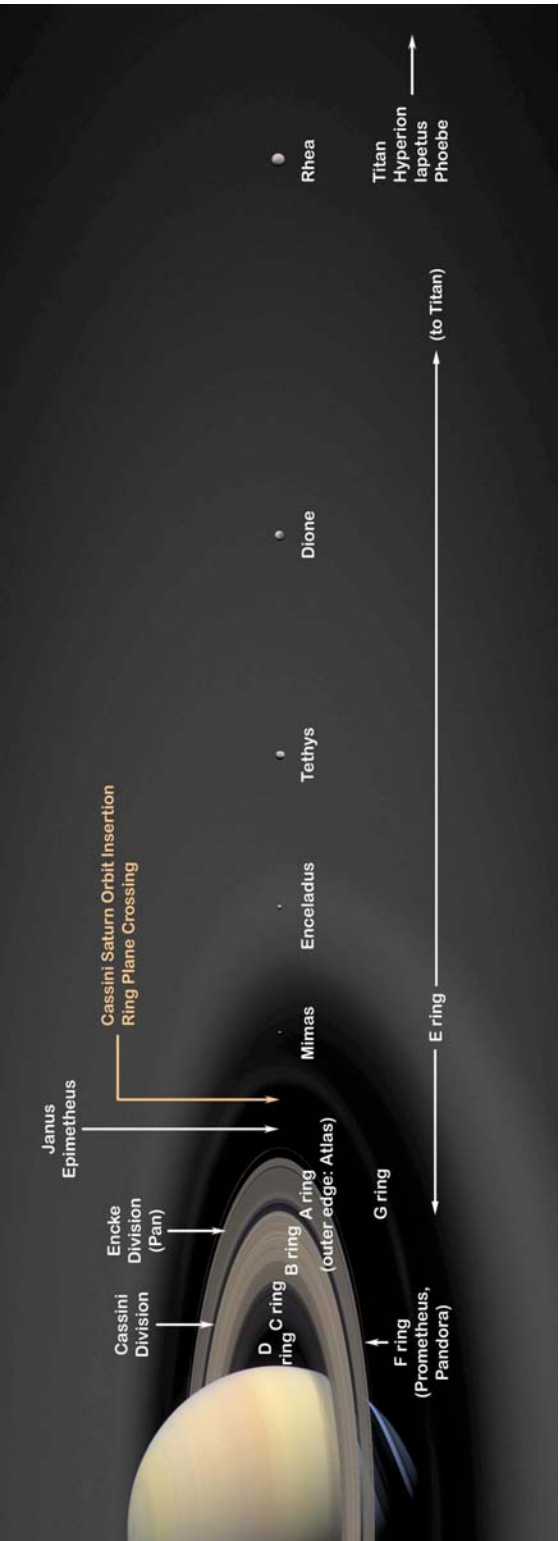
Saturn Ring Structure and Dynamics

The basic structure of Saturn’s rings is depicted in Figure 2.1. Rings A, B, and C (and the Cassini Division, which separates Ring A from B) are collectively known as Saturn’s main rings or the classical ring system. Interior to the main rings is the D ring, which was discovered by a combination of Voyager observations and a single ground-based stellar occultation [Hedman *et al.*, 2007]. From the inner edge of Ring D to the outer edge of Ring A the rings extend radially for 69,875 km, from approximately 66,900 km to 136,775 km from Saturn’s center, or $1.110R_s$ through $2.269R_s$, where $R_s = 60,268$ km is the equatorial radius (at the 1 bar atmospheric pressure level) of Saturn. The main rings are thought to be on the order of 10–20 meters thick [Deau *et al.*, 2008; Charnoz *et al.*, 2009]. Exterior to the main rings, the narrow and braided Ring F is centered at 140,180 km ($2.326R_s$); and the tenuous G and E rings lie between 170,000–175,000 km ($2.82R_s$ – $2.90R_s$) and between 181,000–483,000 km ($3.00R_s$ – $8.01R_s$), respectively. Ring G is composed primarily of dust [Cuzzi *et al.*, 2009], while Ring E is composed primarily of water ice [Hillier *et al.*, 2007].

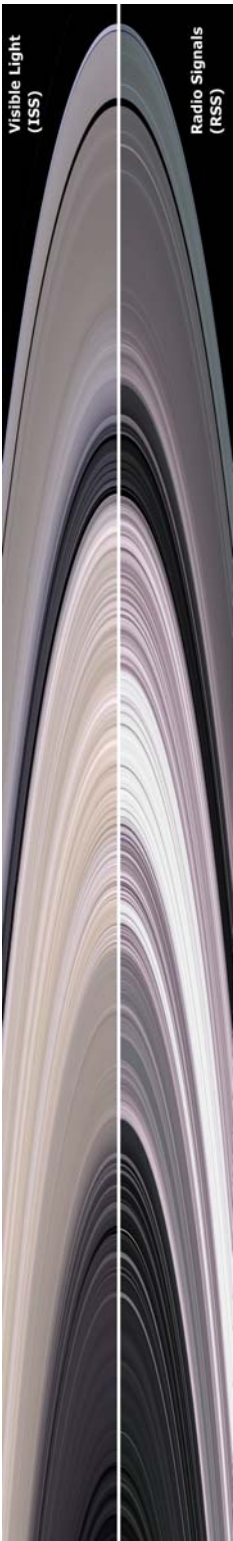
In 2009 the Phoebe ring was discovered [Verbiscer *et al.*, 2009], an $80R_s$ -thick band of dust spanning 3.5×10^6 – 1.8×10^7 km ($59R_s$ – $300R_s$), and is thought to comprise ejecta resulting from meteoroid impacts on the Saturnian moon Phoebe. The Phoebe

ring is in the solar system ecliptic, inclined by about 27° with the other rings, and its particles likely orbit Saturn in retrograde, similar to Phoebe. A comprehensive description of the rings is included in *Dougherty* [2009]. Properties of the various ring regions are summarized in Table 2.1.

Saturn's main rings comprise particles of predominantly crystalline water ice, mixed with impurities that give the rings a slight reddish color [*Cuzzi et al.*, 2009]. Particle sizes range from motes of dust to small moons [*Cuzzi et al.*, 2009; *Charnoz et al.*, 2009]. Figure 2.3 is a false-color image of the rings produced from radio occultation data using techniques described in Section A.2. Colors in the figure indicate which range of ring particle sizes is predominant locally in the population, as described in the figure caption.



(a) Structure of Saturn's ring system



(b) Comparison of the opacity of Saturn's main rings at optical and radio wavelengths. In both images, brightness indicates greater optical depth.

Figure 2.1: Structure of Saturn's rings. (a) and (b) are PIA03550 and PIA07874, respectively, from the NASA Photjournal website. See Table 2.1 for a summary of the location of the various ring regions relative to Saturn's center of mass.

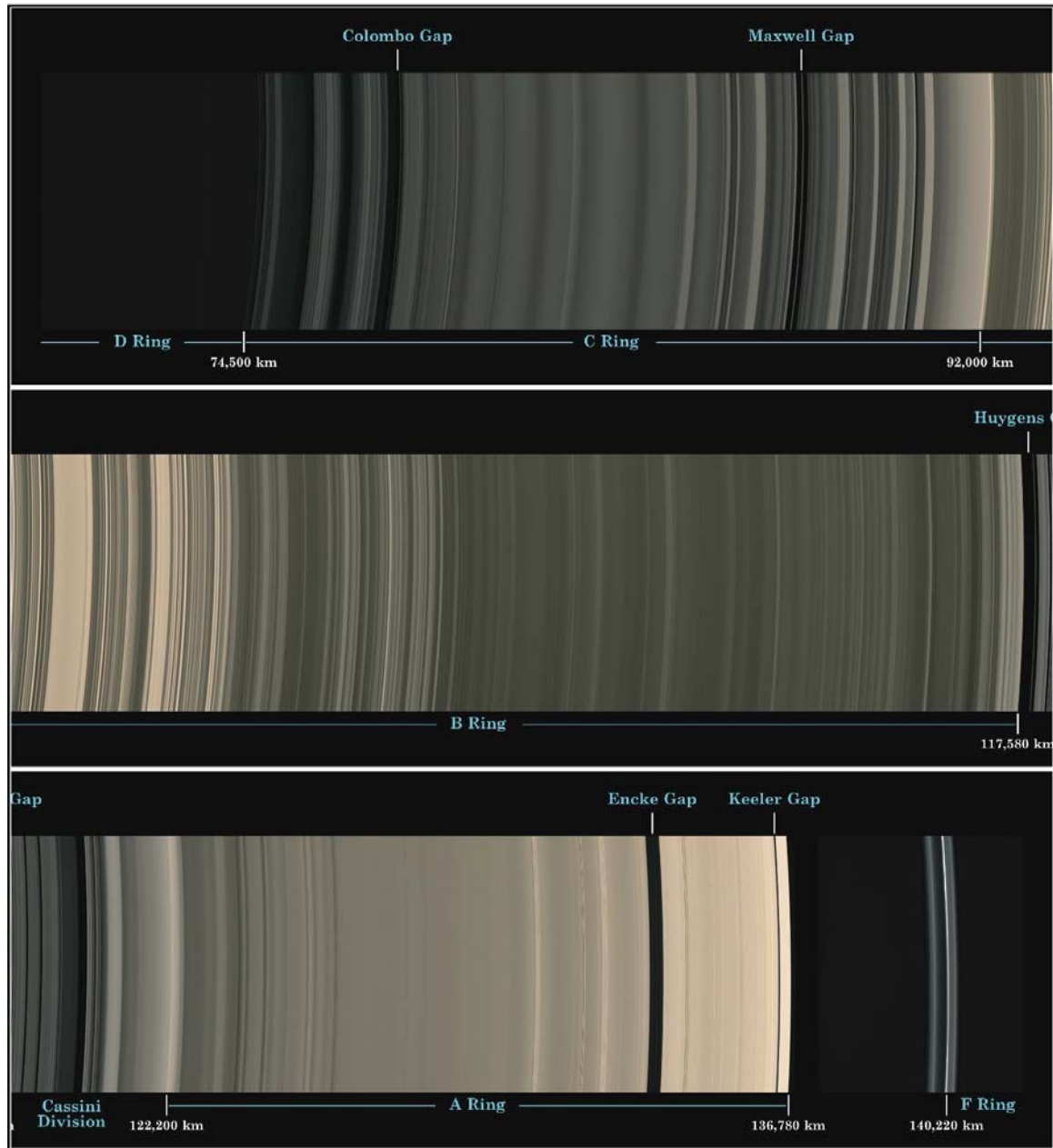


Figure 2.2: Scale and structure of Saturn’s main rings and Ring F. This image is adapted from PIA08389 from the NASA Photojournal website. PIA08389 combines 45 images—15 separate sets of red, green and blue images—taken over the course of about 2.5 hours, as Cassini scanned across the rings. The images were obtained on May 9, 2007, at a distance of approximately 1.1 million km from Saturn. The radial scale is approximately 6 km/pixel.

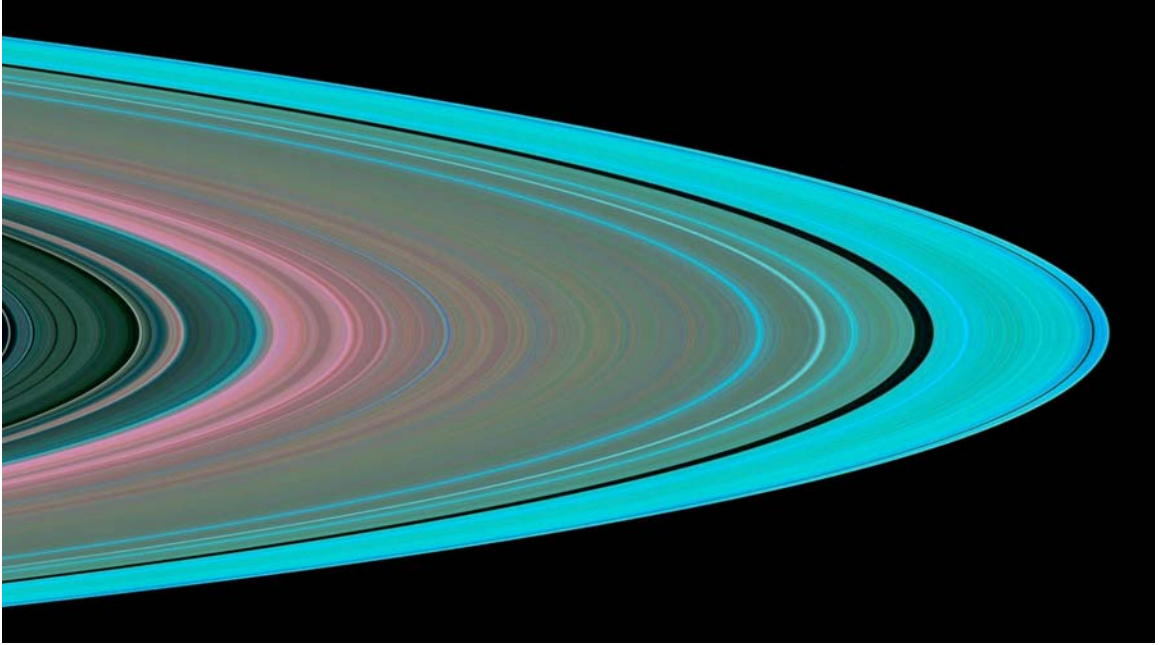


Figure 2.3: Particle size distributions in Saturn's Cassini Division and Ring A. This image was constructed from optical depth profiles produced at three radio wavelengths (0.94, 3.6, and 13 centimeters, or Ka-, X-, and S-bands, respectively). The structural resolution is about 10 kilometers. Shades of red indicate an absence of particles less than 5 centimeters in diameter. Green and blue shades indicate regions where there are particles of sizes smaller than 5 centimeters and 1 centimeter present, respectively. A color shift from red to blue indicates an increase in the relative abundance of smaller (< 5 cm) sized particles. The image indicates a general increase in the population of these small particles with radial distance, from inner to outer Ring A. The deep blue shades in the vicinity of the Keeler gap (the narrow dark band near the edge of ring A) indicate an increased abundance of even smaller particles, of diameter less than a centimeter. It is thought that frequent collisions between large ring particles in this dynamically active region likely fragment the larger particles into more numerous smaller ones. Image is PIA07960, NASA Photojournal website.

Table 2.1: Properties of Saturn's Ring System. Adapted from *de Pater and Lissauer [2001]*.

	Main rings								
	D ring	C ring	B ring	Cassini division	A ring	F ring	G ring	E ring	Phoebe ring
Radial location (R_s)	1.09– 1.24	1.24– 1.53	1.53– 1.95	1.95– 2.03	2.03– 2.27	2.32	2.75– 2.87	3–8	59– 300?
Vertical thickness			< 1 km	< 1 km	< 1 km			10^3 – 2×10^4 km ^a	$4.8 \times$ 10^6 km
Normal optical depth	\approx 10^{-5} – 10^{-4}	0.05– 0.2	1–3	0.1–0.15	0.4–1	1	10^{-5} – 10^{-4}	10^{-7} – 10^{-6}	??
Particle size	μm	mm–m	cm–10 m	cm–10 m	cm–10 m	μm –cm	μm – cm?	$1 \mu\text{m}^b$??

^aIncreases with radial location^bVery narrow distribution

2.1 Ring Macrostructure

If the only forces acting on planetary ring particles were the gravitational pull of the host planet and inter-particle collisional forces, then all planetary ring systems would evolve over time into thin, featureless discs. Perturbations due to the gravitational influence of moons external and internal to the rings act in conjunction with self-gravitational effects to produce large-scale features—or macrostructure—in the rings. Some examples of ring macrostructure include ring divisions, gaps, waves, and edges. These features exist throughout Saturn’s main rings, on length scales of tens to thousands of kilometers.

Ring particles having orbital frequency $n(r)$ that are perturbed from circular orbits will oscillate freely about their reference circular orbit with epicyclic (radial) frequency $\kappa(r)$ and vertical frequency $\mu(r)$. The gravitational consequences of Saturn’s oblateness cause a separation of these frequencies, $\mu(r) > n(r) > \kappa(r)$, and thus the radial location of the vertical and horizontal resonances associated with a particular moon are different. Ring particles orbiting at or near these resonance locations experience coherent ‘kicks’, which over time can contribute to significant forced oscillations (*e.g.*, *de Pater and Lissauer* [2001]).

Resonant forcing of particles in the rings by moons external to a particular ring location can create two main types of ring macrostructure: gaps or ring boundaries, and spiral density or bending waves [*Cuzzi et al.*, 1984; *Rosen*, 1989; *de Pater and Lissauer*, 2001]. These features are generated by torques that transport angular momentum between the resonant moon(s) and ring material. The disturbance (forcing) frequency due to the influence of a particular moon is given by,

$$\omega_f = m_\theta n_s \pm m_z \mu_s \pm m_r \kappa_s \quad (2.1)$$

where the subscript s indicates that ω_f is tied to a specific satellite s , and m_θ , m_z , and m_r are non-negative integers with m_z odd for vertical forcing and even for horizontal forcing [*de Pater and Lissauer*, 2001]. A horizontal resonance condition, also known

as a Lindblad resonance, occurs at the radial location $r = r_L$ when,

$$\omega_f - m_\theta n(r_L) = \pm \kappa(r_L) \quad (2.2)$$

Vertical resonances are excited at $r = r_v$ if,

$$\omega_f - m_\theta n(r_v) = \pm \mu(r_v) \quad (2.3)$$

Eq. (2.2) yields two possible solutions for r_L ; we refer to the lesser (greater) of these as the inner (outer) Lindblad resonance. Similarly, eq. (2.3) yields an inner and outer vertical resonance. The oblateness of Saturn ensures that $r_L > r_v$ for resonances excited by a given moon.

Specific resonances are identified by the ratio,

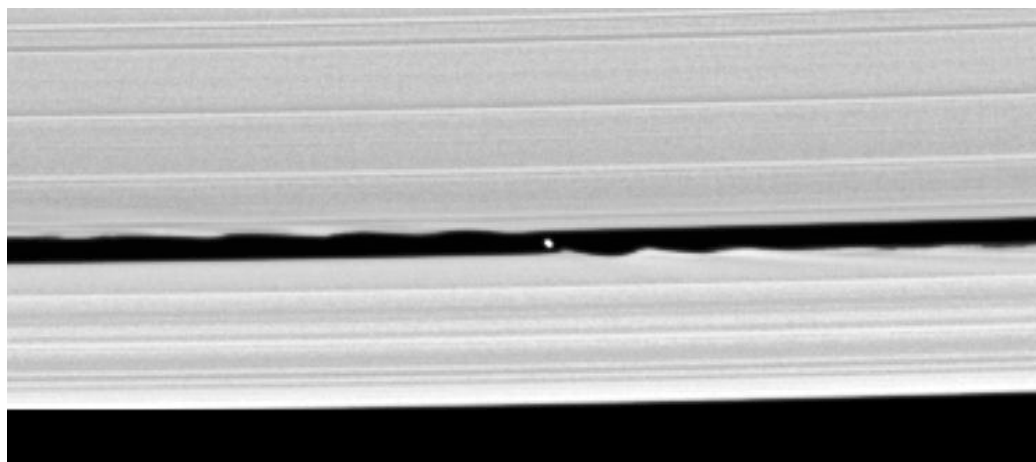
$$\frac{n(r_{v,L})}{n_s} \approx \frac{m_\theta + m_z + m_r}{m_\theta - 1} = \frac{l}{m_\theta - 1} \quad (2.4)$$

The strongest horizontal resonances have $m_z = m_r = 0$, while the strongest vertical resonances have $m_z = 1$, $m_r = 0$. By convention, it is common to reference a resonance by its ratio, written as $l : (m_\theta - 1)$.

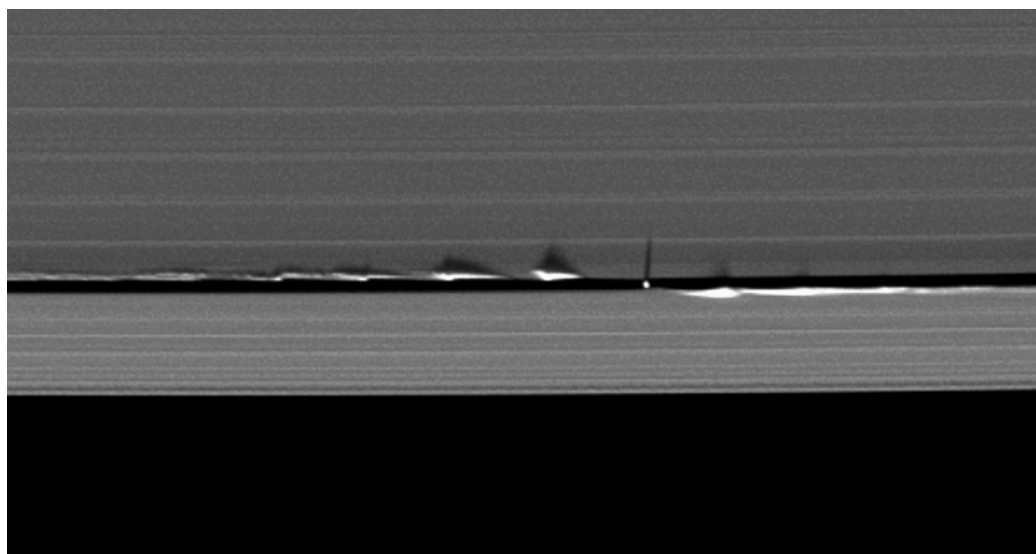
2.1.1 Gaps and Ring Boundaries

Lindblad resonances are responsible for the creation of sharply defined, non-circular ring boundaries. The outer edge of Ring B is coincident with the 2:1 inner Lindblad resonance (ILR) of the moon Mimas, generating an oval boundary that co-rotates with Mimas. Ring A's outer boundary corresponds to the 7:6 resonance of the coorbital moons Janus and Epimetheus, and has a seven-lobed boundary. To create a sharp edge/boundary in the rings or to maintain a ring gap, a resonance must exert sufficient torque on the rings to offset the localized viscous spreading of ring material.

Gaps in the rings are created by the same process that creates edges. In the optically thin Ring C, resonances are responsible for the creation of many gaps, often accompanied by optically thicker ringlets. Gap formation requires more force in the

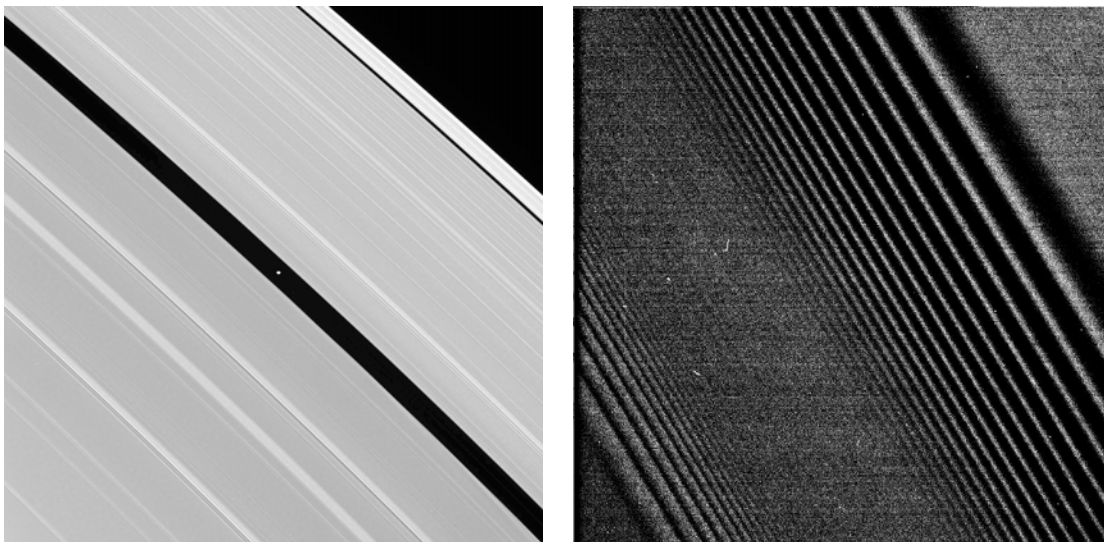


(a) Image PIA06237, NASA Photojournal website.



(b) Image PIA11653, NASA Photojournal website.

Figure 2.4: The Keeler Gap and its shepherding moon Daphnis. (a) Daphnis occupies an inclined orbit within the 42-km wide Keeler Gap. Torques exerted by the moon on ring particles as they move past the moon (moving left-right in this figure) create horizontal and vertical ripples on the inner and outer gap edges. Resolution is 3 km/pixel. (b) The small sun-ring plane angle in this mid-August 2009 Saturn equinox image causes out-of-plane structures to cast long shadows across the rings. The vertical structure of the Keeler Gap edges and the out-of-plane position of Daphnis are captured. Gap edges are 0.5–1.5-km tall; approximately 50–150 times taller than the average ring thickness. Resolution is 5 km/pixel.



(a) Image PIA07587, NASA Photojournal website.

(b) Image PIA06093, NASA Photojournal website.

Figure 2.5: Gaps, Density and Bending Waves in Ring A. (a) The Keeler and Enke Gaps of outer Ring A. The moonlet Pan (28-km diameter) is shown embedded within the Enke gap at the center of this image. The two most prominent bright banded features (lower left) are spiral density waves, which propagate outward through Saturn’s rings. Brighter features indicate regions with higher particle densities (and greater optical depth). The image scale is 5 km/pixel. (b) Density and bending waves in Ring A. This backlit image shows the Prometheus 12:11 density wave (lower left) and the Mimas 5:3 bending wave (middle-right). The scale of this image is about 290 meters/pixel.

optically thick A and B rings—resonances of similar strength to those that produce gaps in Ring C produce only spiral waves in Rings A and B.

Gaps are also created by embedded moons, which act to clear material from a region of the rings. The moonlet called Pan is responsible for the creation of the Enke Gap (Figures 2.1(a), 2.2, and 2.5(a)). In 2005 the Cassini imaging team discovered a 7-km diameter moon, named Daphnis (formerly S/2005 S1), which is responsible for creating the Keeler Gap, shown in Figures 2.2, 2.4, and 2.5(a).

Moonlets too small to create gaps are thought to be responsible for creating so-called ‘propeller’ features in the rings [Colwell *et al.*, 2009]. Propellers consist of elongated enhancements in the local ring particle density which are oriented in the

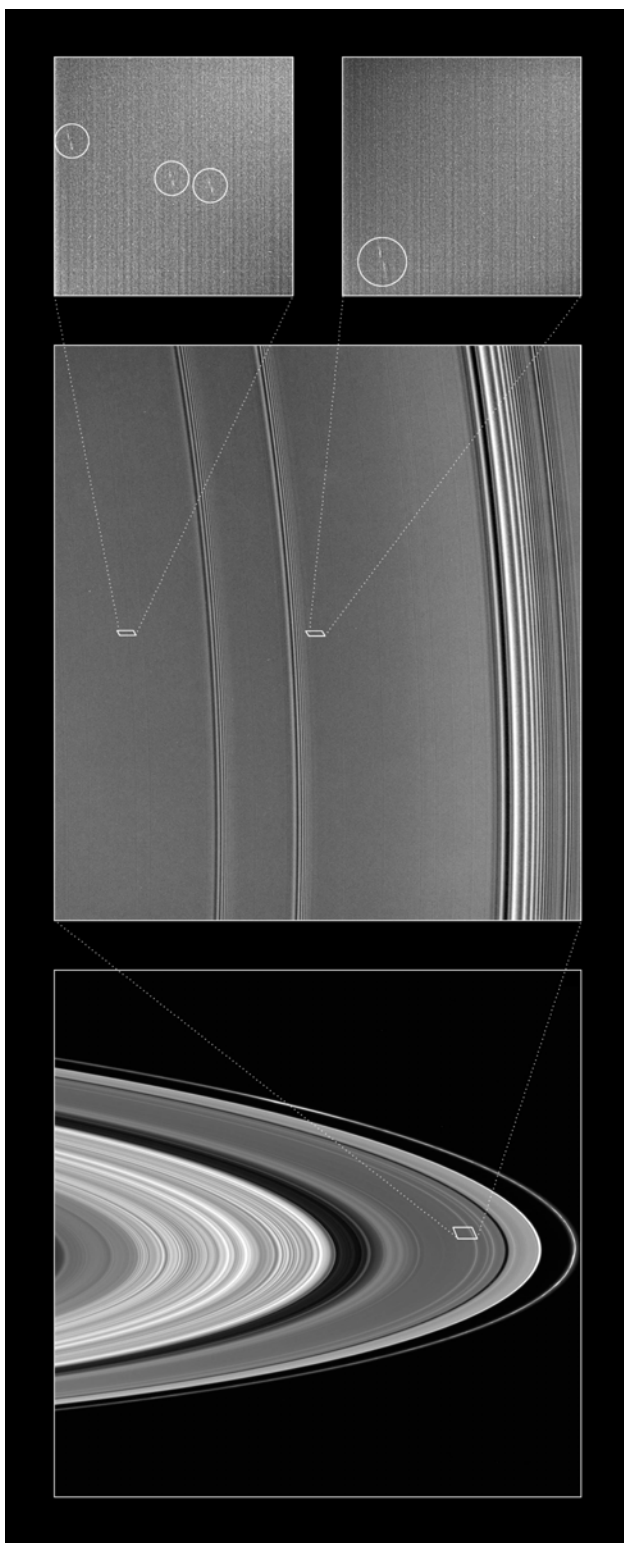


Figure 2.6: Propeller Features in Outer Ring A. The center image is approximately 1,800 km across and shows the Janus/Epimetheus 13:11 density wave at the bottom, as well as two smaller density waves. The propellers appear as double dashes in the two close-up images at the right and are circled. Unseen moonlets lie in the center of each structure. The propellers are about 5 km long from tip to tip and do not change as they orbit the planet. Image resolution of the right-hand panels is 52 meters/pixel. Image is PIA07792, NASA Photojournal website.

direction of orbital motion and extend for several kilometers from tip-to-tip. Propellers can also open local ring gaps. The moonlets responsible for the propeller features shown in Figure 2.6 are thought to be on the order of 40–500 meters in diameter (compare with the 7-km diameter of Daphnis) [*Tiscareno et al.*, 2008].

2.1.2 Spiral Density and Bending Waves

Spiral bending and density waves propagate from all of the strong satellite resonance locations in the rings, when the torques exerted on ring material by the resonance are insufficient to transport material away and maintain edges or gaps. Spiral waves are seen broadly throughout Ring A, and are the cause of the prominent optical depth variations visible in Figures 2.4, 2.5, and 2.6.

Density waves manifest as an in-plane compression and rarefaction of the local number density of ring particles, originating at Lindblad resonance locations in the ring plane. Similarly, bending waves are excited at vertical resonance locations, where the satellite resonance induces small inclinations in the local orbits of ring particles. The resulting vertical excursions (of up to ~ 400 meters [*de Pater and Lissauer*, 2001]) or undulations of particles about the ring plane gives the rings a corrugated appearance. For both density and bending waves, the self-gravity of particles within the ring disk provides the restoring force that allows waves to propagate away from the origin of the resonant disturbance. *Rosen* [1989] produced an excellent visual depiction of density and bending waves, reproduced here in Figure 2.7. The self-gravity of the ring particles effectively distributes the torque applied by the resonant satellite, from particles at r_L or r_v to adjacent particles. Waves are the mechanism by which resonant forcing energy diffuses away from the disturbance. Density waves are excited at the ILR of the resonant satellite, and propagate towards Saturn. Bending waves are excited at the inner vertical resonance (IVR), and propagate outward in the rings away from Saturn, except for so-called nodal bending waves, $m_\theta = 1$, which propagate towards Saturn. For all spiral waves, the number of spiral arms created is equal to m_θ .

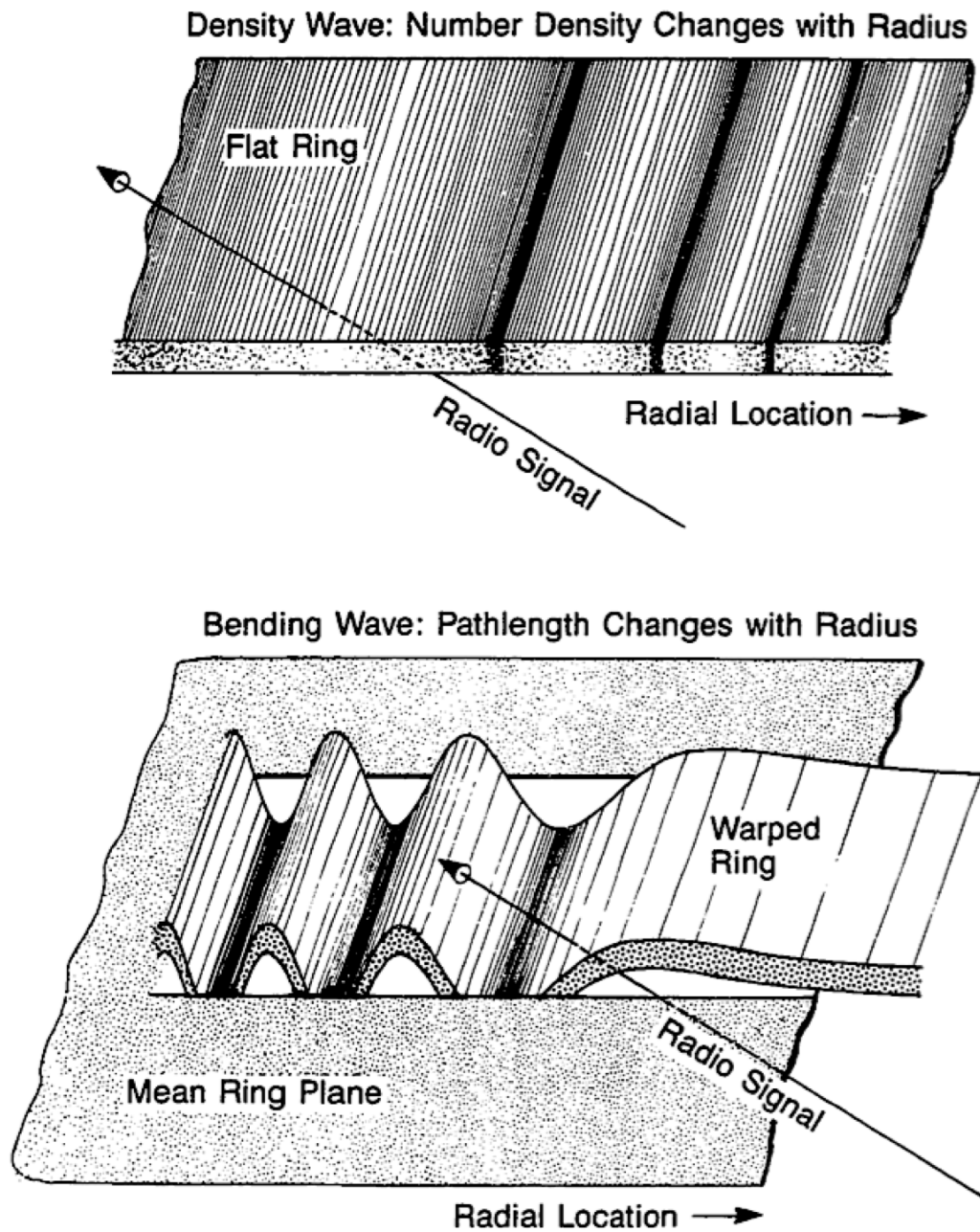


Figure 2.7: Schematic of density and bending waves, showing a probing radio ray. From *Rosen* [1989].

2.2 Ring Microstructure

Small scale structures in the rings, which we denote ring microstructure, form as a result of the influence of inter-particle gravitational and collisional forces, in the presence of the ‘background’ gravitational forces at play locally. We define microstructure as a discernible organization of ring particles into groups or clusters, with length scales on the order of tens to several hundreds of meters. Although the relevant length scales of microstructure itself are as described, a region containing microstructure may extend over tens or thousands of kilometers within the rings. Notable examples of distinctive microstructure include gravitational wakes, and periodic microstructure (PM).

2.2.1 Gravitational Wakes

Dynamical simulations of planetary rings predict that the interplay of collisional and gravitational forces produces gravitational wakes broadly within Saturn’s main rings [Salo, 1992, 1995; Tiscareno *et al.*, 2009; Dougherty, 2009]. Observed optical depth variations with ring longitude in Saturn’s Rings A and B—a phenomenon known as azimuthal asymmetry—provide indirect evidence for the existence of gravitational wakes [Salo *et al.*, 2004; Colwell *et al.*, 2006; French *et al.*, 2007; Dougherty, 2009].

Wakes form in the rings at cant angles of 20° – 25° to the local azimuthal unit vector. For particles in circular orbits, this is also the local particle velocity unit vector. The cant angle is determined by particle self-gravity in combination with the local Keplerian shear, which is the sliding of local, radially adjacent ring particles past each other due to their differing orbital velocities (the orbital velocity of particles in circular orbits is proportional to $\sqrt{1/r}$, where r is the radial distance of an orbiting particle from Saturn’s center of mass). Wakes are ephemeral structures, constantly being pulled apart by Keplerian shear and re-formed by self-gravity. Although their specific composition is in a state of flux, the wake structure remains constant in a statistical sense, as long as the local physical conditions (particle composition, size distribution, density, etc.) remain relatively constant. Figure 2.8 is a snapshot from a dynamical simulation [Salo, 2006] revealing the characteristic pseudo-periodicity and canting typical of gravitational wakes.

It is interesting to note that the spiral arms of the Milky Way galaxy are large-scale examples of gravitational wakes—in fact, this is the application for which the physics was first worked out in detail.

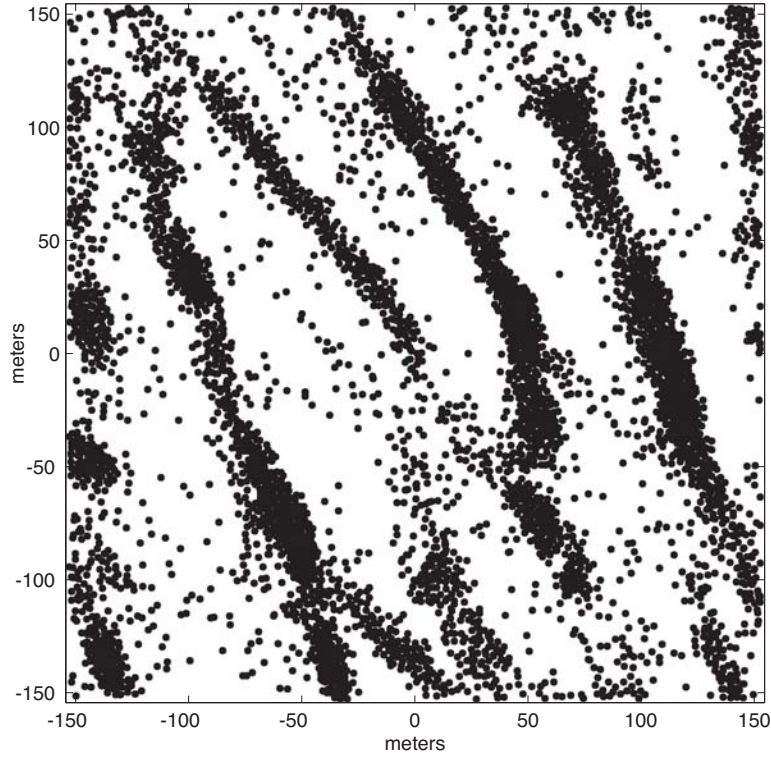


Figure 2.8: Gravitational wakes produced during dynamic simulation of Saturn’s Ring A. The simulation begins with a homogeneous spatial distribution of identically-sized particles. Wakes appear within a few simulated orbital evolutions of the spatial particle distribution. The x-axis is aligned with a radial vector from Saturn’s center; the y-axis is aligned with the azimuthal unit vector at (0,0), and thus points in the direction of Keplerian particle motion. This vignette is a projection of 5330 particles contained in the $300 \times 300 \times 55$ -meter volume defined in the simulation; other defined parameters are optical depth $\tau = 0.5$, surface mass density $\sigma_\rho = 500 \text{ kg m}^{-2}$, volumetric density $\rho = 450 \text{ kg m}^{-3}$, particle radii $a = 1.66 \text{ m}$. The parameters σ_ρ and ρ are discussed in greater detail in Appendix A.

2.2.2 Periodic Microstructure

In addition to the formation of wakes, the dynamical theory of the rings predicts the formation of stable regions of regular, azimuthally-symmetric density fluctuations on the scale of tens to hundreds of meters. The incipient condition believed to be responsible for these structures is known as viscous overstability (VO), a linear instability that occurs when the viscous stresses vary with number density in such a way that Keplerian shear energy reinforces and promotes growing density oscillations [*Latter and Ogilvie*, 2008]. Linear dynamical theory predicts the onset of these density oscillations, and non-linear dynamical theory predicts that the density oscillations saturate most strongly at length scales of 100–200 meters. Simulations by Schmit [*Schmit and Tscharnuter*, 1999; *Schmidt et al.*, 2001] and others have produced instantiations of fine-scale PM due to viscous overstability; see Figure 2.9. Although *Schmidt et al.* [2001] focus on Ring B, the environmental conditions necessary to support stable VO regions exist in parts of Ring A as well (see Chapter 6 for a more detailed discussion). Using the Cassini radio occultation experiment, we have directly observed fine-scale PM in Ring A consistent with the density fluctuations predicted by the saturated state of viscous overstability. Reporting those discoveries constitutes the primary objective of this dissertation.

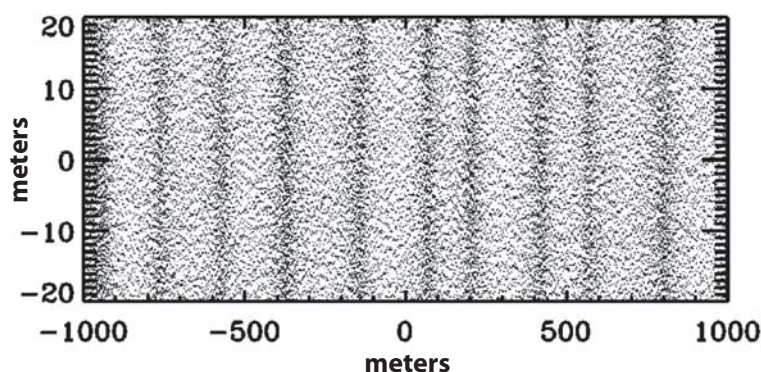


Figure 2.9: Dynamical simulations of the rings reported in *Schmidt et al.* [2001] produce fine-scale periodic microstructure due to viscous overstability (VO), with length scales on the order of 100 meters. The x- and y-axis alignment is as described in Figure 2.8, with simulated optical depth $\tau = 1$, particle radii $a = 1$ meter. Point (0,0) is centered at a distance 100,000 km from Saturn's center, corresponding to inner Ring B (see Figure 2.2).

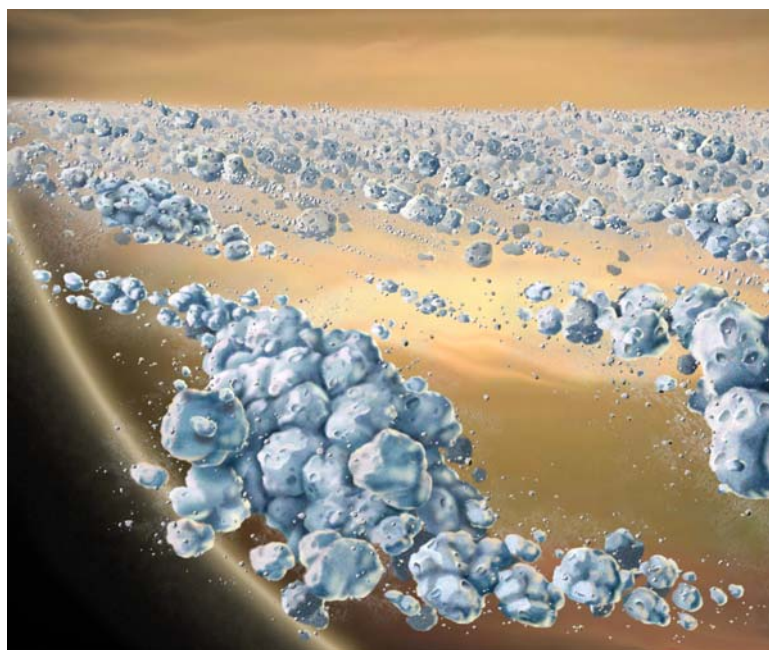


Figure 2.10: Artist Marty Peterson's rendition of the fine-scale composition and structure of Saturn's rings, based on a 1983 illustration by William K. Hartmann. The largest individual particles shown are a few meters across. Image PIA10081, NASA Photojournal website.

2.3 Models of Ring Microstructure

The interplay of forces discussed in Section 2.2 give rise to a broad range of possible microstructure in the rings. To illustrate this, we present a survey of dynamical simulation results for Saturn’s rings in Figure 2.11. Here, simulations are parameterized along two axes: the optical depth τ of the rings, and a ratio r_h which characterizes the importance of self-gravity relative to Saturn’s tidal force (*e.g.*, *Schmidt et al.* [2009]),

$$\begin{aligned} r_h = \frac{R_{\text{Hill}}}{a_1 + a_2} &= \left[\frac{(m_1 + m_2)}{3M_s} \right]^{1/3} \frac{r_o}{a_1 + a_2} \\ &= \left(\frac{\rho_o}{3\rho_s} \right)^{1/3} \left(\frac{r_o}{R_s} \right) \frac{(1 + m_1/m_2)^{1/3}}{1 + (m_1/m_2)^{1/3}} \end{aligned} \quad (2.5)$$

R_{Hill} is the mutual Hill radius for a pair of particles of radius a_1 and a_2 , having masses m_1 and m_2 and density ρ_o , r_o is the radial location of the particles relative to Saturn’s center of mass, and ρ_s and R_s are the mean density and radius of Saturn. Simulations shown in Figure 2.11 assume that ring particles have a normal coefficient of restitution—defined as the ratio of post-collisional to pre-collisional normal velocities of two colliding particles—of $\epsilon_n = 0.5$. ϵ_n is velocity and mass dependent, is sensitive to the mechanical and surface properties of the colliding particles, and can strongly affect the microstructure regimes predicted by dynamical simulations; see *Schmidt et al.* [2009] for more details.

Where self-gravity dominates tidal forces, simulations show that ring particles aggregate into clumps. Where self-gravity effects are relatively small and the optical depth is not too great, populations tend towards homogeneous ring particle distributions. Gravitational wakes can form throughout much of the remaining simulation space, including regions where viscous overstability produces axisymmetric density oscillations as well. In these simulations, the conditions for the onset of overstable oscillations are approximately $\tau > 1$, $r_h < 0.6$.

In this dissertation, we develop a method for estimating the physical dimensions of microstructure in Saturn’s rings by fitting the diffraction signature of various physical ring models to diffraction features contained in signals received from the Cassini

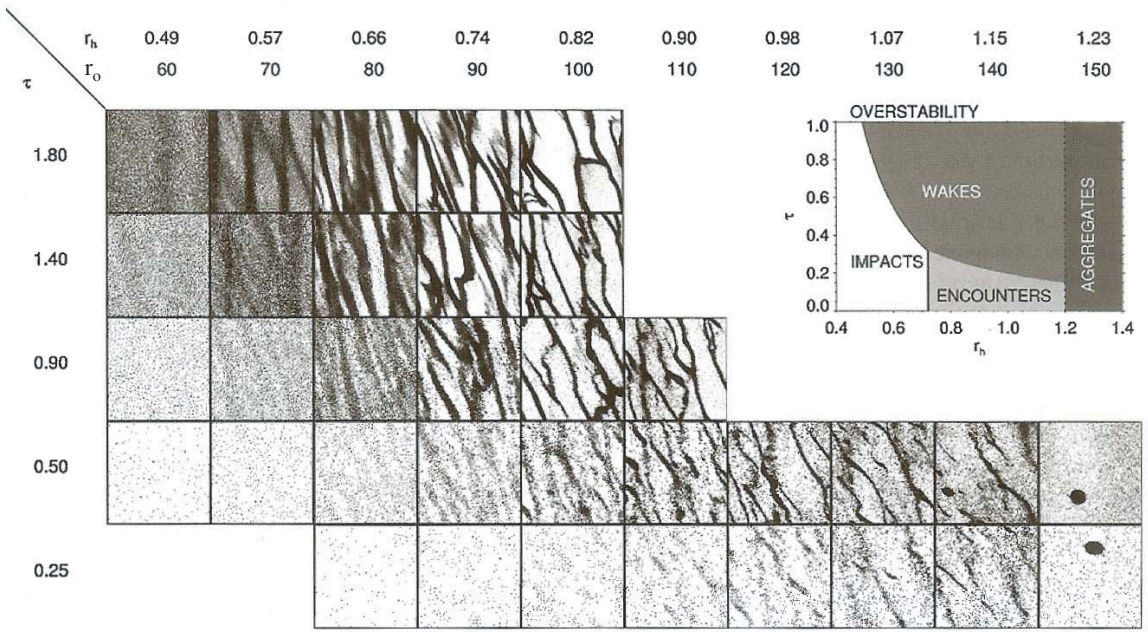


Figure 2.11: A survey of ring microstructure, showing dependence on normal optical depth τ and on the strength of self-gravity relative to tidal forces, quantified by the parameter r_h (see text). The distance r_o from Saturn's center is indicated, paired with the corresponding value of r_h when $\rho_o = 900 \text{ kg m}^{-3}$ (*i.e.*, consistent with the density of water ice). The simulation space comprises identical particles with coefficient of restitution $\epsilon_n = 0.5$. The figure insert shows a schematic of the regions in r_h - τ space where different physical processes control the nature of the ring microstructure that is shown in the main plot. Indicated physical processes are collisional (impacts), pairwise-gravitational (encounters), self-gravitational (aggregates), and a combination of self-gravitational and tidal (wakes). Note that in the upper left region of the plot, $\tau > 1$, $r_h < 0.6$, axisymmetric overstable oscillations coexist with gravitational wakes in the simulation. Adapted from *Schmidt et al.* [2009].

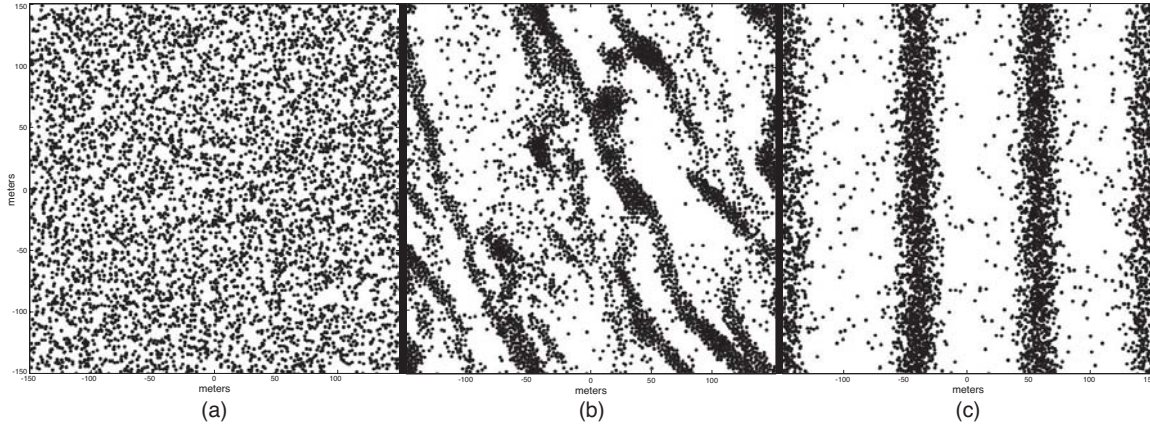


Figure 2.12: Models of ring microstructure. The three panels each contain 5330 3.32-meter diameter particles filling a $300\text{m} \times 300\text{m} \times 55\text{m}$ volume. Populations represent models of (a) homogeneously distributed thick rings, (b) gravitational wakes, and (c) periodic microstructure.

spacecraft during multiple radio occultation observations. To this end, we introduce four microstructure models for use in the fitting process:

1. Homogeneously distributed thick rings
2. Packed (*i.e.*, crowded) monolayers
3. Gravitational wakes
4. Periodic microstructure (PM)

Examples of homogeneous, wake, and PM ring models are shown in Figure 2.12. Packed monolayers are predicted by some ring theorists, who contend that collisional processes drive an evolution towards dynamically ‘cold’ rings comprising a single layer of relatively large particles, surrounded by a cloud of smaller particles [Deau *et al.*, 2008]. Monolayer distributions have been proposed by some researchers to explain evidence of non-homogeneous ring particle distributions seen in radio occultation data (*e.g.*, see Figures 4.5E and 5.1). Clumped microstructure is not modeled, since Cassini signals show no evidence of microstructure in regions where clumping is predicted by dynamical simulations.

The use and parameterization of these models is described in detail in Chapter 5.

2.4 Summary

The dynamical interplay of collisional and gravitational forces produces fine-scale structure in Saturn's rings, manifesting as anisotropic particle distributions. Observations provide evidence for the existence of gravitational or density wakes [*Salo et al.*, 2004], axisymmetric periodic microstructure [*Colwell et al.*, 2007; *Thomson et al.*, 2007], and rarified homogeneous particle distributions. Clumped distributions have been shown to be possible theoretically in computer models of planetary rings, *e.g.*, *Salo* [1992, 1995], but so far have not been observed experimentally in any conclusive way.

In Chapter 3, we examine the electromagnetic (EM) scattering properties of aggregates of icy ring particles. That analysis plays a key role in our treatment of the Cassini radio occultation experiment (which we describe in detail in Chapter 4), since a major component of the received Cassini signal is forward-scattered from ring particles to receivers on Earth. We show that for the purposes of our experiment, a full EM solution is not required to accurately predict the forward scattering behavior of ring microstructure. Rather, we show that a diffraction theoretic approach produces accurate, predictive results that closely mimic the results of EM theory, while greatly reducing the complexity of the forward scattering model.

h

Chapter 3

EM Scattering and Diffraction from Ring Particle Clusters

Small-scale structure in Saturn’s rings is evident in signals received during Cassini radio occultation observations. During those observations—which are described in detail in Chapter 4—individual particles forward-scatter radio signals from within a region of the rings illuminated by Cassini’s high-gain antenna. A small but detectible fraction of that scattered energy propagates along the near-forward or paraxial direction, and is received by antennas belonging to NASA’s Deep Space Network (DSN). Superimposed on the scattered signal is the diffraction signature of the arrangement of those particles in the ring plane.

We seek a method that relates the fine-scale structure of Saturn’s rings to the signals we receive during Cassini radio occultation observations. Perhaps the most straight-forward approach is to model the rings as an aggregate of spheres of varying size, and to compute the far-field forward-scattering behavior of the aggregate using a multi-particle formulation of Mie theory. Using this approach, we solve Maxwell’s equations—subject to the appropriate boundary conditions—by computing field expansions in vector spherical harmonics centered on each sphere in the aggregate. We account for both near- and far-field interactions between the particles, yielding a rigorous electromagnetic solution to the multiple-scattering problem. This suite of expansions is re-expressed relative to a common origin, thereby expressing the total

radiated field in a single coordinate system [Xu, 1995, 1997]. This solution is exact in the limit of the expansions, unrestricted by limiting assumptions (*e.g.*, that the particles are in each other’s far field, etc.). However, the exactness of the multiple Mie scattering solution comes at a high price—computational complexity. As we report in this chapter, the time required to compute the Mie solution grows rapidly with the size of the scatterers—even for a small number of spheres. Since useful models of ring microstructure contain thousands of electrically large (see eq. (3.40)) particles, a multi-particle Mie theory solution to such a model is well beyond the capabilities of our computer simulation resources.

Another method of estimating the EM scattering behavior of the rings is to compute the far-field pattern using scalar diffraction theory. In this chapter we present the results of a comparative study where we model aggregates that contain as many as ten particles, and compute their far-field radiation patterns using both EM and diffraction theory. We show that for the observation conditions of the Cassini radio occultation experiment, the predictions of diffraction theory are nearly identical to those produced using a full EM-theoretic approach, the latter of which is vastly more computationally intensive [Thomson *et al.*, 2006b; Thomson and Marouf, 2009]. We apply this result in Chapter 5, using the diffraction patterns computed from models of ring microstructure (introduced in Chapter 2) in a comparative analysis with forward-scattered Cassini radio signals. We use this procedure to characterize fine-scale periodic structure in Saturn’s rings [Thomson *et al.*, 2007], and present those results in Chapter 6.

3.1 Introduction

Gustaf Mie is commonly acknowledged as the first to publish a complete solution for EM scattering from a single sphere [Mie, 1908]. His solution was formulated by expanding the incident and scattered fields in vector spherical harmonics. Coefficients in the expansion of the incident field are known since the incident field itself is known. The scattered field expansion coefficients are then readily determined from

the appropriate boundary conditions (*e.g.*, *van de Hulst* [1981]; *Bohren and Huffman* [1998]). *Trinks* [1935] was the first to apply the modal expansion method of Mie in conjunction with the translation-addition theorem of vector spherical harmonics, in an effort to extend the Mie approach to scattering from two spheres. However, computational complexities arising from the particular implementation of the translation-addition theorem used limited his results to sphere radii much less than a wavelength (Rayleigh regime). *Liang and Lo* [1967] used an improved formulation of the translation-addition theorem to extend the work of Trinks to treat spheres with radii on the order of a wavelength (resonance region). The two-sphere theory was subsequently extended to spheres of radii on the order of tens of wavelengths when *Bruning and Lo* [1971a, b] developed a recursion relation for the translation-addition theorem, thus improving its computational efficiency.

With the advent of digital computers, researchers began to adapt Mie theory to obtain theoretical solutions for scattering by layered spheres, oblate spheres, and multiple scatterers. *Fuller* [1987] developed an algorithm to compute the multiple scattering problem for up to five electrically large spheres using an order of scattering approach. More recently, Xu [*Xu*, 1995, 1997; *Xu and Gustafson*, 1997] extended the theory to model multi-particle scattering from a system of spherical scatterers, each of fixed radius and refractive index. It is Xu’s algorithm that we use in our study, and his formulation that we present in Section 3.2.2 as background.

For instances in which the wavelength of incident light is small as compared with the size of the spherical particles, provided that the scattering pattern of the aggregate is observed at a sufficient distance from the aggregate itself, scalar diffraction theory yields accurate results for the fields scattered from objects. This was shown analytically for scattering from a single sphere in early work by *Nicholson* [1910, 1912] and *Bromwich* [1920]. For the interested reader we recommend, *e.g.*, *Theimer et al.* [1952] for a more general treatment of the applicability of scalar diffraction theory. The notion that diffraction theory could be applied effectively to aggregates of electrically large particles was bolstered further by the work of *Gresh* [1990], who modeled monochromatic light scattering and extinction cross-sections for systems of spherical particles using Fuller’s multiple scattering code [*Fuller*, 1987]. Her work showed

that for electrically large particles (size parameter $x > 8$, where x is the ratio of 2π times the particle radius to the wavelength λ of the illuminating radiation; see eq. (3.40) below), the projected area of the particle aggregate is the dominant factor in determining the extinction of the incident signal, as is the case for an isolated sphere. Further, Gresh showed that the extinction cross section of aggregates of electrically large particles approaches twice the area blocked by the particles ($C_{\text{ext}} = 2A_{\text{physical}}$)—a well-known paradoxical result predicted by scalar diffraction theory (*e.g.*, *van de Hulst* [1981]), further suggesting that diffraction theory may offer an accurate and computationally efficient alternative to Mie theory.

The study described in this chapter is rooted in work done by *Marouf* [1997] to investigate extinction and forward-scattering of electromagnetic waves by general planetary ring models based on a diffraction screen approach. The models may include particle crowding, clustering, and anisotropic spatial distribution. For this we replace the three-dimensional distribution of particles in the rings by a randomly blocked diffraction screen, placed behind the rings and normal to the incident wave direction. On the screen, the fields are assumed to be zero over the shadow area cast by ring particles, and are the unperturbed incident fields otherwise. The demanding electromagnetic interaction problem is thus replaced by the relatively simpler problem of characterizing the random diffracted field in terms of statistical averages of the stochastic geometry of the shadow area [*Marouf*, 1994].

Here we extend the earlier work of *Marouf* [1993] by considering broad geometrical configurations of particle clusters, and show that for EM scattering from a cluster of electrically large spheres—either singly-sized or belonging to a size distribution—there is excellent agreement between the exact Mie solution and the diffraction theory approximation when the angular range of interest is limited to near-forward scattering. This agreement holds over a broad range of particle separation and orientation configurations relative to the incidence direction, including cases when the projected area of particles overlap. It also holds true for both lossless and lossy dielectric particles. This result indicates that edge diffraction by the shadow area is the dominant contributor to the overall near-forward scattering behavior.

3.2 Theoretical Background

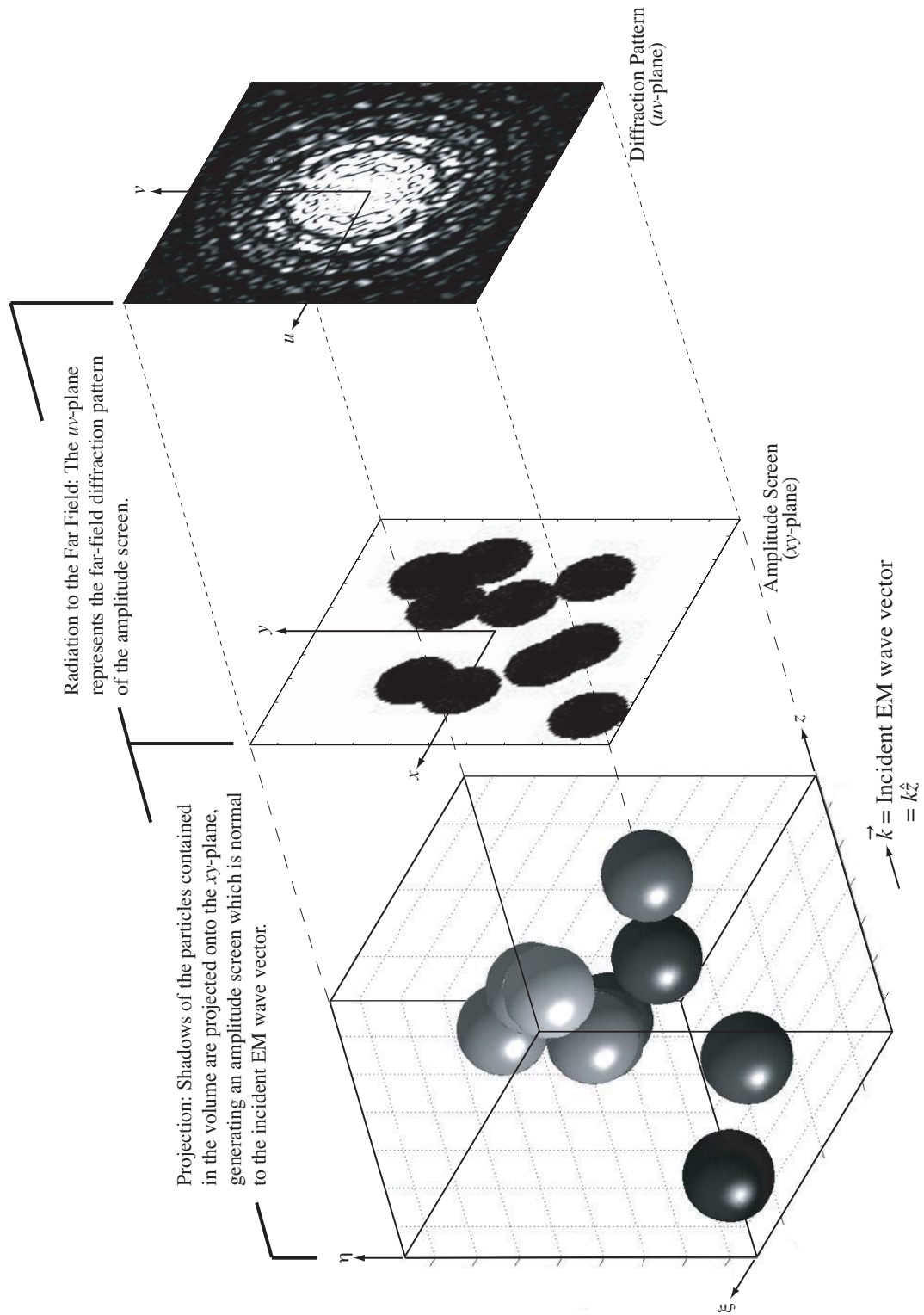
Very different approaches are adopted in the modeling of the scattering problem by a cluster of spherical particles by Mie theory as compared with diffraction theory. With the Mie approach, exact solution of the boundary-value problem begins with a description of the physical system: discrete spheres of specified radius, index of refraction, and center-to-center separation, oriented relative to an incident plane wave and in a pre-defined coordinate system.

By contrast, the diffraction theory model collapses the three-dimensional space occupied by the spheres into a plane which we call the amplitude screen, as shown in Figure 3.1. The amplitude screen is the projection of the 3D volume of spheres into a plane perpendicular to the wave vector \vec{k} ; put another way, the amplitude screen is the geometric projection of the shadows cast by the spheres onto a plane immediately behind the spheres, and perpendicular to the direction of the light illuminating the spheres. The shadow area of the spheres in the amplitude screen is assumed to be completely opaque—regardless of the index of refraction assigned to the original spheres, provided that the index is not very close to 1.

Early intuition may lead one to doubt the utility of diffraction theory to make accurate predictions since the physical model of the system is so distorted. The diffraction theory approach models the spheres as a completely planar and opaque obstruction to the incident wave; or alternatively, by Babinet’s Principle, as an illuminated aperture in an otherwise opaque screen, with the shape of the aperture defined by the projected sphere shadow area. This is clearly quite different from the true physical picture, which is modeled in three dimensions by the Mie formulation. We shall see that, nonetheless, diffraction theory captures the essential physics and produces accurate results in the near-forward scattering direction as long as the spheres are electrically large. We demonstrate this by comparing the intensity of the far-field scattering patterns, along u -axis cuts (see Figure 3.1), predicted by Mie-theoretic and diffraction-theoretic simulation techniques. The theoretical support of each is now discussed.

Next page.

Figure 3.1: Construction of the diffraction screen. Shadows of the particles contained in the $\xi\eta z$ -volume are projected onto the xy -plane, generating an amplitude screen $U(x, y)$ which is normal to the incident wave vector. The far field diffraction pattern $U(u, v)$ of the amplitude screen is found by taking the Fourier transform of $U(x, y)$. The diffraction pattern is sensed in an observation plane (*i.e.*, the uv -plane), located at a distance z (see eq. (3.52)) from the amplitude screen.



3.2.1 Coherent Scattering from a Sphere: Mie Theory

We begin with the differential form of Maxwell's equations,

$$\nabla \times \vec{E} = -\frac{\partial \vec{B}}{\partial t} \quad (3.1)$$

$$\nabla \times \vec{H} = \frac{\partial \vec{D}}{\partial t} + \vec{J} \quad (3.2)$$

$$\nabla \cdot \vec{D} = \rho \quad (3.3)$$

$$\nabla \cdot \vec{B} = 0 \quad (3.4)$$

where \vec{E} is the electric field, \vec{B} is the magnetic flux density, \vec{H} is the magnetic field, \vec{D} is the electric flux density or electric displacement, \vec{J} is the electric current density, and ρ is the volume charge density. For time-harmonic electromagnetic fields in a linear, isotropic, and source-free region of space, Maxwell's equations reduce to,

$$\nabla \times \vec{E} = i\omega\mu\vec{H} \quad (3.5)$$

$$\nabla \times \vec{H} = -i\omega\epsilon\vec{E} \quad (3.6)$$

$$\nabla \cdot \vec{E} = 0 \quad (3.7)$$

$$\nabla \cdot \vec{H} = 0 \quad (3.8)$$

where ω is the angular frequency in radians per second, and μ and ϵ are the permeability and permittivity of the propagating medium, respectively. Here, we adopt the physics convention for time-harmonic fields, $\exp(-i\omega t)$. Note that if no sources are present, \vec{E} and \vec{H} fields are divergence-free (purely solenoidal).

Any physically realizable time-harmonic electromagnetic field must also be a solution of the vector Helmholtz equation,

$$\nabla^2 \vec{E} + k^2 \vec{E} = 0 \quad (3.9)$$

$$\nabla^2 \vec{H} + k^2 \vec{H} = 0 \quad (3.10)$$

Solutions to the scalar Helmholtz equation are easier to find than solutions to the vector Helmholtz equation. Knowing this, *Mie* [1908] constructed a vector function, \vec{M} , from a scalar function ψ and a constant vector \vec{c} ,

$$\vec{M} = \nabla \times (\vec{c}\psi) \quad (3.11)$$

We see from eq. (3.11) that \vec{M} is purely solenoidal, satisfying eqs. (3.7) and (3.8). Substituting \vec{M} for \vec{E} or \vec{H} in eqs. (3.9) or (3.10), respectively, yields,

$$\nabla^2 \vec{M} + k^2 \vec{M} = \nabla \times [\vec{c}(\nabla^2 \psi + k^2 \psi)] = 0 \quad (3.12)$$

Thus \vec{M} satisfies the vector Helmholtz equation if the scalar function ψ satisfies the scalar Helmholtz equation,

$$\nabla^2 \psi + k^2 \psi = 0 \quad (3.13)$$

Let a second vector function be defined,

$$\vec{N} = \frac{\nabla \times \vec{M}}{k} \quad (3.14)$$

It is easily shown that the curl of \vec{N} is also proportional to \vec{M} ,

$$\nabla \times \vec{N} = k\vec{M} \quad (3.15)$$

Since \vec{N} is proportional to the curl of \vec{M} , it also has zero divergence and satisfies the vector Helmholtz equation. \vec{M} and \vec{N} satisfy the Helmholtz equation, are divergence-free, and the curl of \vec{M} is proportional to \vec{N} and vice-versa. These are the salient properties of electric and magnetic fields propagating as a wave in free space. Judicious choice of \vec{M} and \vec{N} ensures that the vector Helmholtz equation is satisfied when ψ satisfies the scalar wave equation, eq. (3.13). The scalar function ψ is often referred to as a ‘generating function’.

The choice of the guiding or pilot vector \vec{c} in eq. (3.11) has a critical influence on \vec{M} . Choosing $\vec{c} = \vec{r}$, where \vec{r} is the radial vector from the origin of the coordinate system to a point in space where the electromagnetic field is evaluated, ensures that

\vec{M} is a solution of the vector Helmholtz equation in spherical coordinates (*e.g.*, *Bohren and Huffman* [1998]).

In spherical coordinates, eq. (3.13) can be written as,

$$\frac{1}{r^2} \frac{\partial}{\partial r} \left(r^2 \frac{\partial \psi}{\partial r} \right) + \frac{1}{r^2 \sin \theta} \frac{\partial}{\partial \theta} \left(\sin \theta \frac{\partial \psi}{\partial \theta} \right) + \frac{1}{r^2 \sin \theta} \frac{\partial^2 \psi}{\partial \phi^2} + k^2 \psi = 0 \quad (3.16)$$

If solutions ψ of the scalar wave equation (3.13) are of the form,

$$\psi(r, \theta, \phi) = R(r)\Theta(\theta)\Phi(\phi) \quad (3.17)$$

then eq. (3.16) is separable into three ordinary differential equations,

$$\frac{d^2 \Phi}{d\phi^2} + m^2 \Phi = 0 \quad (3.18)$$

$$\frac{1}{\sin \theta} \frac{d}{d\theta} \left(\sin \theta \frac{d\Theta}{d\theta} \right) + \left[n(n+1) - \frac{m^2}{\sin^2 \theta} \right] \Theta = 0 \quad (3.19)$$

$$\frac{d}{dr} \left(r^2 \frac{dR}{dr} \right) + [(kr)^2 - n(n-1)] R = 0 \quad (3.20)$$

where m and n are separation constants. Independent solution of eqs. (3.18)–(3.20), and substitution into eq. (3.17) yields two possible solutions of the generating function,

$$\psi_{emn}(r, \theta, \phi) = \cos m\phi P_n^m(\cos \theta) z_n(kr) \quad (3.21)$$

$$\psi_{omn}(r, \theta, \phi) = \sin m\phi P_n^m(\cos \theta) z_n(kr) \quad (3.22)$$

where P_n^m are the associated Legendre functions of degree n and order m , and z_n are any one of four spherical Bessel functions j_n , y_n , $h_n^{(1)}$, or $h_n^{(2)}$ which are selected on the basis of the field structure being modeled. The subscripts e and o of ψ denote even or odd solutions, respectively, controlled by the $\cos m\phi$ or $\sin m\phi$ term. Due to the completeness of the functions comprising eqs. (3.21) and (3.22), any function that satisfies the scalar wave equation (3.16) can be expanded generally as an infinite series in the terms expressed in eqs. (3.21) and (3.22).

Suppose we illuminate a solitary sphere with a coherent plane wave of wavelength λ , and with wave vector $\vec{k} = k\hat{z}$, where $k = \frac{2\pi}{\lambda}$. The electric field incident upon the sphere has the following form,

$$\vec{E}_{\text{inc}} = \vec{E}_o e^{ikz} = E_o (\cos \beta_p \hat{x} + \sin \beta_p \hat{y}) \exp(ikz) \quad (3.23)$$

where β_p is the linear polarization angle. The time-harmonic term $\exp(-i\omega t)$ has been omitted from eq. (3.23), and from subsequent expressions, for brevity. The incident electric field can be expanded in spherical harmonics, yielding the following,

$$\vec{E}_{\text{inc}} = E_o \sum_{n=1}^{\infty} i^n \frac{2n+1}{n(n+1)} \left[\vec{M}_{o1n}^{(1)} - i\vec{N}_{e1n}^{(1)} \right] \quad (3.24)$$

where $\vec{N}_{e1n}^{(1)}$ and $\vec{M}_{o1n}^{(1)}$ are constructed from eqs. (3.11), (3.14), (3.21), and (3.22), above, and are thus functions of $k\vec{r}$, θ , and ϕ (i.e., $\vec{N}_{mn}^{(1)} = \vec{N}_{mn}^{(1)}(k\vec{r}, \theta, \phi)$). The superscript (1) indicates that the spherical Bessel function of the first kind j_n is used in the composition of \vec{N} and \vec{M} ; superscripts (2) , (3) , and (4) correspond to spherical Bessel functions of the second kind y_n , and of the third kind $h_n^{(1)}$ and $h_n^{(2)}$, respectively [Bohren and Huffman, 1998; Stratton, 1941]. Substituting eq. (3.24) into eq. (3.5) and re-arranging yields the incident magnetic field,

$$\vec{H}_{\text{inc}} = \frac{-k}{\omega\mu} E_o \sum_{n=1}^{\infty} i^n \frac{2n+1}{n(n+1)} \left[\vec{M}_{e1n}^{(1)} + i\vec{N}_{o1n}^{(1)} \right] \quad (3.25)$$

where μ is the permeability of the medium in which the sphere aggregate is embedded. Fields scattered from a solitary sphere due to the illuminating field of eqs. (3.24)–(3.25) are given by,

$$\vec{E}_s = E_o \sum_{n=1}^{\infty} i^n \frac{2n+1}{n(n+1)} \left[ia_n \vec{N}_{e1n}^{(3)} - b_n \vec{M}_{o1n}^{(3)} \right] \quad (3.26)$$

$$\vec{H}_s = \frac{-k}{\omega\mu} E_o \sum_{n=1}^{\infty} i^n \frac{2n+1}{n(n+1)} \left[ib_n \vec{N}_{o1n}^{(3)} + a_n \vec{M}_{e1n}^{(3)} \right] \quad (3.27)$$

where a_n and b_n are scattering coefficients, defined in eqs. (3.38) and (3.39) below, in

the context of the multi-particle formulation of Mie theory. A detailed development of eqs. (3.24)–(3.27) is found in Chapter 4 of *Bohren and Huffman* [1998].

3.2.2 Multi-Particle Scattering Using Mie Theory

Following Xu [Xu, 1995, 1997; Xu and Gustafson, 1997], suppose we define an aggregate of L spherical scatterers, occupying some volume in $\xi\eta z$ -space as shown in Figure 3.1. We illuminate this region with the coherent plane wave defined in eq. (3.23). The electric and magnetic fields of the incident plane wave, \vec{E}_{inc} and \vec{H}_{inc} , can be expressed in a coordinate system that is centered on the j^{th} sphere in the aggregate by expanding the fields in vector spherical harmonics [Xu, 1995, 1997]. The development is similar to the solitary sphere modeled in eqs. (3.24) and (3.25) above, except that Xu uses a complex form to reduce eqs. (3.21) and (3.22) to a single equation,

$$\psi_{mn}(r, \theta, \phi) = P_n^m(\cos \theta) z_n(kr) e^{im\phi} \quad (3.28)$$

with $1 \leq n \leq \infty$ and $-n \leq m \leq n$. This yields vectors \vec{N}_{mn} and \vec{M}_{mn} , which are related to the even and odd forms described above by taking the real and imaginary parts of the vector, respectively (e.g., $\vec{N}_{emn} = \Re \{ \vec{N}_{mn} \}$; $\vec{N}_{emn} = \Im \{ \vec{N}_{mn} \}$). Thus in the multi-particle formulation, the incident fields are given by,

$$\vec{E}_{\text{inc}}(j) = - \sum_{n=1}^{\infty} \sum_{m=-n}^n i E_{mn} \left[p_{mn}^j \vec{N}_{mn}^{(1)} + q_{mn}^j \vec{M}_{mn}^{(1)} \right] \quad (3.29)$$

$$\vec{H}_{\text{inc}}(j) = - \frac{k}{\omega \mu} \sum_{n=1}^{\infty} \sum_{m=-n}^n E_{mn} \left[q_{mn}^j \vec{N}_{mn}^{(1)} + p_{mn}^j \vec{M}_{mn}^{(1)} \right] \quad (3.30)$$

where p_{mn}^j and q_{mn}^j are expansion coefficients of the original incident field in the j^{th} coordinate system. The term E_{mn} is a field normalization factor, defined as,

$$E_{mn} = E_o i^n (2n+1) \frac{(n-m)!}{(n+m)!} \quad (3.31)$$

Note that substituting $m = 1$ and eq. (3.31) into eqs. (3.29) and (3.30) and simplifying yields the incident field expansions for the solitary sphere formulation, eqs. (3.24) and

(3.25).

Eqs. (3.29) and (3.30) are slightly modified forms of eq. (17) in *Xu* [1995]. The single superscript in p_{mn}^j and q_{mn}^j is borrowed from *Xu* [1997] (Begin by comparing eq. (30) from *Xu* [1995] with eq. (5) from *Xu* [1997], a later paper with notational improvements).

The field incident upon the j^{th} sphere in the aggregate is a superposition of the original incident field and the fields that are scattered from all of the other spheres in the aggregate,

$$\vec{E}_i(j) = \vec{E}_{\text{inc}}(j) + \sum_{l \neq j} \vec{E}_s^{lj} \quad (3.32)$$

$$\vec{H}_i(j) = \vec{H}_{\text{inc}}(j) + \sum_{l \neq j} \vec{H}_s^{lj} \quad (3.33)$$

where \vec{E}_s^{lj} and \vec{H}_s^{lj} denote the electric and magnetic scattered fields transformed from the l^{th} to the j^{th} local coordinate system. For an individual sphere in the aggregate, these scattered fields have the following form,

$$\vec{E}_s(j) = \sum_{n=0}^{\infty} \sum_{m=-n}^n iE_{mn} \left[a_{mn}^j \vec{N}_{mn}^{(3)} + b_{mn}^j \vec{M}_{mn}^{(3)} \right] \quad (3.34)$$

$$\vec{H}_s(j) = \frac{k}{\omega\mu} \sum_{n=0}^{\infty} \sum_{m=-n}^n E_{mn} \left[b_{mn}^j \vec{N}_{mn}^{(3)} + a_{mn}^j \vec{M}_{mn}^{(3)} \right] \quad (3.35)$$

Terms a_{mn}^j and b_{mn}^j are the scattering coefficients for the j^{th} sphere in the aggregate, and the superscript (3) of the vector spherical wave functions denotes the use of spherical Bessel functions of the third kind (Hankel functions) in the field expansions [*Bohren and Huffman*, 1998]. *Xu* [1997] shows that the scattering coefficients a_{mn}^j and b_{mn}^j , which contain the effects of all multiple scattering behavior exhibited by the aggregate, are determined by solution of the following linear system,

$$a_{mn}^j = a_n^j \left[p_{mn}^j - \sum_{l \neq j} \sum_{\nu=1}^{\infty} \sum_{\mu=-\nu}^{\nu} (A_{mn\mu\nu}^{lj} a_{\mu\nu}^l + B_{mn\mu\nu}^{lj} b_{\mu\nu}^l) \right] \quad (3.36)$$

$$b_{mn}^j = b_n^j \left[a_{mn}^j - \sum_{l \neq j} \sum_{\nu=1}^{\infty} \sum_{\mu=-\nu}^{\nu} (B_{mn\mu\nu}^{lj} a_{\mu\nu}^l + A_{mn\mu\nu}^{lj} b_{\mu\nu}^l) \right] \quad (3.37)$$

where a_n^j and b_n^j are the scattering coefficients of a single, isolated sphere, $1 \leq (j, l) \leq L$, and $A_{mn\mu\nu}^{lj}$ and $B_{mn\mu\nu}^{lj}$ are vector translation coefficients which facilitate the translation of elementary spherical waves from the l^{th} to the j^{th} local coordinate system (see Xu [1996] for a detailed discussion of these coefficients). The coefficients a_n^j and b_n^j are computed directly from Mie theory (the well-known Mie coefficients),

$$a_n^j = \frac{m^j \psi_n(m^j x^j) \psi'_n(x^j) - \psi_n(x^j) \psi'_n(m^j x^j)}{m^j \psi_n(m^j x^j) \xi'_n(x^j) - \xi_n(x^j) \psi'_n(m^j x^j)} \quad (3.38)$$

$$b_n^j = \frac{\psi_n(m^j x^j) \psi'_n(x^j) - m^j \psi_n(x^j) \psi'_n(m^j x^j)}{\psi_n(m^j x^j) \xi'_n(x^j) - m^j \xi_n(x^j) \psi'_n(m^j x^j)} \quad (3.39)$$

where ψ_n and ξ_n are Ricatti-Bessel functions, and their primed counterparts denote differentiation with respect to the argument of the function. We assume here that the permeability of the spheres is identical to that of the surrounding medium. This is not a necessary limitation [Bohren and Huffman, 1998], but it leads to the simpler form of a_n^j and b_n^j presented in eqs. (3.38) and (3.39). At the risk of causing confusion, the symbol commonly used to represent relative refractive index, m , has been used in eqs. (3.38) and (3.39). It is defined as $m^j = \sqrt{\frac{\epsilon_j}{\epsilon_o}}$, where ϵ_j and ϵ_o are the electric permittivity of the j^{th} sphere and of the surrounding medium, respectively. The variable x^j is the electrical size parameter of the j^{th} sphere, defined as,

$$x^j = (ka)^j = \frac{2\pi a^j}{\lambda} \quad (3.40)$$

where a^j is the radius of the j^{th} sphere.

Eqs. (3.36) and (3.37) represent a system of $2LN(N+2)$ equations with an equal number of unknown multiple scattering coefficients, where N is the highest order n required for convergence of the expansion. Although this system could, in theory, be solved by matrix inversion, this is often infeasible when the number of or size of the spheres is large [Xu, 1995]. Fuller *et al.* [1986] employed an order-of-scattering technique to solve for a_{mn}^j and b_{mn}^j . Xu employs an iterative method to find these

coefficients.

In the far field, the total scattered fields from the aggregate of spheres can be expressed as follows [Xu, 1997],

$$\vec{E}_s = \sum_{j=1}^L \exp(-ik\delta^j) \vec{E}_s(j) \quad (3.41)$$

$$\vec{H}_s = \sum_{j=1}^L \exp(-ik\delta^j) \vec{H}_s(j) \quad (3.42)$$

where $\delta^j = \hat{r} \cdot \vec{d}^j$ is the projection of the vector \vec{d}^j , pointing from the center of the aggregate's coordinate system to the center of the j^{th} sphere, along unit vector \hat{r} , which points from the center of the aggregate's coordinate system to an observation point in the far field. Thus the term $\exp(-ik\delta^j)$ is the phase shift, relative to the coordinate system center, introduced by the positional offset of the j^{th} sphere as projected along the line-of-sight to the far field observer. Implicit in this formulation is the limiting approximation that vectors between spheres comprising the aggregate and an observer in the far field are parallel. Combining eqs. (3.41) and (3.42) with eqs. (3.34) and (3.35) yields an expression for the far field scattering pattern of a cluster of spheres,

$$\vec{E}_s = \sum_{j=1}^L \exp(-ik\delta^j) \sum_{n=1}^N \sum_{m=-n}^n iE_{mn} \left[a_{mn}^j \vec{N}_{mn}^{(3)} + b_{mn}^j \vec{M}_{mn}^{(3)} \right] \quad (3.43)$$

$$\vec{H}_s = \frac{k}{\omega\mu} \sum_{j=1}^L \exp(-ik\delta^j) \sum_{n=1}^N \sum_{m=-n}^n E_{mn} \left[b_{mn}^j \vec{N}_{mn}^{(3)} + a_{mn}^j \vec{M}_{mn}^{(3)} \right] \quad (3.44)$$

Note the substitution of N for ∞ in the summation of n .

Far from the scatterers, one may describe the scattered field, and thus the scattering properties of the aggregate by the scattering matrix formulation [van de Hulst, 1981; Bohren and Huffman, 1998]:

$$\begin{bmatrix} E_{\parallel s} \\ E_{\perp s} \end{bmatrix} = \frac{\exp(ik(r-z))}{-ikr} \begin{bmatrix} S_2 & S_3 \\ S_4 & S_1 \end{bmatrix} \begin{bmatrix} E_{\parallel i} \\ E_{\perp i} \end{bmatrix} \quad (3.45)$$

where S_1 through S_4 are the scattering matrix elements for the aggregate, and the subscripts \parallel and \perp indicate the components of the incident and scattered fields which are parallel and perpendicular to the scattering plane, respectively. The scattering plane is defined as the plane containing both the incident wave vector \vec{k} and the scattering direction \hat{r} , which depends on θ and ϕ .

We limited our study to the scattering of like-polarized fields. That is, we computed the parallel-polarized scattered field $E_{\parallel s}$ due to a parallel-polarized incident field $E_{\parallel i} = |\vec{E}_i|$ ($E_{\perp i} = 0$), and computed $E_{\perp s}$ due to a perpendicularly-polarized incident field $E_{\perp i} = |\vec{E}_i|$ ($E_{\parallel i} = 0$). Further limiting our far field observations to be in cuts along the u -axis in Figure 3.1 (*i.e.* $\phi = 0$), we see that $E_{\perp i} = 0$ when \vec{E}_i is ξ -polarized, and $E_{\parallel i} = 0$ when \vec{E}_i is η -polarized. Referring to eq. (3.45), these two polarizations are completely characterized by S_2 and S_1 , respectively. The polarized scattered intensity of the aggregate may now be summarily defined,

$$I_{11}(\theta) = |S_1^\eta(\theta, \phi = 0)|^2 \quad (3.46)$$

$$I_{22}(\theta) = |S_2^\xi(\theta, \phi = 0)|^2 \quad (3.47)$$

where the superscripts ξ and η denote the incident E-field polarization. I_{11} and I_{22} are the polarized scattered intensity patterns of v -polarized scattered light given η -polarized incident light, and u -polarized scattered light given ξ -polarized incident light, respectively. Thus, I_{11} and I_{22} represent orthogonal polarization measurements of the scattered signal along a u -axis cut in the uv -plane (see Figure 3.1).

3.2.3 Diffraction from an Amplitude Screen

We used the shadow projection technique outlined in Section 3.2 and shown in Figure 3.1 to generate an amplitude screen representative of the aggregate of spheres under study. Diffraction is a coherence effect that is produced by a combination of the propagation and interference of waves. Scalar diffraction theory applies—and produces very accurate results—when the diffracting objects are large compared with the wavelength (*i.e.* when the size parameter x is large), and when the diffraction pattern is

observed at sufficient distance from the source of diffraction. In this study we are concerned with the near-forward (or paraxial) far field diffraction pattern of electrically large spheres, where polarization effects are negligible, and thus the requisite criteria of scalar diffraction theory hold.

A partially blocked amplitude screen is illuminated by monochromatic light, which then propagates to a observation plane located at a perpendicular distance z from the amplitude screen. In the paraxial approximation, the diffraction pattern in the uv -plane is given by the Huygens-Fresnel diffraction integral (see, for example, *Goodman* [1995]),

$$U(u, v) = \frac{z}{i\lambda} \iint U(x, y) \frac{\exp(ikr_{01})}{r_{01}^2} dx dy \quad (3.48)$$

where $U(x, y)$ is the scalar field value at a point (x, y) in the amplitude screen, $U(u, v)$ is the scalar field value in the diffraction pattern, and r_{01} is the distance from a point (x, y) in the amplitude screen to a point (u, v) in the observation plane where the diffracted field is sensed (see Figure 3.1),

$$r_{01} = \sqrt{z^2 + (u - x)^2 + (v - y)^2} = z \sqrt{1 + \left(\frac{u - x}{z}\right)^2 + \left(\frac{v - y}{z}\right)^2} \quad (3.49)$$

One of the basic assumptions of scalar diffraction theory is that the observation plane is far removed from the amplitude screen ($z \gg x, y$). Applying a binomial expansion to eq. (3.49), $\sqrt{1 + \epsilon} = 1 + 1/2\epsilon - 1/8\epsilon^2 \dots$, and retaining the first term in the expansion of the amplitude, and first two terms in the expansion of the phase in eq. (3.48),

$$U(u, v) = \frac{e^{ikz}}{i\lambda z} e^{\frac{ik}{2z}(u^2+v^2)} \iint \left[U(x, y) e^{\frac{ik}{2z}(x^2+y^2)} \right] e^{-i2\pi(xf_U+yf_V)} dx dy \quad (3.50)$$

where $f_U = \frac{u}{\lambda z}$ and $f_V = \frac{v}{\lambda z}$ are the spatial frequencies in u and v . Eq. (3.50) is the Fresnel transform of the function $U(x, y)$. Further, we recognize the integral in eq. (3.50) as the Fourier transform of a function $U'(x, y)$, which is the product of the amplitude screen with a quadratic phase term as shown within the square brackets in eq. (3.50). By dropping the third term in the binomial expansion of eq. (3.49), we

have implicitly enforced the criterion that the phase contribution due to the $1/8\epsilon^2$ term must be much less than a radian, or,

$$z^3 \gg \frac{\pi}{4\lambda} [(u-x)^2 + (v-y)^2]_{\max}^2 \quad (3.51)$$

This is the well-known criterion defining the Fresnel diffraction regime (*e.g.*, *Goodman* [1995]). If the phase introduced by the $e^{\frac{ik}{2z}(x^2+y^2)}$ term in eq. (3.50) is also much less than one radian,

$$z \gg \frac{k(x^2 + y^2)_{\max}}{2} \quad (3.52)$$

then eq. (3.50) simplifies further,

$$U(u, v) = \frac{e^{ikz}}{i\lambda z} e^{\frac{ik}{2z}(u^2+v^2)} \iint U(x, y) e^{-i2\pi(xf_U + yf_V)} dx dy \quad (3.53)$$

which is the Fourier transform of $U(x, y)$. Eq. (3.53) is the Fraunhofer far field approximation to the Huygens-Fresnel diffraction integral, and the criterion for its use is given by eq. (3.52). The intensity measured in the far field (*i.e.*, at the observation plane a distance z from the amplitude screen) is equal to the magnitude of the field squared,

$$I(u, v) = U(u, v)U^*(u, v) \propto |\mathcal{F}\{U(x, y)\}|^2 \quad (3.54)$$

where \mathcal{F} is the Fourier transform operator. $I(u, v)$ is proportional to the intensity of the diffracted field.

3.2.4 Mie and Diffraction Theory: Some Practical Considerations

Our code follows the formulation outlined in Section 3.2.2, making no other assumptions in its representation of the aggregate. The maximum number of expansion terms N needed to assure convergence of the solution was determined algorithmically according to the so-called Wiscombe stability criterion [Wiscombe, 1980], which for $8 < x < 4200$ is given by $N = x_{\max} + 4.05x_{\max}^{1/3} + 2$, where x_{\max} is the size parameter of the largest sphere in the aggregate.

The total memory requirement of the multiple scattering coefficients matrix is on the order of $M \sim N^4 + LN^2$, where L is the number of particles, and M is in bytes. For large x , the computational cost of the Mie solution grows, roughly, as $x^4 + Lx^2 + 256x^{4/3}$. An important prerequisite step is to select an appropriate minimum value of x —one which is sufficiently large to ensure that the spheres are in the scalar diffraction theory regime, and yet sufficiently small so that Mie simulation of aggregates computes in a reasonable time.

In adapting our diffraction theory approach to computer simulations, we require some additional approximations beyond those introduced by the shadow projection technique. In order to use a 2D Fast Fourier transform (FFT) to compute the diffraction pattern, we divided the amplitude screen into pixels of size Δx by Δy (we used square pixels, $\Delta x = \Delta y$). Pixel size selection (*i.e.*, choosing the spatial sampling rate) is driven by three factors.

First, we need pixels that are small enough to well-represent the curved shadow edges of a projected cluster of spheres. When viewing the amplitude screen as a whole, the comprising particles should look like circles—not like blocks or staircases.

Second, we need pixels that are small enough to ensure that the main lobe of the diffraction pattern is nearly free from the effects of aliasing. This is an important criterion, since our investigation is focused on near-forward scattering. It is not possible to completely eliminate aliasing, since the Fourier transform of the amplitude screen is not band-limited (due to the finite extent of the shadow area and the discontinuity present along its edge). We select the pixel size to ensure that the spatial sampling frequency f_s is large enough ($f_s = \frac{1}{\Delta x} = \frac{1}{\Delta y}$) to keep the effect of aliasing acceptably small over the main lobe of the diffraction pattern. We set as a weaker criterion that the first sidelobe is also as free as possible of aliasing effects.

Smaller pixels correspond to a higher sampling frequency f_s , and therefore to a lower frequency-domain resolution $\Delta f = \frac{f_s}{K}$, for an FFT of fixed size $K \times K$. The third pixel size selection criterion is that the combined selection of K and Δx , Δy must yield a resolution Δf that is sufficient to reveal details in the diffraction pattern that are necessary for comparison with the Mie results.

To summarize: For the Mie simulations, the size parameter must be large enough

to ensure that particles are within the scalar diffraction theory regime, but as small as possible to minimize the computational cost. For the diffraction theory simulations, we desire small pixels to minimize aliasing and to accurately represent the shape of the particles, but large pixels for computational efficiency and frequency-domain resolution. Selection of specific values for x , Δx , and Δy is discussed in Section 3.3.1. Note that the Mie solution does not contain aliasing effects; its accuracy is limited, however, by the number of expansion terms N used.

3.3 Simulation Results

We now compare Mie and diffraction theory predictions of the far field diffraction pattern for several scenarios. The Mie calculations are performed using spheres of relative refractive index $m = 1.78 + i10^{-4}$. In the microwave frequency range, this corresponds roughly to water ice at temperatures below -5° C [Sadiku, 1985]. We study single-sphere, two- and three-sphere, and ten-sphere systems. We investigate single sphere cases to: (1) select the pixel size of the amplitude screen; and (2) select the minimum x required by this study. The two- and three-sphere simulations are used to examine so-called pathological cases, *i.e.*, cases where we expect discrepancies between Mie and diffraction theory to be largest. The relative placement of spheres in the simulation for the two- and three-sphere cases is determined using pre-defined angles and distances as described in Section 3.3.2, and as shown in Figure 3.3. We generate sphere locations for the ten-sphere cases randomly. Results for those simulations are presented in Section 3.3.3.

Throughout this chapter, we compare the scattered signal intensity predicted by Mie theory with diffraction theory for uz -plane cuts only (see Figure 3.1). This approach simplified the execution of our simulations without loss of generality in our comparison. We generated results for running hundreds of different aggregates, all with unique orientations. The Mie theoretic polarization intensities given in eqs. (3.46) and (3.47) are compared with diffraction theory results by taking a cut of

$I(u, v)$, eq. (3.54), along the u -axis,

$$I_u(\theta_n) = I(u_n, v = 0) \quad (3.55)$$

where u_n denotes the value of u associated with the n^{th} pixel along the u -axis from the boresight (*i.e.*, $\theta = u = 0$) direction. For a diffraction pattern generated by computing the $K \times K$ -point 2D-FFT of an amplitude screen, the angle θ_n is given by,

$$\theta_n = \arctan \left(n \frac{\lambda f_s}{K} \right), \quad 0 \leq n \leq K - 1 \quad (3.56)$$

where n is the pixel number associated with u_n . For brevity, we drop the subscript and refer to θ_n as θ from this point forward.

The two-sphere, three-sphere, and ten-sphere investigations summarized in this chapter represent a total of 445 simulated cases. For the i^{th} case of a given type (*e.g.*, two-sphere, three-sphere, etc.), we define a difference measure Δ_i between Mie and diffraction theory,

$$\Delta_i(\theta) = I_{11}(\theta) - I_u(\theta) \quad (3.57)$$

where $I_{11}(\theta)$ and $I_u(\theta)$ have been normalized by $I_{11}(0)$ and $I_u(0)$, respectively. The maximum difference for the i^{th} case is defined as,

$$\Delta_{i,\max} = |\Delta_i(0 \leq \theta \leq \theta_1)|_{\max} \quad (3.58)$$

where $\theta_1 = \arcsin \left(\frac{3.822}{x_{\max}} \right)$ is the first null in the diffraction pattern of single sphere of size parameter x_{\max} , corresponding to the largest sphere possible in the i^{th} case simulation. For the case where the incident radiation is natural light, the incident energy is unpolarized—all polarizations are equally probable. The scattered field intensity of natural light is determined from the sum $I_{11}(\theta) + I_{22}(\theta)$. In the case of coherent incident radiation, the near-forward diffracted signal is negligibly depolarized and the scattered intensity has the same polarization as the incident intensity. Hence, in eq. (3.57), it is sufficient to use either $I_{11}(\theta)$ or $I_{22}(\theta)$, as we have done.

For each type of case, we define an associated mean difference, $\overline{\Delta}$ and standard

deviation, σ_Δ ,

$$\overline{\Delta}(\theta) = \frac{1}{M} \sum_i^M \Delta_i(\theta) \quad (3.59)$$

$$\sigma_\Delta(\theta) = \sqrt{\frac{1}{M} \sum_i^M (\Delta_i(\theta) - \overline{\Delta}(\theta))^2} \quad (3.60)$$

where M is the total number of cases simulated of each type. The maximum mean difference, $\overline{\Delta}_{\max}$, and maximum standard deviation, $\sigma_{\Delta, \max}$, on the interval $0 \leq \theta \leq \theta_1$ are defined in a manner analogous to eq. (3.58),

$$\overline{\Delta}_{\max} = |\overline{\Delta}(0 \leq \theta \leq \theta_1)|_{\max} \quad (3.61)$$

$$\sigma_{\Delta, \max} = |\sigma_\Delta(0 \leq \theta \leq \theta_1)|_{\max} \quad (3.62)$$

Our angular range of interest is driven by our scientific application: the analysis of radio waves forward-scattered from particles in Saturn's rings during the Cassini ring occultation experiment. In this case, detectable forward-scattered signals are dominated by diffraction by individual ring particles over angles $\theta < \theta_1$.

We discuss the use of these measures in the ensuing sections. Results of the simulations are summarized in Tables 3.1–3.4 and Figures 3.4–3.8.

3.3.1 Scattering from a Single Sphere

The spatial sampling rate (discussed in Section 3.2.4) determines how coarsely or finely the spheres' shadows are discretized in the amplitude screen. Since the far field diffraction pattern (eq. (3.53)) solution for a circular disc exists in closed-form—the so-called Airy pattern, which is of the form $A(\theta) = \left[\frac{2J_1(x \sin(\theta))}{x \sin(\theta)} \right]^2$, with first null θ_1 as defined in the text above—we determined the numerical diffraction pattern by computing the Fourier transform of an amplitude screen representation of a circular disc, and comparing it with the corresponding Airy pattern. We made this comparison while varying the spatial sampling rate of the amplitude screen. Differences between the FFT solution and the Airy pattern are introduced both due to aliasing, and due

to distortions caused by differences between the shape of a perfect circular disc and its discretized counterpart. Based upon these simulations, we chose to use the spatial sampling rate of $\Delta x = \Delta y = \frac{r_{\min}}{12}$ for all multi-particle simulations, where r_{\min} is the radius of the smallest sphere in the aggregate. With this sampling rate, the projected area of a discretized sphere in our simulation was 97.5% of its true cross sectional area (this percentage depends, to a small extent, on the method we used to generate the amplitude screen shadow area within our code), and the effects of aliasing and discretization were mitigated according to our stated criteria. This is seen clearly in Figure 3.2(b)-(d), where the Airy pattern (dotted line) falls on top of the diffraction pattern of the amplitude screen (dashed line) over the main diffraction lobe, as well as the first sidelobe.

Since scalar diffraction theory is valid for large spheres only, and since the computational cost of solving the Mie solution grows very quickly with x and L as discussed in Section 3.2.4, we seek to minimize x while retaining good agreement between Mie and diffraction theory over the main lobe of the diffraction pattern. Figure 3.2(a) summarizes the results. Here we show the difference between diffraction theory and Mie theory, plotted in dB, for spheres of size parameter $x = 20, 40, 80$, and 140 . We normalize the abscissa scale by the value of the first null of a given particle's diffraction pattern; each plot in the figure is scaled accordingly. Based upon these results, and upon the time required to compute them, we determined that spheres of size $x = 40$ were sufficiently large to show good agreement with diffraction theory over the main lobe, while at the same time being computationally manageable. The agreement between Airy, diffraction, and Mie solutions is shown in Figures 3.2(b)–3.2(d) for $x = 40, 80$, and 140 , respectively.

3.3.2 Scattering from Two and Three Spheres

Initially, we constructed sixty-three different configurations of two-particle aggregates, and 176 different configurations of three-particle aggregates as a first foray into multi-particle systems. For the two-particle systems, we varied the separation d between

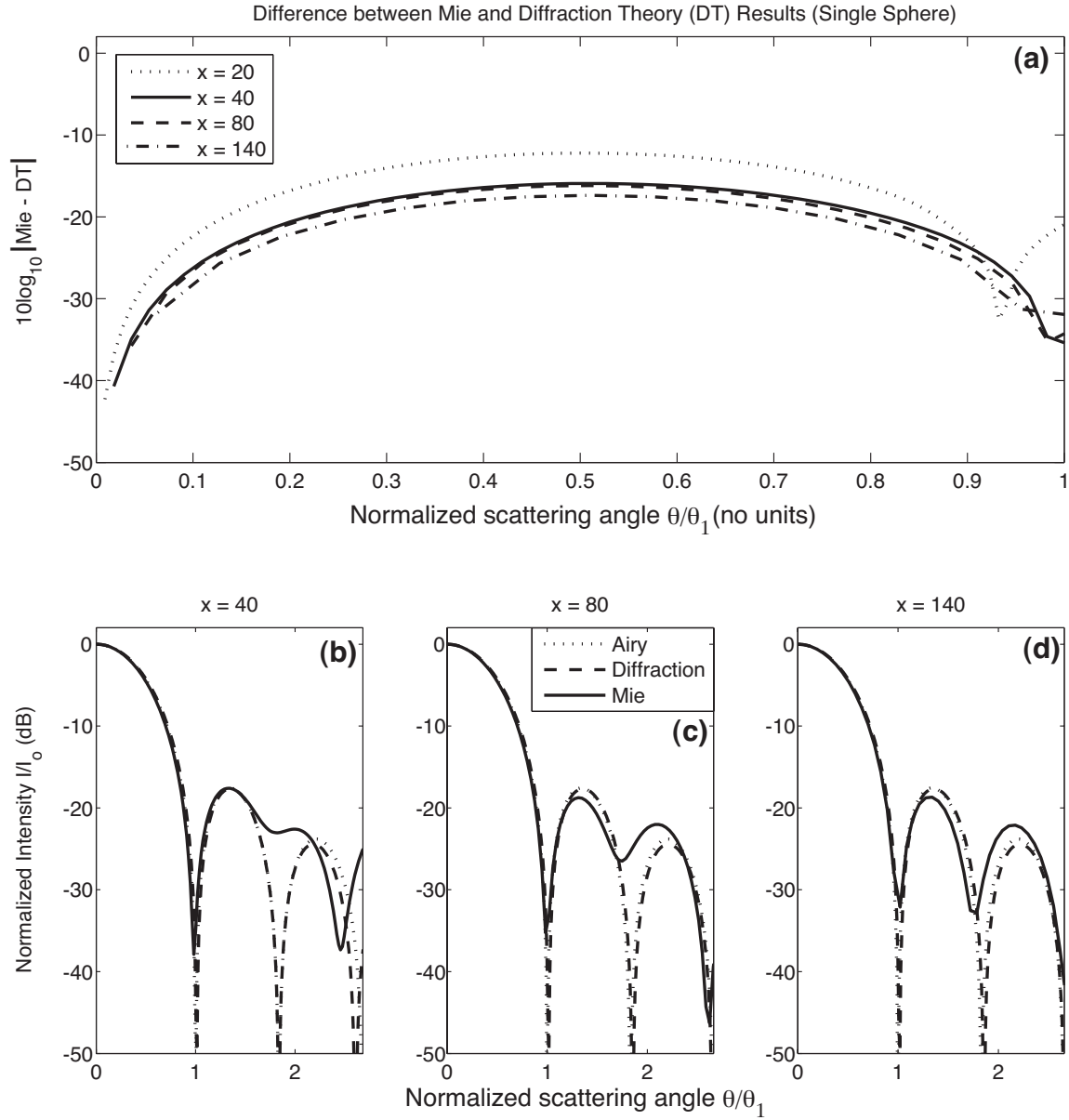


Figure 3.2: Comparison of Mie theory and diffraction theory solutions for scattering of a linearly-polarized plane wave from a single sphere. (a) Difference between Mie and diffraction theory for size parameters ranging from 20 to 140. The data is plotted as a function of angle, normalized to the first null angle θ_1 of the theoretical diffraction pattern of the given particle size x . (b)-(d) Comparison of Mie and diffraction theory with the analytic (Airy) solution for the diffraction pattern of a circular disc, as x increases from 40 to 140.

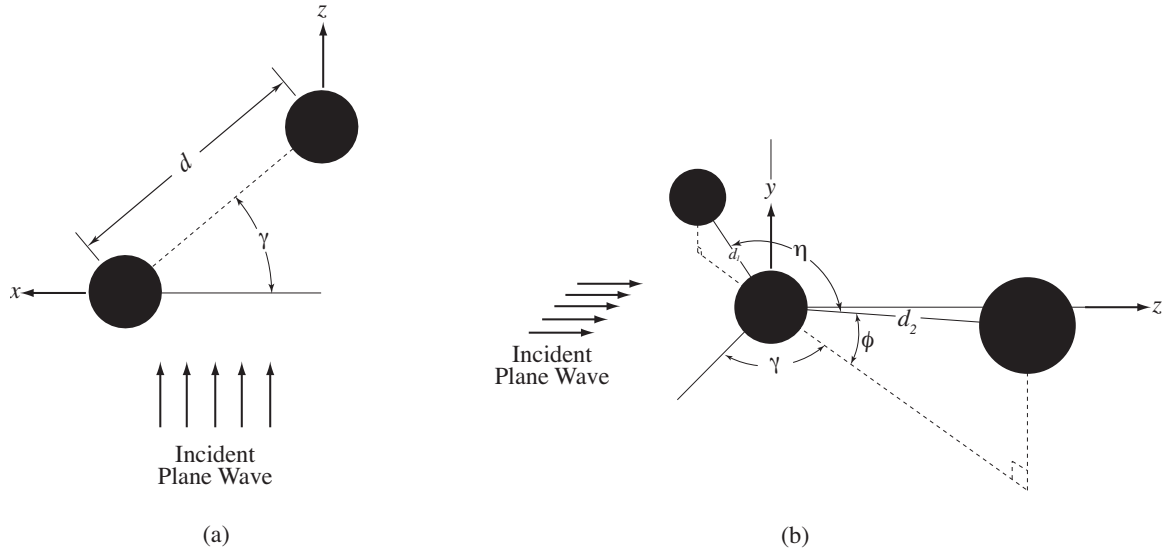


Figure 3.3: Definition of geometry and parameters for simulation of the two- and three-sphere cases. Distances d , d_1 , and d_2 are measured from center-to-center. Spheres are of identical radius a , though differences have been introduced in (b) to provide 3D perspective.

particle centers, and orientation angle γ as shown in Figure 3.3(a). For the three-particle aggregates, we varied the separations d_1 and d_2 , and orientation angles γ , ϕ , and η . These parameters are shown in Figure 3.3(b). We identified the cases that showed the greatest difference between Mie and diffraction theory solutions, and then investigated the corresponding sample subspace more thoroughly with additional simulations. Most of the cases where the difference between Mie and diffraction theory was greatest are pathological—cases that are highly unlikely to arise in nature. However, even for these pathological cases—such as the case of three collinear particles in alignment with the wave vector \vec{k} , for example—the agreement between Mie and diffraction theory over the main diffraction lobe is better than $\Delta_{\max} < 0.14$ for the cases studied.

Two-Sphere Cases

Referring to Figure 3.3(a), we performed initial simulations to investigate the complete parameter space of $d = 2a \rightarrow 7a$, in steps of $1a$, $\gamma = 0^\circ \rightarrow 75^\circ$ in steps of 15° (36 cases). Based on the cases where Δ_{\max} was greatest, we performed further simulations to investigate cases where particles are co-linear or nearly co-linear with the wave vector ($d = 2a \rightarrow 10a$; $\gamma = 0^\circ, 10^\circ$; and $d = 2a \rightarrow 7a$; $\gamma = 90^\circ$). The final simulated parameter space spanned from $d = 2a \rightarrow 10a$, and from $\gamma = 0^\circ \rightarrow 90^\circ$, for a total of $M = 63$ cases.

We computed the difference between the Mie theory and diffraction theory simulation results, $\Delta_i(\theta)$, and the maximum difference, $\Delta_{i,\max}$, over the main diffraction lobe of an $x = 40$ particle (*i.e.*, over the range $\frac{\theta}{\theta_1} = 0 \rightarrow 1$ in Figure 3.4) for each simulation. The three cases for which this maximum difference are least and greatest (*i.e.*, 6 cases in total) are plotted in Figures 3.4(a)-(c) and 3.4(d)-(f), respectively. In all cases, we normalized the plots by the scattering amplitude in the exact forward direction. We summarize the best and worst case results, along with the maximum mean difference $\bar{\Delta}_{\max}$ and maximum standard deviation $\sigma_{\Delta,\max}$, in Table 3.1.

In general, the best results correspond to cases where the sphere pair is touching or nearly touching, and where one sphere does not completely eclipse the other (Figure 3.4(a)-(c)). Some systematic differences over the width of the main lobe characterized

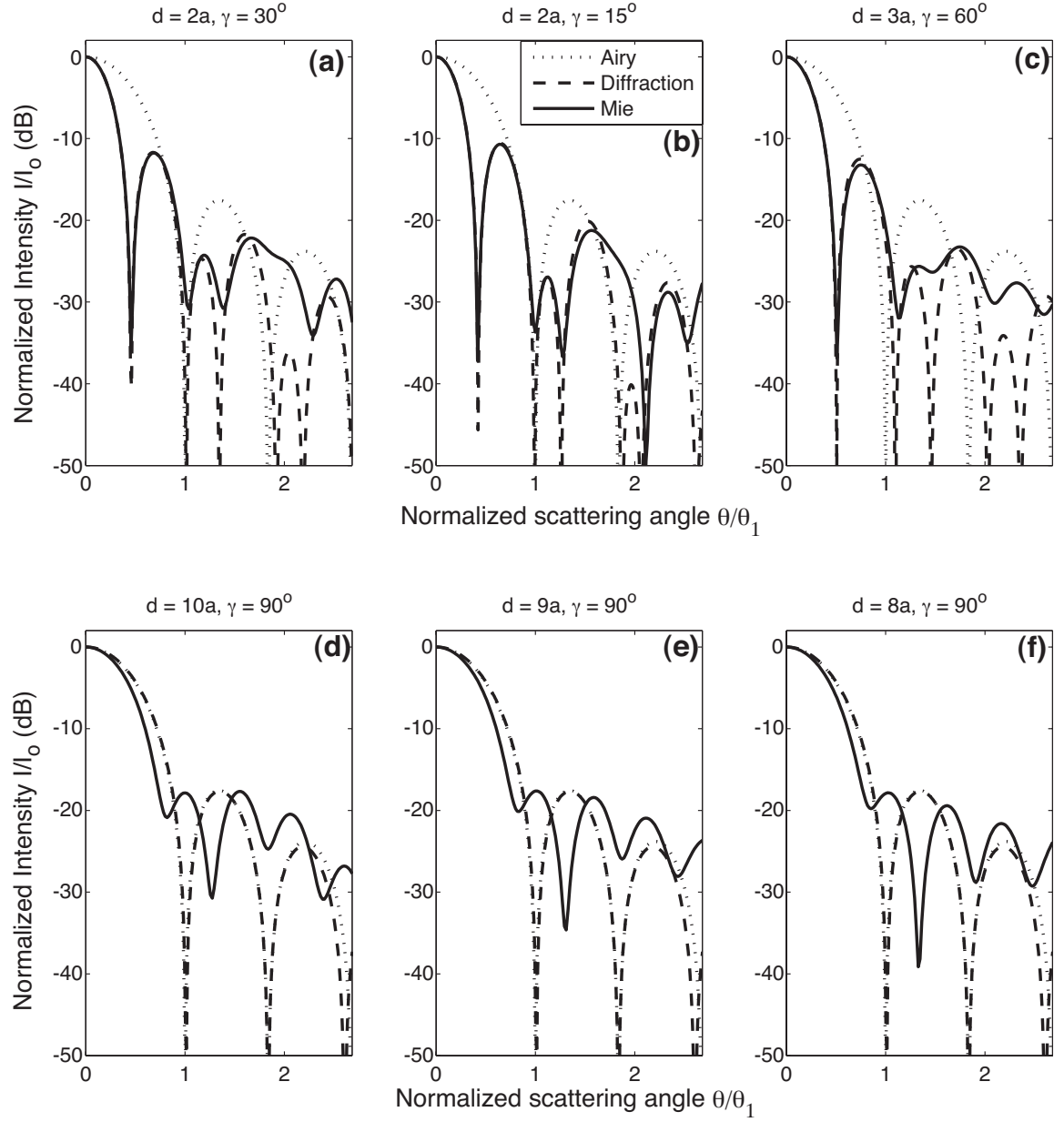


Figure 3.4: Two spherical scatterers ($x = 40$): Comparison of results for the three best cases ((a)-(c)) and three worst cases ((d)-(f)) of 63 simulated cases. Normalizing angle θ_1 is the angle of the first null in the diffraction pattern of a single isolated particle. Parameters d and γ are defined in the text, and in Figure 3.3(a).

Table 3.1: Summary: Two-Sphere Scattering Investigations ($x = 40$). Parameters d and γ are explained in the text and in Figure 3.3(a). For the rows corresponding to specific figures, $\Delta_{\max} = \Delta_{i,\max}$. For the row corresponding to the average of the 63 cases, $\Delta_{\max} = \overline{\Delta}_{\max}$. See Section 3.3 of the text for definitions of various Δ 's.

Case	d	γ	Δ_{\max}	$\sigma_{\Delta,\max}$
Fig. 3.4(a)	$2a$	30°	.0040	—
Fig. 3.4(b)	$2a$	15°	.0061	—
Fig. 3.4(c)	$3a$	60°	.0102	—
Fig. 3.4(d)	$10a$	90°	.1458	—
Fig. 3.4(e)	$9a$	90°	.1375	—
Fig. 3.4(f)	$8a$	90°	.1237	—
Average (63 cases)	—	—	.0151	.0457

cases where the spheres were further apart and one sphere completely eclipsed the other, and thus the shadow projected onto the amplitude screen was that of a single circular disc (Figure 3.4(d)-(f)). In those cases, as expected, the diffraction theory solution closely matches the Airy pattern instead of the Mie solution. The best case corresponds to $d = 2a$, $\gamma = 30^\circ$; The worst case to $d = 10a$, $\gamma = 90^\circ$.

Three-Sphere Cases

Figure 3.3(b) shows the geometry of our three-sphere simulations. The center-to-center distances d_1 and d_2 , and angles η , ϕ , and γ were used to completely parameterize the simulation space. We constructed the geometry from these parameters in the following way: (1) We placed the spheres collinearly along the x -axis with one sphere at the origin, and the other two at distances d_1 and d_2 on either side; (2) We rotated the $+x$ sphere about the z -axis to create the angle η between the 3 spheres; (3) We rotated all three spheres about the z -axis to introduce the angle ϕ as shown; (4) We rotated the three spheres about the y -axis by an angle γ as shown.

We simulated a total of $M = 172$ cases during our investigation of the three-sphere geometry. Initially, we explored the parameter space spanned by $d_1 = 2a, 4a$; $d_2 = 3a, 5a$; $\eta = 45^\circ, 90^\circ, 135^\circ, 180^\circ$; and $\phi, \gamma = 0^\circ, 45^\circ, 90^\circ$ (144 cases). Based upon the results of both these investigations and upon the results of our two-sphere simulations, we extended the parameter space to include simulations of $d_1, d_2 = 2a, 3a, 4a, 5a$;

$\eta = 180^\circ$; $\phi = 0$; and $\gamma = 70^\circ, 80^\circ$ (32 additional cases).

We summarize the results of the three-sphere simulations in Table 3.2. We discovered that the poorest agreement, once again, correspond to the pathological case of a co-linear orientation of spheres whose shadows completely cover one another. The separation distances d_1 and d_2 corresponding to the worst cases did not correspond to the largest distances explored in the simulation space, in contrast to the corresponding two-sphere investigations. The best-case results occurred for small separation distances d_1 and d_2 , and when there was minimal or no shadow overlap due to the choice of η , ϕ , and γ . We present plots of the three best and three worst cases for the three-sphere geometry in Figure 3.5.

Table 3.2: Summary: Three-Sphere Scattering Investigations ($x = 40$). Parameters d_1 , d_2 , η , ϕ , and γ are explained in the text and in Figure 3.3(b). For the rows corresponding to specific figures, $\Delta_{\max} = \Delta_{i,\max}$. For the row corresponding to the average of the 176 cases, $\Delta_{\max} = \overline{\Delta}_{\max}$. See Section 3.3 of the text for definitions of various Δ 's.

Case	d_1	d_2	η	ϕ	γ	Δ_{\max}	$\sigma_{\Delta,\max}$
Fig. 3.5(a)	$2a$	$3a$	45°	0°	45°	.0032	—
Fig. 3.5(b)	$2a$	$3a$	45°	0°	0°	.0069	—
Fig. 3.5(c)	$2a$	$3a$	45°	90°	0°	.0077	—
Fig. 3.5(d)	$4a$	$3a$	180°	0°	90°	.1313	—
Fig. 3.5(e)	$4a$	$5a$	180°	0°	90°	.1262	—
Fig. 3.5(f)	$3a$	$3a$	180°	0°	80°	.1127	—
Average (176 cases)	—	—	—	—	—	.0183	.0304

3.3.3 Scattering from Ten Spheres

The geometry of a ten-sphere aggregate is loosely depicted in Figure 3.1. For each case, we populated a volume of $18 \times 18 \times 12$ units in $\xi\eta z$ -space with 10 spheres, where $x = 40$ spheres had corresponding radii of $a = 2$ units. Sphere placement inside the volume followed a uniform random distribution in space. Spheres were allowed to touch each other, but sphere intersection within the volume was not allowed.

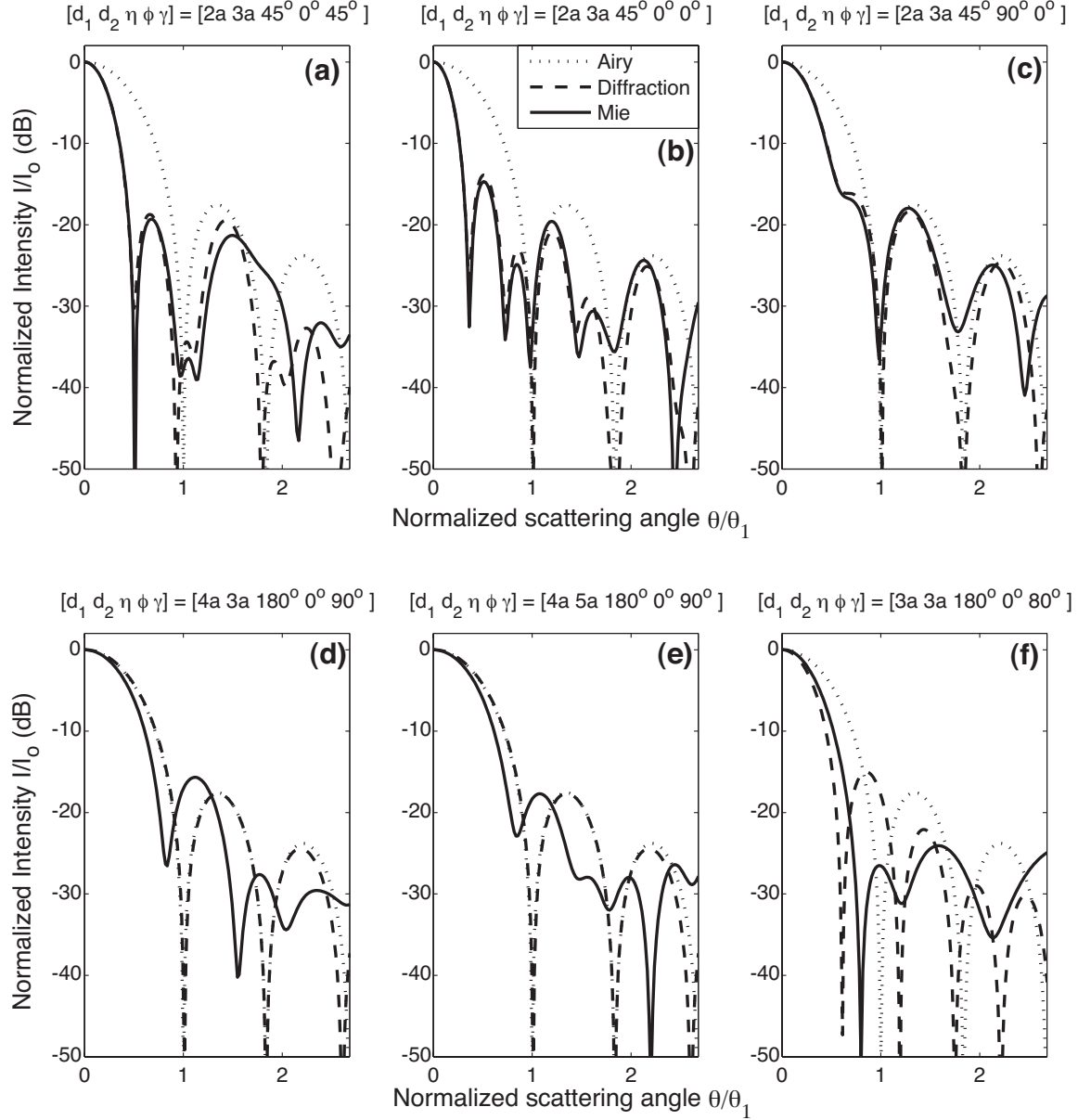


Figure 3.5: Three spherical scatterers ($x = 40$): Comparison of results for the three best cases ((a)-(c)) and three worst cases ((d)-(f)) of 176 simulated cases. Normalizing angle θ_1 is the angle of the first null in the diffraction pattern of a single isolated particle. Parameters d_1 , d_2 , η , γ , and ϕ are defined in the text, and in Figure 3.3(b).

Monodistribution of Sphere Sizes

We simulated one hundred ($M = 100$) independent, randomly generated cases for the ten-sphere monodistribution geometry. Each of these cases had ten $x = 40$ spheres within the prescribed volume, giving a corresponding volume fraction for each case of 0.086. Figure 3.6(a)-(c) shows the diffraction pattern of the three cases for which $\Delta_{i,\max}$ was least, and Figure 3.6(d)-(f) shows the diffraction pattern of the three cases for which $\Delta_{i,\max}$ was greatest. We summarize the results in Table 3.3.

Figure 3.6(e) shows $\Delta_i(\theta)$ for all 100 cases, showing clearly how the differences are distributed as a function of θ . The average $\overline{\Delta}(\theta)$ of the cases in Figure 3.6(e) is shown in Figure 3.6(f). Figure 3.6(g) shows a plot of the standard deviation $\sigma_{\Delta}(\theta)$. The peak value in Figure 3.6(g) corresponds to $\sigma_{\Delta,\max}$, and is given in Table 3.3.

Table 3.3: Summary: Ten-Sphere Scattering Investigations (Monodistribution, $x = 40$). Particle placement within the simulation space follows a uniform random spatial distribution. For the rows corresponding to specific figures, $\Delta_{\max} = \Delta_{i,\max}$. For the row corresponding to the average of the 100 cases, $\Delta_{\max} = \overline{\Delta}_{\max}$. See Section 3.3 of the text for definitions of various Δ 's.

Case	Δ_{\max}	$\sigma_{\Delta,\max}$
Fig. 3.6(a)	.0029	—
Fig. 3.6(b)	.0029	—
Fig. 3.6(c)	.0030	—
Fig. 3.6(d)	.0544	—
Fig. 3.6(e)	.0438	—
Fig. 3.6(f)	.0388	—
Average (100 cases)	.0024	.0186

To investigate the effect of dielectric loss, we simulated 70 additional 10-sphere monodistribution cases. For each case, we varied the complex component of the refractive index between $m'' = 0.1$ and $m'' = 0$. We found that the the effect of loss on the simulated scattering behavior of the cluster was negligible. The results are summarized in Figure 3.7.

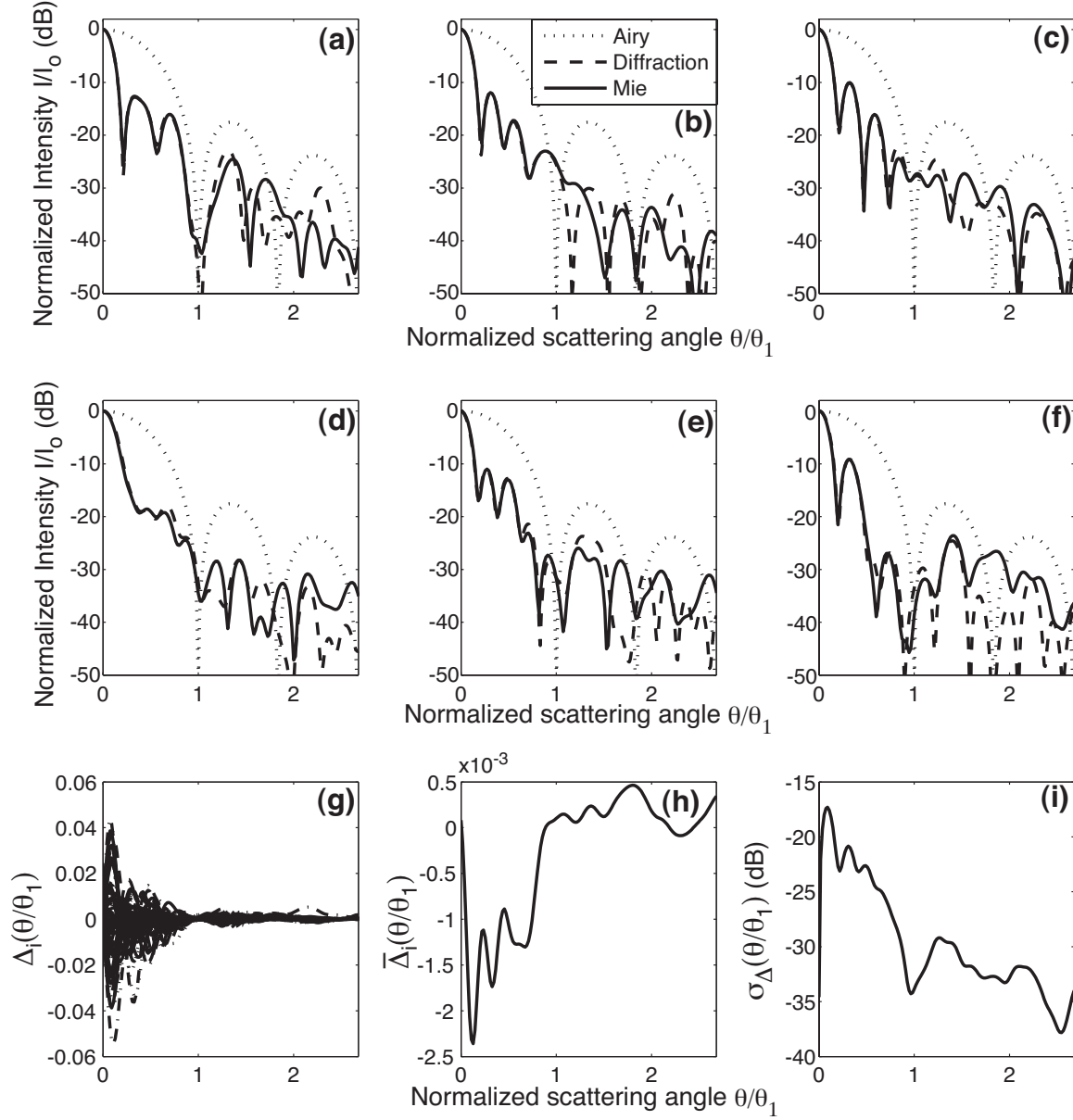


Figure 3.6: Ten identically-sized spherical scatterers ($x = 40$): Comparison of results for the three best cases ((a)-(c)) and three worst cases ((d)-(f)) of 100 simulated cases. Normalizing angle θ_1 is the angle of the first null in the diffraction pattern of a single isolated particle. Associated statistics: (g) superposed differences between Mie and Diffraction theory solutions for each simulated case, (h) average of differences in panel (g), and (i) the corresponding standard deviation.

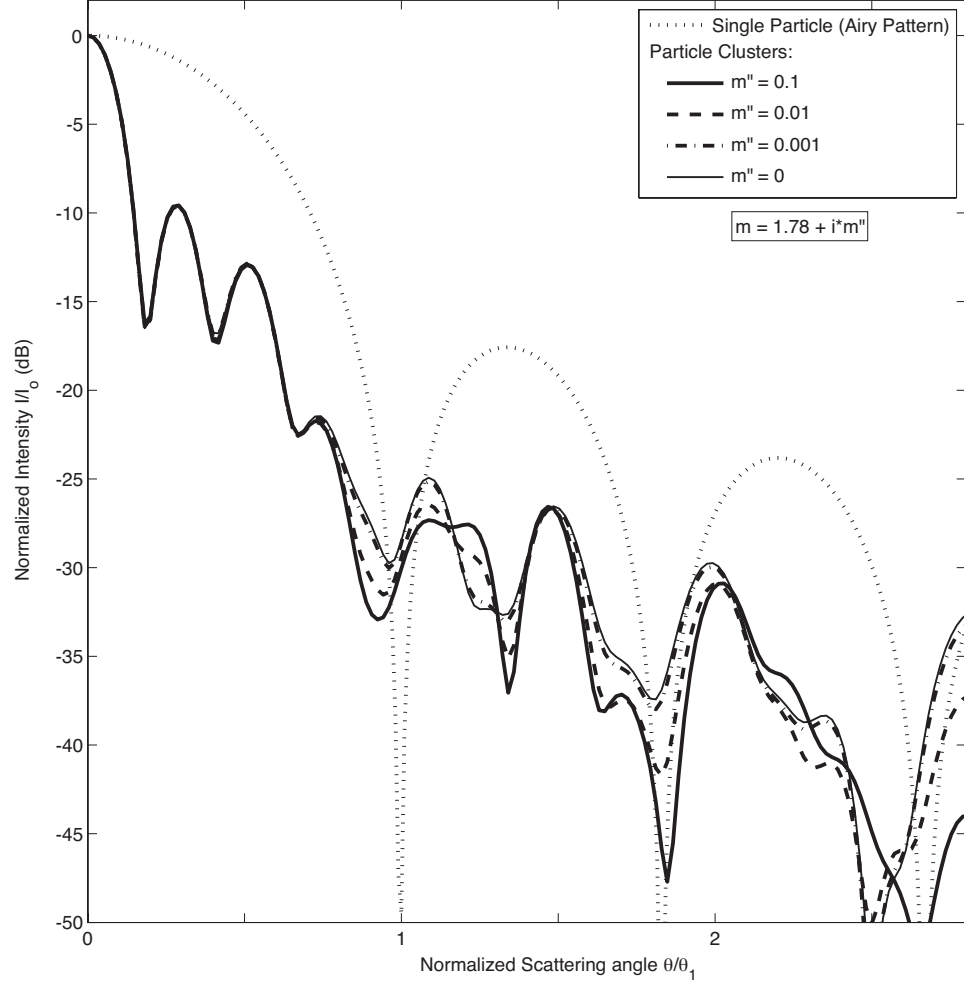


Figure 3.7: Comparison of Mie theoretic solutions for lossy vs. lossless spheres: A study of 70 distinct aggregates of ten identically-sized spherical scatterers ($x = 40$) was performed to characterize the effect of dielectric loss on the far-field radiation pattern. A single case result is shown here, and is typical of our findings. The imaginary component of the refractive index, m'' , is varied between $m'' = 0.1$ and $m'' = 0$, as shown. Comparing the $m'' = 0.1$ and $m'' = 0$ simulations over all 70 cases, we found a worst-case discrepancy of $\Delta_{i,\max} = 0.02$ over the main diffraction lobe of a single particle. The mean and standard deviation of Δ_i for the 70 cases is $\overline{\Delta}_{\max} = 0.0002$ and $\sigma_{\Delta,\max} = 0.007$, respectively. See Section 3.3 for an explanation of the three Δ terms (Note: We have modified the definition of Δ_i (eq. (3.57)) somewhat to apply to the loss study, *i.e.*, $\Delta_i(\theta) = I_{m''=0}(\theta) - I_{m''=0.1}(\theta)$, with commensurate modification to eqs. (3.58)–(3.60)).

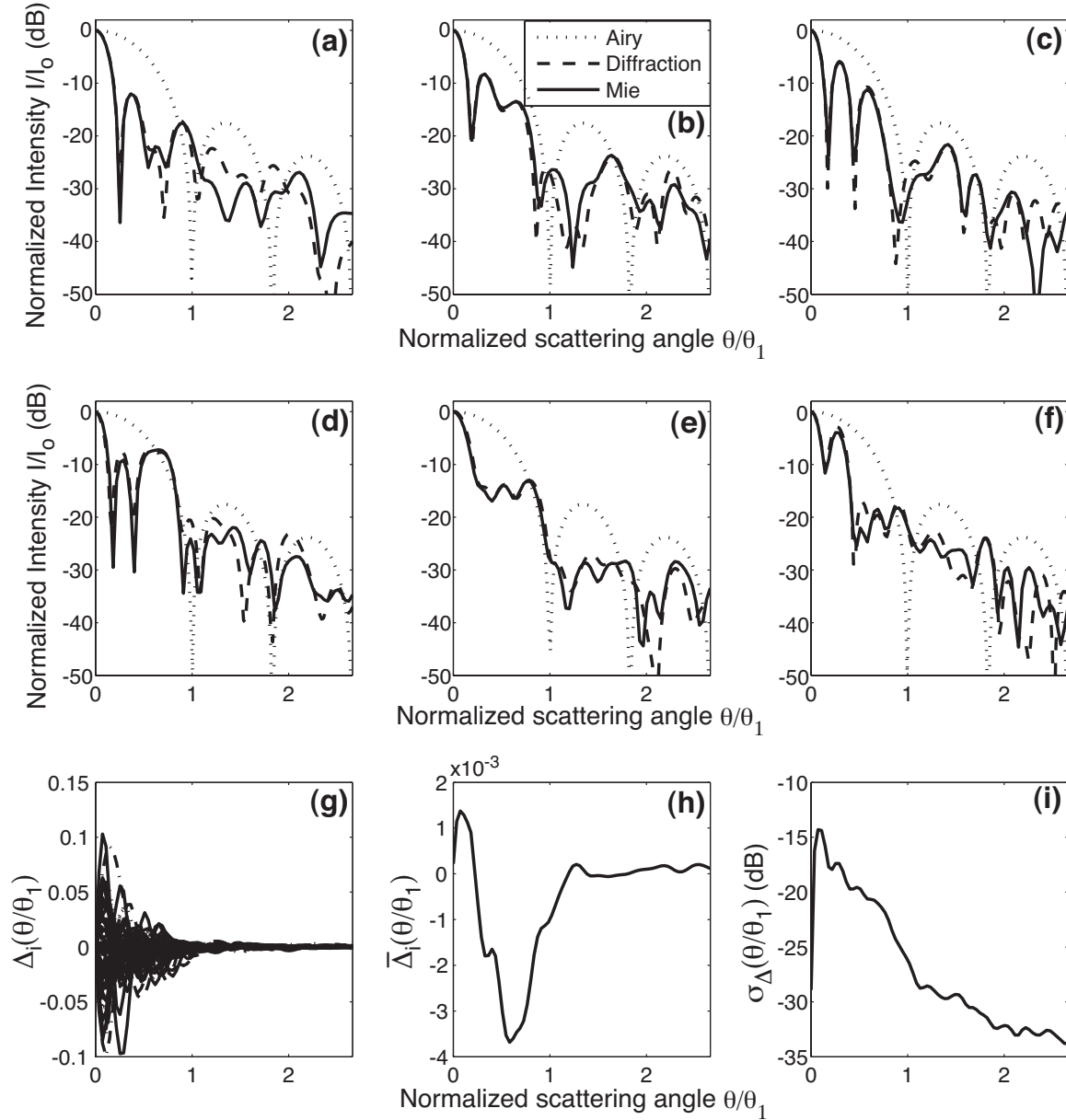


Figure 3.8: Ten spherical scatterers. Particle sizes distributed uniformly between size parameters $x = 40$ and $x = 80$. Comparison of results for the three best cases ((a)-(c)) and three worst cases ((d)-(f)) of 106 simulated cases. Normalizing angle θ_1 is the angle of the first null in the diffraction pattern of a single isolated particle. Associated statistics: (g) superposed differences between Mie and Diffraction theory solutions for each simulated case, (h) average of differences in panel (g), and (i) the corresponding standard deviation.

Uniform Distribution of Sphere Sizes

We simulated one-hundred and six ($M = 106$) independent, randomly generated cases with a uniform distribution in sphere size. The uniform size distribution ranged from $x = 40$ to $x = 80$ ($a = 1 \rightarrow 2$ units). Figure 3.8 shows the simulation results in an analogous manner to the presentation of monodistribution results in Figure 3.6. Once again, we find excellent agreement between Mie and diffraction theory predictions for the far field scattering behavior of the aggregate, though the agreement is not quite as good as it was for the ten-sphere monodistribution case (*cf.*, Table 3.3 and Table 3.4).

Table 3.4: Summary: Ten-Sphere Scattering Investigations (Uniform distribution, $40 \leq x \leq 80$). Particle placement within the simulation space follows a uniform random spatial distribution. For the rows corresponding to specific figures, $\Delta_{\max} = \Delta_{i,\max}$. For the row corresponding to the average of the 106 cases, $\Delta_{\max} = \overline{\Delta}_{\max}$. See Section 3.3 of the text for definitions of various Δ 's.

Case	Δ_{\max}	$\sigma_{\Delta,\max}$
Fig. 3.8(a)	.0048	—
Fig. 3.8(b)	.0083	—
Fig. 3.8(c)	.0091	—
Fig. 3.8(d)	.1028	—
Fig. 3.8(e)	.0996	—
Fig. 3.8(f)	.0972	—
Average (106 cases)	.0037	.0372

3.4 Discussion

In general, we observed excellent agreement between Mie and diffraction theory results for the vast majority of cases simulated during this study. The two- and three-sphere simulation sets contained geometric configurations of particles that produced the worst-case agreement between Mie and diffraction theory. Invariably, the worst-case results correspond to pathological cases where the particle alignment is co-linear with \vec{k} . A similar conclusion was reported by *Marouf* [1993]. Generally speaking, $\Delta_{i,\max}$ increases as the separation between particles in these co-linear pathological

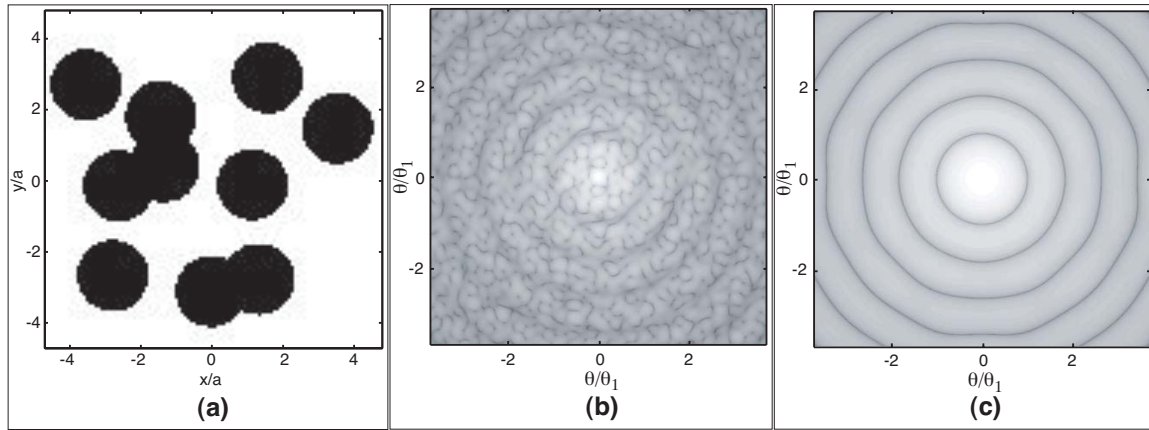


Figure 3.9: (a) An amplitude screen generated from a volume containing ten spheres and (b) its associated diffraction pattern. The scale of the amplitude screen is normalized by the sphere radius a . The diffraction pattern of an single, isolated particle is clearly seen in the diffraction pattern of the aggregate. Fine scale variation in the pattern intensity is due to the phase relationship of the individual particles, which is controlled by their relative spatial positions. Normalizing angle θ_1 is the angle of the first null in the diffraction pattern of a single isolated particle. The case presented in (a), (b) corresponds to Figure 3.6(a). The diffraction pattern of a single, isolated particle is shown in (c) for comparison.

cases increases (see Tables 3.1–3.2), over the range of separations addressed by our study (up to $10a$). Qualitatively speaking, when the \vec{k} -aligned, co-linear particles are separated by a few radii, the diffracted wave from the first particle begins to fill the shadow region behind the first particle before it encounters the second particle, and so on. Clearly, this endfire type of configuration is quite different from scattering from a single sphere, but none of those differences, in terms of projected shadow area on the amplitude screen, are captured by the diffraction theory model. By contrast, when those scattered fields are not allowed to fill in behind the first particle before encountering the second, etc. (*i.e.*, when the particles are touching or very close together), the scattered fields are more similar to those scattered by a single particle, and thus more similar to the diffraction solution of a circular disc. This is true while the particles are in each other's near field, *i.e.*, in the Fresnel region. Note that as the particle separation is increased into the Fraunhofer region for the \vec{k} -aligned, co-linear particle case, we expect the agreement between Mie and diffraction theory to once again improve. We have not attempted to identify the separation distance at which $\Delta_{i,\max}$ stops increasing.

For the ten-sphere simulations, monodistribution and uniform size distribution simulations showed a factor of 15 to 20 difference between best- and worst-case $\Delta_{i,\max}$. As expected, $\overline{\Delta}_{\max}$ was less than the best-case $\Delta_{i,\max}$ for both mono and uniform distributions. We attribute this to the random nature of the spatial distribution, which has a statistically equal likelihood of producing a positive or negative $\Delta_i(\theta)$ for any given θ , and thus we expect $\overline{\Delta}_{\max}$ to tend to zero as $M \rightarrow \infty$.

As the number of particles in an aggregate grows, we expect the effect(s) of any pathological behavior in the population to contribute only minimally to the overall scattering behavior of the aggregate. For the vast majority of the particles in the aggregate, the scattering behavior is well-characterized by diffraction theory, and those behaviors effectively ‘wash out’ any pathological effects that may differentiate the diffraction theory solution from the true EM scattering behavior. To be clear, the underlying assumption here is that the vast majority of particles in the aggregate are not co-linear *and* aligned with \vec{k} , which is certainly the case in radio occultation observations of Saturn's rings.

Interestingly, we observe that the diffraction pattern of a cluster of particles comprises two main components: A component due to the scattering pattern of the individual spheres in the aggregate, and a component representing the spatial arrangement of the individual particles in the aggregate. This is akin to the so-called element and array patterns in antenna theory, where the overall radiation pattern of an antenna array is controlled by both the radiation pattern of the array's individual elements, and by the phase relationship between the elements, which is controlled by the position of the individual elements in space. This is evident in Figure 3.9, where we show the diffraction pattern from an individual sphere alongside the diffraction pattern of a particular ten-sphere aggregate. We discuss this phenomenon in more detail in Section 4.2.

3.5 Amplitude Screen Model Results for Thick, Homogeneous Rings

As discussed in Chapter 2, an interplay of gravitational and collisional forces at the particle-to-particle level result in the formation of microstructure in Saturn's rings, on the scale of tens to hundreds of meters. Dynamical simulations of planetary ring systems show that under most conditions, the steady-state distribution of particles in Saturn's rings is non-homogeneous (see Figure 2.11).

While a homogeneous model is unlikely to well-represent microstructure native to Saturn's main rings A–C (it is a model better suited to Ring D), it is useful for two reasons. First, it provides a baseline case against which we observe degrees of non-homogeneity in our measured experimental data; and second, it provides another opportunity to test our amplitude screen method, since an analytic solution exists for scattering from thick homogeneous rings.

EM forward-scattering from a homogeneous cloud of particles results in a broadening of the forward scattering lobe, relative to the forward scattering lobe of a single particle. Based on this, *Marouf et al.* [1982] worked out an exact analytical solution

for the broadening due to scattering from a many particles thick (MPT), sparsely-populated homogeneous ring model. We proceed by comparing the diffraction results we computed using the amplitude screen method, with corresponding analytic solutions for several instantiations of MPT homogeneous rings ranging in optical depth between $\tau = 0.49$ and $\tau = 8.24$. Note that the use of the MPT model to estimate particle size distributions in the rings is discussed in Section A.2 of Appendix A.

3.5.1 An Analytic Solution for Forward Scattering

Marouf et al. [1982] show that for a MPT ring model, the intensity of the forward-diffraction lobe is given by,

$$I(\tau_q, \theta) = 2\pi \int_0^\infty \rho J_0(2\pi\rho\theta) e^{-\tau_q} \left(e^{\tilde{w}\tilde{\Phi}(\rho)\tau_q} - 1 \right) d\rho \quad (3.63)$$

where θ is the boresight angle, ρ is the independent variable in the transform domain, J_0 is the zeroth-order Bessel function of the first kind, and τ_q is the oblique optical depth as defined in eq. (1.1). \tilde{w} is the averaged single particle albedo, defined as,

$$\tilde{w} = \frac{C_s}{C_s + C_a} \quad (3.64)$$

where C_s and C_a are the average scattering and absorption cross-sections, respectively, and the quantity $C_s + C_a$ is often called the extinction cross section.

Noting that the Hankel transform (see *Bracewell* [2000], for example) is defined as,

$$F(\theta) = 2\pi \int_0^\infty f(\rho) J_0(2\pi\rho\theta) \rho d\rho \quad (3.65)$$

we see that eq. (3.63) is the Hankel transform of the function $f(\rho) = e^{-\tau_q} (e^{\tilde{w}\tilde{\Phi}(\rho)\tau_q} - 1)$. $\tilde{\Phi}(\rho)$ is the Hankel transform of the normalized phase function of a single particle,

$$\tilde{\Phi}(\rho) = 2\pi \int_0^\infty J_0(2\pi\rho\theta) \left(\frac{\Phi(\theta)}{4\pi} \right) \theta d\theta \quad (3.66)$$

where the single particle phase function is given by $\Phi(\theta)$, and is equivalent to the

Fraunhofer diffraction pattern of the particle.

For the sake of simplicity, *Marouf et al.* [1982] develop their methods assuming a Henyey-Greenstein model for $\Phi(\theta)$,

$$\Phi(\theta) = I_o(g) \frac{1 - g^2}{(1 - 2g \cos \theta + g^2)^{3/2}} \quad (3.67)$$

where $g = 1 - 2/x$ is related to the electric size parameter x , previously defined in eq. (3.40), Section 3.2.2. The factor $I_o(g)$ in eq. (3.67) is required to normalize the integral of Φ to 4π over the half-space where Φ applies (see also eq. (3.66)),

$$\int_0^{2\pi} \int_0^{\pi/2} \Phi(\theta) \sin \theta \, d\theta d\phi = 4\pi \quad (3.68)$$

Substituting eq. (3.67) into eq. (3.68) and evaluating yields the following normalizing factor,

$$I_o(g) = \frac{2g}{1 - g^2} \left[\frac{1}{\sqrt{1 - 2g + g^2}} - \frac{1}{\sqrt{1 + g^2}} \right]^{-1} \quad (3.69)$$

For electrically large particles, $g \rightarrow 1$ as $x \rightarrow \infty$. Taking the limit of eq. (3.69) yields $\lim_{g \rightarrow 1} I_o(g) = 1$. For particles larger than $x = 100$ or so, $I_o = 1$ is a reasonable approximation.

The Henyey-Greenstein function is one of many possible model choices to represent $\Phi(\theta)$. For our purposes, we want to make a direct comparison between the predictions of MPT theory and the results produced using the amplitude screen method. Thus for our analysis, a more suitable phase function is the Airy scattering pattern of a single sphere,

$$\Phi(\theta) = I_o(x) \left(\frac{2J_1(x \sin \theta)}{x \sin \theta} \right)^2 \quad (3.70)$$

which we have already shown to be well-approximated by our diffraction theory method. As with the Henyey-Greenstein function above, the normalization factor I_o must be such that eq. (3.68) is satisfied. Substituting eq. (3.70) into eq. (3.68) and solving for I_o yields,

$$I_o(x) = \frac{x^2}{2} \left[1 - \frac{J_1(2x)}{x} \right]^{-1} \quad (3.71)$$

3.5.2 Comparison with the Amplitude Screen Model

Technically, the MPT theory of *Marouf et al.* [1982] requires that ring particles are in each other's far field. However the far field condition is not substantially violated as long as the volume packing fraction of the rings,

$$f_{\text{vol}} = \frac{V_{\text{particles}}}{V_{\text{slab}}} \quad (3.72)$$

does not exceed 3% or so [*Marouf*, 2006–2010]. Here, V_{slab} is the volume of a slab of the rings containing the particles that are projected to create the amplitude screen, and $V_{\text{particles}}$ is the total volume of the ring particles contained within that slab.

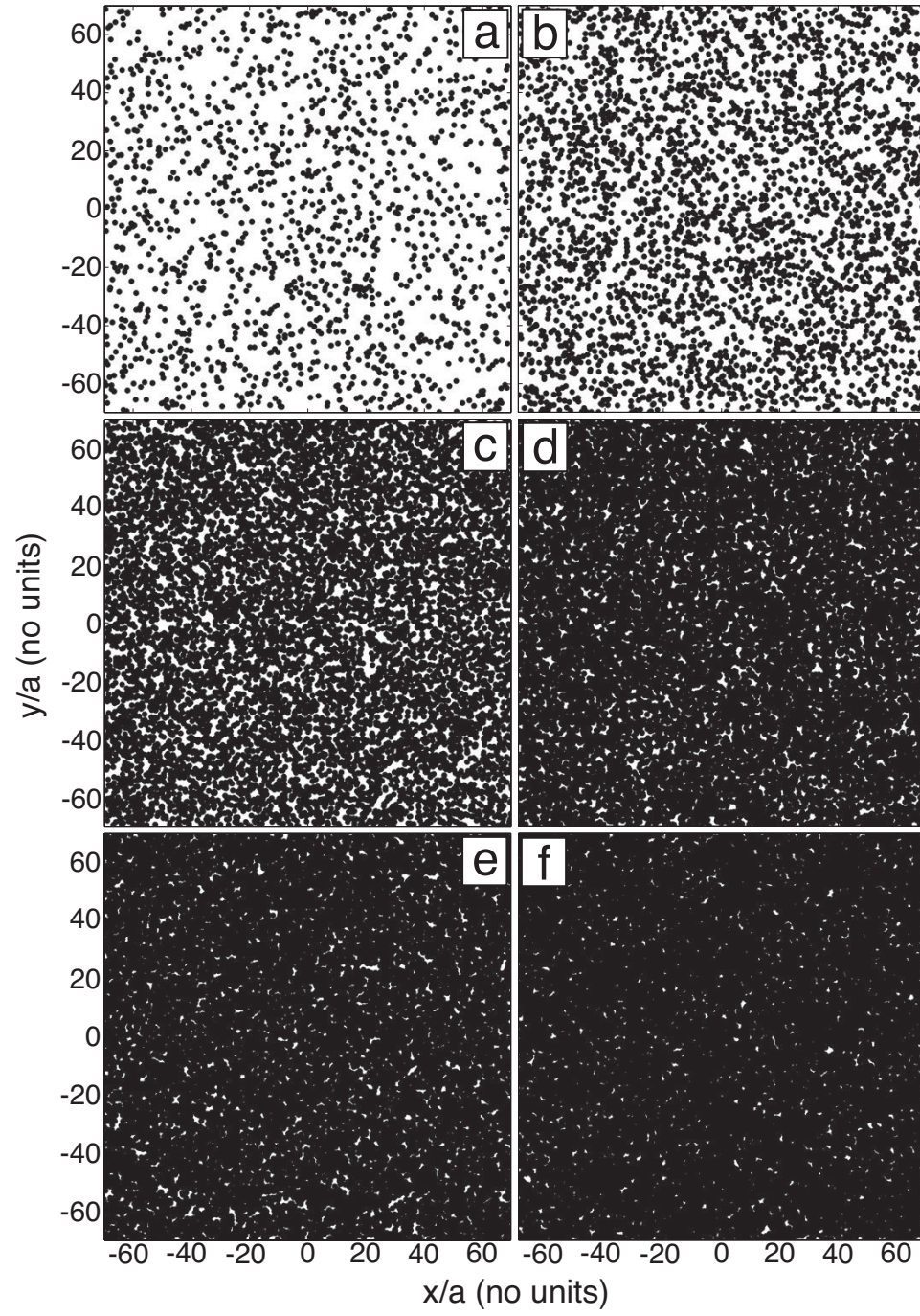
We proceed by comparing forward scattering lobe predictions computed from the theory of *Marouf et al.* [1982]; *i.e.*, using eq. (3.63) with eqs. (3.66), (3.70), and (3.71); with the results of amplitude screen diffraction simulations produced via the methods described previously in this chapter. We construct and populate slab volumes in order to obtain a desired oblique optical depth τ_q , iterating both the number of particles in the model N_p and the thickness of the rings T_r to ensure that the requirements $f_{\text{vol}} \leq 0.03$, and $T_r \geq 30$ are met. T_r is specified in units of particle diameters of the largest particle in the model. According to *Marouf*, these are sufficient conditions for the model to remain consistent with MPT theory. The oblique optical depth τ_q of the amplitude screens is computed according to,

$$\tau_q = -2 \ln \left(1 - \frac{A_p}{A_{\text{tot}}} \right) \quad (3.73)$$

where A_p is the shadow area of all particles projected onto the amplitude screen, and A_{tot} is the total area of the screen. Normal optical depth is related to the oblique optical depth according to eq. (1.2). Eq. (3.73) derives directly from eq. (1.1), since $I_o \propto A_{\text{tot}}^2$ and $I \propto (A_{\text{tot}} - A_p)^2$. For our analysis (and without loss of generality), we chose the ring opening angle $B = 90^\circ$; thus $\tau_q = \tau$. Figure 3.10 shows examples

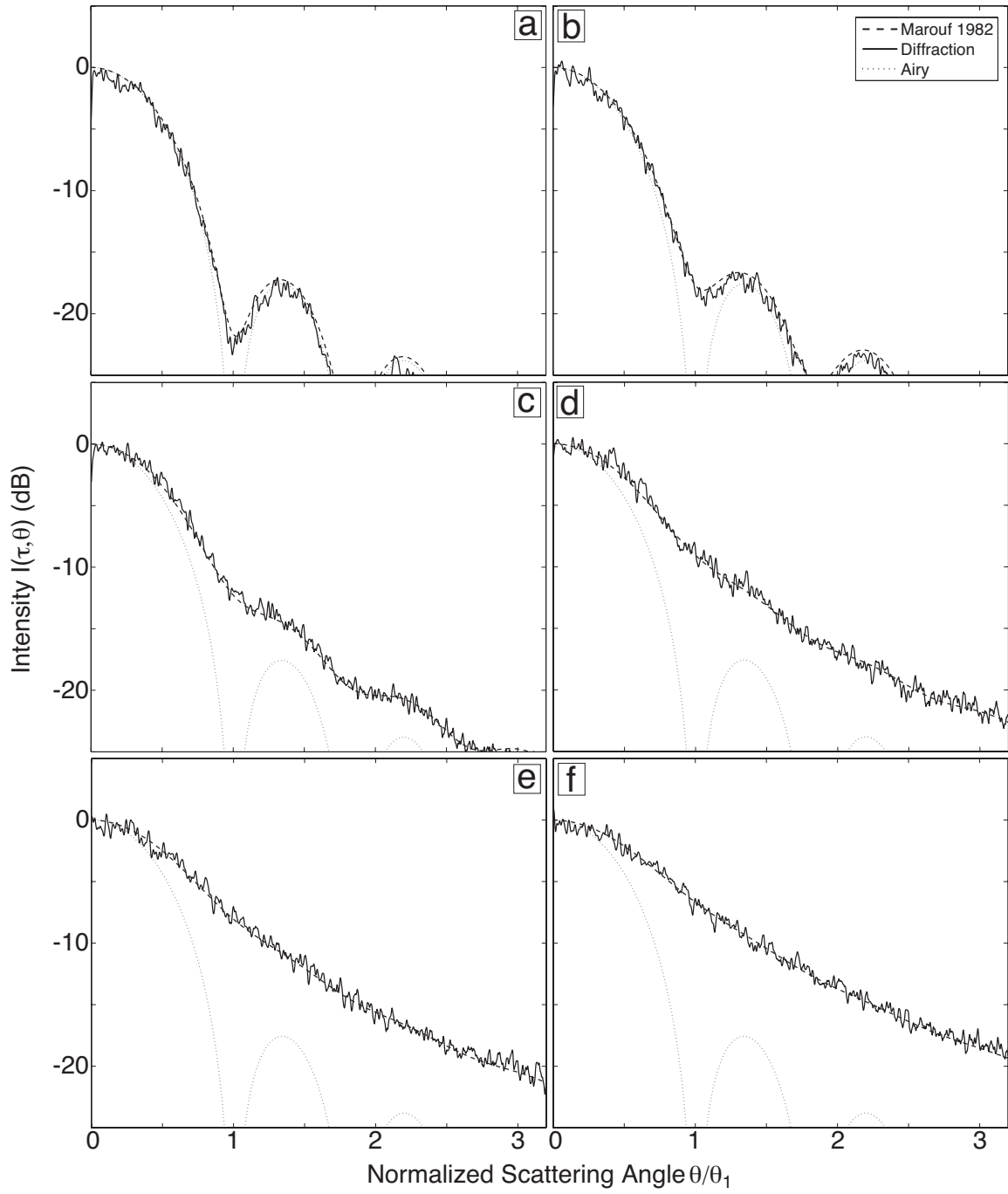
Next page.

Figure 3.10: Amplitude screen models of homogeneous, many particles thick (MPT) rings. The normal optical depth of the models ranges from $\tau = 0.49$ to $\tau = 8.24$. Higher optical depths were achieved by increasing the number of particles N_p in the simulation. The thickness of the rings T_r varies in each case, to ensure that the volume fraction f_{vol} of the rings does not exceed 3%. N simulations were performed for each optical depth value studied, and their diffraction patterns averaged together to produce the solution. Panels (a)–(f) show single instantiations of the N amplitude screens used to obtain the diffraction pattern averages shown in the corresponding panels of Figure 3.11. Cases shown are as follows: (a) $\tau = 0.49$; $T_r = 32$, $N_p = 1500$, $f_{\text{vol}} = 0.001$; (b) $\tau = 1.44$; $T_r = 32$, $N_p = 3500$, $f_{\text{vol}} = 0.014$; (c) $\tau = 3.26$; $T_r = 43$, $N_p = 9870$, $f_{\text{vol}} = 0.029$; (d) $\tau = 5.61$; $T_r = 73$, $N_p = 17,000$, $f_{\text{vol}} = 0.03$; (e) $\tau = 6.61$; $T_r = 86$, $N_p = 20,000$, $f_{\text{vol}} = 0.03$; (f) $\tau = 8.24$; $T_r = 107$, $N_p = 25,000$, $f_{\text{vol}} = 0.03$.



Next page.

Figure 3.11: Comparison of the amplitude screen method with the theory of *Marouf et al.* [1982] for a homogeneous, many particles thick (MPT) model of the rings. Each diffraction solution shown in (a)–(f) is the computed average of N unique diffraction patterns, each derived from an amplitude screen that we generated using an MPT ring model with identical parameters (T_r , N_p , f_{vol}). The parameters were selected to achieve a certain value of τ as indicated below; corresponding single instantiations of these amplitude screens are shown in Figure 3.10(a)–(f). The *Marouf et al.* [1982] solution is generated using eqs. (3.63) and (3.70). The normal optical depths and number of unique averaged diffraction solutions N for each case are: (a) $\tau = 0.49$, $N = 40$; (b) $\tau = 1.14$, $N = 40$; (c) $\tau = 3.26$, $N = 50$; (d) $\tau = 5.61$, $N = 40$; (e) $\tau = 6.61$, $N = 40$; (f) $\tau = 8.24$, $N = 55$. All other relevant parameters are as indicated in Figure 3.10(a)–(f).



of amplitude screens having six different values of τ , ranging between $\tau = 0.49$ and $\tau = 8.24$.

Eq. (3.63) gives the forward scattering lobe of the rings in a statistical sense. To compare this result with our amplitude screen diffraction model, we must compute the average diffraction pattern of N screens while holding N_p and the slab volume constant, thereby generating a statistical representation of scattering from rings of a given packing fraction and optical depth. N must be large enough to average out statistical fluctuations in the results—we determined that $N \geq 40$ is sufficient in our simulations. This topic is addressed in greater detail in Section 5.3.1.

Since the particle placement in each instantiation is unique, there is some variation in the computed optical depth for each screen. For each of the N cases, the value of τ_q is computed using eq. (3.73). The average value of τ_q of the N screens is used in eq. (3.63) for the comparison. We used particles of electrical size $x = 100$ (see eq. (3.40)) for all cases shown.

The results of the comparison are presented in Figure 3.11, showing excellent agreement between the amplitude screen diffraction approach and the analytic expression for forward scattering, based upon the MPT model of the rings presented in *Marouf et al.* [1982]. Similar good agreement between theoretical predictions and numerical simulations of scalar diffraction by randomly blocked amplitude screen ring models was reported by *Marouf* [1994, 1996]. The primary parameter of the thick homogeneous rings model is the desired oblique optical depth τ_q ; or alternatively, the normal optical depth τ . The secondary parameters specifying the model are the thickness of the rings T_r and the volume packing fraction f_{vol} . If the homogeneous model is to conform to the volume packing constraints of the MPT model, then f_{vol} and T_r are independent parameters only as long as the condition $f_{\text{vol}} \leq 0.03$ is satisfied. For a given vignette size—*i.e.*, the x- and y-dimensions of the amplitude screen (see Figure 3.1)—and ring opening angle B , all other variables are specified automatically for the model to remain self-consistent.

3.6 Summary

A rigorous treatment of electromagnetic scattering from a cluster of spheres is afforded by the application of the multiple particle formulation of Mie theory. However, to produce an accurate solution for scattering from electrically large spheres, and/or a large number of spheres, the computational cost of this method is high. For our research interest, scattering from clusters of electrically large Saturn ring particles in the range $x = 100 \rightarrow 400$, the computational requirement imposed by Wiscombe’s criterion and the multi-particle formulation of Mie theory quickly exceeds the capability of today’s computers—even for a small number (*i.e.*, less than 50) of particles. By contrast, the diffraction theory approach, initially developed by *Marouf* [1994, 1996, 1997] and further developed here, captures the behavior of thousands of particles in small vignettes of Saturn’s rings, such as those produced by dynamical simulations [*Salo*, 1992; *Schmidt et al.*, 2001; *Salo et al.*, 2004; *Morishima and Salo*, 2006]. The method is computationally limited only by the size of the 2D-FFT that must be performed on the amplitude screen to generate the diffraction pattern.

By definition, diffraction theory does not account for the electromagnetic coupling between ring particles that may be in each other’s near field—an effect which, under some circumstances, could significantly alter the far field estimate. In this chapter we have demonstrated that the far field radiation pattern produced by EM scattering from aggregates of electrically large spherical dielectric particles is very well-approximated by the results of scalar diffraction by their projected shadow area, as long as the range of angular interest is limited to the near-forward direction. Though the best results are seen for paraxial diffraction angles, diffraction theory shows remarkable agreement with multi-particle Mie theory within the entire main lobe of the particle cluster’s diffraction pattern.

We applied the amplitude screen method to MPT models of homogeneous rings, for which an analytic description of the diffracted far-field exists. Results using the diffraction theory method shows excellent agreement with corresponding analytic solutions, providing a basis for further confidence in the amplitude screen approach.

The diffraction signature of anisotropic structure in Saturn’s rings is evident in

the Cassini radio occultation experimental data [Thomson *et al.*, 2007]. As long as this structure is not hidden by an unfortunate observational alignment with \vec{k} , the likelihood of which is diminished by the near-monolayer thickness of Saturn’s rings, then the diffraction theory approach outlined in this chapter provides a powerful and computationally efficient tool to quantitatively characterize, in a statistical sense, near-forward scattering by particle distributions in Saturn’s rings.

The diffraction theory results contained in this chapter form the foundation for the methods that we have developed to extract estimates of the physical dimensions of ring microstructure from the radio occultation data. Those methods, which are the subject of Chapter 5, combine the results of this chapter with key properties of the signal that we receive from Cassini during radio occultation observations. In the next chapter, we discuss the Cassini radio occultation experiment, and provide detailed descriptions of the observation geometry, and of the properties of both transmitted and received Cassini radio signals.

h

Chapter 4

The Cassini Radio Occultation Experiment

In this chapter, we describe the key aspects of the Cassini radio occultation experiment.

In Section 4.1 we discuss the properties of the transmitted and received signal, the considerations necessary to optimize the spacecraft trajectory for the observations, and present an overview of many of the physical ring properties that can be estimated using radio occultation data. Additional details on these topics are provided in Appendix A.

In Section 4.2 we discuss the specific properties of the received signal that indicate the presence of ring microstructure, and explain some of the limiting aspects of the measurement that affect our ability to estimate microstructure dimensions. We present several examples of Cassini radio occultation data that contain evidence of ring microstructure, that were discovered during post-processing of the Cassini observations. Section 4.2 serves as a prelude to Chapters 5 and 6, where we describe methods to estimate microstructure dimensions from diffracted Cassini radio signals, and report all ring locations where evidence of periodic microstructure (PM) is present in the radio occultation data.

Eight of the first ten radio occultation observations of the Cassini mission occurred during orbital flyby geometries that were optimized for the experiment. In Section

4.3, we discuss the details of this series of optimized observations, which were made between May 3 and August 2 of 2005. Careful analysis of these observations led to the uncovering of periodic microstructure in Rings A and B, along with estimates of its physical dimensions.

4.1 Techniques, Observables, and Properties of the Received Signal

The Cassini spacecraft and NASA’s Deep Space Network (DSN) together form an instrument supporting radio occultation experiments to study Saturn’s rings. In this dissertation, we describe several such occultation experiments using a radio link between Cassini’s radio transmitter and at least one DSN receiver station. The radio link is typically established at least 20 minutes before Cassini is due to pass behind Saturn’s rings, as viewed from the DSN receiver(s). We calibrate the transmitted signal during this time, before the signal begins to interact with the rings. As Cassini continues on its trajectory in Saturn orbit, it moves behind the rings, as viewed from the Earth. When this happens, the signal linking the transmitter and receiver is said to be occulted (*i.e.*, blocked) by the rings. The point where a ray linking the transmitter and receiver intersects the rings is known as the ring piercing point (RPP). The RPP traces out a trajectory in the ring plane that we refer to as the occultation track. The experiment measures a one-dimensional sampling, along the occultation track, of the transmission properties of the rings at radio wavelengths. The geometry of a Saturn ring occultation experiment is shown in Figure 4.1. The occultation track for the May 3, 2005 occultation of Saturn’s rings by Cassini is shown in Figure 4.2.

4.1.1 Transmitted and Received Signals

For Cassini, the transmitted signal is composed of three highly coherent, right hand circularly polarized (RHCP) sinusoidal radio tones, well-separated in frequency, and phase-locked to the same highly coherent local oscillator to ensure that any phase modulation induced in the three transmitted tones by interaction with ring particles

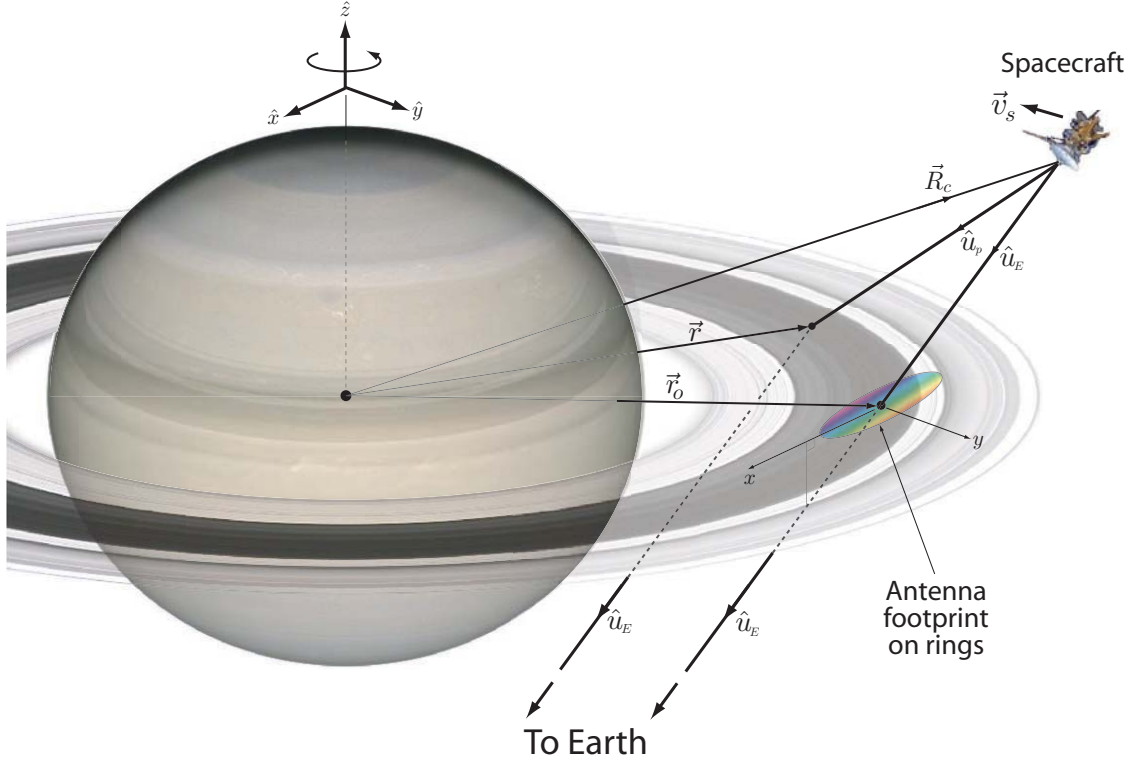


Figure 4.1: Ring Occultation Geometry. In the downlink configuration, a spacecraft traveling at velocity \vec{v}_s points its antenna along the Earth intercept vector \hat{u}_E and transmits a coherent, nearly monochromatic sinusoidal radio wave. The transmitting antenna illuminates a spot on the rings, the size of which has been greatly exaggerated here for clarity. Ring particles within the spot forward-scatter EM energy towards Earth at a frequency that is determined by the geometry and relative motion as per eq. (4.1). The spectrum of color filling the spot in this figure is representative of the resulting Doppler contours on the rings. The vector \vec{r} , which identifies a particular scattering region on the rings, has been drawn outside of the antenna spot—also in the interest of clarity. The \hat{z} -axis is the planet’s pole vector, which also defines the ring plane orientation. The \hat{x} -axis is the unit vector projection of \hat{u}_E into the ring plane, and $\hat{y} = \hat{z} \times \hat{x}$.

is accurately measured. Cassini uses an ultra-stable oscillator (USO) as its local oscillator, with measured phase stability of $\sigma_y = 2 \times 10^{-13}$ over a 1-second interval, where σ_y is the Allan deviation of the USO [Barnes *et al.*, 1971; Kliore *et al.*, 2004]. Cassini transmits at 13 cm, 3.6 cm, and 0.94 cm wavelengths, in the radio bands known as S-, X-, and Ka-band, respectively. One may think of the transmitted

tones as separate radio channels at which the rings are probed. A consequence of the high coherence of the transmitted signal is that radio wave diffraction, caused by structures within the rings, is detectable. We discuss this in greater detail in Section 4.2.

Radio signals from Cassini are received in both left-hand and right-hand circular polarizations, demodulated to an intermediate frequency (IF) band for sampling, and recorded as complex samples of the signal voltage at the receiver output. The demodulation frequency is controlled by a ‘predict’ file, which estimates the so-called sky frequency—the transmitted frequency, Doppler-shifted by the motion of Cassini relative to the DSN receive antenna(s)—using predictive orbital mechanics algorithms and the latest estimates of Cassini’s position and velocity. For the ring observations, the predict file is designed to continuously demodulate the sky frequency to 8 kHz, which is the center of a 16 kHz recording bandwidth, corresponding to 16,000 complex samples per second. The measured properties of the received signal are its polarization, magnitude, and phase; and from these quantities as a function of time we estimate its frequency, power, and power spectrum.

At each of the transmitted frequency channels (*i.e.*, S-, X-, and Ka-bands), the received signal comprises two components [Marouf *et al.*, 1982; Tyler *et al.*, 1983; Marouf *et al.*, 1983]:

1. Direct (Coherent) component: This is the transmitted sinusoid, attenuated and phase shifted by the average effect of its interaction with the interceding ring material along the very-near forward direction, well within the first several Fresnel zones.
2. Scattered (Incoherent) component: This component of the signal corresponds to energy forward-scattered towards the receiver from all of the ring particles illuminated by the transmitting antenna’s beam. The scattered signal is incoherent—both due to the stochastic nature of the location of the scattering ring particles, and due to the Doppler shift induced, relative to the transmit frequency, by the relative motion of the transmitter, ring particles, and the receiver. With the best signal-to-noise ratio (SNR) available during both Cassini

and Voyager observations of Saturn’s rings, the observable bandwidth of the scattered signal was approximately 4 kHz, centered (roughly) on that of the coherent signal (see Figure 4.3).

Schematic illustration of the direct (coherent) and scattered (incoherent) signals, as well as other key features of an example observed spectrum are presented in Figure 4.3.

4.1.2 Trajectory Design and Doppler Contours

Energy is forward-scattered from ring particles illuminated within the beam pattern of the Cassini transmit antenna to the receiver on Earth at a particular Doppler frequency f_D relative to the Doppler-shifted transmit frequency,

$$f_D = \frac{1}{\lambda} (\vec{v}_s - \vec{v}_p) \cdot (\hat{u}_p - \hat{u}_E) \quad (4.1)$$

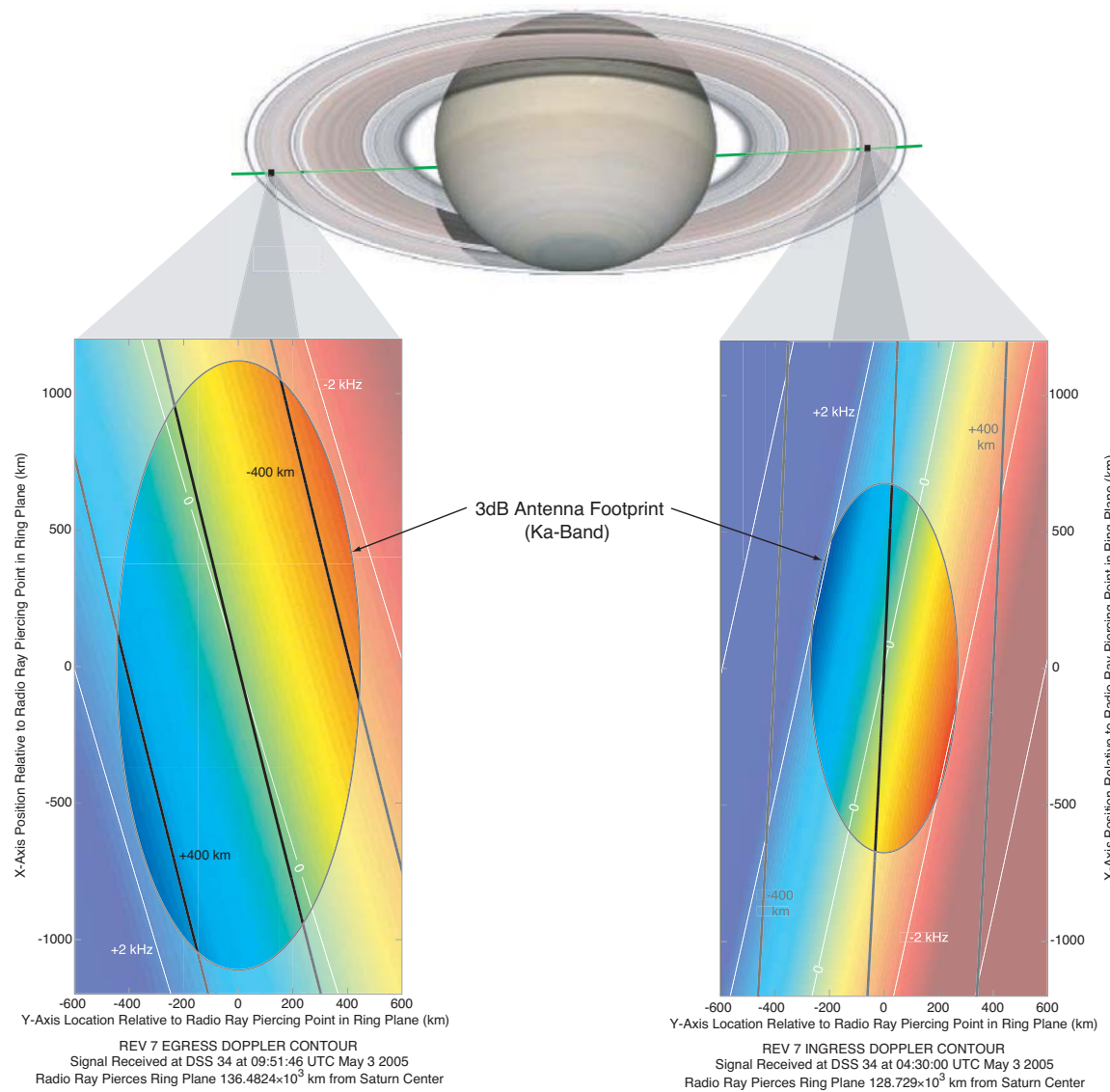
where f_D is in Hz; λ is the wavelength of the transmitted sinusoid; \vec{v}_s and \vec{v}_p are the Saturn-relative velocities of the spacecraft and the scattering ring particle, respectively; \hat{u}_p is the unit vector from the spacecraft to the scattering particle; and \hat{u}_E is the unit vector from the scattering particle to the Earth, where the receiver is located [Marouf *et al.*, 1983]. Eq. (4.1) is a good approximation when the transmitter (receiver) is much further away from the rings than the receiver (transmitter), so that the unit vector from the transmitter (receiver) to receiver (transmitter) is essentially equal to the unit vector from the scattering particle to the receiver (transmitter); see Figure 4.1, and note that \hat{u}_p is represented in the figure by a specific choice of \hat{u} .

Energy that is forward-scattered towards Earth at a specific Doppler frequency f_D (see eq. (4.1)) maps to a locus of points in the ring plane. The Doppler contours presented in Figure 4.2 show two instances during the May 3, 2005 occultation of the Cassini spacecraft by Saturn’s rings. White lines represent 2 kHz intervals in Doppler frequency; shading from blue through red represent the continuum of positively- through negatively-shifted Doppler signals.

The occultation track geometry of the first several diametric Cassini ring occultations were optimized by the Cassini tour designers to best align the contours of

Next page.

Figure 4.2: Occultation Geometry and Doppler Contours. Saturn is shown as it was seen from Earth during Cassini’s REV 7 encounter on May 3, 2005. The green line is the occultation track with ingress on the right and egress on the left, as the spacecraft traveled from right to left in this view. Two Doppler contour maps are shown—one each for specific points during the ingress and egress observation. The antenna spot for the Ka-band transmission are shown superimposed on the contours. The spot size is smaller for the ingress observation because for this particular orbital pass, the spacecraft was closer to the rings during ingress. Bluer color represents a Doppler shift $f_D > 0$; redder color corresponds to $f_D < 0$. Doppler contours at 2-kHz intervals are drawn in white. Contours of constant Saturn radius are shown in black, scaled relative to the radial distance of the ring piercing point (RPP) at $(x, y) = (0, 0)$. The REV 7 observation was optimized for alignment of radial and Doppler contours; however, some misalignment is unavoidable.



constant Doppler frequency with the contours of constant radius, shown in black in Figure 4.2. A close alignment of Doppler with radial location means that individual ringlets/radial structures scatter energy at the same Doppler frequency. Ideally, this leads to a received signal spectrum that maps energy at a given frequency to a specific radial location on the rings. In practice, perfect alignment is extremely difficult if not impossible to achieve, since it requires a very special spacecraft trajectory for each occultation pass.

Because of orbital dynamics constraints, the achievability of good Doppler contour alignment varies from pass to pass. From Figure 4.2, it is clear that the Cassini REV 7 egress observation was better aligned than the REV 7 ingress observation. Nonetheless, the ingress alignment is still reasonably good.

For optimized observations, the Doppler contour gradient within Cassini’s antenna footprint on the rings is reasonably well aligned with the ring piercing point (RPP) velocity vector \vec{v}_{RPP} —Doppler contours tend from low to high frequency across the antenna footprint and in the direction of travel, as is evident in Figure 4.2. As the leading edge of the Cassini high-gain antenna (HGA) pattern encounters a ring feature, energy is scattered from the feature towards Earth at a (relatively) large positive Doppler frequency. As the RPP passes through and past the feature, signals scattered from the feature to Earth sweep from high to low in Doppler.

Since the induced Doppler shift is proportional to λ^{-1} (see eq. (4.1)), longer (shorter) wavelengths yield Doppler contours that are proportionally expanded (contracted) in the ring plane. The Doppler contour expansion (contraction) is matched a commensurate increase (decrease) in the Cassini HGA beamwidth, which is proportional to λ . Since \vec{v}_{RPP} is the same regardless of the transmit frequency, the net effect is that the Doppler contours associated with longer wavelength transmissions transit a feature more slowly, and thus the transition from low to high Doppler frequency occurs over a broader range of radial locations of the RPP. Thus ring features that are visible in spectrograms of the received signal appear slanted at an angle that scales in direct proportion with the transmitted signal wavelength. We illustrate this point in Figure 4.4.

4.1.3 Observables

Despite the simplicity of the basic experiment, a surprising wealth of information can be derived from the received signal. From the coherent component, we obtain high-resolution diffraction corrected estimates of the optical depth of the rings for each of the frequency channels along the occultation track trajectory [Marouf *et al.*, 1986, 2005a, b, 2006a, b, 2007b; Rappaport *et al.*, 2008; Colwell *et al.*, 2009; French *et al.*, 2010]. In turn, the optical depth profiles can be used to estimate accurately the physical dimensions of density and bending waves (introduced in Chapter 2) which exist throughout the rings [Rosen and Lissauer, 1988; McGhee *et al.*, 2006; Rappaport *et al.*, 2006; Marouf *et al.*, 2007a]. Estimates of the local ring thickness and surface mass density follow directly from estimates of the physical dimensions of these waves [Rosen, 1989]. For other resolved ring features, methods have been developed to estimate particle sizes, ring thickness, and the degree of particle crowding [Marouf *et al.*, 1982, 1983; Zebker *et al.*, 1983, 1985]. Optical depth profiles obtained from the Voyager 1 radio occultation of Saturn resulted in the discovery of ten new waves in the rings [Rosen and Lissauer, 1988; Rosen, 1989]. Eight of these waves were identified as being caused by orbital resonances (introduced in Chapter 2) with specific moons; the source of the other two remains a mystery.

Three techniques are used in concert to estimate ring particle size distributions over the millimeter to several tens of meters size range [Marouf *et al.*, 1982, 1983, 1986]. For small particles, combined measurements of the differential extinction and the signal phase at two or more frequencies are used to estimate the number density of ring particles in the millimeter to decimeter size range. The diffraction lobes of particles larger than the Cassini high-gain antenna (*i.e.*, of radius $a > 2$ meters) are narrower than the spacecraft antenna beamwidth; as a result, information regarding the number density of particles in that size range is contained in the scattered signal. Analysis of the scattered signal yields number density estimates for particles ranging in size between approximately 2 meters and several tens of meters; the upper size limit of the estimate is controlled by the sampling interval of the measured diffraction pattern of the rings. For particles in the intervening decimeter to 2 meter size range, a bistatic scattering technique is used to sample the broader diffraction lobes of these particles.

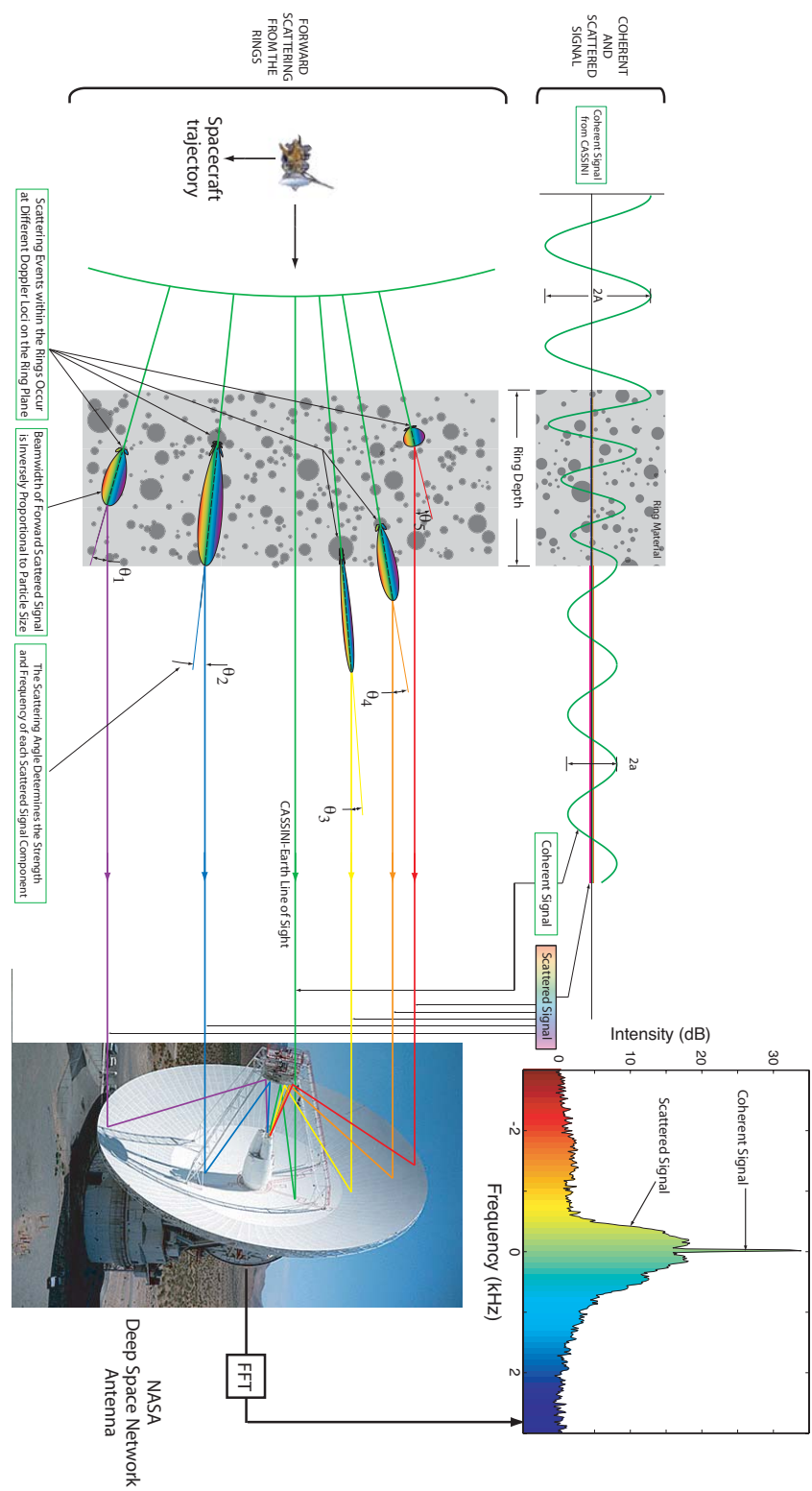
In this case, the Cassini antenna is pointed away from the Earth by an angle that is proportional to $\lambda/2a$ for the smallest particle to be sensed in this size range.

The estimated particle size distributions can be used to compute the expected optical depth at a given frequency, which can be checked against the measured optical depth value as a method for determining the self-consistency of the model and for characterizing the error in the estimate. A theoretical summary of techniques used to produce estimates of these and other quantities is provided in Appendix A.

The high SNR of the Cassini occultation experiments relative to Voyager, combined with the larger ring opening angles of $19.1^\circ - 23.6^\circ$ present during the Cassini's summer 2005 tour of Saturn, has resulted in the richest data set ever gathered with a ring occultation experiment. High SNR is very helpful in these experiments, because it improves our ability to probe the most optically thick regions of the rings (within Ring B), and to detect weaker scattered and diffracted signals originating from within the region of the rings that are illuminated by Cassini's high-gain antenna.

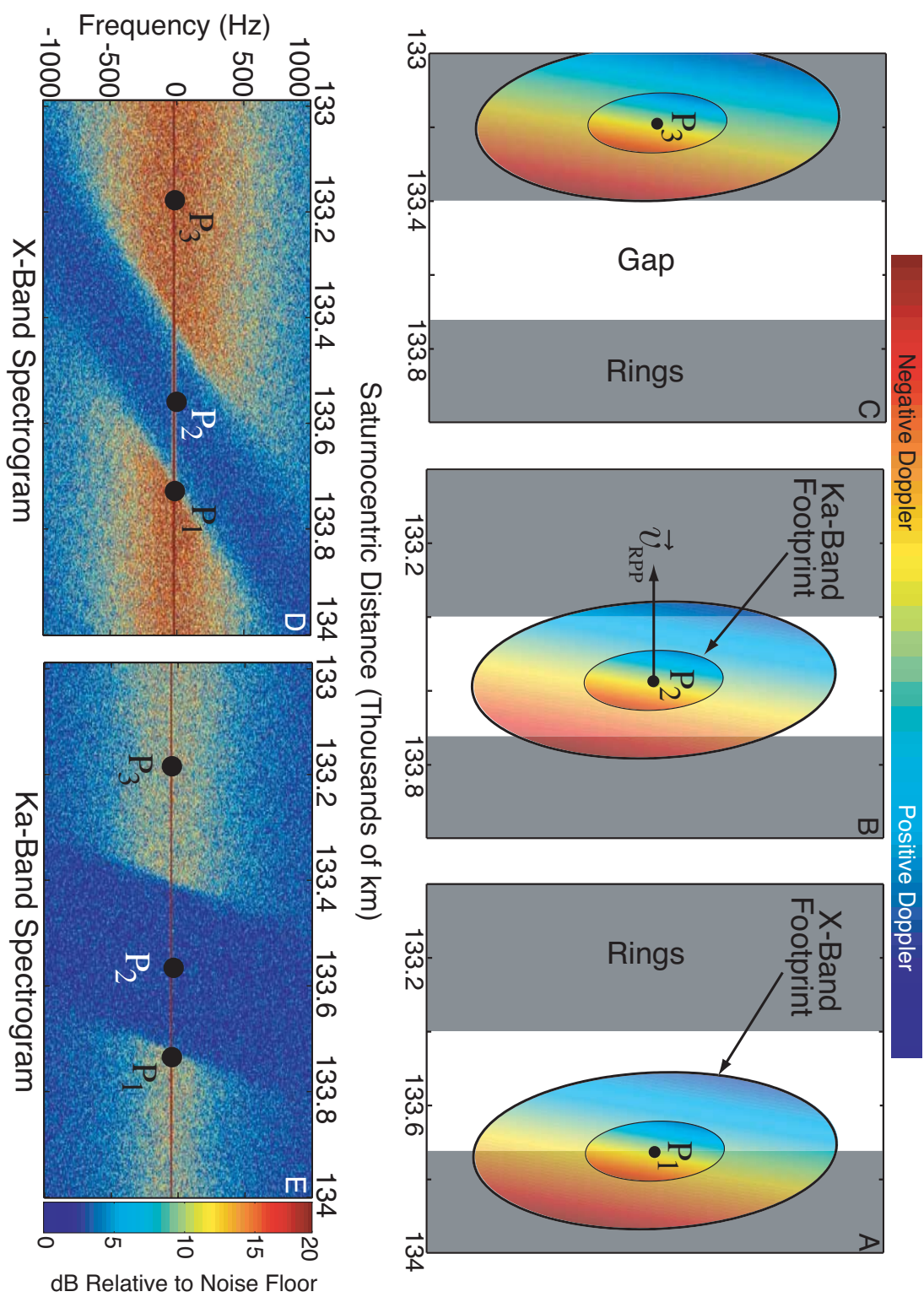
Next page.

Figure 4.3: Ring Occultation Signal Properties. The coherent component of the received signal travels along the very-near-forward direction from the spacecraft to Earth (downlink configuration), with $f_D \approx 0$ due to the forward geometry (see eq. (4.1) with $\hat{u}_p = \hat{u}_E$). The coherent signal is attenuated and phase shifted by its transit of the rings, relative to a coherent reference signal. The incoherent scattered signal is composed of energy scattered from particles along the near-forward direction, and spread in frequency according to eq. (4.1). The forward scattering lobes of particles are drawn here as a spectrum of color to emphasize the geometric dependence of f_D . The power spectrum of actual Cassini data from a radial location of $r \approx 2.1R_s$ (Ring A) is shown, color-coded to be self-consistent with the scattering depiction in the figure, and with the Doppler contours of Figure 4.2. The non-Gaussian nature of the scattered signal indicates the presence of fine-scale structure in this region of the rings.



Next page.

Figure 4.4: Doppler signature of a gap in the rings. Distinct features in Saturn’s rings appear slanted in spectrograms of Cassini radio occultation data. The slant angle depends on the wavelength of the transmitted signal, as is evident by comparing the X- and Ka-band spectrograms shown in panels **D** and **E**, respectively. Panels **A–C** depict an ingress occultation sequence, and show portions of the X- and Ka-band antenna footprints on the rings (centered on P , the ring piercing point (RPP)) moving with velocity \vec{v}_{RPP} as shown. In panels **A–C**, the values and relative scaling of the X- and Ka-band Doppler contours are represented by color within the antenna footprints as described in the caption of Figure 4.2. In panels **D–E**, color represents the power contained in the scattered signal, as shown in the scale included to the right of panel **E**. Points P_1 – P_3 represent distinct locations $|\vec{r}_o|$ of P during its motion along the occultation track (not shown). At P_1 (panel **A**), the positively Doppler-shifted (*i.e.*, blue-shifted) portion of both the Ka- and X-band footprints are illuminating the gap, which scatters no energy. Therefore only red-shifted Doppler signal energy is received when the RPP is located at P_1 . At P_2 , the X-band signal scatters large positive and negative Doppler-valued signals from the leading and trailing gap edges only, with no scattering in-between. The Ka-band footprint is completely contained within the gap, scattering no energy. At P_3 , both footprints fully illuminate the rings, and broadband scattering is received at both wavelengths. Compare panels **A–C** and their descriptions with the scattered spectrum at points P_1 – P_3 in panels **D** and **E**.



4.2 Detection of Microstructure in the Rings

Cassini radio signals at S-, X-, and Ka-bands (13-, 3.6-, and 0.94-cm λ) are generated from a single ultra-stable oscillator (USO), as described in Section 4.1. A consequence of the high coherence of the transmitted signal is that radio wave diffraction, caused by structures within the rings, is detectable. Diffracted signals originating from ring microstructure and macrostructure (see Chapter 2) contribute to the shape and features of the frequency spectrum of the received signal. Radio waves diffracted from large-scale structures such as ring divisions and gaps—with length scales on the order of tens to thousands of kilometers—modulate the amplitude of the coherent component of the received signal. This was first observed and reported during the Voyager radio occultation experiment; see *Marouf and Tyler* [1982] for an excellent example of microwave edge diffraction from the Encke gap.

The high-resolution optical depth profiles mentioned in Section 4.1 are obtained by removing the effects of diffraction from the received coherent signal, producing sharpened optical depth profiles that are not diffraction-limited (*e.g.*, *Marouf et al.* [1986]; *Rosen* [1989]). This process is described in detail in Appendix A. In this case, diffraction is an unwanted artifact that corrupts the measured direct signal, degrading the resolution of the profiles to scales larger than several Fresnel scales of diffraction.

4.2.1 Diffraction from Ring Microstructure

Diffraction effects are processed out of received Cassini signals to sharpen optical depth profiles of the rings. But diffraction is not always an unwanted signal artifact of the measurement technique—in our analysis, we use diffracted signals to detect and estimate the dimensions of ring microstructure.

Where microstructure exists within the rings, the local optical depth may vary significantly over short distances. As the Cassini radio signal probes the rings along the occultation track, these variations modulate the amplitude of the coherent signal with much greater frequency than the modulation induced by macrostructure. For structures on the order of tens to hundreds of meters, the corresponding optical depth variation is well-sampled by the experiment (the 16-kHz sample rate corresponds to

one sample every 1–2 meters of RPP movement along the occultation track; see v_{RPP} in Table 4.1). In the special case of periodic microstructure, the induced amplitude modulation is also periodic, and the frequency spectrum of the received signal (at S-, X-, and Ka-bands) contains sidelobes similar to those characteristic of an AM radio signal. A complementary point of view is that periodic microstructure in the rings behaves like a diffraction grating (to first order), producing detectible first-order diffraction (grating) lobes when illuminated by the highly coherent transmitted signal from Cassini.

The diffraction signature of individual particles and of their arrangement in an aggregate is contained in the overall diffraction pattern of ring microstructure, as shown in Chapter 3. The scattering behavior of microstructure is analogous to the far-field radiation pattern of a multi-element antenna, which is computed from the far-field pattern of the comprising antenna elements in combination with the phase relationships between those elements—the so-called element and array factors mentioned in Section 3.4.

In a ring occultation experiment, the physical dimensions of ring microstructure are inferred from its diffraction signature in a statistical sense only for two main reasons. First, ring particles are moving at speeds ranging between approximately 16 and 24 km/s in their Keplerian orbits about Saturn, within the main rings. We sample the radio signals at 16 kHz and Fourier transform blocks of 4096 complex samples; thus one spectral frame of processed data corresponds to approximately 1/4-second of observation time. Ring particles move approximately 4–6 km along their orbits during this period, and the RPP moves between 5–6 km along the occultation track. This motion effectively averages the diffraction signature of any microstructure comprising particles imaged during a given spectral frame. We could reduce the integration time in an effort to minimize this effect, but the improvement is not beneficial (particles move several meters during a single sample) and doing so degrades the SNR of the spectral frame. And second, the microstructure itself (to varying degrees that depend on the strength of and type of microstructure) is constantly being destroyed and re-formed within the rings, as mentioned in Section 2.2.

Nonetheless, we expect estimates of ring microstructure dimensions that derive

from its diffraction signature to be accurate measures of the local averages of those dimensions. The reason for this is that locally, the statistics of ring microstructure are controlled by properties such as particle size distribution, volume and surface mass density, local gravitational influences, etc., which do not change significantly on the spatial scale of the 4–6 km sample averaging (in most regions of the rings), or on the temporal scale of the Cassini mission’s lifetime.

4.2.2 Evidence of Ring Microstructure

Examples of diffraction from ring microstructure are shown in Figure 4.5. Panels **A** and **B** show spectrograms of the received signal, produced from X-band data received during our May 3, 2005 ring occultation experiment. Periodic microstructure is evident here (see figure caption), within the regions bounded by dashed lines (*i.e.*, within the regions 123.15–123.3 and 123.7–124.4 thousand km from Saturn’s center). We average these regions to produce the spectra shown in panels **C** and **D**.

In panel **C**, sharp sidelobes at ± 70 – 100 Hz relative to the strong (~ 35 dBn, or decibels relative to the sensible noise floor) coherent signal are clearly seen. These sidelobes are characteristic of diffraction from regions of periodic optical depth within the rings; they represent the first-order diffraction lobes of periodic microstructure. The coherent carrier and sidelobes are superimposed on a broader scattered signal, which peaks at ~ 10 – 12 dBn in the center of the panel and appears consistent with homogeneously-distributed rings or possibly a packed monolayer structure; *cf.* Figures 3.11 and 5.10.

Panel **D** also contains evidence of PM, although the sidelobe peaks are not as prominent as in Panel **C**. In this case, the background scattered signal shows an asymmetry characterized by a near-linear decrease in the scattered signal power over the interval -500 to 500 Hz. This is caused by averaging the scattered signal over a range that includes an absence of positive Doppler scattering—see the portion of the averaged region that is close to 123.7×10^3 km in panel **A**.

We averaged the spectrogram in Panel **B** to produce the spectrum shown in Panel **E**. Here, we also see evidence of microstructure. Though more subtle than indications

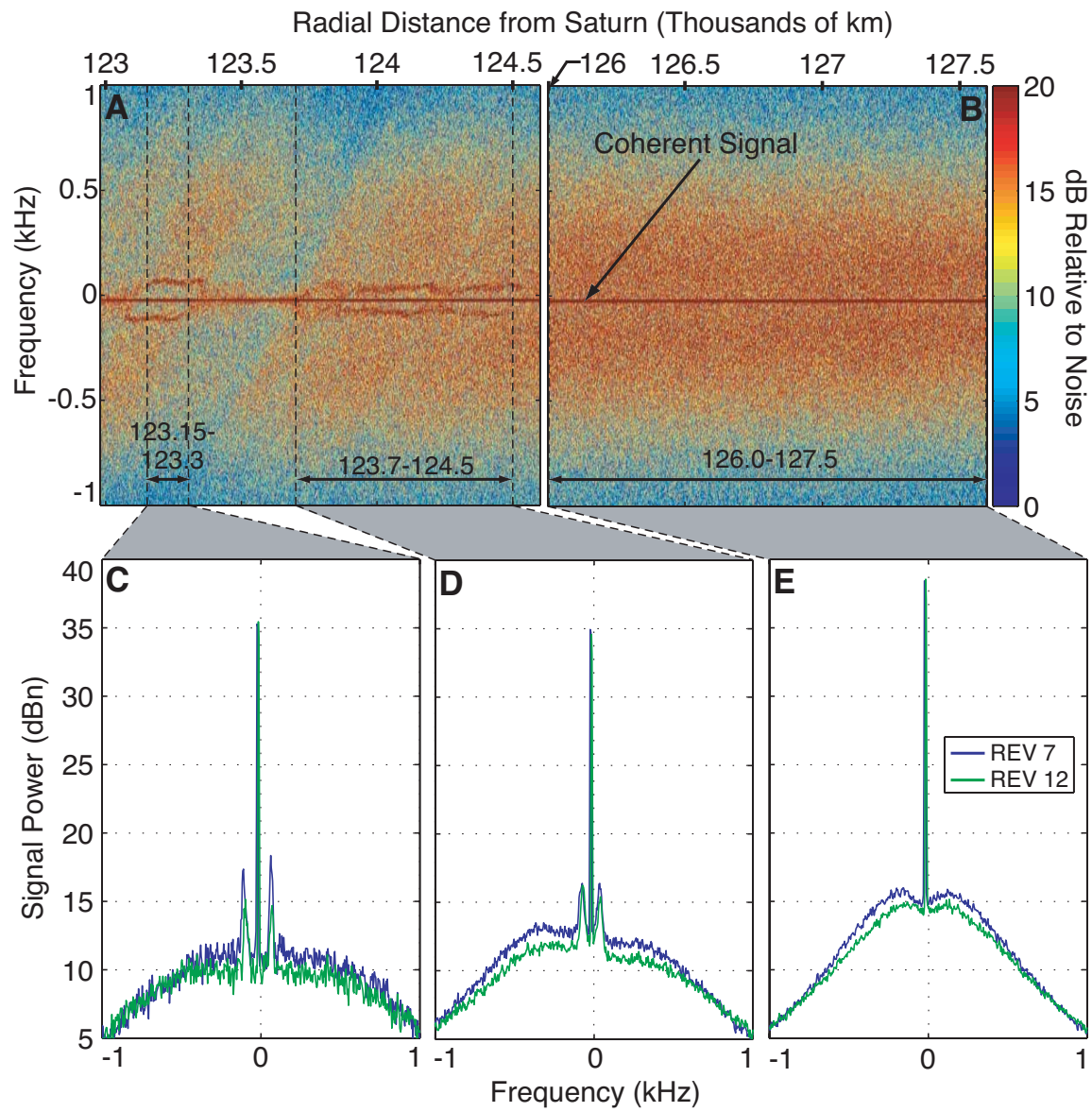
of PM, the double humps on either side of the coherent signal may possibly indicate the presence of gravitational wakes, which are known to exist broadly throughout Rings A and B [*French et al.*, 2007]. Compared with Panel **C**, the humps in Panel **E** show an enhancement in the scattered power in the range -500–500 Hz, where the peak signal level of the humps is ~ 15 dBn, compared with ~ 10 –12 dBn seen in Panel **C**. In Chapter 5, we show that simulated RF signals forward-scattered from gravitational wakes produce similar enhancements in near-forward scattering, reminiscent of the humps shown in Panel **E**; see Figure 5.10.

PM features evident in our spectrograms show an obvious slanting that depends on the transmitted signal wavelength, similar to the feature slanting discussed in Section 4.1.2 and illustrated in Figure 4.4. There is no high-to-low frequency sweeping associated with diffraction from ring microstructure—the Doppler frequency of the first-order diffraction sidelobes is controlled by the physical dimensions of the PM. The slanting of the feature is evident in the different radial locations that mark the beginning (and end) of the positive and negative Doppler sidelobes diffracted by the PM feature.

For PM features in the rings, the measured Doppler frequency of the sidelobes is the same at all three Cassini transmit wavelengths. This is because the sidelobe diffraction angle θ_d (discussed in greater detail in Section 5.2) and the spacing of Doppler frequency contours (discussed in Section 4.1.2) in the ring plane are both proportional to λ , compensating for each other exactly. The slanting and Doppler properties of signals diffracted from PM are explained illustratively in Figure 4.6. We explain the properties of PM diffraction more thoroughly in Section 5.2.

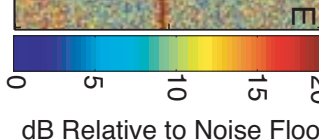
Next page.

Figure 4.5: Diffraction from ring microstructure. Panels **A** and **B** show spectrograms of X-band (3.6-cm λ) received during REV 7 ingress Cassini radio occultation observations. The coherent signal is the horizontal red line near the center of the spectrograms. In **A**, the diffraction signature of microstructure appears as roughly parallel lines displaced ± 70 –100 Hz from the coherent signal. Three sets of dashed lines and indicated ranges in **A** and **B** identify the swaths averaged to form the spectral plots shown in **C**–**E**, as shown. Spectrograms of REV 12 ingress data (not shown) were also averaged and are plotted in **C**–**E**. REV 7 occultation data produced a stronger scattered signal than REV 12 data because Cassini was $\approx 70,000$ km closer to the rings during REV 7 (see Fig. 4.9). In **C**, we see the sharp first-order diffraction lobes characteristic of periodic microstructure (PM). The PM signal is superimposed on background scattering that appears fairly homogeneous. PM is also evident in **D**, but the sloped background scattering shelf indicates that the PM is superposed on an unknown anisotropic background structure. The soft double lobes in **E** are characteristic of scattering from crowded monolayers, but it is unknown if that is uniquely true or if gravitational wakes or other anisotropy in the rings could produce this spectrum. The magnitude of the coherent signals in **C**–**E** vary inversely with average optical depth $\bar{\tau}$ over the region ($\bar{\tau} \approx 1.1$ in panels **C**–**D**; $\bar{\tau} \approx 0.8$ in panel **E**). In all panels, signal power is plotted in decibels relative to the sensible noise floor, abbreviated dBn.



Next page.

Figure 4.6: Doppler signature of periodic microstructure in the rings. Panels **A–C** depict an ingress occultation sequence, showing a portion of the Cassini high-gain antenna (HGA) footprint transiting the rings from right to left with velocity \vec{v}_{RPP} . The rings piercing point (RPP) is shown at three distinct locations P_1 – P_3 during the panel sequence. A small blue (red) dot represents the origin within the HGA beam of the positive (negative) Doppler-shifted first-order diffraction lobes of the PM at X-band. At these locations, Cassini signals are diffracted through an angle θ_d towards Earth; see Section 5.2 for a more thorough explanation. Similarly, a large blue (red) dot represents the origin of S-band sidelobe diffraction within the HGA footprint. X- and S-band signals originate in different locations because θ_d is proportional to λ ; Doppler frequencies are the same at all transmitted λ because the Doppler contour spacing in the ring plane is proportional to λ in a way that exactly compensates for differences in θ_d at different transmit wavelengths. The slanting of PM features in the spectrograms is proportional to the distance between the diffraction lobes (*i.e.*, the red/blue dots) at each transmitted λ —thus spectrograms of the S-band data appear more slanted than X-band, which appear more slanted than Ka-band. Compare panels **A–C** and their descriptions with the scattered spectra at points P_1 – P_3 in panels **D** and **E**. See Figure 6.3 for a comparison of PM diffraction at 13-, 3.6-, and 0.94-cm wavelengths.



4.3 Cassini Ring Occultation Observations, May–August 2005

The Cassini spacecraft flew 4 orbits of Saturn between May 3 and August 2 of 2005 that were optimized to align Doppler contours with radial contours, as described in Section 4.1. These four orbits, named REV 7, 8, 10, and 12 according to a NASA/JPL Cassini Tour convention, produced data for both ingress and egress observations on each orbital flyby, generating eight radio occultation data sets at each of the three transmit frequencies (13 cm, 3.6 cm, and 0.94 cm wavelength) for a total of 24 data sets.

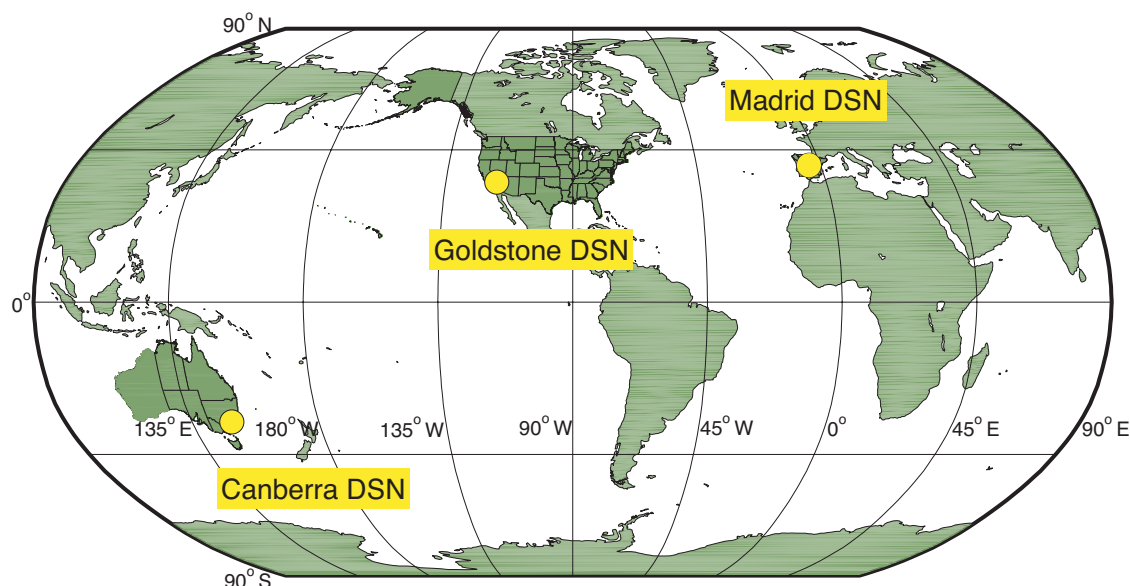


Figure 4.7: Location of DSN complexes around the world.

As mentioned in Section 4.1, NASA’s Deep Space Network (DSN) is an integral component in the ring occultation experiment. There are three primary DSN facilities: Goldstone ($35^{\circ} 25.529'$ North, $116^{\circ} 53.383'$ West), Madrid ($40^{\circ} 25.738'$ North, $4^{\circ} 14.963'$ West), and Canberra ($35^{\circ} 24.160'$ South, $148^{\circ} 58.878'$ East), each separated from the other by approximately 120° of longitude (see Figure 4.7) in order to provide near-constant coverage to any spacecraft mission served by the DSN. The choice of

DSN location and receiver was dictated by the frequency coverage required by the experiment, and by the visibility of Cassini at the three DSN sites during Earth receive time (ERT) of Cassini’s signal. Generally, this is determined by the elevation angle of Cassini above the local horizon; see Appendix B. Cassini signals are received at the DSN ground stations approximately 80–90 minutes after their transmission, delayed by the one-way light time from Cassini to the Earth present during the summer of 2005.

The local ring longitude and Cassini-RPP distance of the REV 7, 8, 10, and 12 observations are shown in Figures 4.8 and 4.9, respectively. For our purposes, zero local ring longitude is defined by the projection in the ring plane of the unit vector pointing from Saturn to the Earth at the time of the observation.

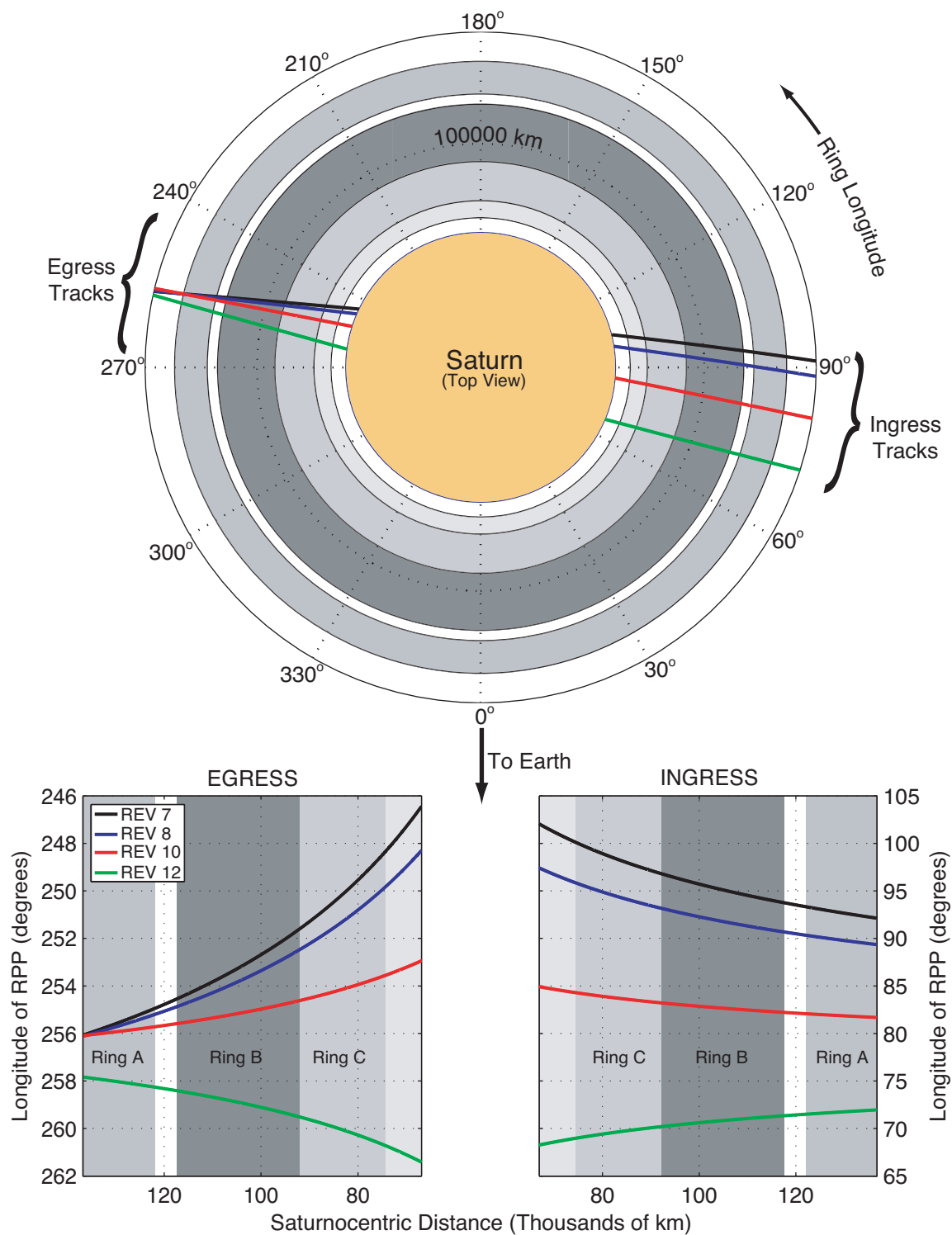
4.3.1 Details of the REV 7–12 Observations

The predicted timing, geometry, and operational details of the REV 7, 8, 10, and 12 observations are summarized in Figures 4.10–4.13 [Marouf, 2006–2010]. The start and end Earth receive times of the live movable block (LMB) are given in coordinated universal time (UTC) in the upper right and left of the figures (Figure 4.10 gives times in pacific time (PT) as well). The LMB is a planned sequence of operations that must be performed during the observation, which is uploaded as a single block to the spacecraft to command its onboard equipment. Event times within an LMB are relative to an epoch that can be updated a week to ten days before a given experiment, based on an accurate spacecraft trajectory prediction.

The orientation of Saturn as seen from the Earth is shown in the center of Figures 4.10–4.13. The occultation track is shown as a black line with ticks marking 10 minute intervals in time during Cassini’s orbital pass; the A, B, C, and F rings are also labeled. In the lower half of Figure 4.10, the start and end times of ring (ROI, ROE) and Saturn (SOI, SOE) occultation ingress and egress events are noted in both UTC and PT. The predicted beginning and end times of geometric occultation ingress and egress are also noted. In Figures 4.11–4.13, ROC and SOC are used instead to denote blocks of time corresponding to ring and Saturn occultations, respectively.

Next page.

Figure 4.8: Occultation track longitudes during the REV 7, 8, 10, and 12 ring occultation observations, May–August 2005. The upper graphic shows the occultation tracks as seen from above Saturn’s north pole. For our purposes, zero longitude is defined as the projection in the ring plane of the vector from Saturn to Earth at the time of the observation. In the lower panels, the ingress and egress occultation longitudes are plotted separately and in greater detail. Rings A–D are shown as shaded bands in the upper panel (all unlabeled), and also in the lower panels where only Ring D is unlabeled, for brevity.



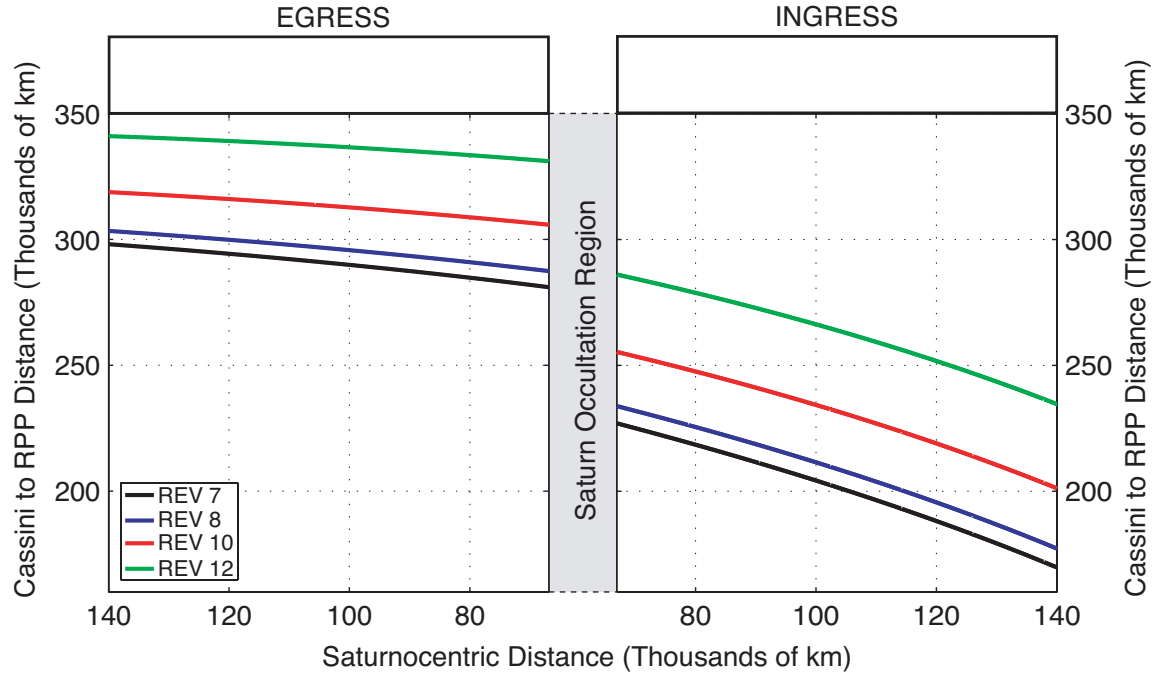


Figure 4.9: Distance from Cassini to the ring piercing point (RPP) during the REV 7, 8, 10, and 12 observations. Ingress and egress are shown separately, with a broken region in-between representing the 133,800-km span between inner Ring D ingress and inner Ring D egress. A graphic panel corresponding to the brightness of Saturn’s rings in backscattered light is shown along the top of the plots to lend some visual context to the Saturnocentric distance axis.

The DSN complex(es) used during each observation are shown as color-coded bars at the bottom; green for Canberra, blue for Goldstone, and yellow for Madrid. Within a DSN complex, the specific antennas used are identified by their deep space station (DSS) number. DSS 14, 43, and 63 are 70-meter (diameter) antennas, while the others are either 25-meter or 34-meter antennas. The antennas are pointed during the experiment by a combination of monopulse (MP; see *Gudin and Gawronski* [2000] for a description of the monopulse tracking method) and blind pointing methods. The timing of enabling and disabling monopulse (EMP, DMP) is labeled explicitly in Figures 4.11–4.13.

The type of transmitted signal is denoted at the bottom of the figures as either two-way non-coherent (TWNC) off (1-way), or 1-way downlink; both descriptions

correspond to a one-way transmission generated by Cassini's ultra-stable oscillator (USO).

The specific sequence and predicted timing of the comprising events of the REV 7, 8, 10, and 12 radio occultation observations are included in Appendix B, along with plots of Cassini's elevation as a function of ERT at the available DSN receiving stations.

Table 4.1: Summary of Geometric Occultation Parameters

REV	Date/Times (2005 PDT) ^a	ϕ_{RPP}^b (degrees)	r_{Co}^c ($\times 10^3$ km)	v_{RPP}^d (km/s)	\bar{B}^e
7I	May 02 (21:18:47–22:51:01)	92.0–101.9	172.9–227.0	21.9–23.6	23.6
7E	May 03 (01:23:50–02:52:08)	246.5–256.1	281.0–297.6	23.2–23.7	23.6
8I	May 21 (01:45:58–03:18:19)	89.2–97.3	180.4–233.8	21.8–23.4	23.2
8E	May 21 (05:55:12–07:23:37)	248.3–256.1	287.4–302.9	23.1–23.6	23.2
10I	Jun 26 (11:48:41–13:21:57)	81.5–84.8	204.2–255.4	21.5–23.0	22.0
10E	Jun 26 (16:07:25–17:36:45)	253.0–256.1	305.9–318.4	22.7–23.2	22.0
12I	Aug 02 (02:23:09–03:58:34)	68.1–71.2	237.6–286.1	21.3–22.7	20.5
12E	Aug 02 (06:48:18–08:19:56)	257.9–261.4	331.1–340.8	22.4–22.8	20.5

^aTimes defined when the ring piercing point (RPP) is within Rings A–D^b ϕ_{RPP} = longitude of the RPP^c r_{Co} = distance from Cassini to the RPP^d v_{RPP} = speed of the RPP in the ring plane^e Average of the ring opening angle B

Cassini First Diametric Radio Occultation of Saturn's Rings and Atmosphere: Rev 7, May 2-3, 2005 (DOY 122-123)

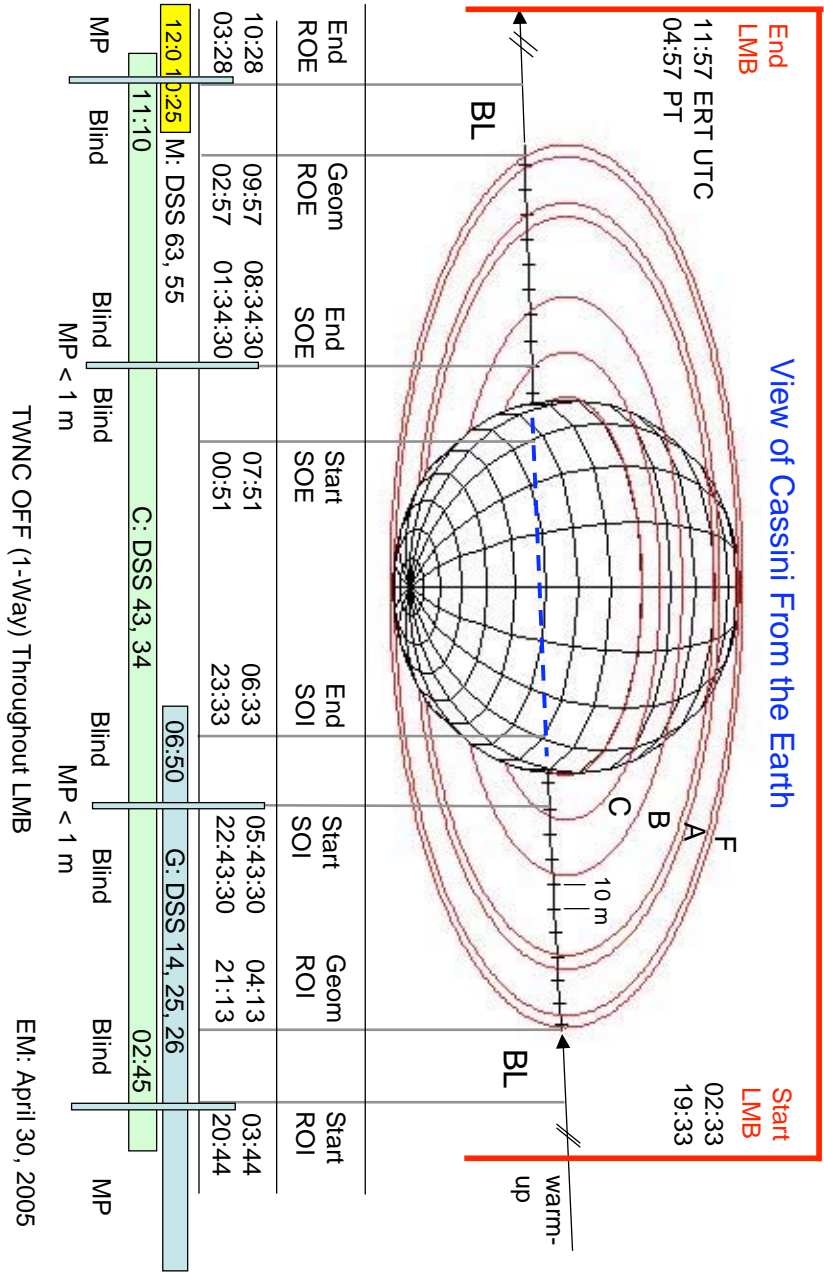
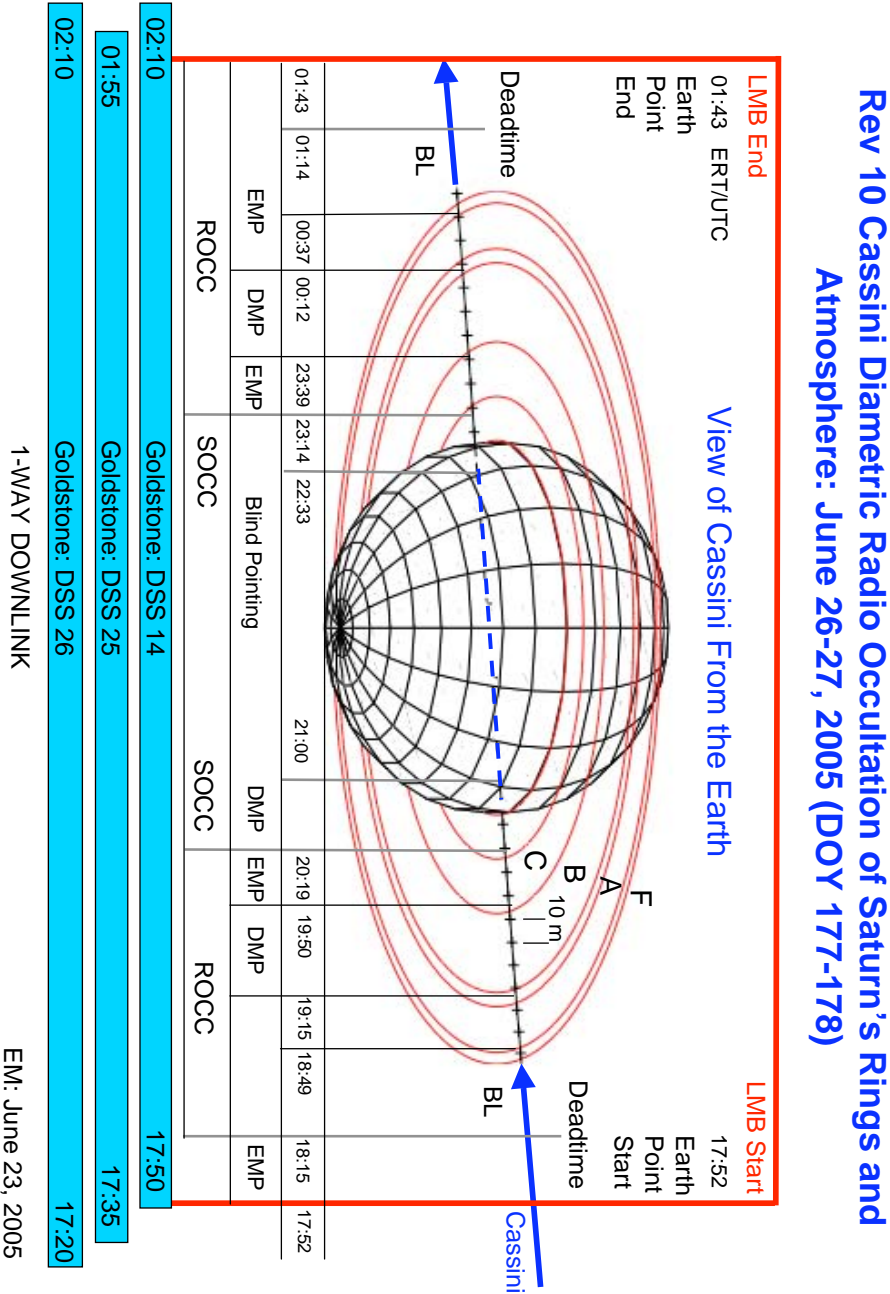


Figure 4.10: REV 7 predicted observation timing and geometry. Figure courtesy of Essam Marouf.

[illegible]

Figure 4.11: REV 8 predicted observation timing and geometry. Figure courtesy of Essam Marouf.



Cassini Sixth Diametric Radio Occultation of Saturn's Rings and Atmosphere: Rev 12, August 2, 2005 (DOY 214)

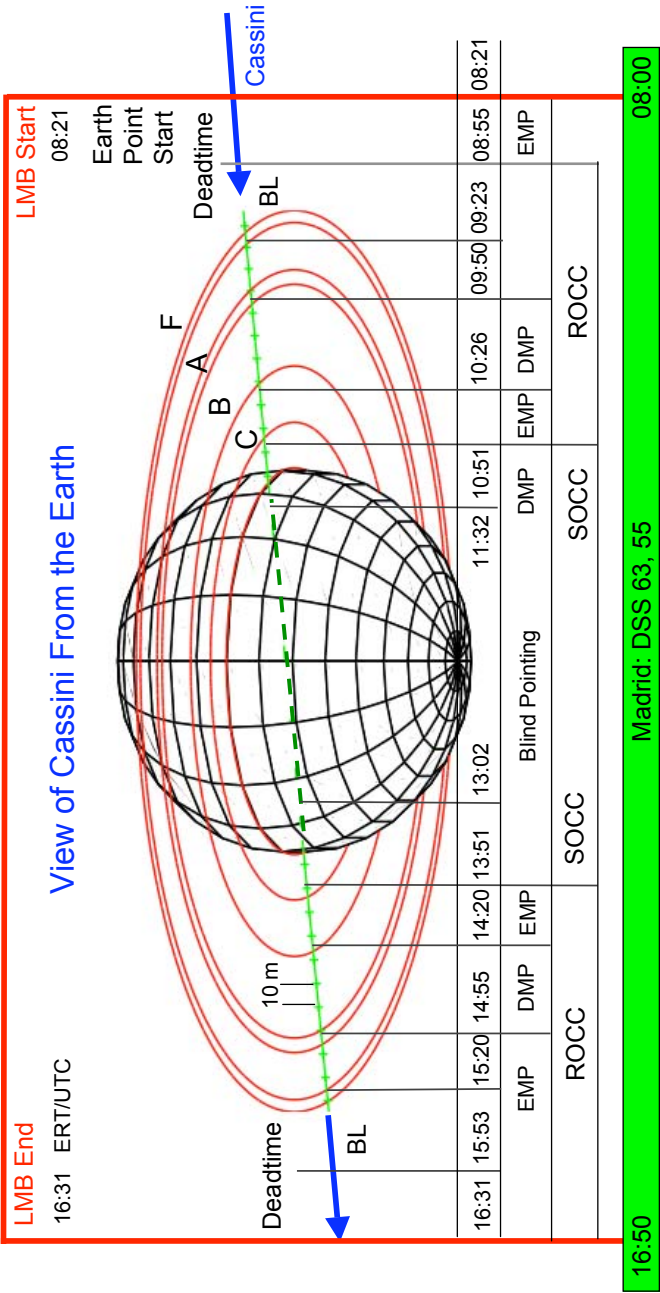


Figure 4.13: REV 12 predicted observation timing and geometry. Figure courtesy of Essam Marouf.

4.4 Summary

In this chapter we have briefly described the Cassini radio occultation of Saturn's rings. In the experiment, the radio occultation signal received is a superposition of coherent waves transmitted through the rings, energy diffracted from ring structures contained within the first several Fresnel zones, and energy forward-scattered towards Earth by illuminated ring particles. Despite its simplicity, the Cassini radio occultation experiment yields estimates of many physical features in the rings, on scales varying from thousands of kilometers down to individual particle sizes. A detailed summary of quantities that are estimated using radio occultation data is included in Appendix A.

The diffracted signal contains information about the fine-scale structure of the rings—*i.e.*, the arrangement of ring particles on scales of tens to hundreds of meters. Evidence for the presence of ring microstructure is given in Section 4.2. Although we are not able to measure the exact compositional geometry of microstructure deterministically, the Cassini radio observations contain the equivalent of a spatial average of the microstructure over a range of ring longitudes (*i.e.*, in azimuth). From this we estimate the microstructure dimensions in a statistical, averaged sense. In the next chapter, we detail our methods for producing those estimates.

h

Chapter 5

Fitting Microstructure Models to Radio Occultation Data

In Chapter 3, we showed that the far-field radiation pattern produced by EM scattering from an aggregate of electrically large particles is well-approximated by the diffraction pattern of a representative amplitude screen, when observations are limited to the near-forward direction. We construct the amplitude screen by projecting the shadow area of the aggregate particles into a plane perpendicular to the wave vector \vec{k} of the illuminating EM wave. In Chapter 4, we described the Cassini radio occultation experiment, and showed that the measured data contains clear evidence for the existence of microstructure in the rings.

In this chapter, we build upon the results of Chapter 3 and present a set of techniques to estimate the physical dimensions of microstructure evident in regions of Saturn’s rings. We begin this chapter with an overview of those techniques.

5.1 Overview of the Method

The goal of the analysis described in this chapter is to match models of ring microstructure to the evidence of microstructure that we see in the Cassini radio occultation data. To this end, we have developed a forward-theoretic modeling approach that we apply specifically to regions in the rings that contain periodic microstructure

(PM), producing estimates of the structural wavelength λ_{gr} and orientation ϕ_{gr} as a function of radial location of these structures in the rings. We report those results in Chapter 6.

In general, the technique relies upon the diffraction theory results of Chapter 3. We begin with a parameterized model of ring microstructure, which we select from one of the four basic microstructure models we introduced in Section 2.3,

1. Homogeneously distributed thick rings
2. Packed monolayers
3. Gravitational wakes
4. Periodic microstructure (PM)

We create parameterized models of these four types of ring microstructure either by using the amplitude screen methods described in Chapter 3, or by using analytic methods that are based on diffraction theory. These two distinct methods are described in detail in Sections 5.2.1 and 5.2.2, respectively.

We generate amplitude screens using two distinctly different procedures. In the first procedure, we employ particle aggregate models to represent ring microstructure, as described in Chapter 3. With the particle aggregate model, we describe the behavior and/or location of individual particles statistically in terms of means and standard deviations, producing unique instantiations (or realizations) of microstructure that each follow the same underlying statistics. In the second procedure, we construct an amplitude screen that has sinusoidally-varying transmittance, which we generate without the need to place and project the shadows of an aggregate of particles. We use the particle aggregate model to represent all four types of ring microstructure listed above; we use the sinusoidal transmittance model to represent the periodic or pseudo-periodic nature of gravitational wakes and PM only.

From the amplitude screens, we compute far-field diffraction patterns in the spatial frequency domain. The diffraction pattern of all instantiations are averaged to produce a mean diffraction pattern for a given set of underlying microstructure statistics. In the case of the sinusoidal transmittance model, we do not need to perform this averaging since the sinusoidal screen does not contain any statistical variation.

We map locations in the ring plane where signals originate to the angular frequency domain associated with the Cassini transmissions at 13-, 3.6-, and 0.94-cm wavelengths, and then compute the Doppler frequency f_D associated with signals originating from those locations. The amplitude of the Doppler-shifted signals are scaled by the antenna gain and diffraction pattern amplitude, and summed to produce a synthetic received signal corresponding to a specific ring piercing point (RPP) location during a particular radio occultation observation.

For periodic microstructure, we reduce the complexity of this process by seeking only the Doppler frequencies at the location in the ring plane where the first-order diffraction lobes originate. We further simplify this task by defining an analytic expression, based on diffraction theory, that yields the location of the lobes in the ring plane. This analytic description does not require the creation of amplitude screens, and depends only on a given set of physical parameters that we describe later in this chapter.

We optimize our choice of the microstructure’s model parameters using a least-squares approach to drive the convergence of the simulated received signal spectrum to the actual received signal spectrum for selected spectral features, thus obtaining estimates of the model parameters that best fit the radio occultation experimental data for a particular location in the rings over multiple observations. For the case of PM, we optimize λ_{gr} and ϕ_{gr} to match the first-order sidelobe frequencies only, simplifying the problem significantly.

In Section 5.2.1, we describe the method for generating amplitude screens that represent vignettes of ring microstructure. This section highlights the generality—and hence the modeling power—of the amplitude screen method. In Section 5.2.2, we describe analytic models that provide an additional means to model two specific types of microstructure.

In Sections 5.3–5.4 we show how the models of Section 5.2 are used in conjunction with Cassini radio occultation measurements to produce estimates of ring microstructure.

5.2 Microstructure Modeling Techniques

In this section we discuss two different methods for modeling ring microstructure. The first method employs the amplitude screen modeling approach, which we described in detail in Chapter 3. The amplitude screen method yields diffraction patterns $\overline{U}(u, v)$ that represent the statistically-averaged far-field scattering behavior of a particular microstructure model with a given set of model parameter values.

In the second method, we apply analytic expressions that take model parameters and either describe $\overline{U}(u, v)$ directly, or skip ahead to a later step in the process (described in Section 5.3) where we find the Doppler frequencies associated with key features in the diffracted signal spectrum.

5.2.1 Microstructure Simulations using the Amplitude Screen Method

We generate amplitude screens using either the particle projection technique (see Figure 3.1), or by using a screen transmittance function T to generate amplitude screens with sinusoidally varying transmittance. Henceforth, we shall refer to the screens produced using these two techniques as particle aggregate models and sinusoidal transmittance models, respectively. Regardless of the technique used to generate the screen, the far field diffraction pattern of the microstructure is computed via the method described in Chapter 3.

We create particle aggregate models either by explicitly specifying the mean and standard deviation of physical dimensions and other model parameters (which are discussed below for each model), or by using the results of dynamical planetary ring simulations that produce evolutions of ring particle distributions that obey the underlying physics of the model. Since the diffraction signature of microstructure is not particularly sensitive to the size distribution of the particles, we populate our models with identically-sized particles.

Homogeneously Distributed Thick Rings

We provide only a brief summary of the homogeneous, many particles thick (MPT) rings model here, since it was described in detail in Section 3.5. We parameterize the model by the normal or oblique optical depth τ or τ_q , respectively; the volume packing fraction f_{vol} (eq. (3.72)); and the thickness of the rings T_r . As described in Section 3.5, f_{vol} and T_r cannot always be selected independently. The number of particles N_p contained in the vignette is a secondary parameter, used to achieve the correct value of τ while adhering to the MPT requirement that $f_{\text{vol}} \leq 0.03$. The linear dimensions x_{max} and y_{max} of the vignette affect the value of N_p required to achieve a given τ ; see eq. (3.73). Examples of amplitude screen vignettes corresponding to these different parameters are given in Figure 3.10.

Packed Monolayers

Dynamical models predict that some regions of Saturn's rings may comprise a single monolayer of relatively large ring particles, surrounded by a cloud of smaller particles; the ensemble being no more than 50–100 meters thick in total (*e.g.*, *Deau et al.* [2008]). As a monolayer of ring particles becomes crowded, the spatial distribution of particles becomes less random, and more like a lattice as the particles pack closer and closer together. This results in a distinct deviation from the broadened Airy diffraction pattern produced by homogeneous rings.

As crowding in the monolayer increases, simulations show increased extinction in near-forward scattering (relative to the MPT model) that improves and eventually matches MPT model scattering at angles close to $\theta \approx 0.5\theta_1$; see Figure 5.1. In the figure, both the MPT and monolayer models have $\tau = 0.78$, and θ_1 is the first null in the diffraction pattern of a single particle as defined in Section 3.3. This behavior was reported by *Marouf* [1996, 1997].

We use particle aggregate models to represent packed monolayer microstructure. Generating parameters to the packed monolayer model include optical depth (τ or τ_q), particle radius a , vignette dimensions x_{max} and y_{max} . These parameters, in turn, specify the number of particles N_p contained within the vignette. The thickness of a

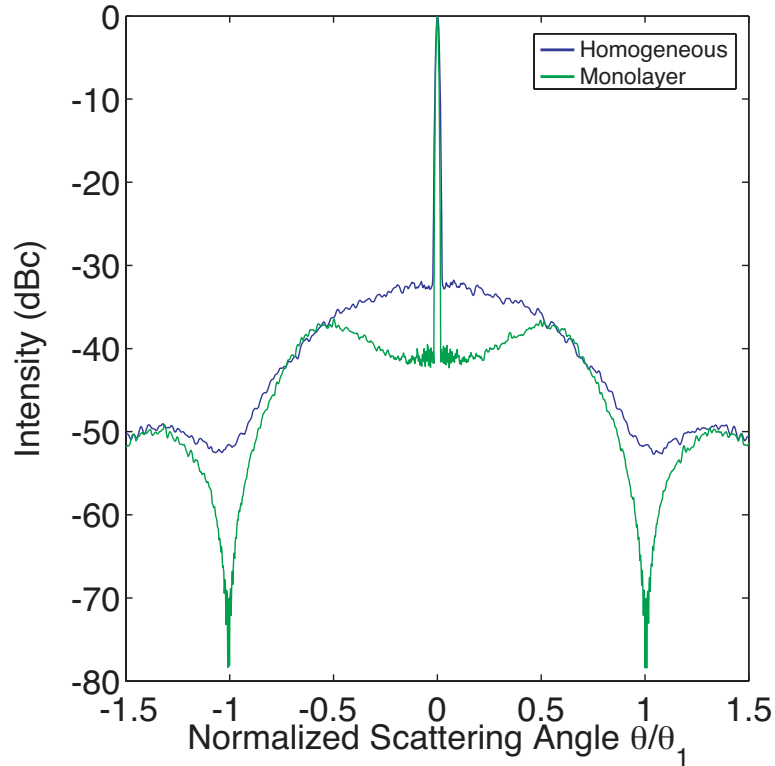


Figure 5.1: Comparison of scattering from homogeneous MPT, and packed monolayer models of planetary rings. In both cases, the average diffraction pattern of $N = 100$ amplitude screens are shown. We created the amplitude screens using a normal projection of the rings; *i.e.*, $\tau_q = \tau$. The average optical depth for both cases is $\tau = 0.78$. In the figure, the abscissa scale is normalized to the first null in the diffraction pattern of a single particle, θ_1 .

packed monolayer is fixed at $T_r = 1$.

Gravitational Wakes

Gravitational wakes are thought to be common throughout Saturn's Rings A and B, as discussed in Chapter 2. These are pseudo-periodic structures that are in a constant state of dissolution and re-formation, and are aligned in the ring plane at angles of 20° – 25° to the local azimuthal unit vector (*e.g.*, *French et al.* [2007]). Particle aggregate models of gravitational wakes can be produced from the output of dynamical simulations (Figure 5.2(a)), or by explicitly specifying the mean and

standard deviation of wake spacing and orientation (cant angle) as shown in Figure 5.3.

In Figure 5.2, we show amplitude screens and diffraction patterns that we created using the results of dynamical simulations performed by Heikki Salo at the University of Oulu [Saló, 2006]. Saló's simulations produced a time-domain evolution of the position and velocity of 5330 1.66-m radius ring particles as the particles orbit Saturn. Other physical parameters specified in the model are surface mass density $\sigma_\rho = 500 \text{ kg m}^{-2}$, and volume mass density $\rho = 450 \text{ kg m}^{-3}$ (σ_ρ and ρ are described in more detail in Appendix A). Initially, the particles are homogeneously distributed within the $300 \times 300 \times 55 \text{ m}$ simulation volume; the volume is centered in the ring plane at a distance of 100,000 km from Saturn's center.

During the simulation, Saló's code outputs the position of all particles contained within the simulation volume at the end of each of 100 successive orbits of Saturn. For the given input parameters, the homogeneous initial distribution of particles evolves to a distribution that contains distinct wakes, as seen in Figure 5.2(a), by the tenth orbit. A detailed description of the simulation is given in Saló [1995].

Saló shared with us the files containing the position of each of the 5330 particles at the end of each of 100 consecutive simulated orbits of Saturn (*i.e.*, 100 files in total). We used these files to create $N = 90$ amplitude screens, corresponding to the particle aggregates defined by Saló's files for orbits 11–100, and in which gravitational wakes are evident. Figure 5.2(a) is an amplitude screen produced from one of Saló's particle position files. In Figure 5.2(b) we show the average diffraction pattern of $N = 90$ vignettes. Figure 5.2(c) is a plot of the diffracted signal intensity along the dashed line shown in white in Figure 5.2(b), which is oriented at a cant angle of approximately 25° to the u -axis, showing the enhanced scattering in the very near forward direction that is characteristic of wakes. Figures 5.2(b)–(c) show diffraction in the spatial frequency domain; a method for transforming to the Doppler frequency domain and comparing the results with Cassini data is the subject of Section 5.3.

We also represent gravitational wakes using the parameterized, statistically generated particle aggregate model shown in Figure 5.3. The model is specified by its optical depth (either τ or τ_q), the mean $\bar{\lambda}_{\text{gr}}$ and standard deviation σ_{gr} of the wake

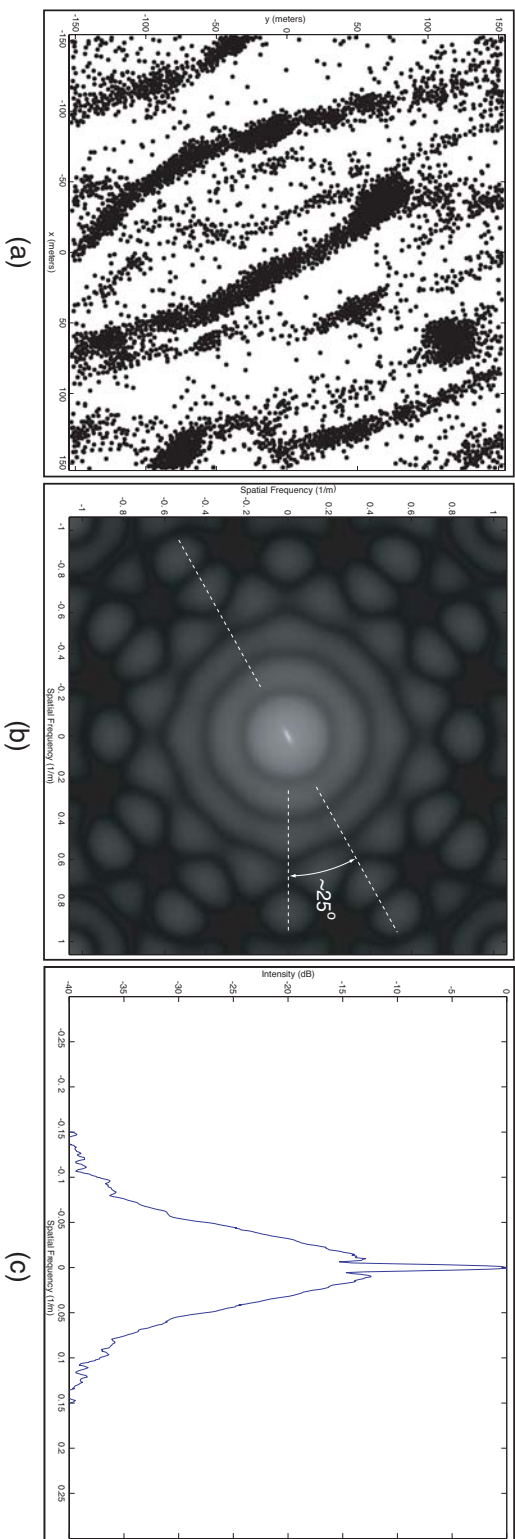


Figure 5.2: Diffraction signature of gravitational wakes. Gravitational wake structures are clearly visible in (a), which shows a 300×300 meter vignette of the rings generated during dynamical simulations. The simulated physical ring properties are typical of Saturn’s Ring A ($\tau = 0.5$; surface mass density $\sigma_\rho = 500 \text{ kg m}^{-2}$; ring density $\rho = 450 \text{ kg m}^{-3}$; particle radius $a = 1.66 \text{ m}$; see Appendix A. In (a), the y -axis is aligned with the local Keplerian motion of a ring particle. We computed the diffraction pattern U of 90 independent amplitude screens (of which (a) is one); the intensity-averaged ($I = UU^*$) diffraction pattern of those screens is shown in (b). The signature of individual particles is preserved in the large-scale diffraction pattern (*i.e.*, the Airy disk is visible in (b); see also Figure 3.9)), while the diffraction signature of the wakes is visible as a small, bright smear at the center of the plot. The diffracted field intensity along a line—oriented at $\approx 25^\circ$ as shown in (b)—through wake signature shown in Figure 4.3. The two small peaks on either side of the central peak in the diffraction pattern indicate the wakes’ mean structural period, while the cant angle of $\approx 25^\circ$ is the average wake cant angle with respect to the azimuthal unit vector $\hat{\phi}$ in the rings (*i.e.*, with respect to \hat{y} in this figure). The particle distributions were provided by Heikki Salo, University of Oulu.

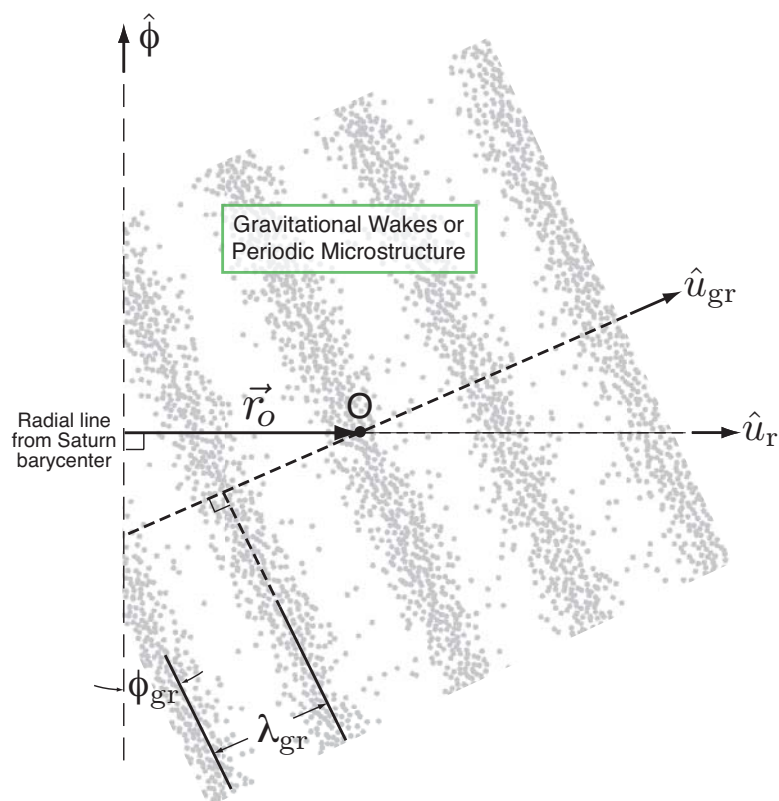


Figure 5.3: Statistically generated amplitude screen model of gravitational wakes or periodic microstructure, showing placement in the ring plane. The vector \vec{r}_o defines the position of the ring piercing point O relative to Saturn's barycenter; \hat{u}_r is the unit vector pointing from Saturn's barycenter to the RPP. The orientation of the structure in the ring plane is specified by \hat{u}_{gr} (alternatively by ϕ_{gr}). The mean structural period λ_{gr} is shown; its standard deviation σ_{gr} (not labeled) controls the width of the normally-distributed particle clusters that form the wakes and/or PM.

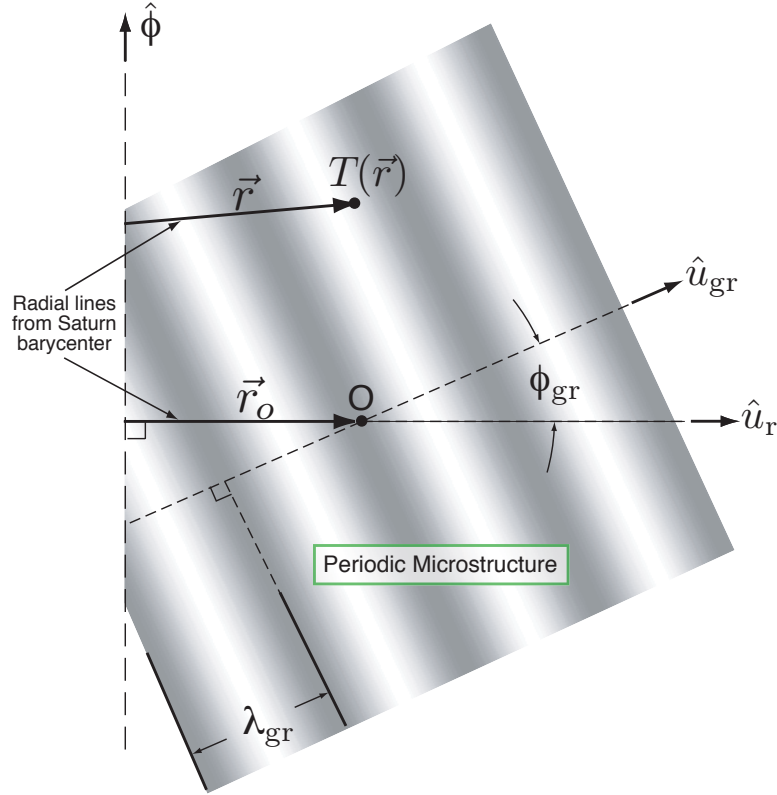


Figure 5.4: Deterministic sinusoidal transmittance amplitude screen model of periodic microstructure, showing placement in the ring plane. The screen transmittance $T(\vec{r})$ is defined in eq. 5.1, where \vec{r} is a position vector originating at Saturn's barycenter, as is \vec{r}_o which defines the RPP. The angle between \vec{r} and \vec{r}_o is exaggerated here, for clarity. All other labels and geometry are as in Figure 5.3 (note that σ_{gr} is not defined in this model).

spacing, and the orientation or cant angle ϕ_{gr} of the wakes in the ring plane, relative to the azimuthal unit vector $\hat{\phi}$. This wake model is further constrained by specifying the ring thickness T_r or the packing fraction f_{vol} . We populate a ring slab volume according to the defined statistics, and the number of particles N_p is adjusted iteratively in our model until the output of eq. (3.73) equals the defined optical depth specification.

Periodic Microstructure

With the Cassini radio occultation experiment, we have detected periodic microstructure at five distinct locations in the rings [Thomson *et al.*, 2007]. Colwell *et al.* [2007] and Sremcevic *et al.* [2009] used the Cassini ultraviolet imaging spectrograph (UVIS) to detect PM in regions of Rings A and B, and reported results that are consistent with our observations.

As was the case for gravitational wakes, particle aggregate models of PM are produced either by using the output of dynamical simulations to determine the ring particle locations in the ring plane, or by using the statistically generated parameterized model shown in Figure 5.3. For PM investigations, the particle aggregate model is useful for investigating the impact of the orientation angle ϕ_{gr} and ring thickness T_r on the observed optical depth. However, if our goal is simply to identify the geometry required to produce the first-order diffraction lobes that are the hallmark of PM (*e.g.*, Figure 4.5(a)–(b)), then we only need a model that is specified by λ_{gr} and ϕ_{gr} .

For this, we define an amplitude screen with transmittance $T(\vec{r})$, containing a deterministic sinusoidal amplitude component. The model is completely specified by four parameters, which are: i) the average transmittance \bar{T} of the screen, ii) the sinusoidal amplitude ΔT of the variation in screen transmittance, iii) the structural period λ_{gr} , and iv) the orientation vector \hat{u}_{gr} (or alternatively, ϕ_{gr}), which we define relative to an axisymmetric orientation. With this,

$$T(\vec{r}) = \bar{T} + \Delta T \cos\left(\frac{2\pi(\vec{r} \cdot \hat{u}_{\text{gr}})}{\lambda_{\text{gr}}}\right) \quad (5.1)$$

where \vec{r} is the radius vector from Saturn's center to points within the amplitude screen; see Fig. 5.4 for the screen geometry. The parameter \bar{T} is determined by the observed normal optical depth τ ,

$$\bar{T} = \exp\left(\frac{-\tau}{2\mu_o}\right) \quad (5.2)$$

where $\mu_o = \sin B$, and B is the ring opening angle (see Figure 5.8; *cf.* Fig. 15 of Tyler [1987]). The parameter ΔT is determined from the observations according to,

$$\Delta T = 2\bar{T} \cdot (\Delta I)^{-1/2} \quad (5.3)$$

where ΔI is the ratio of the observed intensity of the zeroth-order (the coherent signal) and first-order diffraction lobe in the received signal spectra, accounting for the gain of the illuminating antenna. The fine-scale variation in normal optical depth, τ_{fs} , within a specific PM feature is related to these parameters,

$$\tau_{\text{fs,max}} = -2\mu_o \ln(\bar{T} - \Delta T) \quad (5.4)$$

$$\tau_{\text{fs,min}} = -2\mu_o \ln(\bar{T} + \Delta T) \quad (5.5)$$

We also use the deterministic sinusoidal screen transmittance model (Figure 5.4) to represent gravitational wakes.

5.2.2 Microstructure Modeling using Analytic Methods

In Section 5.2.1, we discussed the use of either a statistical particle aggregate model or a deterministic sinusoidal screen transmittance model to construct amplitude screens (see Chapter 3) that represent one or more of the four types of microstructure introduced in Section 2.3 and discussed again in Section 5.1.

We now describe two analytic microstructure models that yield expressions of the model diffraction pattern U or intensity $I = UU^*$. For the case of periodic microstructure, we give an equation that describes the location of the first-order diffraction lobes in the ring plane. The key advantage to the analytic approach is that it eliminates the need to generate amplitude screens and compute their diffraction patterns.

Homogeneous MPT Model

An expression for the far-field diffraction pattern associated with the homogeneous, many particles thick microstructure model was given in Section 3.5 [Marouf *et al.*, 1983],

$$I(\tau_q, \theta) = 2\pi \int_0^\infty \rho J_0(2\pi\rho\theta) e^{-\tau_q} \left(e^{\tilde{w}\tilde{\Phi}(\rho)\tau_q} - 1 \right) d\rho \quad (3.63)$$

with

$$\Phi(\theta) = I_o(x) \left(\frac{2J_1(x \sin \theta)}{x \sin \theta} \right)^2 \quad (3.70)$$

$$I_o(x) = \frac{x^2}{2} \left[1 - \frac{J_1(2x)}{x} \right]^{-1} \quad (3.71)$$

Here, we assume that the far field intensity is symmetric, so $I(\theta) = I(u, v)$ where $\theta = \beta = \sqrt{\beta_x^2 + \beta_y^2}$ and eq. (5.10) describes the mapping between (u, v) and (β_x, β_y) . We discussed the relationship between I and U in Chapter 3 (see eq. (3.54)).

Diffraction Grating Model

The sinusoidal transmittance amplitude screen model described in Section 5.2.1 is behaviorally similar to a diffraction grating. Using the same model description, defined by eqs. (5.1)–(5.5), we introduce a diffraction grating model that is solved analytically rather than by computing the diffraction pattern of an amplitude screen.

For a given λ_{gr} and ϕ_{gr} , the theoretical diffraction pattern of an illuminated diffraction grating contains three distinct spectral peaks corresponding to the zeroth-order signal and the two first-order diffraction lobes, as shown in Figure 5.5 (see also Figure 5.11). The lobes diffract at an angle θ_d relative to the line-of-sight that is determined by the grating period λ_{gr} and the wavelength λ of the illuminating radio wave,

$$\theta_d = \frac{\lambda}{\lambda_{\text{gr}}} \quad (5.6)$$

Signals diffracted from the rings corresponding to the first-order lobes of a sinusoidal grating appear to originate from locations S_1 and S_2 in the ring plane, defined by the position vectors,

$$\vec{S}_{1,2} = \vec{r}_o \mp \left(\frac{|\vec{r}_{\text{co}}| \sin \theta_d}{\sin(\gamma \mp \theta_d)} \right) \hat{u}_{\text{gr}} \quad (5.7)$$

relative to Saturn's center of mass. Here, \vec{r}_o is the radius vector from Saturn's center

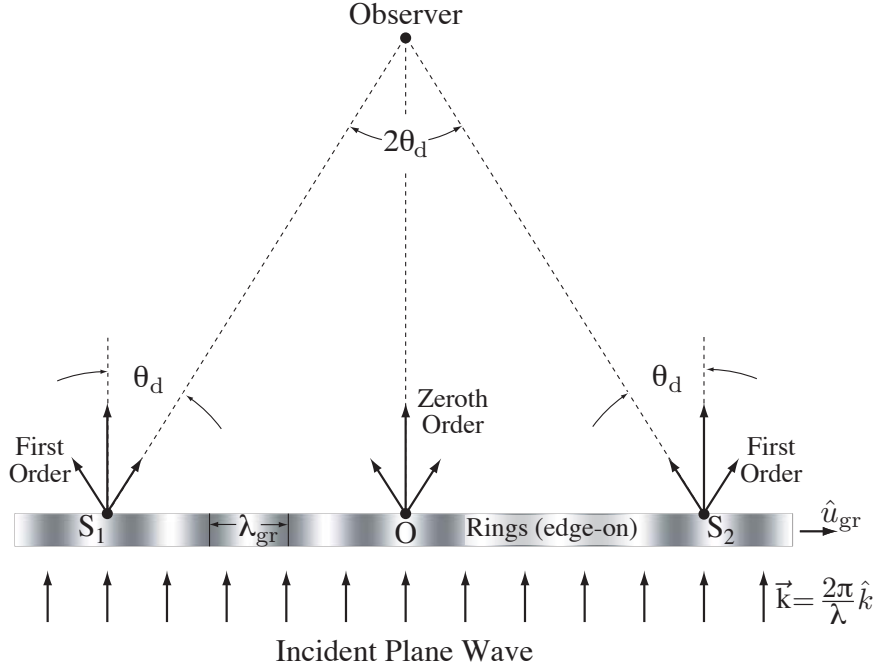


Figure 5.5: Properties of a sinusoidal diffraction grating. First-order lobes are diffracted at an angle θ_d with respect to the incident plane wave vector \vec{k} , in the plane containing both \vec{k} and the grating orientation vector \hat{u}_{gr} . Energy diffracted towards the observer by the first-order lobes originates at S_1 and S_2 , which are along the line of diffraction grating lobes, defined as the intersection of the plane containing \hat{k} and \hat{u}_{gr} , and the ring plane (see also Figure 5.6). The line of diffraction grating lobes is also the line oriented along \hat{u}_{gr} that includes point O. This description is also valid for signals originating at the observer and arriving at the distant source of the illuminating plane wave in this figure, by reciprocity. Compare with Figures 5.6 and 5.12.

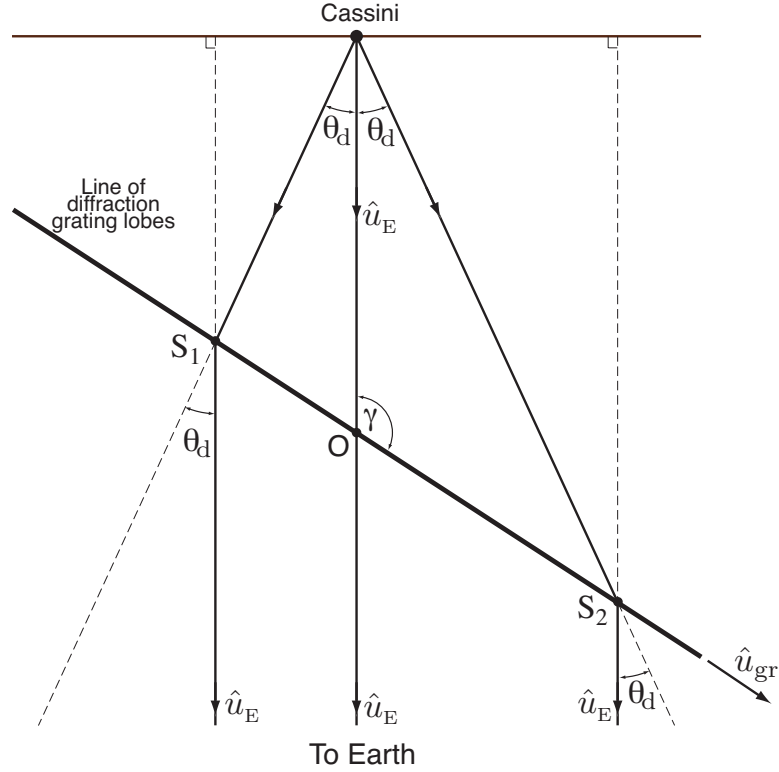


Figure 5.6: Diffraction grating and Cassini observation geometry. The view shown is drawn in the plane that contains \hat{u}_{gr} and \hat{u}_E (note that $\hat{u}_E = \hat{k}$); the line of diffraction grating lobes is in the plane of the page. The ring plane, containing a sinusoidal diffraction grating parameterized by λ_{gr} and \hat{u}_{gr} , protrudes from the page at an unspecified angle. Angle γ is between $-\hat{u}_E$ and \hat{u}_{gr} . Point O defines the RPP; S_1 and S_2 are points in the ring plane where Cassini signals diffracted through an angle θ_d are redirected towards Earth along \hat{u}_E . Compare with Figures 5.5, and 5.12.

to the ring intercept point O , \vec{r}_{co} is the vector from the Cassini spacecraft to point O ($\vec{r}_{\text{co}} = \vec{r}_o - \vec{R}_c$; see Figure 4.1 or 5.12), and $\gamma = \cos^{-1}(-\hat{u}_{\text{E}} \cdot \hat{u}_{\text{gr}})$; see Figure 5.6.

5.3 Comparing Model Behavior with Radio Occultation Measurements

We match power spectral features derived from the diffraction pattern of presumed ring microstructure models with key features in the power spectrum of signals received from Cassini, which contain the diffraction signature of the true ring microstructure. Our approach comprises two main techniques: a general technique, and a faster, simpler technique that is specific to periodic microstructure. We used the second technique to produce the estimates of the physical dimensions of PM in the rings that we present in Chapter 6.

With either the general or PM-specific approach, we adopt the implicit assumption that the nature of the microstructure is statistically stationary over multiple Cassini observations. In our case, the stationary assumption spans the May–August 2005 timeframe of the observations we use in our analysis.

The methods we describe in this chapter require accurate estimates of the position and velocity of Cassini, Saturn, and the Earth in order to reconstruct the observational geometry and to calculate associated quantities—such as \vec{r}_o and f_{D} —required in the analysis. To this end, we use the *SPICE* information system, which is provided to the scientific community and maintained by the NASA/JPL Navigation and Ancillary Information Facility (NAIF). *SPICE* includes a large suite of software (mostly in the form of subroutines) to assist scientists in planning and interpreting scientific observations from space-based instruments. The Cassini project office releases files called *SPICE* kernels on a regular basis, which contain the best estimate of Cassini’s actual trajectory during a fixed range of dates. NAIF also releases kernel files for all major solar system objects (planets, moons, etc.). We incorporated *SPICE* subroutines in our code in order to read *SPICE* kernel files and compute highly-resolved estimates of the Cassini radio occultation geometry.

5.3.1 General Approach

In this section, we outline a general approach that applies to all models that use ring particle aggregates to represent ring microstructure. We describe an iterative fitting procedure for estimating ring microstructure at a single location \vec{r}_o in the rings. The iterative process is repeated for multiple \vec{r}_o to resolve microstructure features that span a range of ring radii.

To be clear, a full development and application of the general approach is beyond the scope of this dissertation. However, the general approach provides an excellent pedagogical framework with which to present the basic concepts and procedures that are essential to the techniques we use to fit models of periodic microstructure to the Cassini data. Our PM model fitting techniques derive from the general method but are specialized for PM analysis and therefore limited by comparison, as we describe in Section 5.3.2. A complete development of the general approach is an important future step in the analysis of Cassini radio occultation data to investigate the nature of ring microstructure.

Generating the Diffraction Screens: Particle Aggregate Models

We begin with a region of the rings containing microstructure that we wish to investigate, and we choose a particle aggregate model from those introduced in Section 5.2.1 to fit to the measured Cassini radio occultation data. For each unique set of model parameters (*i.e.*, unique values of parameters τ , λ_{gr} , σ_{gr} , ϕ_{gr} , T_r , etc.), we generate N amplitude screens, each of which are unique instantiations or vignettes corresponding to a single statistical description of the rings.

Each vignette is generated as shown in Figure 3.1—by projecting the shadows of particles into a plane perpendicular to the unit wave vector $\hat{k} = \hat{u}_E$. Particle positions in our model use the coordinate system introduced in Figures 4.1 and 4.2, where \hat{z} is Saturn’s pole vector, \hat{x} is the unit vector projection of \hat{u}_E in the ring plane, and $\hat{y} = \hat{z} \times \hat{x}$. The position (x, y) of particles is preserved in the creation of the amplitude screen—thus $\Delta x = \frac{\Delta y}{\sin B}$ for amplitude screens constructed using an equal number of pixels in x and y . Figure 5.7 depicts the projection process as it pertains explicitly

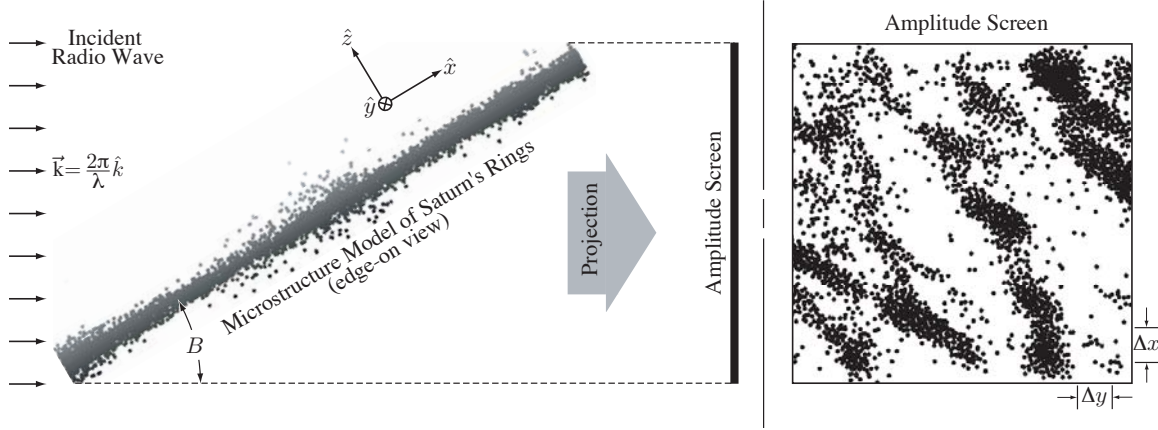


Figure 5.7: Constructing amplitude screens from models of ring microstructure. The general procedure for screen construction is explained in Chapter 3. Significant ring particle overlap is evident along the x -dimension in the amplitude screen, due to the acute ring opening angle. If the two dimensions of the amplitude screen comprise the same number of pixels, then $\Delta x = \frac{\Delta y}{\sin B}$, where B is the ring opening angle defined in Section 1.2.

to the rings.

There is often a tradeoff to be made between resolving the diffraction signature of individual particles and that of the structures formed by those particles, as discussed in Section 3.2.4. Figure 5.2(b) illustrates the problem: when the microstructure has characteristic dimensions that are many particles in extent, the spectral diffraction signature of the microstructure exists on a proportionally smaller scale than the particles. This is due to the inverse relationship that exists between dimensions in the spatial domain and the spatial frequency domain.

For microstructure vignettes that are hundreds of particles long in x and/or y , it is impractical to resolve the diffraction pattern of both the particles and the structure since the small values of Δx and Δy required quickly lead to very long numerical transforms. Depending on the nature of the microstructure, it may be necessary to increase Δx and Δy in order to properly sample the structure, thus decreasing the spatial sampling frequency f_{sx} (f_{sy}) and the frequency-domain resolution Δf_x (Δf_y). In the limit, we can reduce the spatial resolution to one pixel per particle, focussing in on the diffraction signature of microstructure in the process.

We compute the diffraction pattern of the N amplitude screens using the methods described in Chapter 3. We apply a 2D Hamming function to each amplitude screen *a priori* to mitigate the spectral leakage effects associated with the finite length of the FFT. We average the N diffraction patterns incoherently (*cf.*, eq. (3.54)) to obtain,

$$\overline{U}(u, v) = \sqrt{\frac{1}{N} \sum_{i=1}^N U_i(u, v) U_i^*(u, v)} \quad (5.8)$$

thus creating a single diffraction pattern $\overline{U}(u, v)$, that represents the statistical behavior of the particular model type (wakes, PM, etc.) and unique parameter values.

We choose N large enough to reduce the statistical noise in the spatial frequency domain, inherently introduced by amplitude screen models that contain statistically-defined dimensions. A possible criterion for N is to require the maximum difference between the diffraction patterns produced by averaging $(N - 1)$ and N diffraction patterns to be less than a small value ϵ ,

$$\epsilon \geq \left| \frac{1}{N} \sum_{i=1}^N U_i^2(u, v) - \frac{1}{N-1} \sum_{i=1}^{N-1} U_i^2(u, v) \right|_{\max} \quad (5.9)$$

where ϵ is on the order of a few percent, and $U^2 = UU^*$.

We apply a linear paraxial transformation to map the spatial frequency domain $\overline{U}(u, v)$ to the angular frequency domain $\overline{U}(\beta_x, \beta_y)$,

$$\beta_x = \lambda u \quad \beta_y = \lambda v \quad (5.10)$$

where λ is the wavelength of the Cassini signal used in the analysis (either 13 cm, 3.6 cm, or 0.94 cm; see Section 4.1).

Generating the Diffraction Screens: Screen Transmittance Models

The sinusoidal screen transmittance model depicted in Figure 5.4 is defined deterministically, not statistically. In this case we compute $\overline{U}(\beta_x, \beta_y)$ using a single amplitude screen for each unique set of parameter values (*i.e.*, $N = 1$). Otherwise, the procedure

is exactly the same as that described above for particle aggregate models.

Doppler Signal Synthesis

The incoherent or scattered signal spectrum is a superposition of signals forward-scattered or diffracted towards Earth from regions in the rings that are illuminated by the Cassini high-gain antenna. We receive these signals at Earth, and each is Doppler-shifted with respect to the transmitted signal frequency as discussed in Section 4.1.

To test a presumed model of ring microstructure, we must synthesize a received signal spectrum $I_s(f_D)$ that corresponds to the average diffraction pattern $\bar{U}(\beta_x, \beta_y)$ of the specific model, and which is consistent with the observational geometry of the actual experiment. Reconstructing the observational geometry ensures a correct mapping of Doppler frequency f_D to precise locations in the ring plane.

Figures 5.8 and 5.9 show the geometry and general approach of the Doppler synthesis method. A fraction of the Cassini transmitted signal power that propagates along \hat{u}_p to illuminate point P is diffracted through an angle β_p to propagate along \hat{u}_E towards Earth. For P located at a point (x_i, y_j) in the ring plane (the xyz coordinate system is explained in Figure 4.1), the signal intensity scattered from P towards Earth depends on both the diffraction pattern $\bar{U}(\beta_{x_i}, \beta_{y_j})$ of the rings and on the incident power illuminating the rings, which in turn is a function of the gain of the Cassini high-gain antenna (HGA),

$$I_s(\beta_x, \beta_y) = G(\beta_x, \beta_y) \cdot \bar{U}^2(\beta_x, \beta_y) \quad (5.11)$$

$I_s(\beta_x, \beta_y)$ is the normalized intensity of signals scattered to Earth from points in the rings defined by β_x and β_y , and $G(\beta_x, \beta_y) = G(\beta)$ is the pattern gain of the Cassini antenna (*cf.*, eq. (3.70)),

$$G(\beta) = \left[\frac{2J_1(\eta ka \sin \beta)}{\eta ka \sin \beta} \right]^2 \quad (5.12)$$

where $\beta = \sqrt{\beta_x^2 + \beta_y^2}$. Here, J_1 is the first-order Bessel function of the first kind, a is the radius of the Cassini high-gain antenna ($a = 2$ meters), $k = 2\pi/\lambda$, and η is a factor

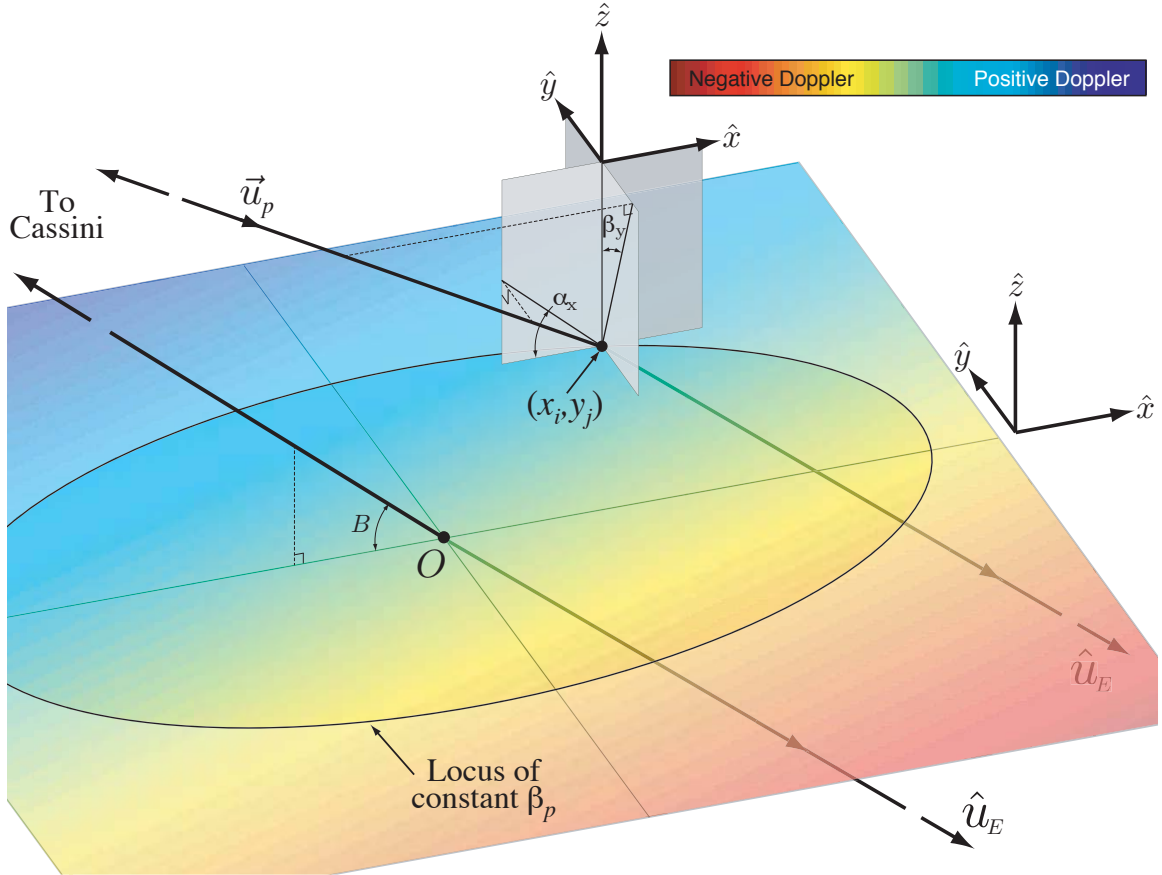


Figure 5.8: Diffraction and Doppler geometry in the ring plane. Radio waves propagating along \hat{u}_p from Cassini intercept the rings at point P , located at (x_i, y_j) in the ring plane. Microstructure present in the rings in the vicinity of P diffracts a portion of the transmitted signal energy towards Earth along \hat{u}_E . The diffraction angle $\beta_p = \cos^{-1}(\hat{u}_p \cdot \hat{u}_E) = \sqrt{\beta_{x_i}^2 + \beta_{y_j}^2}$ is subtended between \hat{u}_p and \hat{u}_E . The angle $\alpha_{x_i} = B + \beta_{x_i}$ is formed by projecting the ray \vec{u}_p linking Cassini and point P at (x_i, y_j) into the $\hat{x}\hat{z}$ plane; similarly, β_{y_j} is formed by projecting \vec{u}_p into the $\hat{y}\hat{z}$ plane, as shown. Angle B is the rings opening angle, and the subscripts i and j have been dropped from α_{x_i} and β_{y_j} in the figure, for brevity. For a given observational geometry, signals scattered towards Earth from point P map to a particular Doppler frequency f_D . Doppler values are represented graphically in the figure by a color spectrum as in Figure 4.2, but are not to scale. The line-of-sight ray linking Cassini and Earth pierces the rings at point O . The reader is referred to Figure 4.1 for a more general view of the geometry shown in detail in this figure.

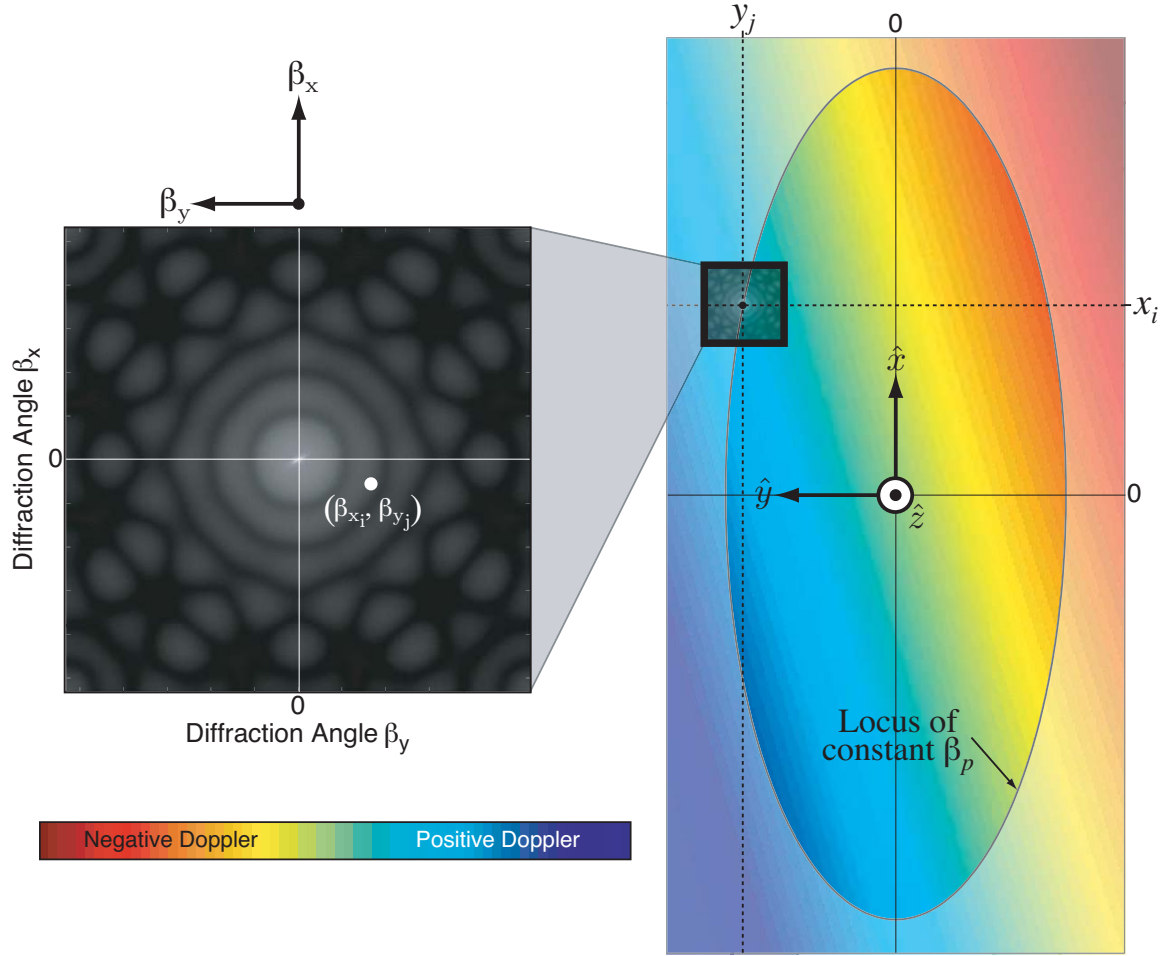


Figure 5.9: Determining the magnitude $\bar{U}(\beta_{x_i}, \beta_{y_j})$ and Doppler frequency f_{D_p} of signals received from point P in the ring plane. Radio waves transmitted by Cassini and illuminating the rings at point P at (x_i, y_j) are diffracted by an angle $\beta_p = \sqrt{\beta_{x_i}^2 + \beta_{y_j}^2}$ towards the Earth, as shown in Figure 5.8. For a given observational geometry, and an assumed model of ring microstructure producing an average diffraction pattern $\bar{U}(\beta_x, \beta_y)$, each ordered pair $(\beta_{x_i}, \beta_{y_j})$ maps to a single point (x_i, y_i) in the ring plane. Signals from P are received at a relative magnitude $I_s(\beta_{x_i}, \beta_{y_j})$, defined in eq. (5.11), and at the Doppler frequency associated with P . Contributions from all points in the rings are used to synthesize a received signal spectrum $I_s(f_D)$ associated with a particular model of ring microstructure.

that accounts for the deliberate de-focussing of the Ka-band signal in the HGA. For Cassini, $\eta = 1$ for X- and S-band transmissions, and $\eta = 0.806$ for Ka-band, yielding

a half-power beamwidth of $\beta_{\text{HP}}|_{\text{Ka}} = 0.0015$ radians.

Since each unique ordered pair $(\beta_{x_i}, \beta_{y_j})$ maps to a single point (x_i, y_j) in the ring plane, and each point in the ring plane has an associated Doppler frequency f_{D} , we can synthesize a received signal spectrum that corresponds to a specific model of ring microstructure and occultation signal wavelength—represented by $I_s(\beta_x, \beta_y)$ —and to a specific observational geometry. For each value of (β_x, β_y) , we compute the corresponding position vector \hat{u}_{p} (see Figure 5.8) by first finding the vectors \vec{x} and \vec{y} that locate the point (x, y) relative to the RPP,

$$\vec{x} = \frac{|\vec{r}_{\text{co}}| \sin(\beta_x)}{\cos B} \hat{x} \quad (5.13)$$

$$\vec{y} = |\vec{r}_{\text{co}}| \tan(\beta_y) \hat{y} \quad (5.14)$$

where \hat{x} and \hat{y} are as shown in Figure 4.1, B is the ring opening angle, and \vec{r}_{co} was introduced in eq. (5.7). The vector from Cassini to (x, y) is given by $\vec{r}_{\text{p}} = \vec{r}_{\text{co}} + \vec{x} + \vec{y}$, and it follows that \hat{u}_{p} is defined as,

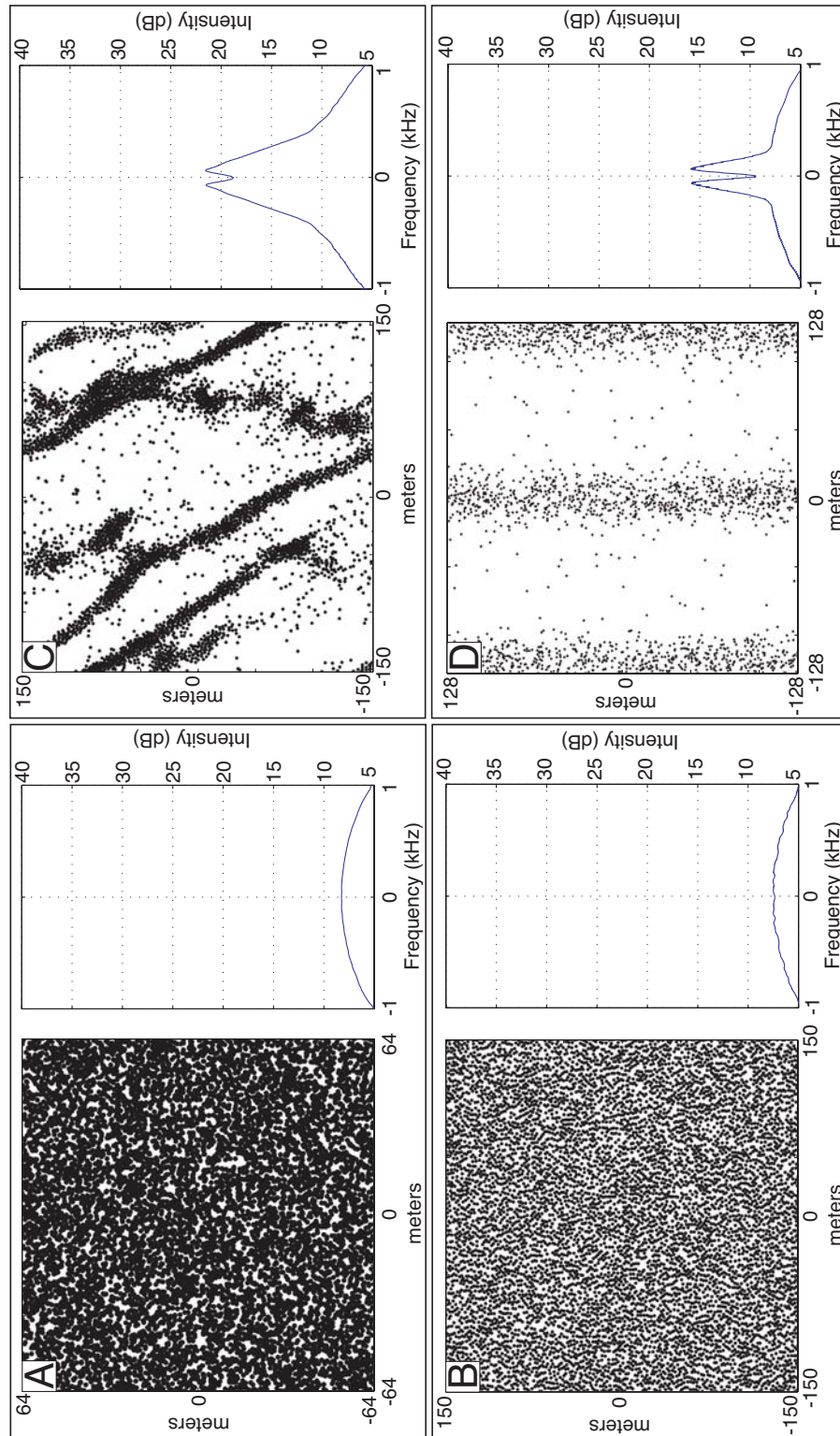
$$\hat{u}_{\text{p}} = |\vec{r}_{\text{p}}|^{-1} \vec{r}_{\text{p}} \quad (5.15)$$

For homogeneous ring models, we compute the Doppler frequency f_{D} associated with each (β_x, β_y) , using the computed value of \hat{u}_{p} in eq. (4.1). For other models of ring microstructure we use modified formulae to compute f_{D} , which we discuss below and define in eqs. (5.17)–(5.17).

We store the numerical values of $I_s(\beta_x, \beta_y)$ and the associated Doppler values f_{D} in corresponding $K \times K$ matrices, and then collapse the matrices into two vectors of length $1 \times K^2$. We sort values contained in the Doppler vector in ascending order, and commensurately re-order the I_s vector. Finally, a histogram algorithm is used to sum the I_s vector in Doppler bins that are sized to match the frequency bin size of the measured Cassini signal, thus producing the synthesized received signal spectrum $I_s(f_{\text{D}})$.

Next page.

Figure 5.10: Synthesis of $I_s(f_D)$ from models of ring microstructure. Panels **A–D** show single instantiations of amplitude screens representing a particular microstructure model, along with the Doppler power spectra $I_s(f_D)$ that we synthesized from the average of $N = 100$ unique diffraction patterns $U(\beta_x, \beta_Y)$. The different microstructure models shown represent a range of simulated optical depths. Shown are **A** a homogeneous MPT ring model ($\tau_q = 3.26$, $N_p = 9870$, $T_r = 43$), **B** a packed monolayer model ($\tau_q = 1.53$, $N_p = 4000$, $T_r = 1$), **C** gravitational wakes ($\tau_q = 0.60$, $N_p = 5330$, $T_r = 17$), and **D** periodic microstructure ($\tau_q = 0.15$, $N_p = 2170$, $T_r = 6$). In all panels, $I_s(f_D)$ is synthesized at X-band, assuming the REV 7 ingress geometry and $|\vec{r}_o| = 123,100$ km from Saturn’s barycenter. The bias of all synthesized Doppler spectra have been chosen to facilitate comparison with the power spectra of microstructure contained in Figures 4.5 and 6.4. The coherent signal component is not included in $I_s(f_D)$. In panel **B**, the near-forward extinction associated with scattering from packed monolayers (shown in Figure 5.1) is spread over roughly ± 2 kHz (see the 3 dB beam pattern in Figure 4.2), and therefore is not distinctly seen in our synthesis. Note the scattering enhancement in the near-forward direction produced by gravitational wakes, panel **C**, as compared with the more superimposed sidelobe nature produced by periodic microstructure, panel **D**. These results are preliminary and are intended for qualitative comparisons and/or illustrative purposes only.



Computing the Doppler Frequency

Eq. (4.1) describes the Doppler frequency expected due to forward-scattering from ring particles. When anisotropic models of ring microstructure (such as gravitational wake or PM models) are considered, significant contributions to the received signal spectrum are attributed to diffraction from the periodic or pseudo-periodic clusters of particles contained in those models. For non-homogeneous models, it is not the motion of the constituent particles that predominantly determines the Doppler frequency or frequencies associated with distinctive spectral features—it is the apparent motion of the entire structure in the ring plane. For example, an azimuthally symmetric structure (*i.e.*, $\hat{u}_{\text{gr}} = \hat{u}_r$; see Figures 5.3 and 5.4) may comprise many particles moving at Keplerian velocities, but the structure itself appears stationary. Regular microstructure appears to move at a velocity \vec{v}_{gr} in the ring plane [Thomson *et al.*, 2007],

$$\vec{v}_{\text{gr}} = (\vec{v}_{\text{p}} \cdot \hat{u}_{\text{gr}}) \hat{u}_{\text{gr}} \quad (5.16)$$

Diffracted radio waves from the structure are Doppler-shifted accordingly,

$$f_{\text{D}_{\text{gr}}} = \frac{1}{\lambda} (\vec{v}_{\text{s}} - \vec{v}_{\text{gr}}) \cdot (\hat{u}_{\text{p}} - \hat{u}_{\text{E}}) \quad (5.17)$$

We use eq. (5.17) in place of eq. (4.1) to synthesize $I_s(f_{\text{D}})$ for models of periodic microstructure and gravitational wakes. From this point forward we refer to $f_{\text{D}_{\text{gr}}}$ using f_{D} and an equation reference, for brevity.

Figure 5.10 shows a set of results generated by applying the frequency synthesis techniques using several models of ring microstructure. In the figure, we chose the scale and bias of the panels containing synthesized frequency responses $I_s(f_{\text{D}})$ to facilitate a qualitative comparison with the measured power spectra shown in Figures 4.5 and 6.4. The observational geometry used in the synthesis corresponds to the REV 7 Cassini occultation experiment, at a point during the ingress observation when the Cassini-Earth line-of-sight pierced the rings at $|\vec{r}_{\text{o}}| = 123.1 \times 10^3$ km. These results are preliminary and are intended for qualitative comparisons and/or illustrative purposes only. See the figure caption for more details.

5.3.2 Periodic Microstructure

For the case of periodic microstructure, the sharp first-order diffraction lobes characteristic of PM (see the simulation results shown in Figure 5.11) allow us to greatly simplify the modeling procedure. In this case, synthesis of $I_s(f_D)$ is not required—rather, we need only find the two Doppler frequencies, f_{D1} and f_{D2} , corresponding to the peaks of the first-order diffraction lobes.

Sinusoidal Transmittance Model

We use the first-order diffraction lobe peaks β_1 and β_2 evident in the angular frequency domain of the sinusoidal transmittance model to compute the diffraction lobe peaks f_{D1} and f_{D2} in the Doppler frequency domain. Figure 5.11 shows an example of a diffraction pattern $U(\beta_x, \beta_y)$ generated from a sinusoidal transmittance model of periodic microstructure, as detailed in Section 5.2.1. We use a peak-finder algorithm to uniquely determine the two first-order diffraction lobe peaks in $U(\beta_x, \beta_y)$, which we show located at (β_{x1}, β_{y1}) and (β_{x2}, β_{y2}) in the figure. We find the associated Doppler frequencies f_{D1} and f_{D2} directly using the approach described in eqs. (5.13)–(5.15) above; eq. (5.17) is used to compute the specific Doppler frequencies.

Analytic Diffraction Grating Model

The procedure for finding f_{D1} and f_{D2} is even simpler for the (analytic) diffraction grating model, which is depicted in Figure 5.12. In this case, there is no need to generate any amplitude screens. For a specific observational geometry, we compute \vec{S}_1 and \vec{S}_2 using eq. (5.7). Then $\vec{r}_{pi} = \vec{r}_{co} + \vec{S}_i$, and we compute \hat{u}_{p1} and \hat{u}_{p2} using eq. (5.15). Substituting into eq. (5.17) yields f_{D1} and f_{D2} , respectively.

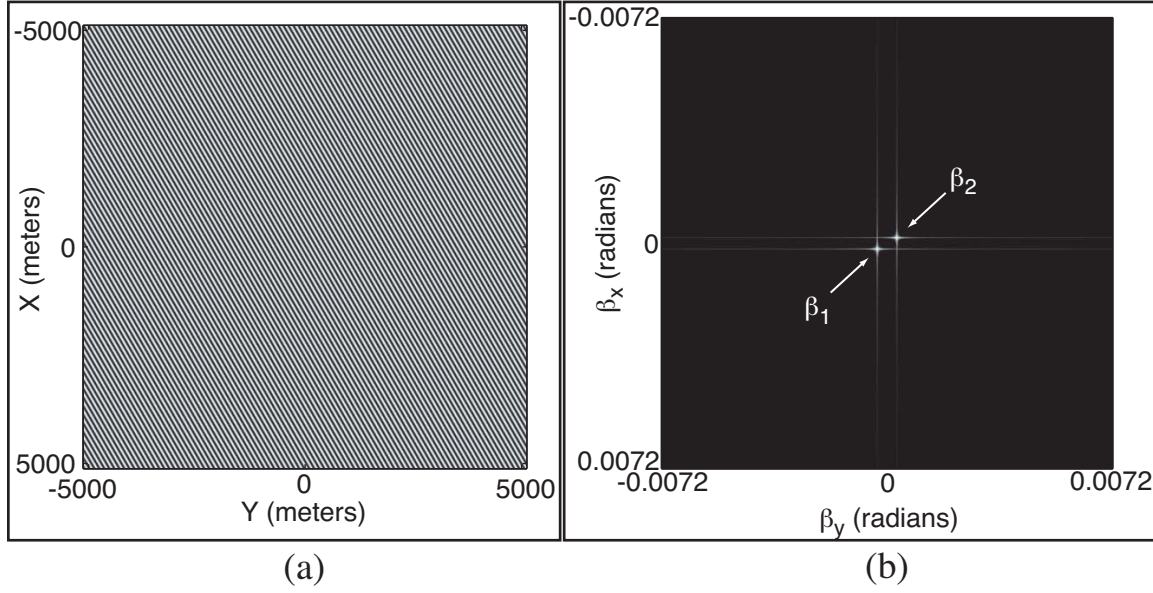


Figure 5.11: An example of (a) the sinusoidal transmittance model of periodic microstructure, $\lambda_{\text{gr}} = 100$ m, and (b) its associated diffraction pattern $U(\beta_x, \beta_y)$. Values of β are computed for an X-band signal, $\lambda = 3.6$ cm. Note the spacing $\Delta\beta = |\vec{\beta}_1 - \vec{\beta}_2| = 2s_o$, where $s_o = \lambda_{\text{gr}}^{-1}$.

5.4 Least-Squares Fitting of Model Parameters to the Data

We use an iterative least-squares fitting approach to determine the optimal set of model parameters that fit the synthesized frequency spectrum to the frequency spectrum of the Cassini data. For periodic microstructure models, we only fit at two locations in the spectrum. Specifically, we fit the measured first-order diffraction lobe frequencies, designated f_{m1} and f_{m2} , to the sidelobe frequencies in the synthesized spectrum, f_{D1} and f_{D2} . In this case, it is not necessary to synthesize $I_s(f_D)$. For the PM model case, we now describe the process of fitting model parameters to the experimental data.

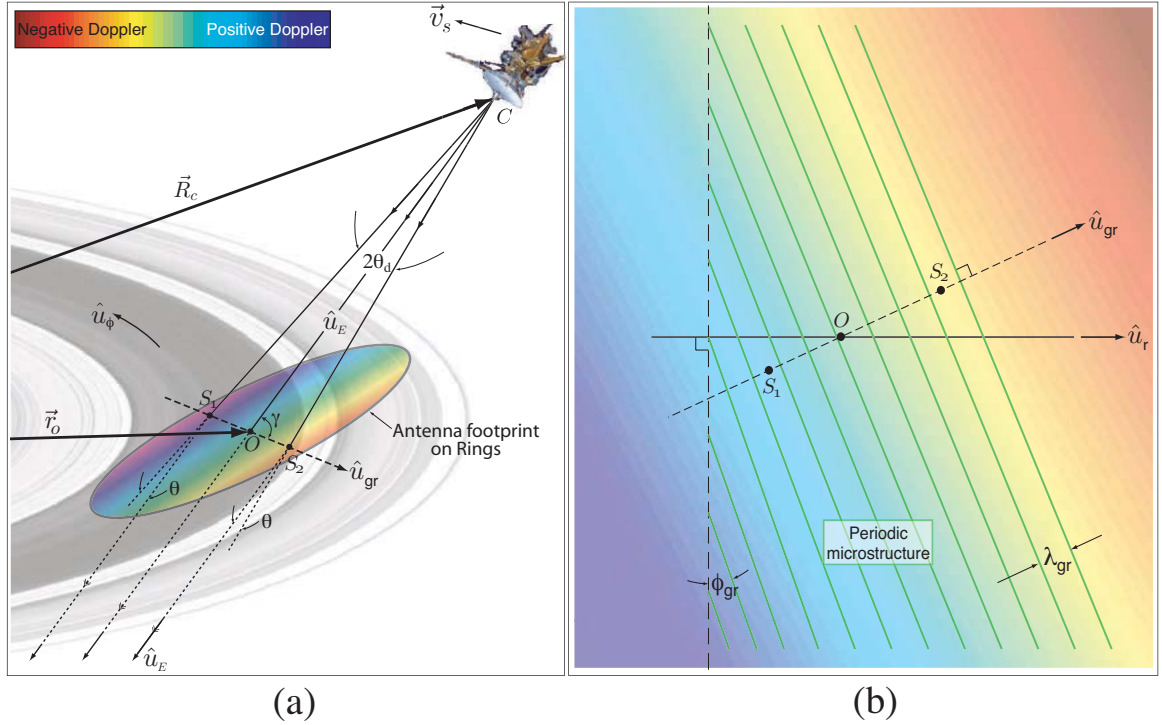


Figure 5.12: Diffraction grating model of periodic microstructure in the rings. (a) Line-of-sight ray linking Cassini and Earth is directed along \hat{u}_E and pierces the ring plane at point O ; \hat{u}_{gr} is in the plane of the rings, and defines the orientation of the periodic structure. Points S_1 and S_2 correspond to locations in the ring plane where first-order diffraction grating lobes of the structure originate and propagate along \hat{u}_E to the Earth-based receiver. The grating lobes are directed at angle $\pm\theta_d$ relative to \hat{u}_E . All angles shown are in the plane defined by \hat{u}_E and \hat{u}_{gr} . Color within the antenna footprint represents variations in the Doppler shift of signals scattered to Earth by the rings; the antenna footprint size is exaggerated for clarity. (b) The grating is represented by parallel green lines in this schematic top view of the rings. Signals diffracted to Earth from S_1 and S_2 are Doppler-shifted by f_{D1} and f_{D2} relative to the signal along the line-of-sight, represented by the colors at S_1 and S_2 . $\hat{u}_r = |\vec{r}_o|^{-1}\vec{r}_o$ is the radial unit vector pointing from the center of Saturn to O .

5.4.1 Fitting Models of Periodic Microstructure

Figure 5.13 shows the spectrum of the Ka-band Cassini received signal recorded during the REV 7 ingress occultation observation, May 3, 2005. The spectrum shown is an average over a 25-km range along the occultation track, centered on a point $r_o =$

123,249 km from Saturn's center.

For each radial location $|\vec{r}_o|$ in the rings for which we wish to fit a model of periodic microstructure, we must first determine the actual first-order diffraction lobe frequencies, f_{m1} and f_{m2} , from the measured Cassini radio occultation data. Using a four-parameter Gaussian model,

$$F(f; \bar{P}_i) = C_i \exp\left(-\frac{(f - f_{mi})^2}{2\sigma_i^2}\right) + F_{oi} \quad (5.18)$$

we adjust the amplitude C_i , standard deviation σ_i , bias F_{oi} , and first-order diffraction lobe frequencies f_{mi} , where $i = 1, 2$, to fit the measured data as shown in Figure 5.13. The vector $\bar{P}_i = [C_i \ f_{mi} \ \sigma_i \ F_{oi}]$ defines the model's independent fitting parameters. The Gaussian model (eq. (5.18)) is fit to the Cassini spectral data using a least-squares optimization routine that employs a Levenberg-Marquardt algorithm to minimize the sum-of-squares error $\Gamma(\bar{P})$ according to,

$$\Gamma(\bar{P}) = \sum_{k=1}^K [I(f_k) - F(f_k; \bar{P})]^2 \quad (5.19)$$

where $I(f_k)$ is the intensity of the received signal spectrum at frequency f_k , and $F(f_k; \bar{P})$ is the parameterized function that minimizes $\Gamma(\bar{P})$; in this case, given by eq. (5.18). Here, we limit the range of frequencies, f_1 to f_K , such that $F(f_k; \bar{P})$ is optimized to fit either the upper or lower diffraction lobe—never both at once. This is depicted in Figure 5.13 by a distinct break in the red line representing the Gaussian model fit to each diffraction lobe.

The Levenberg-Marquardt algorithm interpolates between the Method of Gradient Descent, and the Gauss-Newton algorithm. The Levenberg-Marquardt algorithm is more robust than the Gauss-Newton algorithm, capable in many cases of finding a solution even when the starting guess \bar{P}_o is very far from the final minimum.

We apply this fitting process to all of the Cassini datasets included on our analysis, and at each radial location in the rings under investigation. For each Cassini dataset, the fitting process yields six frequency estimates— $f_{\sigma 1-}$, f_{m1} , $f_{\sigma 1+}$, $f_{\sigma 2-}$, f_{m2} , and $f_{\sigma 2+}$ —that fit the received signal spectrum at a single radial location in the rings. The

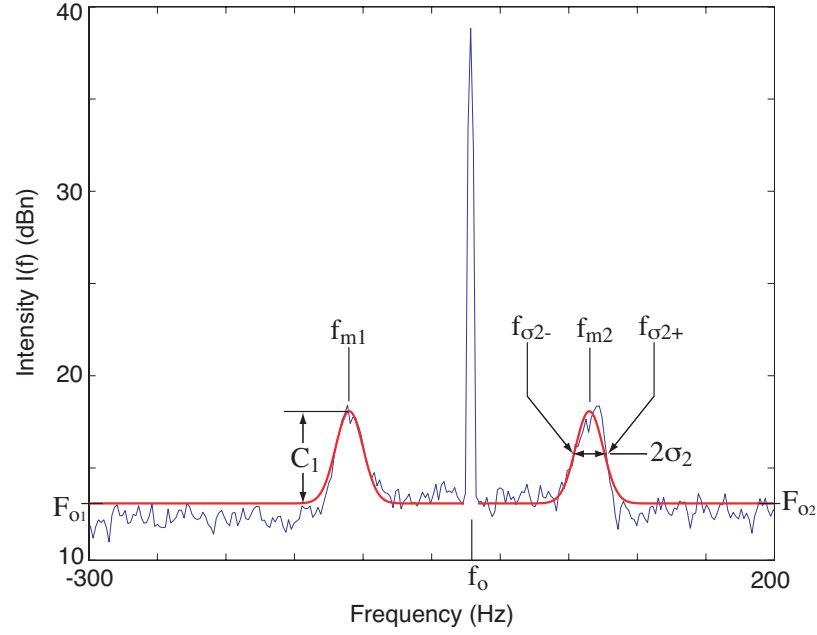


Figure 5.13: Estimating the first-order diffraction lobes of periodic microstructure using a Gaussian model. The measured data (shown in blue) was recorded during the ingress portion of the Cassini REV 7 radio occultation experiment. The plot shows the Ka-band ($\lambda = 0.94$ cm) received signal, averaged over approximately 25 km of radial extent along the occultation track centered at $|\vec{r}_o| = 123,249$ km from Saturn's barycenter. Key parameters of the Gaussian fitting function, defined in eq. (5.18), are shown. $f_{\sigma i-}$ and $f_{\sigma i+}$ denote the frequency at one standard deviation on either side of the peak f_{mi} .

Gaussian peaks f_{m1} and f_{m2} are our estimates of the mean Doppler frequency of the first-order diffraction lobes in the Cassini data. We use the estimates $f_{\sigma i+} = f_{mi} + \sigma_i$ and $f_{\sigma i-} = f_{mi} - \sigma_i$ to estimate a frequency spread that characterizes deviation from the assumed monochromatic model; specifically, we define upper and lower bounds on the diffraction lobe Doppler frequencies as $(f_{\sigma 1-}, f_{\sigma 2+})$ and $(f_{\sigma 1+}, f_{\sigma 2-})$, respectively. We use the frequency spread to estimate the corresponding spread in the diffraction grating model parameters.

The diffraction grating model comprises two parameters, λ_{gr} and ϕ_{gr} , as described in Section 5.2.2. To fit λ_{gr} and ϕ_{gr} to the data we apply the Levenberg-Marquardt least-squares algorithm a second time—this time, we fit the diffraction grating model to the measured data,

$$\Gamma(\vec{r}_o, \vec{P}) = \sum_{i=1}^{i_{\max}} \sum_{j=1}^M \left[f_{mi_j}(\vec{r}_o) - f_{Di_j}(\vec{r}_o, \vec{S}_{i_j}; \vec{P}) \right]^2 \quad (5.20)$$

where $i_{\max} = 2$. The output of the Levenberg-Marquardt algorithm that minimizes eq. (5.20) is a least-squares estimate of the model parameters $\vec{P} = [\lambda_{\text{gr}} \ \phi_{\text{gr}}]$ that best fits all of the Cassini data used in the analysis, at a single radial location $|\vec{r}_o|$ in the rings. The function f_{Di_j} is given by eq. (5.17), which we use to compute f_{D1_j} and f_{D2_j} for each of the M Cassini data sets, where the j^{th} observation geometry is completely specified by \vec{r}_o and \vec{S}_i (eqs. (5.6) and (5.7)) for each Cassini observation. Nominally, the algorithm fits f_{Di_j} to the diffraction lobe frequency estimates f_{mi_j} produced using eq.(5.19), as described above. We compute all pertinent geometric quantities—such as the position and velocity of Cassini, Saturn, the rings, and Earth at the time of each observation—using trajectory and other ancillary SPICE files provided by the Cassini Navigation Team at JPL, as described at the beginning of Section 5.3.

We repeat the fitting process using our $\pm\sigma$ estimates, using $f_{\sigma i+}$ and $f_{\sigma i-}$ in place of f_{mi} in eq. (5.20) to place upper and lower bounds (respectively) on estimates of λ_{gr} and ϕ_{gr} at a particular radial location.

For analysis, we have a total of 24 data sets available; *i.e.*, 3 transmitted signals (13, 3.6, and 0.94 cm- λ) recorded on ingress and egress observations during four Cassini orbits (REVs 7, 8, 10, and 12). We use a subset of these data sets in our

estimates of PM features in the rings for reasons discussed in Chapter 6.

5.4.2 Other Models

The procedure described for fitting models of periodic microstructure to Cassini signals applies to other microstructure models as well, although generally the less distinct spectral features (relative to the sharp features present in the PM signal spectrum) attributable to other microstructure tends to complicate the fitting process. In the worst case, one may choose to fit every point in the synthetic spectrum $I_s(f_D)$ to corresponding points in the Cassini received signal. Difficulties arise here, since this approach requires the absolute signal level of I_s to be physically consistent with the measured Cassini received signal spectrum; a challenging task indeed. This approach can easily lead to large i_{\max} (which is the number of points in the synthetic spectrum), and thus large number of data points in the least-squares algorithm eq. (5.20).

A more reasonable approach is to select key features in the received signal spectrum that are easily distinguished, and thus only require estimating the frequency f_D at which they occur. Here, i_{\max} is the number of spectral features used in the fitting process. The fitting algorithm for this problem is similar to that of eq. (5.20), with appropriate modifications to the function f_{Di_j} . This approach greatly simplifies the fitting process by eliminating the need to accurately synthesize the signal bias contained in $I_s(f_D)$.

A detailed discussion of techniques for fitting models other than periodic microstructure is beyond the scope of this dissertation.

5.5 Summary

In this chapter, we have explained the framework of a general method for fitting models of ring microstructure to signals received from Cassini during radio occultations of the rings. We have developed the method in more detail for the specific case of fitting periodic microstructure models to the Cassini data. For the case of PM, the method

does not require synthesis of a received signal spectrum $I_s(f_D)$ —we need only estimate the Doppler frequencies f_{D1} , f_{D2} of the first-order diffraction lobes produced by the periodic structure, and evident in the Cassini received signal spectrum at specific locations in the rings.

In the next chapter, we present experimental evidence for the presence of periodic microstructure in the rings, detected during our preliminary analysis of Cassini radio occultation data. We presented a subset of this evidence previously in Section 4.2. We apply our PM analysis to the data, and present estimates of the structural period and orientation of the PM in all regions of the rings where it is detected. These results are also reported in *Thomson et al.* [2007].

h

Chapter 6

Estimates of Periodic Microstructure in Saturn's Rings

Radio occultation of Saturn's rings by the Cassini spacecraft on May 3, 2005, revealed several remarkable phenomena in Rings A and B. In limited regions of the rings, the observations indicate the presence of periodic microstructure. The uncovering of these structures [Thomson *et al.*, 2006a, 2007] is based on our observation of diffraction effects in 0.94- and 3.6-cm wavelength (λ) coherent sinusoidal signals transmitted from Cassini through the rings, and received at the ground stations of the Deep Space Network (DSN).

As we have discussed in previous chapters, the periodic variations in the optical depth of the rings where PM is present diffract the incident electromagnetic wave in a manner similar to that produced by a giant diffraction grating. The sharpness of the spectral features in the observed diffraction signature permits inference of the structural period, λ_{gr} , with resolution of few tens of meters. The observed first-order diffraction lobes that we detect are typically 5–10 dB stronger than the spectral power of the background broadband scattered signal. The absence of detectable higher-order diffraction lobes in the computed spectra indicates that the optical depth variation of the structure is close to sinusoidal within the 5–10 dB detection limit.

In this chapter, we apply the analysis methods explained in Chapter 5 to the PM signals we detected in our Cassini radio data, and present our estimates of the

physical dimensions of the PM in regions of the rings in which we detect it.

6.1 A Survey of Periodic Microstructure in Saturn's Rings

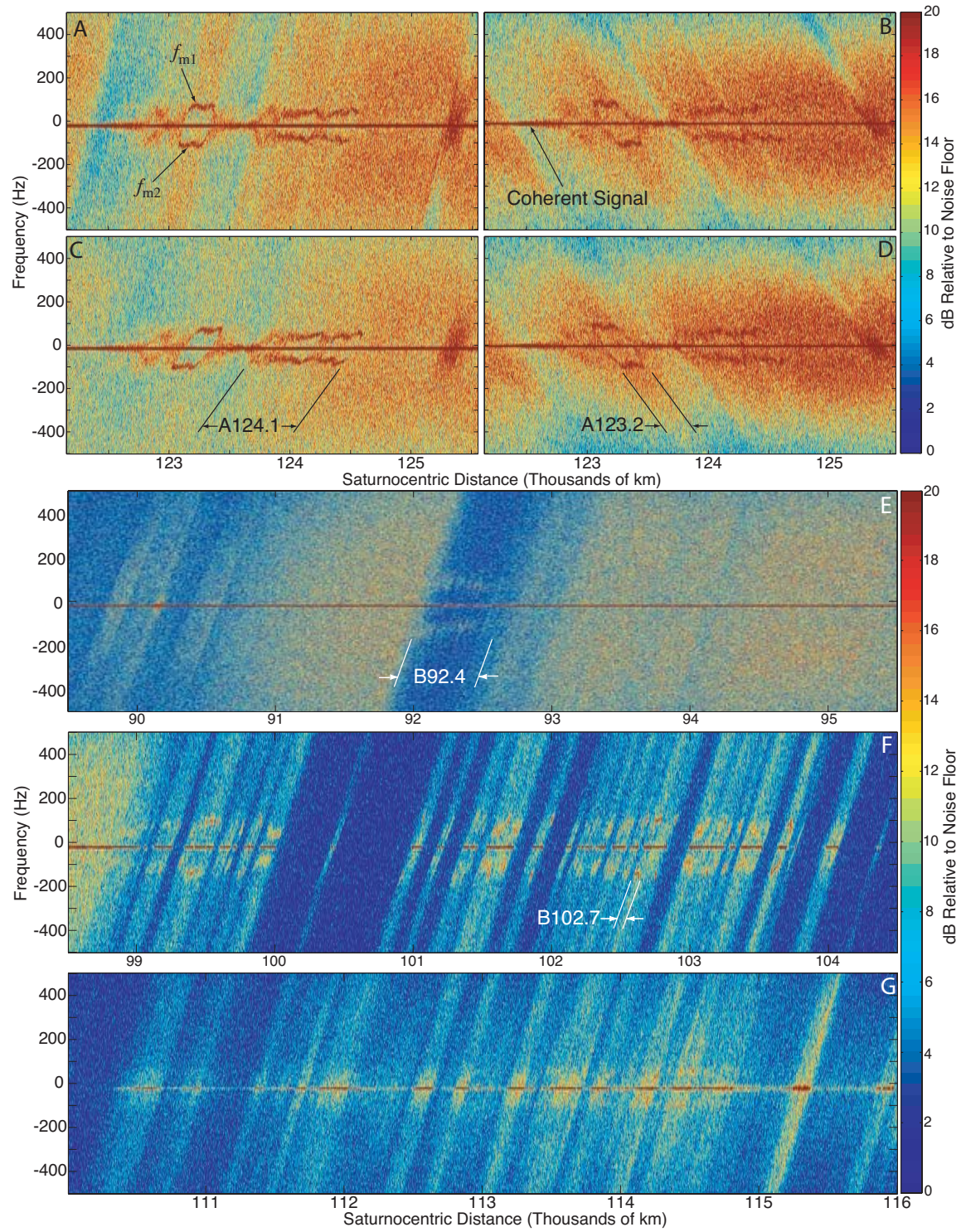
We identify PM features at two locations in the inner part of Ring A, within radial bands of $123.05\text{--}123.4 \times 10^3$ km and $123.6\text{--}124.6 \times 10^3$ km (350 and 1000 km wide, respectively). We designate these two features A123.2 and A124.1, respectively. In Ring B, PM is detected within two broad regions, previously designated B2 and B4 [Marouf *et al.*, 2006b], spanning $99.0\text{--}104.5 \times 10^3$ km and $110.0\text{--}117.5 \times 10^3$ km, respectively. The intervening region, B3, spanning $104.5\text{--}110.0 \times 10^3$ km, is an optically thick region that almost completely extinguishes the radio signals except for some narrow regions. PM is also evident close to the inner edge of region B1 ($92.0\text{--}99.0 \times 10^3$ km), within the radial band $92.1\text{--}92.6 \times 10^3$ km (500 km wide), a feature we designate B92.4. The PM features were observed during eight optimized radio occultation passes between May 3, 2005 and August 2, 2005, and appear relatively unchanged during that observational period as shown in Figure 6.2. The most obvious features are A123.2 and A124.1, which are evident in all three Cassini transmit bands as shown in Figure 6.3. No PM features are evident in other regions of Ring A, or in Rings C or the Cassini Division.

Panels **A** to **D** in Figure 6.1 depict four spectrograms of the signal observed over the inner region of Ring A. The presence of the periodic structure is evidenced by dark red lines in the spectrograms, running roughly parallel to the coherent signal at ≈ 0 Hz, but offset from it on either side by roughly 70–100 Hz. They were observed on both the ingress and egress sides and on different orbits (see caption of Fig. 6.1). We interpret these spectrally localized features as the signature of the first-order grating lobes generated by diffraction from periodic ring structure. Similarly, panels **E** to **G** depict three spectrograms of the signals received from feature B92.4 near inner B1 and its neighborhood, and from within regions B2 and B4. The grating lobe signature is less distinct than in Ring A because of the larger background optical depth, but

nevertheless is clear in several locations where the optical depth is sufficiently low to allow signal detection.

Next page.

Figure 6.1: Spectrograms of 3.6 cm- λ signal observed during May 3, 2005 ring occultation ingress (panels **A**, **E**, **F** and **G**) and egress (panel **B**), and on August 2, 2005 occultation ingress (panel **C**) and egress (panel **D**). The coherent signal is the horizontal red line near the center of each panel. The diffraction signature of periodic microstructure appears as roughly parallel horizontal lines displaced ± 70 –100 Hz from the coherent signal in Ring A (**A**–**D**) and ± 50 –120 Hz Ring B (**E**–**G**). The signature is clearly evident for the two indicated features in inner Ring A, over the roughly 500 km inner part of region B1 (**E**) and over most of the detectable subregions of the ≈ 5000 km-wide region B2 (**F**). It is more muted over most of region B4 (**G**). Other evident broadband features correspond to energy forward scattered by the background structure in the rings.



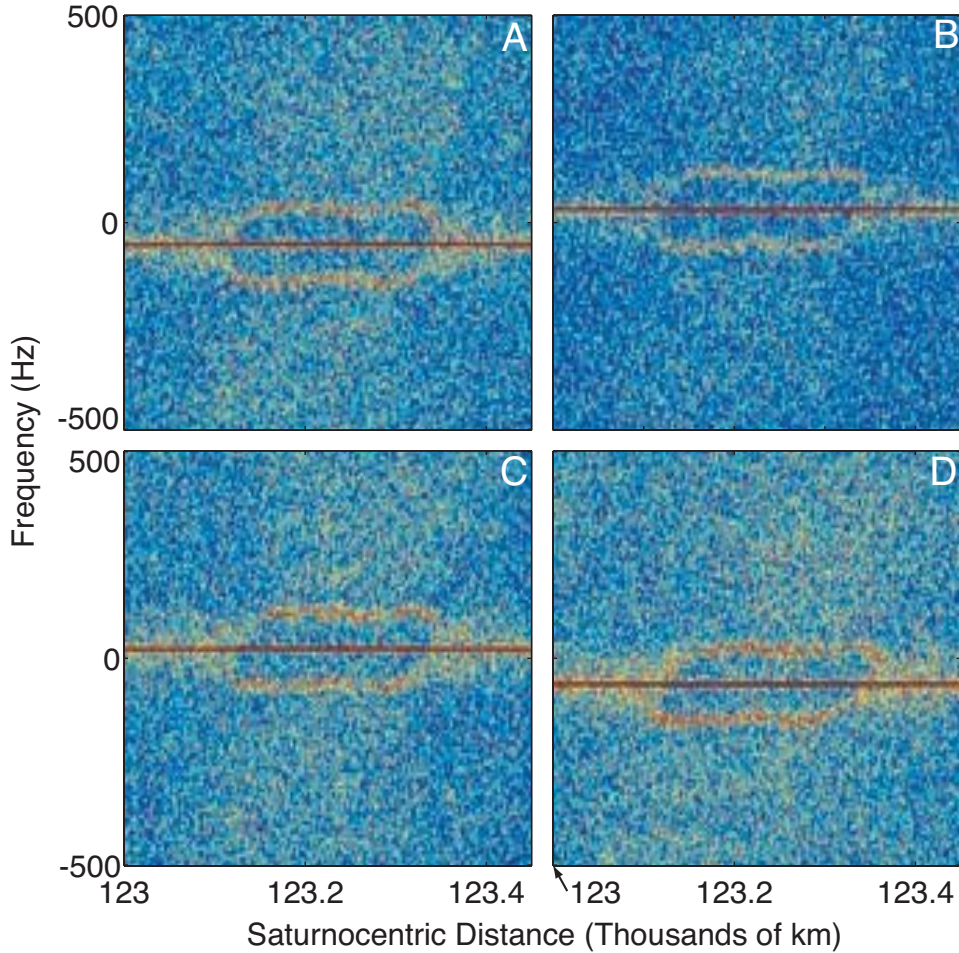


Figure 6.2: Evidence of periodic microstructure feature A123.2 in spectrograms of Cassini radio occultation data. Panels **A–D** contain spectrograms of the Ka-band ($\lambda = 0.94$ cm) ingress data taken during the REV 7, 8, 10, and 12 observations, respectively, spanning a three month time period between May 3–August 2, 2005. During this time period, the PM feature appears unchanged. The coherent signal is evident in the data as a solid red line through the features. The coherent signal frequency is slightly different in each panel due to small errors in the sky frequency predictions used to heterodyne the RF signal, as discussed in Section 4.1.

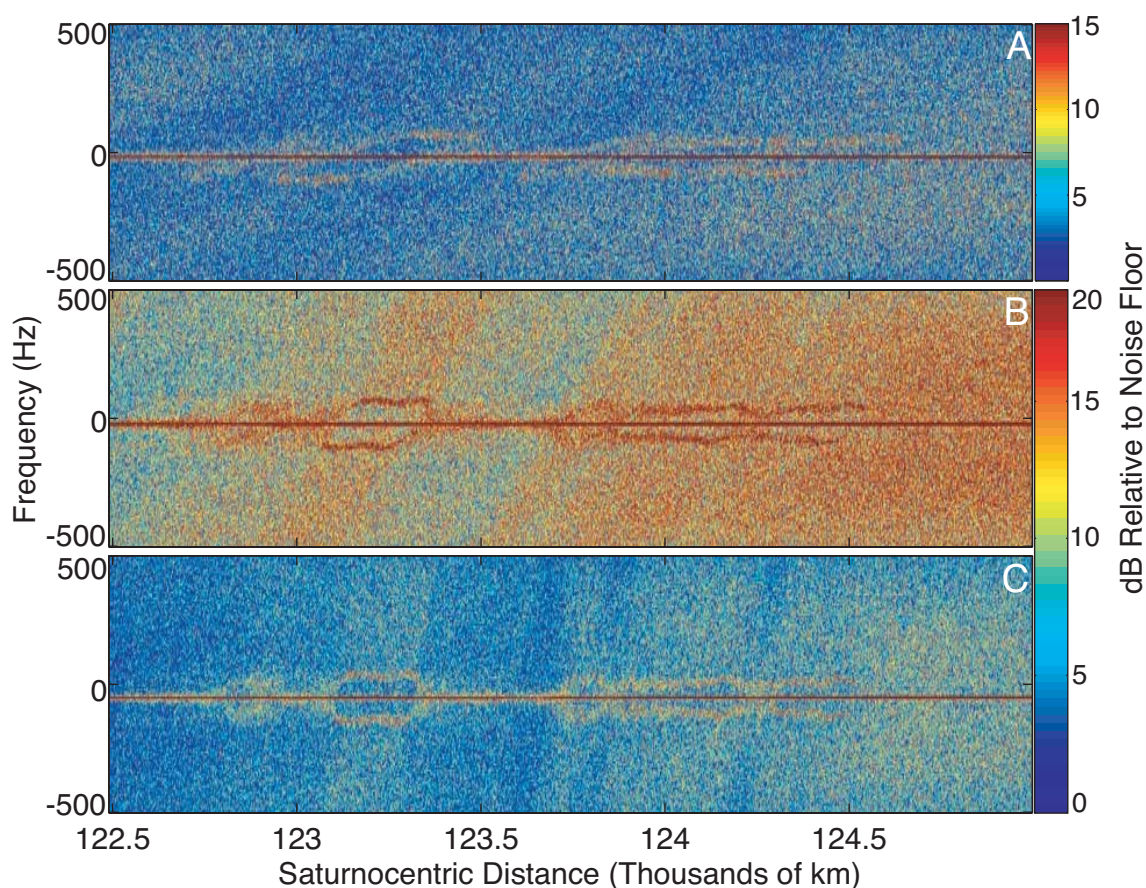


Figure 6.3: PM features A123.2 and 124.1 are seen in spectrograms of Cassini S-, X-, and Ka-band ($\lambda = 13$, 3.6, and 0.94 cm, respectively) radio occultation data, shown in panels **A–C**, respectively. The slanting of the feature in the frequency domain is a function of the wavelength of the observation, as described in Section 4.1.2. The higher SNR of the X- and Ka-band signals is evident in the brightness of the features and the color scaling, relative to the S-band data.

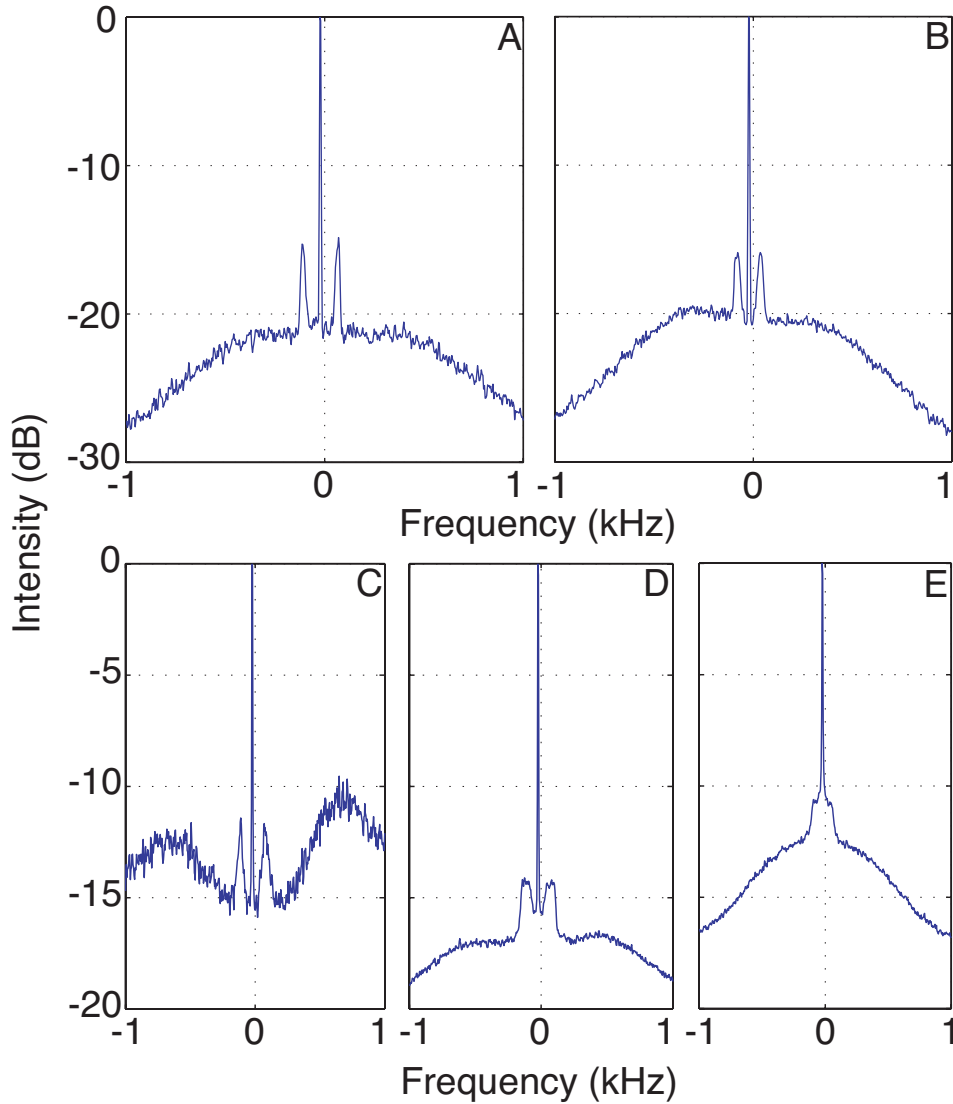


Figure 6.4: Power spectra of periodic microstructure features in Saturn's rings. Panels **A–E** are produced using 3.6 cm- λ (X-band) radio occultation data recorded during the Cassini REV 7 ingress observation of the rings. Panel **A** shows the received signal spectrum of feature A123.2., averaged over the radial range $123.1\text{--}123.35 \times 10^3$ km. Similarly, panels **B–E** show the spectra of features A124.1 and B92.4, and regions B2 and B4, respectively. The radial range of the signal averaging in panels **B–E** is $123.9\text{--}124.5 \times 10^3$ km, $92.28\text{--}92.5 \times 10^3$ km, $99\text{--}104 \times 10^3$ km, and $110\text{--}116 \times 10^3$ km, respectively. In each panel, the signal intensity is plotted in decibels relative to the average coherent signal intensity over the extent of each particular feature. All distances are given with respect to Saturn's geometric center. Compare with Figures 4.5, 5.10, 6.1–6.3; see the text for a more detailed discussion.

6.2 Estimates of Physical Parameters λ_{gr} and ϕ_{gr}

The results we present in this chapter derive from our analysis of REV 7, 8, 10, and 12 ingress and egress observations, which occurred between May 3 and August 2, 2005. These observations were optimized for the experiment, as described in Chapter 4.

For features A123.2 and A124.1 (Fig. 6.1), we estimate λ_{gr} , ϕ_{gr} in approximately 25-km radial steps across the features. Within each step, a series of spectral slices of the received signal are non-coherently averaged to reduce noise and sharpen the diffraction lobes, facilitating cleaner Gaussian fits. The procedure is applied to both the 0.94 cm- and the 3.6 cm- λ measurements from each of the eight ring observations.

We apply the diffraction grating modeling approach described in Chapter 5 to obtain estimates of the PM features identified in Section 6.1. We present our estimates of λ_{gr} and ϕ_{gr} for ring features A123.2, A124.1, and B2 in Figure 6.5. The figure is presented in four parts, (a)–(d), and each part contains four panels, **A–D**. Part (a) and (b) contain estimates of λ_{gr} and ϕ_{gr} , respectively, computed using the diffraction grating model explained in Section 5.2.2. Parts (c) and (d) depict estimates of λ_{gr} and ϕ_{gr} that we compute using the sinusoidal transmittance screen model described in Section 5.2.1. In all parts (a)–(d), panels **A** and **B** correspond to features A123.2 and A124.1, respectively, and panels **C** and **D** correspond to two sub-regions of B2, which we discuss in more detail below. Each panel of Figure 6.5 contains parameter estimates we obtained by processing the Ka-band data, shown in blue; blue dots represent point estimates of either λ_{gr} or ϕ_{gr} ; a blue shaded region represents the uncertainty bounds on the estimate, computed from $f_{\sigma 1-}$, $f_{\sigma 1+}$, $f_{\sigma 2-}$, and $f_{\sigma 2+}$ as explained in Section 5.4. Similarly, red dots and shaded regions correspond to the estimates we produced using X-band data. Purple regions mark the overlap of blue and red regions. The mean values $\bar{\lambda}_{gr}$ and $\bar{\phi}_{gr}$ are shown as dashed lines in the figure.

Estimates of λ_{gr} for features A123.2 and A124.1 are presented in Figure 6.5(a) panels **A** and **B**, respectively. Across the ‘flattest’ part of feature A123.2, λ_{gr} varies between 140–160 meters. Near the edge of A123.2, the structural period λ_{gr} sharply increases; this does not appear to be a general characteristic of PM feature boundaries, *cf.* panels **B–D** of Figure 6.5. Averaging the λ_{gr} estimates across all of A123.2 yields

an average structural period $\bar{\lambda}_{\text{gr}} = 163^{+6}_{-6}$ meters, where the bound on the average is the standard deviation of the fluctuations in the estimates across the feature. For feature A124.1, λ_{gr} varies between 180–250 meters with an average $\bar{\lambda}_{\text{gr}} = 217^{+8}_{-8}$ meters. Possible systemic deviation from the mean estimate is evident in Figure 6.5(a), panel **B**.

Colored regions in Fig. 6.5 characterize the deviations from the local estimates λ_{gr} and ϕ_{gr} due to Doppler spreading of the observed spectral features around the mean frequency. As evident, the deviations for A124.1 are larger than for A123.2. Spectral spreading of the first-order diffraction lobe frequencies seen in A124.1, combined with a general increase in the background scattered signal level in A124.1 as compared with A123.2, leads to estimates of f_{mi} with larger standard deviation. For A123.2, the 0.94 cm- λ estimates were better constrained than the 3.6 cm- λ estimates, primarily because of the weaker background scattered signal at 0.94 cm- λ .

In presenting the estimates of λ_{gr} and ϕ_{gr} for region B2, we have removed the large optical depth feature between $100.0\text{--}101.1 \times 10^3$ km (see Figure 6.1, panel **F**), thus splitting B2 into two sub-regions as shown in Figure 6.5, panels **C** and **D**. In general, estimates of λ_{gr} within B2 vary between 100–200 meters, with $\bar{\lambda}_{\text{gr}} = 146^{+14}_{-14}$ meters. Spectral averages for B2 were computed over approximately 100 km-wide bands to mitigate noise. The spread in the B2 estimates is better-constrained than the Ring A results for two reasons. First, we are averaging over 100-km as opposed to 25-km. Second, because the background scattered signal is much weaker in B2 than in Ring A, the grating lobes peaks appear more distinct, enhancing the ability to estimate f_{mi} .

For the relatively optically thick ($\tau > 2$) feature B92.4 and region B4, the measured grating lobes appear less spectrally confined compared with region B2 and Ring A features. Because of SNR limitations, we only use 3.6 cm- λ data in our estimates. For B92.4, we estimate f_{mi} from one spectral average over most of its radial extent of a 500-km band between $92.1\text{--}92.6 \times 10^3$ km. The feature-wide average $\bar{\lambda}_{\text{gr}}$ is approximately 115^{+20}_{-15} meters. For B4, we spectrally averaged a 5000-km swath from $110.0\text{--}115.0 \times 10^3$ km, yielding $\bar{\lambda}_{\text{gr}} \approx 250^{+150}_{-75}$ meters.

Results for all regions studied show that the data is best fit with diffraction grating

Table 6.1: Summary of PM Features in the Rings

Feature	Radial Location (km)	Grating Model		Sine Screen Model	
		$\bar{\lambda}_{\text{gr}}$ (m)	$\bar{\phi}_{\text{gr}}$ (deg.)	$\bar{\lambda}_{\text{gr}}$ (m)	$\bar{\phi}_{\text{gr}}$ (deg.)
A123.2	$123.05\text{--}123.4 \times 10^3$ km	163	-0.30	157	-0.06
A124.1	$123.6\text{--}124.6 \times 10^3$ km	217	-2.7	202	-2.8
B92.4	$92.1\text{--}92.6 \times 10^3$ km	115	-0.43	118	-2.0
B2	$99.0\text{--}104.5 \times 10^3$ km	146	-0.48	138	1.5
B4	$110.0\text{--}117.5 \times 10^3$ km	250	-1.6	240	-1.9

models that are approximately axisymmetric. The corresponding ϕ_{gr} estimates are presented in Figure 6.5(b). For features A123.2 and A124.1, ϕ_{gr} varies in the range $-3^\circ \leq \phi_{\text{gr}} \leq 3^\circ$ across the most prominent part of the features (see also *Thomson et al.* [2006a]). Estimates of ϕ_{gr} across feature B2 are somewhat chaotic, most likely due to the large and rapid changes in optical depth evident throughout this region; see Figure 6.7(c). The average estimates $\bar{\phi}_{\text{gr}}$ for features A123.2, A124.1, and B2 are -0.30° , -2.7° , and -0.48° , respectively. Feature-wide estimates of ϕ_{gr} for B92.4 and B4 are $-0.43^{+0.25}_{-0.44}$ degrees and $-1.6^{+0.88}_{-1.8}$ degrees, respectively.

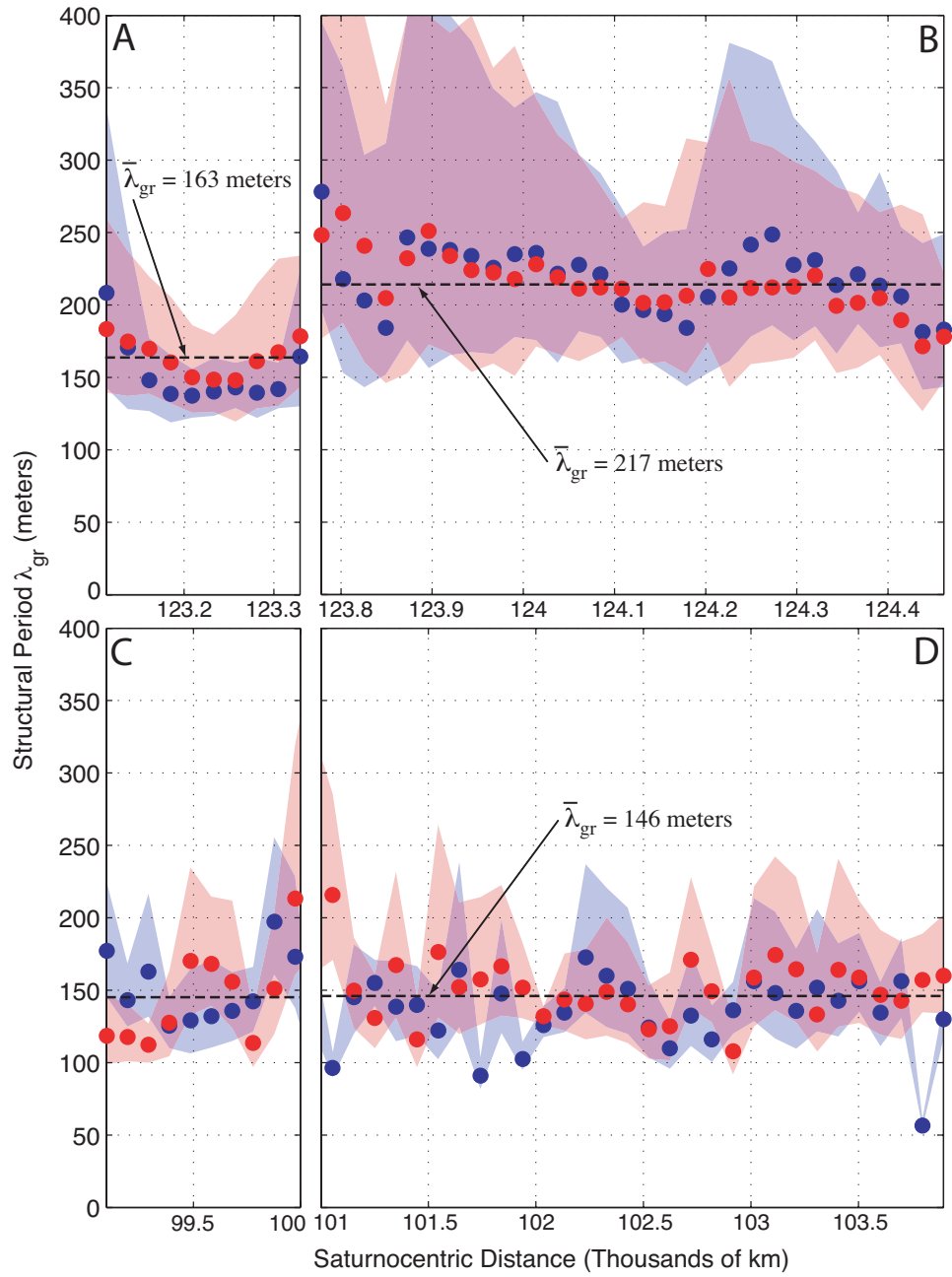
As a comparison, we also applied the sinusoidal transmittance screen model described in Section 5.2.1 to obtain estimates of PM features in the rings, obtaining very similar results as compared with the diffraction grating model, as expected. Those results are presented in Figure 6.5(c)–(d). Estimates of $\bar{\lambda}_{\text{gr}}$ and $\bar{\phi}_{\text{gr}}$ using both methods are summarized in Table 6.1.

Our observations of fine-scale, axisymmetric structures in the rings are consistent with those reported by other Cassini instrument science teams for a subset of the structures reported here. Images of the rings presented in Fig. 5A and 5F of *Porco et al.* [2005] show fine-scale irregular structure, though the pixel resolution of these images is not sufficient to capture the true nature of the structure. Fig. 5A captures the middle of B92.4, while Fig. 5F shows a region very close to A123.2. *Colwell et al.* [2007] report evidence for 160-m structure in the vicinity of 114.15×10^3 km, within the outer part of region B4. This is comparable to our estimate for this region, though a direct comparison is difficult to make since we report only an average over a broad,

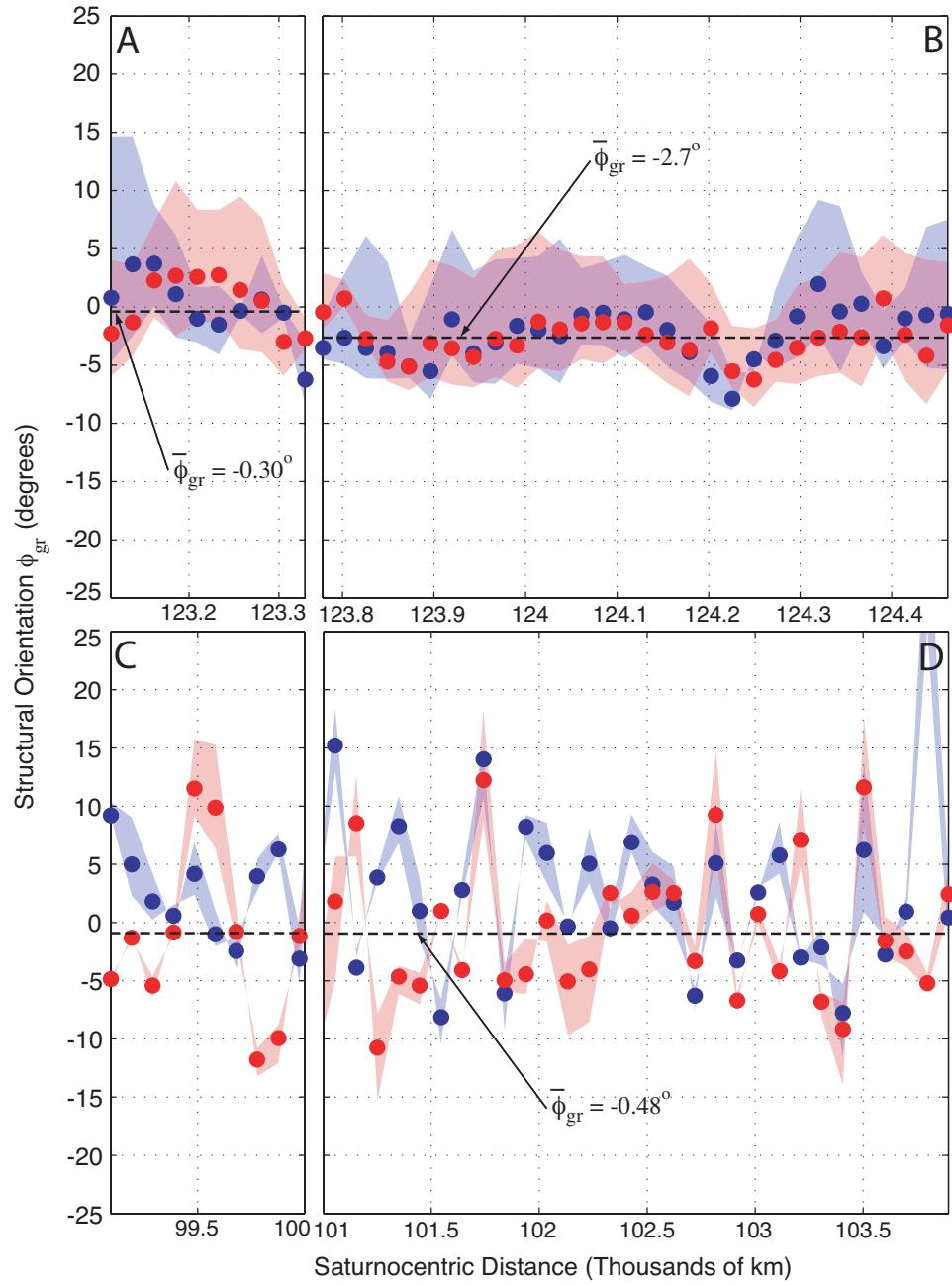
5000 km swath between $r_o = 110 \times 10^3$ km and $r_o = 115 \times 10^3$ km.

Next four pages.

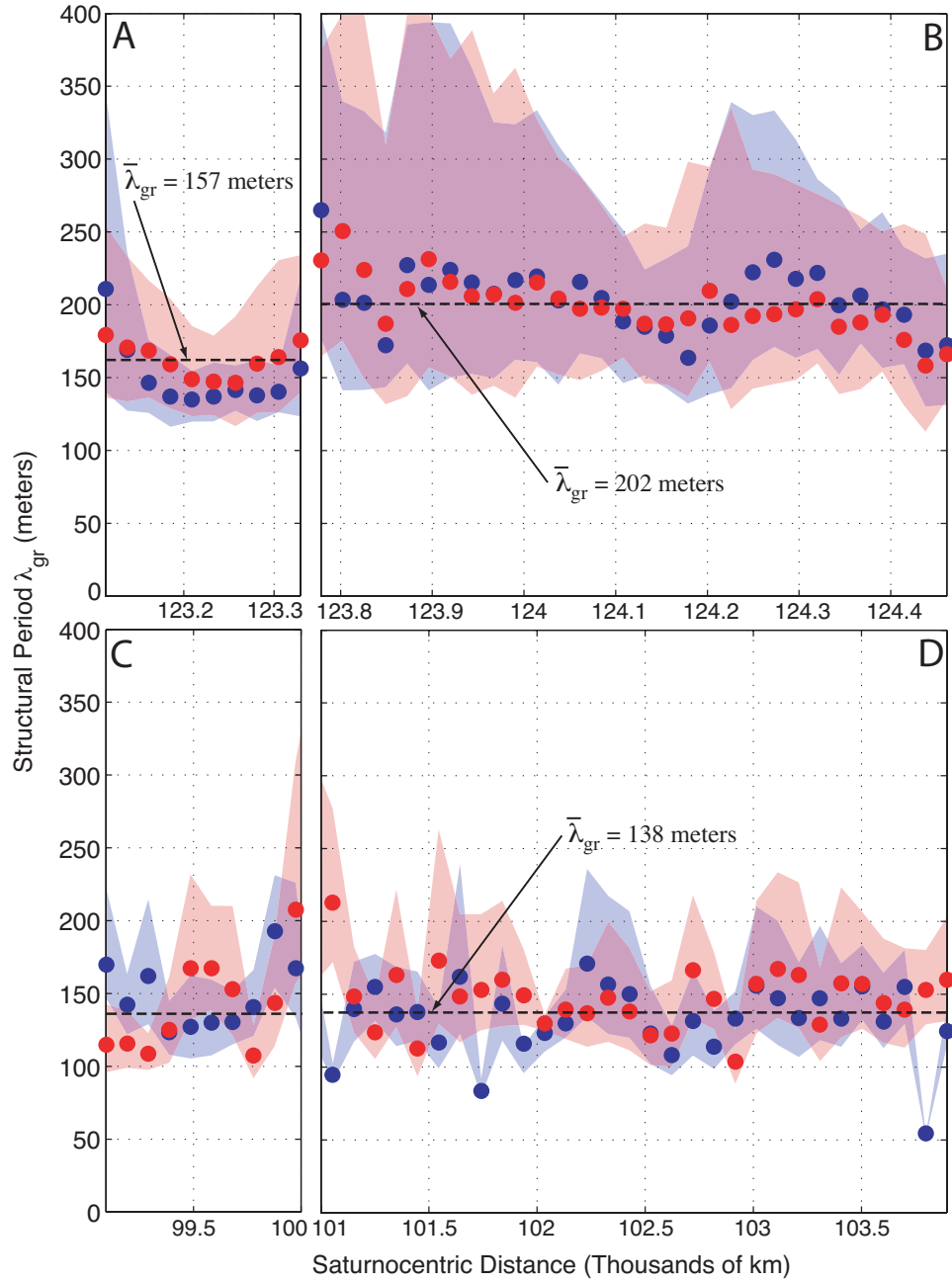
Figure 6.5: Estimates of the structural period λ_{gr} and orientation ϕ_{gr} of periodic microstructure detected in Saturn's rings. Estimates of λ_{gr} and ϕ_{gr} produced using a diffraction grating model are shown in Figures (a) and (b), respectively; Figures (c) and (d) show estimates of λ_{gr} and ϕ_{gr} produced with a sinusoidal transmittance screen model. In each of Figures (a)–(d), panels **A** and **B** detail features A123.2, A124.1, while **C** and **D** show region B2. Estimates in red are 3.6 cm- λ data, estimates in blue are 0.94 cm- λ data. The red and blue shaded regions correspond to the spread in λ_{gr} computed based on the 1- σ width of Gaussian functions fitted to the observed spectral features in the 3.6 and 0.94 cm- λ observations, respectively. Light purple is shown where the red and blue regions overlap. The dashed lines represent the average of the estimates, $\bar{\lambda}_{\text{gr}}$ and $\bar{\phi}_{\text{gr}}$, across a given region.



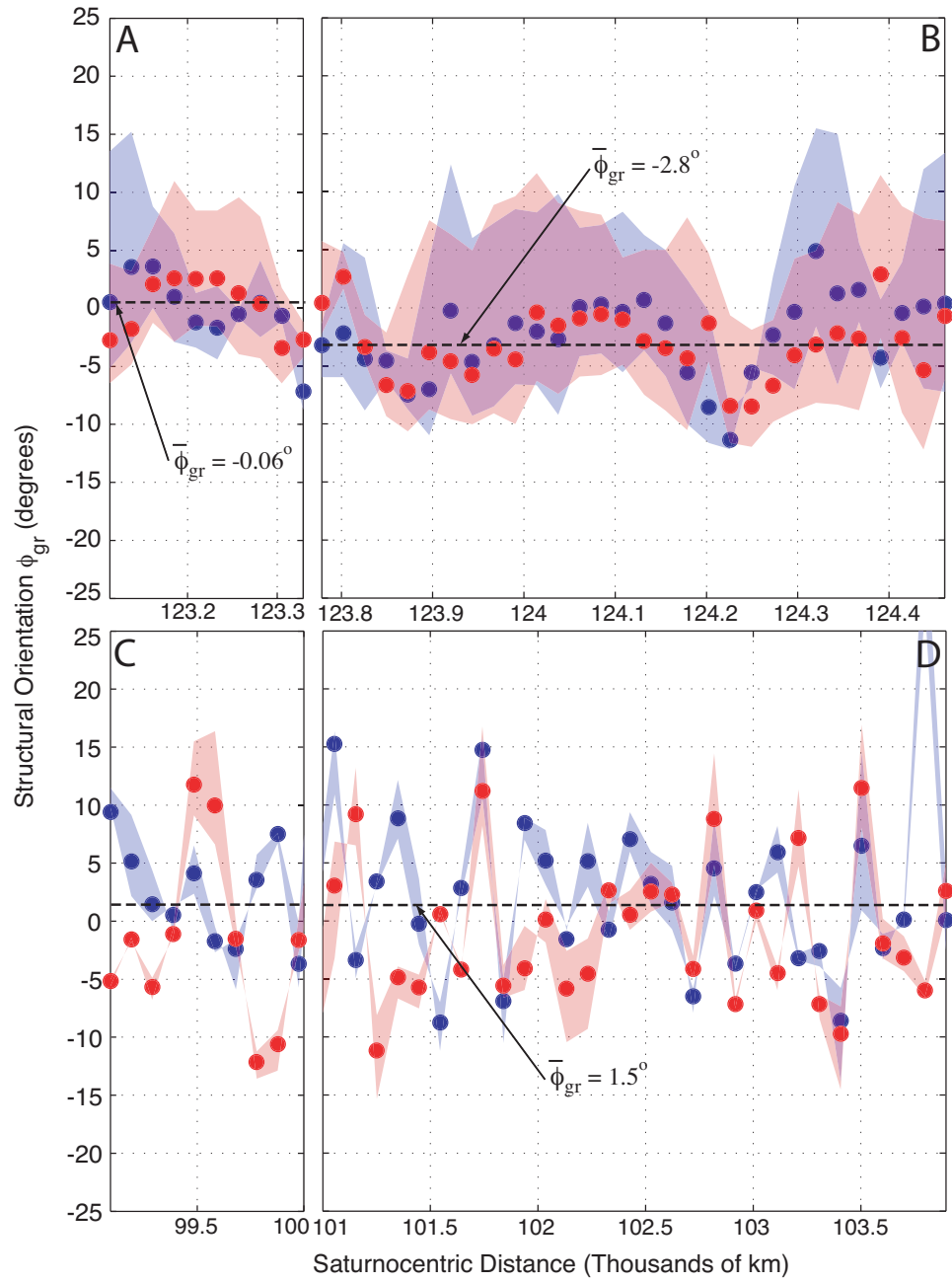
(a) Estimates of the structural period λ_{gr} using a diffraction grating model.



(b) Estimates of the structural orientation ϕ_{gr} using a diffraction grating model.



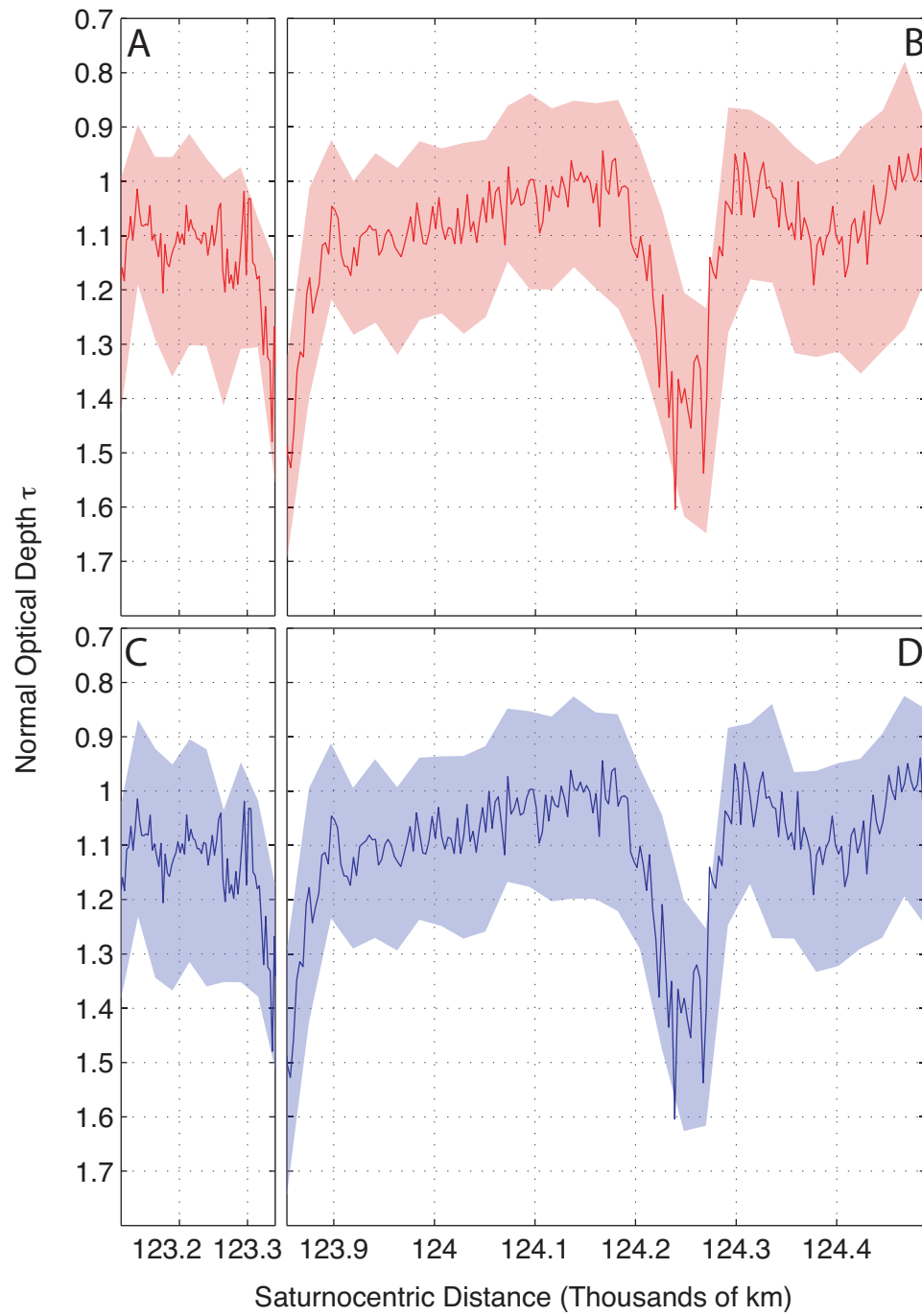
(c) Estimates of the structural period λ_{gr} using a sinusoidal amplitude screen model.



(d) Estimates of the structural orientation ϕ_{gr} using a sinusoidal amplitude screen model.

Next page.

Figure 6.6: Fine-scale optical depth variation τ_{fs} within features in Ring A is shown using REV 7 ingress data. Feature A123.2 estimates are shown in panels **A** and **C**; feature A124.1 estimates are shown in panels **B** and **D**. Ka- and X- band data are shown in blue and red, respectively. Estimates of the normal optical depth τ retrieved by analysis of the coherent signal are shown as solid lines in the plots. The fine-scale optical depth variation τ_{fs} is indicated by the shaded area.



6.3 Optical Depth Variation within Features A123.2 and A124.1

In Ring A, PM features exhibit first-order diffraction lobes that are 5–10 dB above the background scattered signal, as shown in Figures 4.5 and 5.13. Taking advantage of the high SNR in this region, we applied the theory of Section 5.2.1, eqs. (5.2)–(5.5), to estimate the fine-scale variation in optical depth τ_{fs} that exists within features A123.2 and A124.1. The results are presented in Figure 6.6, which shows that τ varies by approximately ± 0.3 within the two features. Estimates we calculated using both Ka-band and X-band data produced consistent results for $\tau_{\text{fs,min}}$ and $\tau_{\text{fs,max}}$.

6.4 Discussion

The origins of periodic microstructure in the rings is a subject of ongoing debate and research. At present, a phenomenon known as viscous or pulsation overstability is the leading dynamical theory to explain the existence of PM in Saturn's rings (*e.g.*, *Cuzzi et al.* [2002]). In this section we discuss the threshold conditions for the onset of viscous overstability (VO) in the rings, and compare those conditions with our observations to determine whether the VO threshold criteria explains the limited regions where PM is detected. We also present and discuss evidence in our data that may possibly indicate regions of Ring B where PM is superimposed on other microstructure.

6.4.1 Concurrent Microstructure

Salo et al. [2001] report that axisymmetric periodic structure due to viscous overstability co-exists with gravitational wakes in dynamical simulations, as long as the wakes are not too prominent. This coexistence is not predicted by any known analytic theory [*Schmidt et al.*, 2009].

Evidence for the existence of gravitational wakes is clearly present in the radio occultation data in both Rings A and B [*Marouf et al.*, 2006a]. The broad presence

of gravitational wakes across Rings A and B has been observed in back-scattered and UBVRI-filtered optical images of the rings taken using the Hubble Space Telescope (HST) [*French et al.*, 2007], and at radiometric wavelengths using the Very Large Array (VLA) [*Dunn et al.*, 2007].

There is evidence contained in our scattered signal observations that hints at a superposition of PM with other microstructure. In panels **C–D** of Figure 6.4, we see varying degrees of a double-humped structure in the forward scattering lobe—in addition to the distinct sidelobes associated with PM—that may indicate the presence of gravitational wakes, or possibly a packed monolayer of large particles (*cf.* Figure 5.1). Using the received signal synthesis technique explained in Chapter 5, we have been unable to produce a synthesized spectrum $I(f_D)$ from packed monolayer models that contains these double-humped features (Figure 5.10). However, we have not performed a thorough investigation of the packed monolayer model parameter space, and thus we are unable to rule out monolayers as a possible cause of humps in the signal spectrum. In panel **E** the narrow forward-scattering pattern, as compared with that of all the other panels in the figure, as well as the small region of enhancement in very near forward-scattering that is visible very close (in frequency) to the coherent signal may indicate the presence of gravitational wakes in combination with larger particle sizes (on average). This conjecture is unproved, and we leave the analysis of this phenomenon as a suggestion for future work.

6.4.2 The Onset of Viscous Overstability

In dynamical studies of dense rings, viscous overstability is accompanied by the formation of axisymmetric structures with small-scale periodicity on the order of one to few hundreds of meters [*Schmit and Tscharnuter*, 1999; *Salo et al.*, 2001; *Schmidt et al.*, 2001; *Salo and Schmidt*, 2009]. Recent theoretical studies by *Latter and Ogilvie* [2008, 2009] investigate the onset of viscous overstability (VO) using dense kinetic gas theory to model the rings, and propose that nonlinear wavetrains arising naturally in a viscously overstable disk can explain the presence of axisymmetric periodic microstructure.

Planetary rings become overstable if the extent to which viscosity increases with optical depth exceeds a certain rate (*e.g.*, *Schmidt et al.* [2009]). *Latter and Ogilvie* [2008] conclude that regions of overstability are possible anywhere in the rings, as long as a threshold optical depth τ_{th} is exceeded, although they also conclude that the filling factor—not τ , explicitly—is the parameter that determines the onset of VO. In both theoretical and dynamical studies, models of the rings predict a threshold optical depth on the order of $\tau_{\text{th}} \sim 1$.

Other than τ_{th} , specific estimates of the physical conditions that produce viscously overstable regions vary. *Schmit and Tscharnuter* [1995] say that VO onset occurs when,

$$\beta = \frac{d[\ln \nu \sigma_\rho]}{d[\ln \sigma_\rho]} \geq \text{sufficiently large} \quad (6.1)$$

where ν is the kinematic shear viscosity, and σ_ρ is the surface mass density of the rings. *Salo et al.* [2001] interpret the results of *Schmit and Tscharnuter* [1995] to yield the following VO onset condition,

$$\beta = \frac{d\nu}{d\tau} \left(\frac{\tau}{\nu} \right) > \beta_{\text{cr}} = \frac{1}{9} \quad (6.2)$$

This is inconsistent with dynamical simulation results generated by *Schmidt et al.* [2001], who propose a different VO onset condition,

$$\beta = \frac{d[\ln \nu]}{d[\ln \sigma_\rho]} \geq \beta_{\text{cr}} = 1 \quad (6.3)$$

which is derived from hydrodynamic theory and is consistent with dynamical simulation results [*Schmidt et al.*, 2001]. This appears now to be a generally agreed-upon threshold condition [*Schmidt et al.*, 2009].

Several forms exist in the literature for computing ν . *Colwell et al.* [2009] report that,

$$\nu = k_1 \frac{c^2}{\Omega} \frac{\tau}{\tau^2 + 1} + 4k_2 \Omega \tau a^2 \quad (6.4)$$

where c is the velocity dispersion of ring particles, Ω is the angular velocity of Keplerian ring particles, a is the radius of ring particles, and k_1 and k_2 are “constants of order unity”. An alternative is offered by *Schmit and Tscharnuter* [1995],

$$\nu = 0.26 \frac{c^2}{\Omega} \tau^{1.26}, \quad 0 \leq \tau \leq 2 \quad (6.5)$$

We seek to determine if the VO onset condition β_{cr} is correlated with the presence of PM in our observations. To this end, we compute ν using both eqs. (6.4) and (6.5). For Ring A, we obtain values of σ_ρ as a function of the radial position in the rings by interpolating between mean estimates of σ_ρ reported in Table 1 of *Spilker et al.* [2004]. Therein, mean values range between $11.3 \leq \sigma_\rho \leq 65.2 \text{ g cm}^{-2}$. These are consistent with values used by *Salo et al.* [2001] to simulate regions of similar optical depth. *Schmit and Tscharnuter* [1995, 1999] report values of $\sigma_\rho \approx 100 \text{ g cm}^{-2}$ in Ring B.

Schmit and Tscharnuter [1995] use a velocity dispersion value of $c = 0.2 \text{ cm s}^{-1}$ in Ring B. *Sremcevic et al.* [2008] measure the velocity distribution by analyzing spiral density wave measurements obtained from stellar occultation experiments, yielding an estimate of $c = 0.2\text{--}0.5 \text{ cm s}^{-1}$ in Ring A. We use $c = 0.2 \text{ cm s}^{-1}$ in our calculations.

We use eqs. (6.1)–(6.3) to compute the parameter β . In Figure 6.7(a) we show β , computed using eq. (6.3) and with values of ν obtained using eq. (6.5), superimposed on a spectrogram of the Ring A PM features A123.2 and A124.1. Results show that β tends to zero in regions where PM is established, and oscillates between large positive and negative values (*i.e.*, $\beta > \pm 10$) in the intervening regions. This behavior is phenomenologically the same as the estimates of β we produce using eqs. (6.1) and (6.2) as well, although the actual computed values vary.

Our β calculation is inconclusive, due to our poor knowledge of the fine-scale variation of σ_ρ in the rings. In Figure 6.7(a), the behavior of β is dominated by the optical depth variation contained in the numerator term $\partial[\ln \nu]$ of eq. (6.3); *cf.* eq. (6.5). In computing the denominator term $\partial[\ln \sigma_\rho]$, σ_ρ is estimated at 1117 radial locations by interpolating amongst the 40 points reported in *Spilker et al.* [2004]. This produces a smoothly-varying curve $\sigma_\rho(r)$, which is undersampled for use in a

rate-of-change calculation.

We could not compute β in Ring B, since we do not have an estimate of $\sigma_\rho(r)$ in that region (recall we have only a single value, $\sigma_\rho \approx 100 \text{ g cm}^{-2}$). Plots of the numerator $\partial[\ln \nu]$ alone over radial regions bounding feature B92.4, and regions B2 and B4, yielded results that are also inconclusive.

In summary, better estimates of $\sigma_\rho(r)$ are needed in order to compute meaningful estimates of β .

6.4.3 Optical Depth Characteristics of PM Regions

Although our calculations of the VO onset condition $\beta \geq \beta_{\text{cr}}$ are not conclusive, a preliminary assessment of the correlation between measured optical depth characteristics and the presence of PM yields more promising results. Here, we focus our attention on Ring A and feature B92.4, since the highly oscillatory nature of the optical depth in regions B2 and B4, combined with the large observed optical depth, renders any conclusions drawn from our observations in those regions more uncertain.

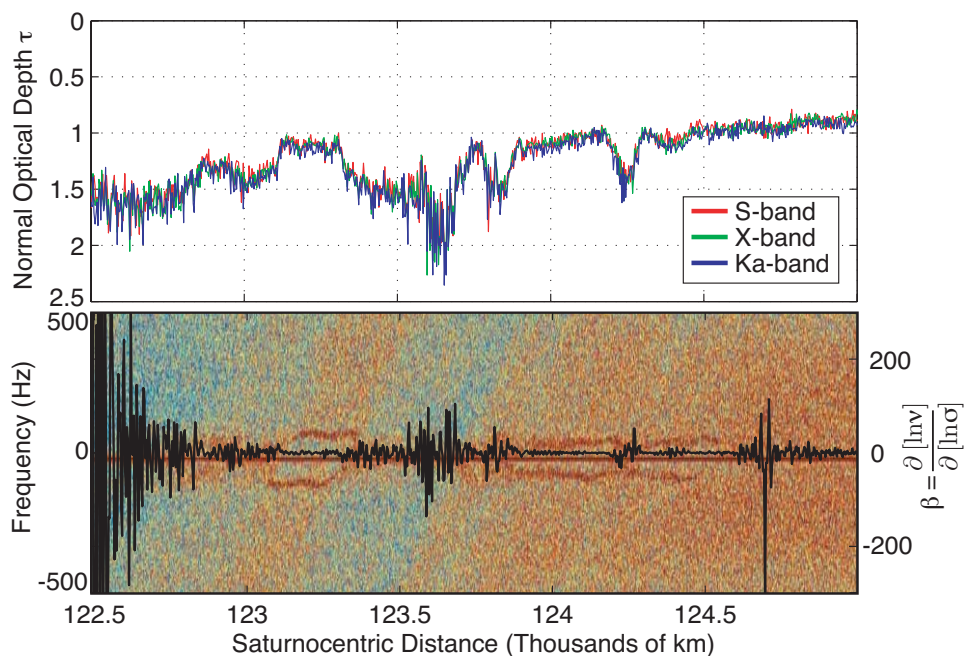
Optical depth observations suggest that regions of PM are bounded by sharp transitions in ring optical depth, combined with the condition that the normal optical depth $\tau > 1$. In Ring A, relatively sharp transitions in optical depth on the order of $\Delta\tau > 0.3$ appear to bound PM feature A123.2 on either side, and feature A124.1 on the low side (*i.e.*, on the side closest to Saturn); see Figure 6.7(a). On its upper side (*i.e.*, $r \approx 124,500 \text{ km}$), feature A124.1 appears to dissipate as the local optical depth decreases below $\tau \approx 1$. This is consistent with the predictions of hydrodynamical theory and with the results of dynamical simulations, as discussed in Section 6.4.2.

In feature B92.4, we see similar behavior—the region containing PM is bounded by sharp transitions in optical depth, where $\Delta\tau > 0.3$ on both sides of the feature. This is evident in Figure 6.7(b).

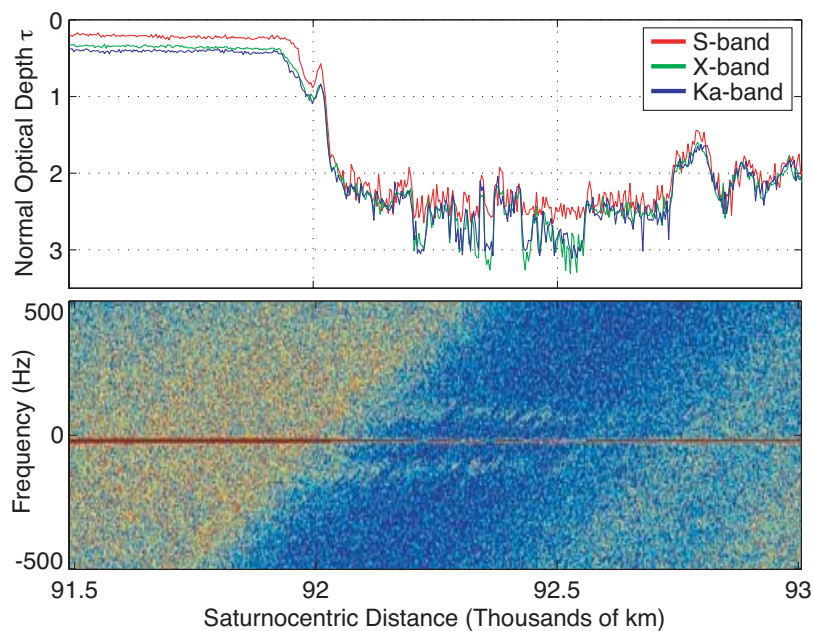
The same is true of regions B2 and B4. However, the optical depth in these regions exceeds the measurement capability of the radio instrument in many places, making it impossible to determine whether PM features exist continuously across B2 and B4, or whether the sharp transitions in optical depth—to values of τ that completely

Next two pages.

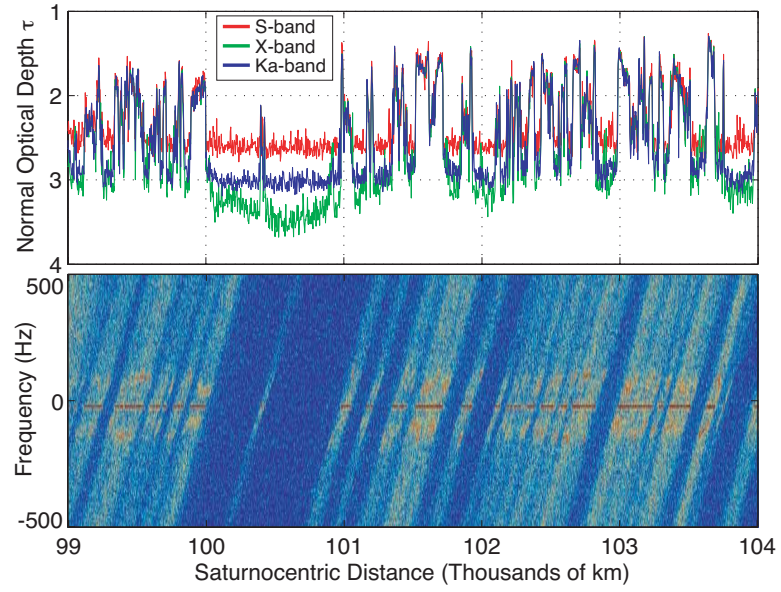
Figure 6.7: Optical depth and spectrogram plots of periodic microstructure features observed during the REV 7 ingress occultation. In each plot, the top panel shows the optical depth at 13, 3.6, and 0.94 cm wavelengths (S-, X, and Ka-band, respectively). The spectrograms are produced from the X-band ($\lambda = 3.6$ cm) received signal. Shown are (a) features A123.2 and A124.1; (b) feature B92.4; (c) the B2 region; and (d) the B4 region. In (a), we overlay the computed value of the dynamical parameter β (see eq. (6.3)) on the spectrogram plot. According to *Schmidt et al.* [2009], the onset of viscous overstability occurs when $\beta \geq 1$. Our calculations are not conclusive on this point. See the text for a more detailed discussion.



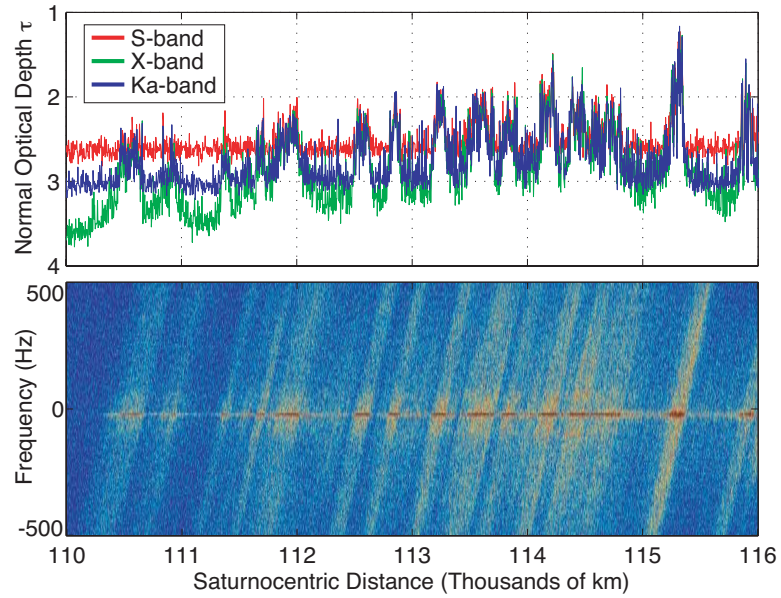
(a) Normal optical depth and spectrogram of features A123.2 and A124.1. The parameter β is superimposed (in black) on the spectrogram, with scale provided at the right of the figure. See Figure 6.3 for a clean spectrogram of these features.



(b) Normal optical depth and spectrogram of feature B92.4.



(c) Normal optical depth and spectrogram of the B2 region.



(d) Normal optical depth and spectrogram of the B4 region.

extinguish the radio signals—actually bound regions containing PM.

It is foolish to mistake correlation with causation, and we do not make that mistake here. Our intent is to make a preliminary report of our observations regarding τ and the presence of PM. A definitive cause of PM in Saturn's rings remains to be proved; that task is beyond the scope of this dissertation.

6.5 Summary

We have uncovered and reported on five distinct instances of periodic microstructure in Saturn's Ring A and B. The mean structural period $\bar{\lambda}_{\text{gr}}$ of the PM we observe varies between 115–250 meters. We determine that all PM regions are approximately axisymmetric, with mean estimates of the orientation (using both the grating and sinusoidal screen methods) ranging between $-2.8^\circ \leq \bar{\phi}_{\text{gr}} \leq 1.5^\circ$. The results of these investigations are reported formally in *Thomson et al.* [2007].

Axisymmetric structure with small-scale periodicity on the order of hundreds of meters is predicted by both hydrodynamic theory, and by dynamical simulations of the rings. These structures appear in regions of the rings that exhibit a phenomenology known as viscous overstability (VO), the onset of which is controlled by a parameter β , and by the condition that $\tau > 1$.

We observe the termination of feature A124.1 at approximately $r = 124,500$ km when the optical depth τ decreases below $\tau \approx 1$, which is consistent with theory [*Latter and Ogilvie*, 2008; *Schmidt et al.*, 2009]. Elsewhere, we observe the termination of PM features when relatively large changes in optical depth, $\Delta\tau > 0.3$ or so, occur.

Theory and dynamical simulation results predict that regions where the shear viscosity is increasing much faster than the optical depth mark the onset of viscously overstable regions. Measures of this are formalized by the parameter β , versions of which are presented in eqs. (6.1)–(6.3). We are unable to effectively compute β in the rings due to the poor spatial resolution of our surface mass density σ_ρ estimates in regions of the rings where PM exists. Thus we cannot conclusively state whether or not the conditions for VO have been strictly met in the regions where we have observed PM. We leave this as an open question for future researchers to answer.

\hbar

Chapter 7

Summary and Conclusions

In this chapter we summarize the findings of our work, and its relevance in the context of the pre-Cassini understanding of Saturn’s rings. This is followed by a discussion of the assumptions and limitations inherent to our model, and the associated implications for our results. Suggestions for future work are discussed in the final section.

7.1 General Results

The methods that we have developed for estimating the dimensions of microstructure in Saturn’s rings rely on our ability to apply scalar diffraction theory to the analysis of forward scattering from ring microstructure. We have proved that the assumptions of scalar diffraction theory are satisfied by the conditions of the radio occultation experiments. Specifically, we showed that as long as the ring particles are electrically large, and as long as we are measuring radio signals in the near-forward scattering direction, then scalar diffraction theory produces estimates of the scattering pattern that closely mimic those produced using full electromagnetic theory. Both of these conditions are met by the experiment. Our detailed analysis is shown in Chapter 3 and also in *Thomson and Marouf* [2009].

We have shown that axisymmetric periodic microstructure with length scales varying between 100–250 meters exists in (at least) five distinct regions within Saturn’s

rings. We uncovered two distinct features in Ring A at radial locations $123.05\text{--}123.4\times 10^3$ km and $123.6\text{--}124.6\times 10^3$ km, which we have named A123.2 and A124.1, respectively. These features have mean structural periods ranging between 160–220 meters. At a radial location spanning $92.1\text{--}92.6\times 10^3$ km in Ring B, feature B92.4 is detectible with an estimated mean structural period of 115 meters. PM structure is seen in two broad regions of Ring B known as B2 and B4, located at $99\text{--}104.5\times 10^3$ km and $110\text{--}117.5\times 10^3$ km, respectively. Here, we estimate mean structural periods of 146 meters and 250 meters, respectively. These details are summarized in Chapter 6 (see Table 6.1). The results are also reported in *Thomson et al.* [2007].

Prior to Cassini, the existence of axisymmetric periodic microstructure had been predicted by dynamicists investigating the properties of planetary rings. Some scientists had applied dynamical theory specifically to Saturn’s Ring B, which was known (after Voyager) to contain regions of sharply oscillating optical depth. However, no measurements of ring optical depth existed on length scales that could detect PM features with wavelengths on the order of 100 meters, which was the value of λ_{gr} predicted by dynamicists.

Our results were among the first direct observations of these features in the rings. We had the good fortune to be in the right place at the right time—and with the right instrument—to validate the predictions of the dynamical theory.

7.2 Assumptions and Limitations

Several assumptions were incorporated in the development of our methods. First, we have assumed in our analysis that features contained in the rings do not change during the period of our observations, which spanned the dates May 3–August 2, 2005. The observations we made during this period were used together to produce estimates of the dimensions of detected periodic microstructure. We believe that this is a reasonable assumption, since we do not detect any evidence that either the location of the features, or the physical dimensions of the features changed significantly during that three-month period. This is not surprising, since the collisional and gravitational forces that create these features are not changing on short time scales. It is possible

that inter-particle collisions could break larger ring particles apart over time, driving an evolution in the particle size distributions local to a PM feature that could perhaps change the dimensions of the feature in some measurable way. However, we believe that those mechanisms take place on time scales that are longer than the 3-month period of the observations we use in our analysis, although that point is not proved.

In fitting our PM models to the data, we assume a sinusoidal variation in optical depth. The optical depth variation of PM regions in the rings, caused by VO and predicted by hydrodynamic theory and dynamical simulations, are not purely sinusoidal. Theory predicts a nonlinear periodic structure, and thus diffraction from PM should produce higher order sidelobes in the received signal. The best-case SNR we achieved with first-order sidelobe measurements was on the order of 5–10 dBn (the 3.6 cm- λ measurements of feature A123.2); higher order diffraction lobes were not detected within this 5–10 dB detection limit. From this, we surmise that most of the diffracted signal power is contained in the first-order lobes, and that our estimates of structural period and orientation should be correct, even if the precise variation of optical depth within a period of the structure remains unknown.

Another limitation in our method is caused by the slanting of features in our spectrograms, as explained in Section 4.1.2. Currently, our sidelobe peak estimation algorithm, eq. (5.20), fits a Gaussian function to the diffraction sidelobes at each step in $|\vec{r}_o|$ without de-slanting the spectrogram to remove the effect of the finite HGA spot size. Thus, we incur errors in our estimates of the physical dimensions of PM. Because of its greater slant angle, the X-band data is more vulnerable to this error than is Ka-band. The errors are greatest in parts of a PM feature where the physical dimensions are changing—at either end of feature A123.2, for example. In the middle of a feature, the Doppler frequencies associated with PM are relatively constant, which lessens the estimation error. Averaging over broader swaths in the rings also reduces the error, but yields a coarser spatial resolution of our λ_{gr} and ϕ_{gr} estimates. The limitation due to spectral slanting represents the most significant weakness in our model.

7.3 Contributions

As we have stated in Section 1.3, the major contributions of this work are as follows:

1. We uncovered five distinct locations in Saturn’s rings A and B exhibiting highly periodic, fine-scale variation in the ring optical depth. The physical period of these variations range between 100–250 meters [*Thomson et al.*, 2007].
2. An exhaustive study, comparing the results of a multiple scattering formulation of Mie theory against the results of scalar diffraction theory. The study, which examined 2-, 3-, and 10-sphere clusters of particles, shows that diffraction theory accurately predicts the far-field scattering pattern of particle aggregates, as long as the region of interest is limited to electrically large particles scattering in the near-forward direction [*Thomson and Marouf*, 2009].
3. Derivation of the exact solution for the five-term power-law expression of Allan variance, showing that the exact solution and the well-known approximate solution converge very quickly; *i.e.*, the approximate form is sufficient and satisfied by most imaginable measurement conditions [*Thomson et al.*, 2005]. An adaptation of this paper is included as Appendix D.
4. Demonstration of the equivalence of the Radon and Abel Transforms, as they are applied in atmospheric radio occultation [*Thomson and Tyler*, 2007]. An adaptation of this paper is included as Appendix E.

7.4 Future Work

Prior to Cassini, the only radio occultation data available for Saturn’s rings were gathered during the Voyager 1 flyby of Saturn on November 13, 1980; a single egress pass lasting approximately 1000 seconds, with a ring opening angle of $B \approx 6^\circ$.

Cassini has produced multiple radio occultation datasets, sampled during observations that span a range of ring opening angles between $0 \leq B \leq 23.6$, and over many ring longitudes. With multiple experimental observations—at radio and other

wavelengths—of the same ring system now available, the time evolution of rings can be studied. The azimuthal asymmetry of Saturnian ring optical depth, thought to be produced by canted gravitational wakes [*Salo*, 1992; *Salo et al.*, 2004], can be measured by comparing occultation tracks at different Saturnian longitudes. Analysis of the effect of changing observational parameters, such as ring opening angle and longitude, add a new dimension to data reduction that is certain to result in a more complete picture of the structure and dynamics of the rings, and how they evolve over time.

There are many opportunities for improvement, extension, or application of the methods developed in this dissertation. On the signal processing side, more advanced peak detection methods could be used to produce better Gaussian (or other) fits to features of the received signal, improving the input to our estimation codes. Advanced estimation methods, such as Kalman filtering, could be applied to use different kinds of data together to produce better estimates of physical microstructure dimensions. Advanced signal processing methods could also be used to determine definitively the sensitivity of the measurement to the presence of higher-order diffraction lobes in the received signal, and to verify with greater confidence that they are not hidden in our received signal.

Theoretical studies that determine the uniqueness of scattering from homogeneous rings, monolayers, clumped ring models, gravitational wakes, and periodic microstructure can be performed by using the amplitude screen method in combination with statistical methods. The findings of such a study could help guide the use of different microstructure models in cases where diffraction features contained in the scattered signal are more subtle, and therefore determining the underlying microstructure is more challenging.

Collaborative partnerships with ring dynamicists could yield estimates of many underlying physical properties of the rings that that best-fit regions of the rings containing detected microstructure. In this scenario, dynamical simulations are used to generate vignettes of the rings that contain microstructure. The underlying physical properties—such as surface mass density, ring thickness, etc.—are varied in the optimization that fits synthesized spectral features to those detected in the Cassini

received signal.

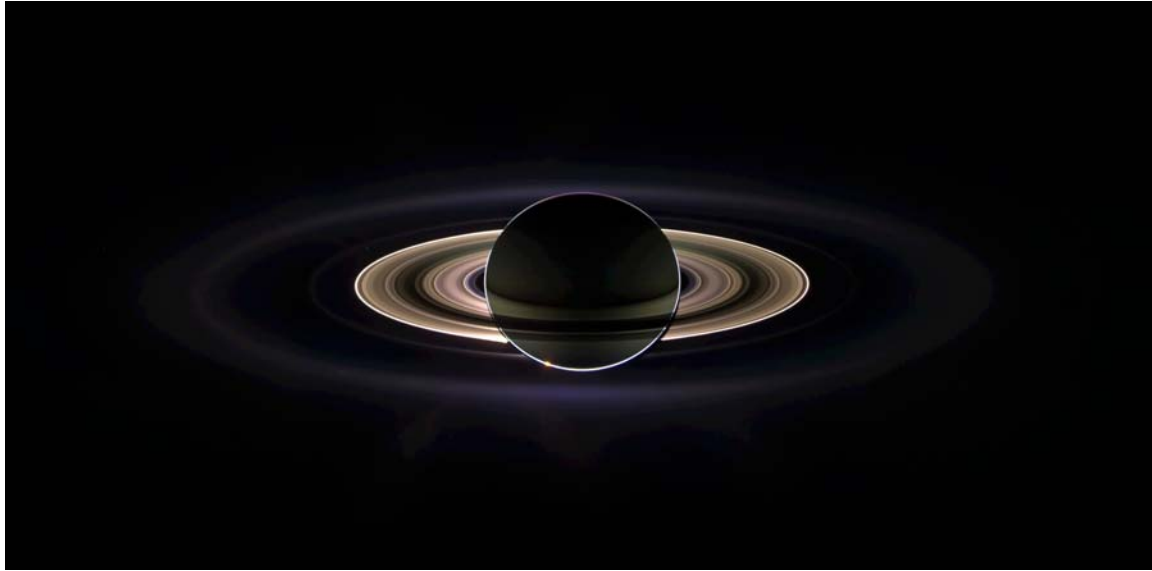


Figure 7.1: This panoramic view of the unlit side of Saturn and the rings is a composite of 165 images taken by the Cassini wide-angle camera during approximately three hours on Sept. 15, 2006. Colors in the mosaic were created by digitally assembling ultraviolet, infrared and clear filter images, then adjusting the composite to resemble natural color. Cassini was over 1 billion km from Earth, approximately 2.2 million km from Saturn, and 15 degrees above the ring plane when the images in this mosaic were taken. The resolution of Saturn in the image is about 260 km/pixel. Image is PIA08329, NASA Photojournal website.

h

Appendix A

Radio Occultation Studies of Planetary Rings

The following sections contain a brief theoretical overview of ring radio occultation analysis. In Section A.1, we describe how the coherent component of the received signal is processed to obtain optical depth profiles for both circular and elliptical ring systems. We describe factors that limit profile resolution and measurement sensitivity. Section A.2 explains how we estimate particle size distributions by analyzing the scattered signal, and by analyzing optical depth measurements taken at different radio frequencies. We include a brief discussion of methods used to obtain estimates of the surface mass density of the rings.

A.1 Optical Depth Profiles

The average effect of scattering from ring particles along the very-near-forward path from the transmitter to receiver (well within the first several Fresnel zones) causes an amplitude and phase modulation of the coherent component of the received signal. Extinction (*i.e.*, attenuation) of the transmitted signal by interceding ring material is characterized in terms of the optical depth of the rings.

Optical depth is a measure of a medium's opacity to the propagation of radiation of a certain wavelength. If the rings are illuminated with an incident electromagnetic

wave of intensity I_o , and the intensity just behind the rings is I , the oblique optical depth τ_q is defined as,

$$\tau_q = -\ln(I/I_o) \quad (1.1)$$

For the classical many particles thick (MPT) ring model, the normal optical depth τ is related to the oblique optical depth by,

$$\tau = \mu_o \tau_q \quad (1.2)$$

where $\mu_o = \sin B$ is the sine of the ring opening angle B , which is the angle that the wave vector \vec{k} of the incident light makes with the ring plane; or alternatively, the angle between the plane of the rings and the plane defined by the transmitter, receiver, and the geometric center of the planet under study; see Figure 5.8. The wavelength dependence of optical depth, though not explicitly stated here, is an important feature of the rings that can be exploited to determine ring particle sizes, as discussed in more depth in Section A.2.

Mathematically, the rings can be modeled as a thin screen of complex transmittance. During a radio occultation experiment, the screen is illuminated on one side by a coherent plane wave. The amplitude and phase of the wave at any point immediately behind the screen is the product of the incident wave's complex amplitude, and the complex screen transmittance at that point. Following Huygens-Fresnel theory, spherical waves propagate away from secondary point sources formed behind the screen, generating a diffraction pattern in all of space behind the screen. The receiver 'flies' through this diffraction pattern, sampling the magnitude and phase of the diffracted field. These one-dimensional (*i.e.*, along the receiver trajectory) samples are used to reconstruct the assumed 1-D transmittance profile of the rings, and from that the optical depth.

The diffracted received signal \hat{T} is related to the complex transmittance of the rings T by a modified form of the Huygens-Fresnel integral [Marouf *et al.*, 1986],

$$\hat{T}(r_o, \phi_o) = \frac{\sin B}{i\lambda} \int_0^{2\pi} \int_0^\infty T(r, \phi) \frac{e^{i\psi(r_o, \phi_o; r, \phi)}}{|\vec{R}_c - \vec{r}|} \rho \, dr d\phi \quad (A.1)$$

where \vec{r} is the vector from the planet's center to the point (r, ϕ) in the rings. The estimate \hat{T} contains energy scattered from everywhere the rings are illuminated; in the theoretical limit, from everywhere in the r - ϕ plane, as evidenced by the integration limits in eq. (A.1). The point where the line of sight between the transmitter and receiver intersects the ring plane is given by $\vec{r}_o \rightarrow (r_o, \phi_o)$; \vec{R}_c is the vector from the center of the planet under study to the spacecraft; and λ is the wavelength of the transmitted signal. The phase function ψ is given by,

$$\psi(r_o, \phi_o; r, \phi) = kD \left[\sqrt{1 + 2\xi + \eta} - (1 + \xi) \right] \quad (\text{A.2})$$

where

$$\xi = \cos B(r_o \cos \phi_o - r \cos \phi) \quad (\text{A.3})$$

$$\eta = [r^2 + r_o^2 - 2rr_o \cos(\phi - \phi_o)] / D^2 \quad (\text{A.4})$$

and $D = |\vec{R}_c - \vec{r}_o|$, $k = \frac{2\pi}{\lambda}$.

A.1.1 Circular Rings

If we assume that the rings are locally circular, as is likely the case for Saturn, then azimuthal symmetry $T(r, \phi) = T(r)$ yields a simplified form of eq. (A.1),

$$\hat{T}(r_o) = \frac{\sin B}{i\lambda} \int_0^\infty r T(r) \int_0^{2\pi} \frac{e^{i\psi(r_o, \phi_o; r, \phi)}}{|\vec{R}_c - \vec{r}|} d\phi dr \quad (\text{A.5})$$

Further simplification of eq. (A.5) is possible by evaluating the ϕ -integral using the stationary phase method [Marouf *et al.*, 1986]. If there exists a value of $\phi = \phi_s$ that solves $\frac{d\psi}{d\phi} = \frac{\partial\psi}{\partial\phi} = 0$ that is valid for any value of r , and which also satisfies the criterion that $|\vec{R}_c - \vec{r}_s| \approx D$, where $\vec{r}_s \rightarrow (r, \phi_s)$, then eq. (A.5) reduces to,

$$\hat{T}(r_o) = \frac{1 - i}{2F} \int_{-\infty}^\infty T(r) e^{i\psi(r_o, \phi_o; r, \phi_s)} dr \quad (\text{A.6})$$

where the Fresnel scale F is defined as,

$$F = \sqrt{\frac{\lambda D}{2} \left(\frac{1 - \cos^2 B \sin^2 \phi_o}{\sin^2 B} \right)} \quad (\text{A.7})$$

In general, an exact solution to eq. (A.6) does not exist. Several approximate solutions were developed by *Marouf et al.* [1986], and have been used to process both Voyager and Cassini radio occultation data. Marouf obtained a quadratic approximation of ψ by expanding ψ in powers of the parameter $(r_o - r)/D$ and retaining only terms up to and including the second order in the expansion (see the section titled *Quadratic Approximation of ψ* in Appendix A of *Marouf et al.* [1986]), thus reducing eq. (A.6) to,

$$\hat{T}(r_o) = \frac{1 - i}{2F} \int_{-\infty}^{\infty} T(r) e^{i\frac{\pi}{2} \left[\frac{r_o - r}{F} \right]^2} dr \quad (\text{A.8})$$

This equation has an exact mathematical inverse,

$$T(r) = \frac{1 + i}{2F} \int_{-\infty}^{\infty} \hat{T}(r_o) e^{-i\frac{\pi}{2} \left[\frac{r - r_o}{F} \right]^2} dr_o \quad (\text{A.9})$$

which, under ideal conditions, may be used to determine the complex transmittance of the rings $T(r)$ from the diffraction-limited observations $\hat{T}(r_o)$. A fourth-order polynomial approximation to ψ (see the section titled *Polynomial Approximation of ψ* in Appendix A of *Marouf et al.* [1986]) yields,

$$T(r) = \frac{1 + i}{2F} \int_{-\infty}^{\infty} \hat{T}(r_o) e^{-i[C_2(r - r_o)^2 + C_3(r - r_o)^3 + C_4(r - r_o)^4]} dr_o \quad (\text{A.10})$$

Equations (A.9) and (A.10) have the form of Fresnel transforms, which are convolution integrals of the form,

$$T(r) = \hat{T}(r) * h(r) = \int_{-\infty}^{\infty} \hat{T}(r_o) h(r - r_o) dr_o \quad (\text{A.11})$$

In fact, eqs. (A.8) and (A.9) define a Fresnel transform pair. One can think of the application of eqs. (A.9) or (A.10) as analogous to applying a matched filter, $h(r)$, to the measurement $\hat{T}(r)$. The filter compensates for the effect of the Huygens-Fresnel wavelets that propagate from all locations on the rings and sum together, via

superposition, to form $\hat{T}(r)$. An estimate of the true complex transmittance $T(r)$ is recovered, limited by the quadratic or quartic phase approximations introduced above, as well as other practical limitations mentioned below.

A.1.2 Elliptical Rings

A technique for analyzing elliptical rings was developed while processing radio occultation data collected during Voyager 2's encounter with Uranus [Gresh *et al.*, 1989; Gresh, 1990]. For elliptical rings, the locus of points in r and ϕ defining an individual ringlet adhere to the following,

$$r = \frac{a(1 - e^2)}{1 + e \cos \nu} \quad (\text{A.12})$$

where a is the semi-major axis of the ellipse, e is the eccentricity, $\nu = (\phi - \omega)$ is the mean anomaly (see Vallado [2001], for example), and ω is the angle of periapse. The complex transmittance may be written as,

$$T(r, \phi) = T(a) = \int_{-\infty}^{\infty} \delta(a - a') T(a') da' \quad (\text{A.13})$$

where the transmittance is now parameterized for each elliptical ringlet by its semi-major axis a . The limits of the integration here serve as a mathematical convenience [Gresh *et al.*, 1989; Gresh, 1990]. Substitution of eq. (A.13) into eq. (A.1) yields,

$$\hat{T}(r_o, \phi_o) = \frac{\sin B}{i\lambda} \int_{-\infty}^{\infty} T(a') \left[\int_0^{2\pi} \int_0^{\infty} \delta(a - a') \frac{e^{i\psi(r_o, \phi_o; r, \phi)}}{|\vec{R}_c - \vec{r}|} r \, dr d\phi \right] da' \quad (\text{A.14})$$

Since the δ -function effectively defines a path of integration in r - ϕ space, the contents of the square brackets in eq. (A.14) can be replaced by a contour integral,

$$\hat{T}(r_o, \phi_o) = \frac{\sin B}{i\lambda} \int_{-\infty}^{\infty} T(a') \int_C \frac{e^{i\psi(r_o, \phi_o; r, \phi)}}{|\vec{R}_c - \vec{r}|} \frac{dl}{|\nabla a'(r, \phi)|} da' \quad (\text{A.15})$$

where dl is a unit element along the path C defined by the ellipse satisfying eq. (A.13) for $a = a'$, and $\nabla a'$ is the two-dimensional gradient of a' with respect to r and ϕ .

Eq. (A.15) is the elliptical analogue to eq. (A.5) for circular rings. Following the same methodology, the stationary phase method is applied to simplify eq. (A.15) by searching along the contour C for the ordered pair (r_s, ϕ_s) that satisfies the condition,

$$\left. \frac{d\psi}{d\phi} \right|_{\phi_s} = \left(\frac{\partial\psi}{\partial\phi} + \frac{\partial\psi}{\partial r} \frac{\partial r}{\partial\phi} \right)_{\phi_s} = 0 \quad (\text{A.16})$$

Note that unlike the case of circular ringlets, r now varies with ϕ during the search for the stationary phase point. This criterion applies to stationary phase analysis for both circular and elliptical ring cases, though it is simpler for circular rings since $\frac{\partial r}{\partial\phi} = 0$. If the effect of ellipticity on $\frac{d^2\psi}{d\phi^2}$ at $\phi = \phi_s$ is neglected, stationary phase analysis of the contour integral results in a simplification of eq. (A.15) to the following,

$$\hat{T}(r_o) \approx \frac{1-i}{2F} \int_{-\infty}^{\infty} T(r) e^{i\psi(r_o, \phi_o; r_s, \phi_s)} dr \quad (\text{A.17})$$

Equation (A.17)—for elliptical rings—and eq. (A.6)—for circular rings—differ only in their corresponding stationary phase points. The form of these two equations is identical, and thus identical methods (via eqs. (A.9) or (A.10), for example) can be used to retrieve the ring transmittance profile for either geometric case, subject to the correct use of r_s and ϕ_s .

A.1.3 Resolution Limitations in the Reconstruction Process

Several Fresnel scales F would define the resolution limit of the optical depth profiles obtained from the diffraction-limited observations $\hat{T}(r_o)$ prior to diffraction correction [Rosen, 1989]. Once eq. (A.9) or (A.10) is applied to remove the effects of diffraction from the data, the theoretical resolution limit approaches the size of the receiving antenna as $\text{SNR} \rightarrow \infty$ and $\Delta r_o \rightarrow 0$, where Δr_o is the sample spacing. Since this resolution requires an infinite number of samples, each with well-determined phase generated by perfect oscillators (*i.e.* zero phase noise) at the transmitter and receiver, it is a very difficult limit to achieve indeed.

In practice, the reconstruction process is limited to resolutions on the order of a few hundred meters for Saturn's rings and several tens of meters for Uranus' rings. For

Saturn, profile resolutions of 400 meters are more typical best-case reconstructions. Limiting factors include the non-constancy of F , the extent of the data used in processing, the phase stability of the on-board reference UltraStable Oscillator (USO), amplitude variation due to antenna pointing errors, and the stochastic variation of the signal amplitude and phase [Marouf *et al.*, 1986; Rosen, 1989].

A new symbol, \hat{X} , is introduced to represent the true received signal in the presence of noise. Thermal noise introduced primarily by the ground station antenna constitutes an additive noise component ($\hat{X} = \hat{T} + \hat{n}$), while multiplicative phase noise ($\hat{X} = \hat{T}e^{i\hat{\phi}_n}$) is introduced by phase instabilities in both the transmitter and receiver reference oscillators. Including these non-idealities, eq. (A.10) is re-written to more accurately reflect the actual reconstruction process,

$$X(r) = \frac{1+i}{2F} \int_{r-W/2}^{r+W/2} \hat{X}(r_o) w(r-r_o) e^{-i[C_2(r-r_o)^2 + C_3(r-r_o)^3 + C_4(r-r_o)^4]} dr_o \quad (\text{A.18})$$

where the finite extent of the data used to reconstruct $X(r)$ is treated by applying a window function w with width W about the point r . Eq. (A.18) has been used to reconstruct optical depth profiles of Saturnian and Uranian rings using Voyager radio occultation data, and of Saturn's rings using Cassini data [Marouf, 2006–2010].

Using the quadratic phase approximation, eq. (A.8), the observed ring transmittance can be viewed as the convolution of the actual ring transmittance $T(r)$ with a filter of phase,

$$\phi_Q(r_o) = \frac{\pi}{2} \left(\frac{r_o}{F} \right)^2 \quad (\text{A.19})$$

The effect of finite filter width W is quantified for the quadratic phase case by calculating the derivative of the phase to get the spatial frequency [Rosen, 1989],

$$f_Q \triangleq \frac{1}{2\pi} \frac{d\phi_Q(r_o)}{dr_o} = \frac{r_o}{2F^2} \quad \text{cycles/meter} \quad (\text{A.20})$$

The bandwidth of an unweighted ($w = 1$) reconstruction filter of width W is therefore $f_{Q,BW} = \frac{W}{2F^2}$, and the resolution of this filter is the reciprocal of filter bandwidth,

$$\Delta R_W \triangleq \frac{1}{f_{Q,BW}} = \frac{2F^2}{W} \quad \text{meters} \quad (\text{A.21})$$

Marouf et al. [1986] derive eq. (A.21) using a different approach.

The spatial sampling frequency is defined as the reciprocal of the radial sample spacing, $f_s = \Delta r_o^{-1}$. In order to avoid aliasing in the reconstruction of the complex transmittance, the filter bandwidth may not exceed the complex sampling frequency, or $f_{Q,BW} \leq f_s$. Thus a maximum is imposed upon the width of the reconstruction filter,

$$W_{max} = \frac{2F^2}{\Delta r_o} \quad (\text{A.22})$$

When $W = W_{max}$, the best possible resolution of $\Delta R_{Wmin} = \Delta r_o$ is achieved. In practice, a window function other than $w = 1$ is applied to the filter in order to reduce reconstruction artifacts induced by the effect of unwanted sidelobes, which result from abrupt amplitude transitions at the edges of the window function. Strong sidelobes in the filter function erode the dynamic range of the reconstruction process, inhibiting the resolution of regions where transmittance changes abruptly, such as at ring gap edges. Rosen studied the effect of windowing on profile reconstruction, and discusses the associated issues in *Rosen* [1985] and *Rosen* [1989]. He determined that the application of a Kaiser-Bessel window (with weighting parameter $\alpha = 2.5$) offers a reasonable tradeoff between resolution and sensitivity, improving the dynamic range of the reconstruction process from 13dB to 57dB, while reducing the resolution to,

$$\Delta R \approx 1.65 \Delta R_W \quad (\text{A.23})$$

Limitations on ΔR are also introduced by the variation and uncertainty of F within the filter window W , and by the quadratic and quartic (4th-order polynomial) phase approximations to ψ used in the reconstruction integrals of eq. (A.9) and eq. (A.10), respectively. The interested reader is referred to *Marouf et al.* [1986] for a detailed review of these effects.

Historically, eq. (A.18) with its quartic polynomial phase approximation was used

to reconstruct ring transmittance profiles for Voyager 1's observations of Saturn [Tyler *et al.*, 1983; Marouf *et al.*, 1986; Rosen, 1989], and Voyager 2's observations of Uranus [Gresh *et al.*, 1989; Gresh, 1990; Marouf, 2006–2010]. Theoretically, the polynomial coefficients C_n are properly computed from derivatives of ψ during the Taylor series analysis. In practice, this proved prohibitively difficult due to ψ 's functional dependence on ϕ_s . Instead, the coefficients C_n in eq. (A.18) were determined using a fitting algorithm, and the integral computed using numerical methods [Marouf *et al.*, 1986]. The resolution of the reconstructed noisy profiles $X(r)$ depend on the width W and shape of the window. Longer window lengths W lead to higher resolution profiles, but an accurate determination of ϕ_c is required over the full width of the window. Thus the largest single limitation in the profile resolution is the accurate determination of the phase ϕ_c over many seconds, thus enabling the use of a large data window W .

A.1.4 Profiling Ring Optical Depth

Since $I/I_o = |X|^2$, eq. (1.1) can be re-written as,

$$\tau_q = -\ln(X_R^2 + X_I^2) \quad (\text{A.24})$$

where X_R and X_I are the real and imaginary components of the retrieved ring transmittance in the presence of noise, respectively ($X = X_R + iX_I$). The phase shift introduced in the coherent carrier wave is denoted ϕ_c ,

$$\phi_c = \arctan\left(\frac{X_I}{X_R}\right) \quad (\text{A.25})$$

Uncertainty inherent in the noisy measurement $X(r)$ of the true ring transmittance $T(r)$ sets limits on the confidence with which one can report the optical depth $\tau(r)$. Marouf *et al.* [1986] defined confidence intervals for τ in terms of a threshold optical depth τ_{th} ,

$$\tau_{\text{th}} = -\mu_o \ln(CP_N/2) \quad (\text{A.26})$$

where P_N is the post-reconstruction noise power, and C is a random variable that

has χ^2 statistics and two degrees of freedom. For the Kaiser-Bessel window discussed in Section A.1.3, the post-reconstruction noise power is given by,

$$P_N = 0.32\hat{P}_N \frac{W}{W_{max}} = 0.32\hat{P}_N \frac{\Delta r_o}{\Delta R_W} \quad (\text{A.27})$$

which depends on the total noise power \hat{P}_N at a fixed sampling rate,

$$\hat{P}_N = \frac{1}{\text{SNR}_o} \frac{\dot{r}_o}{\Delta r_o} \quad (\text{A.28})$$

SNR_o is the free-space signal-to-noise ratio of the observation, integrated over a one-second interval, and \dot{r}_o is the time rate-of-change of the ring plane intercept, also known as the ring piercing point (RPP).

The confidence region is defined by *Marouf et al.* [1986] as a circle of radius $\sqrt{CP_N/2}$ in the complex transmittance plane, centered on the true complex ring transmittance $T = T_R + iT_I$,

$$(X_R - T_R)^2 + (X_I - T_I)^2 = CP_N/2 \quad (\text{A.29})$$

The probability $P(\chi^2 < C)$ that the noisy recovered complex ring transmittance X is within the confidence region defines the confidence interval of τ , expressed in terms of upper and lower bounding values. *Marouf et al.* [1986] report that for 50%, 70%, and 90% confidence, $C = 1.39, 2.41$, and 4.61 , respectively. In general, the confidence interval of τ is given by [*Marouf et al.*, 1986],

$$\tau_L = \tau_{th} - 2\mu_o \ln [e^{-(\tau - \tau_{th})/(2\mu_o)} + 1] \quad 0 \leq \tau \leq \infty \quad (\text{A.30})$$

$$\tau_U = \begin{cases} \tau_{th} - 2\mu_o \ln [e^{-(\tau - \tau_{th})/(2\mu_o)} - 1] & 0 \leq \tau \leq \tau_{th} \\ \infty & \tau \geq \tau_{th} \end{cases} \quad (\text{A.31})$$

where τ_L and τ_U are the lower and upper confidence bounds on τ . Note that the threshold optical depth τ_{th} discussed in this section and defined in eq. (A.26) is different from the τ_{th} discussed in Section 6.4.2.

A.2 Particle Size Distributions

Radio occultation techniques provide estimates of the number density of ring particles of a given physical size contained in a ring system under study using two distinct methods. First, large particles—particles ranging from a radius a_{\min} that is roughly the size of the spacecraft antenna (Cassini’s high gain parabolic antenna has a diameter of four meters), and up to radius a_{\max} that is limited by the spectral resolution and corresponding SNR of the experiment—are sensed by analyzing the aggregate forward scattering lobe of the received signal. Second, particles ranging in diameter from decimeters down to the order of the shortest wavelength used in the experiment are sensed by a comparison of the optical depth of the rings at two (or more) frequencies [Marouf *et al.*, 1982, 1983; Zebker *et al.*, 1985].

Generally, the number density $n(a)$ of particles in the rings are modeled as a power-law distribution of the particle radius a ,

$$n(a) = \left(\frac{a_o}{a}\right)^q n(a_o) \quad (\text{A.32})$$

The parameter a_o is chosen for convenience in fitting eq. (A.32) to the data, and the power law index q controls the exponential rate at which the number density of particles decreases as a function of their radius. The term $n(a)$ is also referred to as the particle size distribution. The general definition of $n(a)$ is,

$$n(a) = \frac{dN(a)}{da} \quad \text{particles/m}^2 \text{ per meter} \quad (\text{A.33})$$

where $N(a)$ is the cumulative distribution of all particles of radius $\leq a$ present in a column of unit cross-sectional area perpendicular to the ring plane. The product $n(a)da$ is the number of particles of radii between a and $a + da$ existing in that same column.

We now discuss both methods used to obtain particle size distributions: Analysis of the near-forward scattered signal (suprameter-sized particles), and analysis of the differential optical depth (submeter-sized particles).

A.2.1 Suprameter-Sized Particles

The incoherent component of the received radio occultation signal contains information about the size of the particles that forward-scatter the transmitted signal to the receiver. Following *Marouf* [1975], *Marouf et al.* [1982], and *Marouf et al.* [1983], the power spectral density of the scattered signal of a given angular frequency ω , and at a given time t , can be expressed as,

$$S(\omega, t) = \int_{spot} \sigma_d(\beta, \vec{r}) \frac{G^2(\beta, t)}{|\vec{R}_c - \vec{r}|^2} \delta(\omega - \Omega(\vec{r})) d\vec{r} \quad (\text{A.34})$$

where $\sigma_d(\beta, \vec{r})$ is the differential scattering cross section of the rings per unit surface area, β is the scattering angle relative to the Earth-spacecraft line of sight, G is the spacecraft's antenna gain pattern, and $\delta(\omega - \Omega(\vec{r}))$ is a delta function defining the locus of points scattering at a particular frequency $\omega = \Omega(\vec{r})$. Eq. (A.34) is formulated for an uplink geometry, although the equation holds for a downlink configuration as well due to reciprocity. The integration in eq. (A.34) is performed over the antenna beam pattern, as it is projected on the rings.

If the contours of constant Doppler Ω are aligned with ringlet contours (be they elliptical or circular), then the power scattered by a particular ringlet is given by,

$$P_s(t) \triangleq \int_{\omega_1(t)}^{\omega_2(t)} S(\omega, t) \quad (\text{A.35})$$

$$= \int_{ringlet} \sigma_d(\beta) \frac{G^2(\beta, t)}{|\vec{R}_c - \vec{r}|^2} \delta(\omega - \Omega(\vec{r})) d\vec{r} + \epsilon \quad (\text{A.36})$$

where the error term ϵ is introduced primarily by misalignments between ringlet features and the Doppler contours. The two frequencies $\omega_1(t)$ and $\omega_2(t)$ correspond to the frequencies at the inner and outer edge of a ringlet feature. Eq. (A.36) can be solved [*Marouf et al.*, 1983; *Zebker et al.*, 1983] to obtain the scattering cross section $\sigma_d(\beta)$, given the received signal time sequence and its corresponding geometry.

The shape of the scattering cross section $\sigma_d(\beta)$ is a composite result of scattering from the entire ensemble of particles that interact with the EM wave as it propagates

through the rings. Factors such as the thickness of the rings, and the density and size distribution of particles within the rings influence the number of particles (in a statistical sense) that the EM wave interacts with, thus influencing the shape of $\sigma_d(\beta)$. Multiple scattering events within the rings leads to a convolutional broadening of the scattering lobe of $\sigma_d(\beta)$.

The Hankel transform of the single-scattering cross section of the rings, $\tilde{\sigma}_{d1}(\rho)$, is related to the Hankel transform of the differential scattering cross section $\tilde{\sigma}_d(\rho)$. For the case of a many particles thick (MPT) model of the rings, the equation relating the two is [Marouf *et al.*, 1983],

$$\tilde{\sigma}_{d1}(\rho) = \mu_o e^{-\tau_q} \ln(1 + \mu_o^{-1} \tilde{\sigma}_d(\rho) e^{\tau_q}) \quad (\text{A.37})$$

Zebker *et al.* [1985] derived a similar expression, corresponding to a ring model composed of a finite number T_r of thin layers (FNL). The layers are defined such that each particle in a given layer acts independently of any other particles in that layer,

$$\tilde{\sigma}_{d1}(\rho) = \mu_o e^{-\tau_q/T_r} \left([1 + \mu_o^{-1} \tilde{\sigma}_d(\rho) e^{\tau_q}]^{1/T_r} - 1 \right) \quad (\text{A.38})$$

The action of eqs. (A.37) and (A.38) may be interpreted as a nonlinear filtering operation in the Hankel transform domain, effectively compensating for the lobe broadening introduced by multiple scattering and observed in $\tilde{\sigma}_d(\rho)$, thus recovering the single scattering term $\tilde{\sigma}_{d1}(\rho)$.

Marouf *et al.* [1983] showed that the equivalent single-scattering cross section $\sigma_{d1}(\beta)$ derives from,

$$e^{\tau_q} \sigma_{d1}(\beta) = \frac{k^2}{4} \int_{a_{\min}}^{a_{\max}} a^4 \left[\frac{2J_1(ka\beta)}{ka\beta} \right]^2 n(a) da \quad (\text{A.39})$$

where a is the particle radius, $k = \frac{2\pi}{\lambda}$ is the propagation constant of the transmitted EM wave of wavelength λ , and J_1 is the first-order Bessel function of the first kind. The integration limits $a_{\min} \leq a \leq a_{\max}$ define the range of particle sizes that can be sensed by processing the incoherent, forward-scattered signal. These limits are controlled by the SNR of the received signal, and the size of the spacecraft antenna

constrains a_{\min} as discussed above. *Marouf et al.* [1983] also show that the product $e^{\tau_q} \tilde{\sigma}_{d1}(\rho)$ can be related directly to particle size distribution models of ring systems,

$$e^{\tau_q} \tilde{\sigma}_{d1}(\rho) = \pi \int_{a_{\min}}^{a_{\max}} a^2 C\left(\frac{\lambda \rho}{a}\right) n(a) da \quad (\text{A.40})$$

where the function $C(z) = (2/\pi)[\cos^{-1}(z) - z(1 - z^2)^{1/2}]$ for $0 \leq z \leq 1$; $C(z) = 0$ elsewhere, arises from taking the Hankel transform of eq. (A.39) since,

$$\mathcal{H} \left\{ \left[\frac{2J_1(ka\beta)}{ka\beta} \right]^2 \right\} = \frac{4\pi}{(ka)^2} C\left(\frac{\lambda \rho}{a}\right) \quad (\text{A.41})$$

The script letter \mathcal{H} denotes the Hankel transform operation. Combining eq. (A.40) with eqs. (A.37) and (A.38) yields two equations, corresponding to the MPT model of the rings,

$$\mu_o \ln(1 + \mu_o^{-1} \tilde{\sigma}_d(\rho) e^{\tau_q}) = \pi \int_{a_{\min}}^{a_{\max}} a^2 C\left(\frac{\lambda \rho}{a}\right) n(a) da \quad (\text{A.42})$$

and to the FNL model of the rings,

$$\mu_o T_r e^{-\tau_q/T_r} \left([1 + \mu_o^{-1} \tilde{\sigma}_d(\rho) e^{\tau_q}]^{1/T_r} - 1 \right) = \pi \int_{a_{\min}}^{a_{\max}} a^2 C\left(\frac{\lambda \rho}{a}\right) n(a) da \quad (\text{A.43})$$

The left-hand side of eqs. (A.42) and (A.43) are completely determined from the data and the choice of ring thickness model (MPT or FNL). The right-hand side of eqs. (A.42) and (A.43) are essentially determined by the number density $n(a)$, which may be recovered by inverting the integral equations above numerically. Alternatively, the parameters a_o and q in the power-law model of $n(a)$, eq.(A.32), are adjusted in an iterative process until the left-hand side of eqs. (A.42) and/or (A.43) matches the right-hand side, thus fitting a power-law model of the particle size distribution in the rings to the measured data.

A.2.2 Submeter-Sized Particles

The optical depth of the rings, as measured at a given wavelength, is related to the particle size distribution $n(a)$ and the extinction efficiency $Q_{ext}(a, \lambda)$ of the rings,

$$\tau(\lambda) = \int_0^\infty \pi a^2 Q_{ext}(a, \lambda) n(a) da \quad (\text{A.44})$$

for the MPT ring model [Marouf *et al.*, 1982, 1983], and,

$$\tau(\lambda) = 2\mu_o N \left[\int_0^\infty \frac{\pi a^2}{2\mu_o N} Q_{ext}(a, \lambda) n(a) da - 1 \right] \quad (\text{A.45})$$

for the FNL model of the rings [Zebker *et al.*, 1985]. For the purpose of calculation, it is common (*e.g.*, Marouf *et al.* [1983]) to model the ring particles as dielectric spheres with an index of refraction $\tilde{m} = m' - im''$, and to compute Q_{ext} using Mie theory (a brief introduction to Mie theory is presented in Chapter 3). The extinction efficiency varies with $\frac{a}{\lambda}$ from $Q_{ext}(\frac{a}{\lambda} \ll 1) \ll 1$ to $Q_{ext}(\frac{a}{\lambda} \gg 1) \approx 2$ (the so-called extinction paradox). For Voyager at Saturn, the parameter a_{\min} was assumed to fall well within the Rayleigh range of the shortest radio wavelength.

If we have optical depth measurements at two or more frequencies, then we can take advantage of the dependence of Q_{ext} on $\frac{a}{\lambda}$ to obtain an estimate of the populations of different particle sizes. Taking the difference,

$$\Delta\tau_{12} = \tau(\lambda_1) - \tau(\lambda_2) \quad (\text{A.46})$$

For a measured $\Delta\tau$, an assumed a_{\min} well within the Rayleigh range, and given values of a_{\max} and q , one may re-arrange eq. (A.46) to solve for $n(a_o)$. Furthermore, computing $\frac{\Delta\tau}{\tau(\lambda_1)}$ from the measured data yields q for a given a_{\max} [Marouf *et al.*, 1983]. In principle, the differential phase,

$$\Delta\phi_{12} = \phi(\lambda_1) - \left(\frac{\lambda_2}{\lambda_1} \right) \phi(\lambda_2) \quad (\text{A.47})$$

can be used as an additional means to estimate the number density. Generally, $\Delta\phi$ is positive for $a \lesssim \lambda$; $\Delta\phi \rightarrow 0$ for $a \ll \lambda$; and $\Delta\phi < 0$ suggests the presence of charged

particles [Gresh *et al.*, 1989; Gresh, 1990].

For an assumed power law distribution, differential measurements of optical depth place a lower bound on q , an upper bound a_{\min} , and constraints on the relationship between q and a_{\min} between these bounds. Measures of differential optical depth produced from Cassini data at three frequencies (S-, X-, and Ka-bands) were used to make the image shown in Figure 2.3, which is color-coded to show the range of particle sizes populating the rings.

A.2.3 Surface Mass Density and Ring Thickness

The local surface mass density of the rings can be estimated by measuring the wavelength λ_w of spiral bending waves and density waves present in the ring system. Bending and density waves are introduced in Section 2.1.2.

In the asymptotic far-field of a bending wave—*i.e.*, far enough from the resonance location for the wavelength of the disturbance to be relatively constant—the inviscid (undamped) linear theory gives the following [de Pater and Lissauer, 2001; Shu, 1984],

$$\lambda_w = \frac{4\pi^2 G \sigma_\rho}{m_\theta^2 [\omega_f - n(r)] - \mu^2(r)} \quad (\text{A.48})$$

For density waves, we have a similar expression,

$$\lambda_w = \frac{4\pi^2 G \sigma_\rho}{m_\theta^2 [\omega_f - n(r)] - \kappa^2(r)} \quad (\text{A.49})$$

where $G = 6.67428 \times 10^{-11} \text{ m}^3\text{kg}^{-1}\text{s}^{-2}$ is the universal gravitational constant, σ_ρ is the surface mass density of the rings, ω_f is the forcing frequency of the wave, m_θ is the azimuthal symmetry number, $\mu(r)$ is the natural vertical oscillation frequency of a ring particle, $\kappa(r)$ is the natural epicyclic (radial) oscillation frequency of a ring particle, and $n(r)$ is the orbital angular frequency of a local ring particle. The quantity $\mu(r)$ ($\kappa(r)$) is the frequency at which the Saturnian moon responsible for the local resonance is tugging ring particles in a direction perpendicular to (radially within) the ring plane, to excite the bending (density) wave. In reality, these waves are damped,

since collisions between particles remove energy from the wave. The damping rate can be used to estimate the thickness of the rings [*de Pater and Lissauer*, 2001].

If we have measurements of λ_w and we know which moon is responsible for the wave, then eqs. (A.48) and (A.49) can be rearranged and solved to yield estimates of σ_ρ (*e.g.*, *Gresh et al.* [1986]; *Rosen* [1989]; *Rosen et al.* [1991a, b]). Surface mass density estimates can also be obtained from the number density estimates described in Section A.2, subject to estimates or assumptions of the bulk density of the ring particles [*Marouf et al.*, 1983; *Zebker et al.*, 1985; *Rosen*, 1989].

A.3 Summary

Radio occultation can provide rich information about the structure and physical properties of planetary rings. The information includes:

1. Reconstructed ring optical depth profiles. Theoretically, the diffraction-corrected profiles can approach resolutions of approximately a few hundred meters for Saturn's rings, and few tens of meters for Uranus' rings.
2. Identification of bending and density waves in the rings, and of their associated forcing resonances.
3. Characterization of time-evolution and azimuthal asymmetry effects by processing data from multiple occultations.
4. Supra-meter particle size distribution estimates derived from processing the scattered signal.
5. Sub-meter particle size distribution estimates derived from differential optical depth measurements.
6. Surface mass densities estimated from waves, and from number density (particle size distribution) estimates.
7. Statistical characterization of fine-scale (length scales of tens to hundreds of meters) microstructure, such a gravitational wakes and periodic microstructure, by analysis of diffracted signals.

\hbar

Appendix B

Cassini 2005 Radio Occultation Timelines

In this appendix we present the predicted timeline of the Cassini REV 7, 8, 10, and 12 experiments [Marouf, 2006–2010]. We also show plots of the local elevation angle of Cassini at the Goldstone (G), Canberra (C), and Madrid (M) DSN complexes during REVs 7, 8, 10, and 12. In the plots, the term BOT stands for beginning of track, which is the time that a DSN complex begins to track Cassini. Similarly, EOT stands for end of track. The radio occultation observation time is shown in light blue at the top of the elevation angle plots, for reference.

Rev 7 Cassini Radio Science Occultation: Event Times on DOY 122/123
 Essam Marouf & Richard French 4/28/05

	SCET UTC	ERT UTC OWLT =	Pacific Time GMT-7hrs	Comments
Start LMB: Enable Monopulse	1:15:00	2:33:03	19:33:03	TWNC OFF (1-Way) Throughout
Disable Monopulse	2:24:57	3:43:00	20:43:00	Blind pointing is initialized by Monopulse
Start Baseline	2:26:34	3:44:37	20:44:37	Free-space: ~51, 39, 41 dB-Hz @ X, S, and Ka
Ring F	2:55:25	4:13:28	21:13:28	Narrow isolated ring: not much effect expected
Ring A in	3:00:43	4:18:46	21:18:46	Sudden drop in signal level
Enke Gap	3:05:12	4:23:15	21:23:15	Brief recovery of strong signal level
Ring A out	3:21:03	4:39:06	21:39:06	Strong signal expected in the Cassini Div
Ring B in	3:27:09	4:45:12	21:45:12	Signal level drops substantially
Ring B out	4:00:38	5:18:41	22:18:41	Signal level throughout Ring B is unknown!
Ring C out	4:23:13	5:41:16	22:41:16	High signal level but with fast fluctuations
Enable Monopulse	4:25:27	5:43:30	22:43:30	Monopulse offset used to reinitialize blind
Disable Monopulse	4:26:17	5:44:20	22:44:20	blind pointing
Ionosphere in	4:28:40	5:46:43	22:46:43	Multipath? (more than one spectral line?)
Troposphere in	4:38:59	5:57:02	22:57:02	Signal level drops systematically and fast
End of Ingress	5:14:34	6:32:37	23:32:37	Signal absorbed in Saturn's atmosphere
Behind Saturn				
Start of Egress	6:33:34	7:51:37	0:51:37	Signal level builds up systematically
Troposphere out	7:03:50	8:21:53	1:21:53	Pointing error may affect free-space signal level
Ring C in	7:15:23	8:33:26	1:33:26	Strong, dynamically changing signal level
Ionosphere out	7:16:18	8:34:21	1:34:21	Multipath? (more than one spectral line?)
Enable Monopulse	7:16:27	8:34:30	1:34:30	Monopulse offset used to reinitialize blind
Disable Monopulse	7:17:07	8:35:10	1:35:10	blind pointing
Ring B in	7:37:32	8:55:35	1:55:35	Signal level drops substantially
Ring B out	8:09:38	9:27:41	2:27:41	Signal level unknown (small) throughout Ring B
Ring A in	8:15:22	9:33:26	2:33:26	Signal level comes back up in the Cassini Division
Enke Gap	8:30:00	9:48:03	2:48:03	Clear dynamic signal throughout most of Ring A
Ring A out	8:34:04	9:52:09	2:52:09	Sudden transition to free-space signal level
Ring F	8:38:52	9:56:55	2:56:55	Rings F is only detectable in postprocessing
End of Baseline	9:09:34	10:27:37	3:27:37	Pointing error may affect free-space signal level
Enable Monopulse	9:11:00	10:29:03	3:29:03	To assess blind pointing error during rings egress
End LMB	10:39:00	11:57:03	4:57:03	End of the radio occultation experiment

Note: Some Ring Edges are known to be noncircular, which will affect event times above

Figure B.1: Predicted Cassini REV 7 Radio Occultation Events Timeline. Figure courtesy Essam Marouf (SJSU) and Aseel Anabtawi (JPL).

Rev 8 Cassini Radio Science Occultation: Event Times on DOY 2005-141
Essam Marouf 5/19/05
DRAFT

	SCET UTC	ERT UTC OWLT = 1:20:16	Pacific Time GMT-7hrs 7:00:00	Comments
Start LMB	2:59:44	4:20:00	21:20:00	Earth poined, but no DSN stations are tracking
DSS-34: Begin-of-Track	5:34:44	6:55:00	-0:05:00	No downlink until 08:11:14
DSS-34: Enable Monopulse	6:50:58	8:11:14	1:11:14	Cassini HGA is Earth pointed at this time
Start Baseline	6:50:58	8:11:14	1:11:14	Free-space: ~51, 39, 41 dB-Hz @ X, S, and Ka
Ring F	7:20:19	8:40:35	1:40:35	Narrow isolated ring: not much effect expected
Ring A in	7:25:41	8:45:57	1:45:57	Sudden drop in signal level
Enke Gap	7:30:11	8:50:27	1:50:27	Brief recovery of strong signal level
Ring A out	7:46:07	9:06:23	2:06:23	Strong signal expected in the Cassini Div
DSS-34: Disable Monopulse	7:52:00	9:12:16	2:12:16	Monopulse offset used to initialize blind pointing
Ring B in	7:52:15	9:12:31	2:12:31	Signal level drops substantially
DSS-55: Begin-of-Track	7:54:44	9:15:00	2:15:00	In Ring B: on blind pointing till exit from Ring B
Ring B out	8:25:49	9:46:05	2:46:05	Signal level in Ring B is small
DSS-34: Enable Monopulse	8:26:00	9:46:16	2:46:16	Monopulse enabled ~10 sec afterexit from Ring B
DSS-55: Enable Monopulse	8:26:00	9:46:16	2:46:16	Monopulse enabled ~10 sec afterexit from Ring B
Ring C out	8:48:22	10:08:38	3:08:38	High signal level but with fast fluctuations
DSS-34: End-of-Track	8:49:44	10:10:00	3:10:00	Canberra sets during the occultation period
DSS-55: Disable Monopulse	8:52:30	10:12:46	3:12:46	Monopulse offset used to initialize blind pointing
Ionosphere in	8:54:30	10:14:46	3:14:46	Strong signal level
Troposphere in	9:06:00	10:26:16	3:26:16	Signal level drops systematically and fast
End of Ingress	9:32:58	10:53:14	3:53:14	Signal absorbed in Saturn's atmosphere
Behind Saturn				
Start of Egress	11:00:58	12:21:14	5:21:14	Signal level builds up systematically
Troposphere out	11:33:00	12:53:16	5:53:16	Pointing error may affect free-space signal level
Ionosphere out	11:44:49	13:05:05	6:05:05	Strong signal level
DSS-55: Enable Monopulse	11:43:30	13:03:46	6:03:46	Monopulse enabled ~1 m before Ring C
Ring C in	11:44:32	13:04:48	6:04:48	Strong, dynamically changing signal level
DSS-55: Disable Monopulse	12:06:29	13:26:45	6:26:45	Monopulse offset used to initialize blind pointing
Ring B in	12:06:39	13:26:55	6:26:55	Signal level drops substantially
Ring B out	12:38:50	13:59:06	6:59:06	Signal level is small in Ring B
DSS-55: Enable Monopulse	12:39:00	13:59:16	6:59:16	Monopulse enabled ~10 sec afterexit from Ring B
Ring A in	12:45:35	14:05:51	7:05:51	Signal level comes back up in the Cassini Division
Enke Gap	12:59:17	14:19:33	7:19:33	Clear dynamic signal throughout most of Ring A
Ring A out	13:03:22	14:23:38	7:23:38	Sudden transition to free-space signal level
Ring F	13:08:12	14:28:28	7:28:28	Rings F is only detectable in postprocessing
End of Baseline	13:38:58	14:59:14	7:59:14	Strong signal level
End LMB	14:47:44	16:08:00	9:08:00	End of the rev. 8 radio occultation experiment

Note: Some Ring Edges are known to be noncircular, which will affect event times above

Figure B.2: Predicted Cassini REV 8 Radio Occultation Events Timeline. Figure courtesy Essam Marouf (SJSU) and Aseel Anabtawi (JPL).

APPENDIX B. 2005 OBSERVATIONS

Rev 10 Cassini Radio Science Occultation: Event Times on DOY 177-178, 2005
Essam Marouf 5/23/05

	SCET UTC	ERT UTC OWLT = 1:23:17	Pacific Time GMT-7hrs 7:00:00	Comments
DSS-26: Begin-of-Track	15:56:43	17:20:00	10:20:00	Cassini HGA is not Earth pointed
DSS-25: Begin-of-Track	16:11:43	17:35:00	10:35:00	Cassini HGA is not Earth pointed
Start LMB	16:29:00	17:52:17	10:52:17	Cassini HGA Earth pointing starts
DSS-25: Enable Monopulse?	16:29:43	17:53:00	10:53:00	Enable monopulse ASAP after BOT
DSS-26: Enable Monopulse	16:29:43	17:53:00	10:53:00	Enable monopulse ASAP after BOT
Start Baseline	16:52:30	18:15:47	11:15:47	Start of the RSS occultation experiment
Ring F	17:19:58	18:43:15	11:43:15	Rings F is only detectable in postprocessing
Ring A in	17:25:24	18:48:41	11:48:41	Sudden drop in signal level
Enke Gap	17:29:58	18:53:15	11:53:15	Brief recovery of strong signal level
Ring A out	17:46:07	19:09:24	12:09:24	Strong signal expected in the Cassini Div
DSS-25: Disable Monopulse?	17:51:50	19:15:07	12:15:07	Monopulse offset used to reinitialize blind pntng
DSS-26: Disable Monopulse	17:51:50	19:15:07	12:15:07	Monopulse offset used to reinitialize blind pntng
Ring B in	17:52:20	19:15:37	12:15:37	Signal level drops substantially
Ring B out	18:26:17	19:49:34	12:49:34	Signal level throughput Ring B is small
DSS-25: Enable Monopulse?	18:26:47	19:50:04	12:50:04	Monopulse enabled ~ 30 s after exit from Ring B
DSS-26: Enable Monopulse	18:26:47	19:50:04	12:50:04	Monopulse enabled ~ 30 s after exit from Ring B
Ring C out	18:49:00	20:12:17	13:12:17	High signal level but with fast fluctuations
DSS-25: Disable Monopulse?	18:56:00	20:19:17	13:19:17	Monopulse offset used to reinitialize blind pntng
DSS-26: Disable Monopulse	18:56:00	20:19:17	13:19:17	Monopulse offset used to reinitialize blind pntng
Ionosphere in	18:57:58	20:21:15	13:21:15	Strong signal level
Troposphere in	19:07:28	20:30:45	13:30:45	Signal level drops systematically
Ka-Band signal loss	19:13:28	20:36:45	13:36:45	Likely disappearance of the Ka-band signal
X-band signal loss	19:14:58	20:38:15	13:38:15	Likely disappearance of the X-band signal
S-band signal loss	19:16:08	20:39:25	13:39:25	Likely disappearance of the S-band signal
End of Ingress	19:37:30	21:00:47	14:00:47	End of Saturn ingress occultation
Behind Saturn				

Figure B.3: Predicted Cassini REV 10 Ingress Radio Occultation Events Timeline. Figure courtesy Essam Marouf (SJSU) and Aseel Anabtawi (JPL).

Behind Saturn					
Start of Egress	21:09:30	22:32:47	15:32:47	Start of Saturn egress occultation	
Expected weak S-Band signal	21:31:50	22:55:07	15:55:07	S-Band starts to build up systematically	
Expected weak X-band signal	21:33:00	22:56:17	15:56:17	X-Band level starts to build up systematically	
Expected weak Ka-band signal	21:34:29	22:57:46	15:57:46	Ka-Band level starts to build up systematically	
Troposphere out	21:40:29	23:03:46	16:03:46	Blind pointing error may affect signal level	
Ionosphere out	21:49:49	23:13:06	16:13:06	Strong signal level	
DSS-25: Enable Monopulse?	21:51:00	23:14:17	16:14:17	Monopulse enabled ~3 m before Ring C	
DSS-26: Enable Monopulse	21:51:00	23:14:17	16:14:17	Monopulse enabled ~3 m before Ring C	
Ring C in	21:53:43	23:17:00	16:17:00	Strong dynamically changing signal level	
DSS-25: Disable Monopulse?	22:15:29	23:38:46	16:38:46	Monopulse offset used to reinitialize blind	
DSS-26: Disable Monopulse	22:15:29	23:38:46	16:38:46	Monopulse offset used to reinitialize blind	
Ring B in	22:15:59	23:39:16	16:39:16	Signal level drops substantially	
Ring B out	22:48:34	0:11:51	17:11:51	Signal level is small in Ring B	
DSS-25: Enable Monopulse?	22:49:04	0:12:21	17:12:21	Monopulse enabled ~30 s after exit from Ring B	
DSS-26: Enable Monopulse	22:49:04	0:12:21	17:12:21	Monopulse enabled ~30 s after exit from Ring B	
Ring A in	22:54:24	0:17:41	17:17:41	Signal level comes back up in the Cassini Division	
Enke Gap	23:09:20	0:32:37	17:32:37	Clear dynamic signal throughout most of Ring A	
Ring A out	23:13:29	0:36:46	17:36:46	Sudden transition to free-space signal level	
Ring F	23:18:23	0:41:40	17:41:40	Rings F is only detectable in postprocessing	
End of Baseline	23:51:00	1:14:17	18:14:17	End of the rev 10 radio occultation experiment	
End LMB	0:20:06	1:43:23	18:43:23	End of Earth pointing period	
DSS-25: End-of-Track	0:31:43	1:55:00	18:55:00		
DSS-26: End-of-Track	0:46:43	2:10:00	19:10:00		

Note: Some Ring Edges are known to be noncircular, which will affect event times above

Figure B.4: Predicted Cassini REV 10 Egress Radio Occultation Events Timeline. Figure courtesy Essam Marouf (SJSU) and Aseel Anabtawi (JPL).

Rev 12 Cassini Radio Science Occultation: Event Times on DOY 214, 2005
Essam Marouf 7/29/05

	SCET UTC	ERT UTC OWLT =	Pacific Time GMT-7hrs	Comments
DSS-55: Begin-of-Track	6:36:05	8:00:00	1:00:00	Cassini HGA is not Earth pointed
Start LMB	6:57:00	8:20:55	1:20:55	Cassini HGA Earth pointing starts
DSS-55: Enable Monopulse	6:57:00	8:20:55	1:20:55	Enable monopulse ASAP after BOT
Start Baseline	7:31:16	8:55:11	1:55:11	Start of the RSS occultation experiment
Ring F	7:53:40	9:17:35	2:17:35	Ring F is only detectable in postprocessing
Ring A in	7:59:12	9:23:07	2:23:07	Sudden drop in signal level
Enke Gap	8:03:51	9:27:46	2:27:46	Brief recovery of strong signal level
Ring A out	8:20:19	9:44:14	2:44:14	Strong signal expected in the Cassini Div
DSS-55: Disable Monopulse	8:26:09	9:50:04	2:50:04	Monopulse offset used to reinitialize blind pntng
Ring B in	8:26:39	9:50:34	2:50:34	Signal level drops substantially
Ring B out	9:01:24	10:25:19	3:25:19	Signal level throughout Ring B is small
DSS-55: Enable Monopulse	9:01:54	10:25:49	3:48:36	Monopulse enabled ~ 30 s after exit from Ring B
Ring C out	9:24:41	10:48:36	3:48:36	High signal level but with fast fluctuations
DSS-55: Disable Monopulse	9:27:05	10:51:00	3:51:00	Monopulse offset used to reinitialize blind pntng
Ionosphere in	9:27:30	10:51:25	3:51:25	inapcat parameter ~ 68,000 km
Troposphere in	9:37:58	11:01:53	4:01:53	Signal level drops systematically
loss of Ka-Band signal	9:43:46	11:07:41	4:07:41	Likely disappearance of the Ka-band signal
loss of X-band signal	9:44:46	11:08:41	4:08:41	Likely disappearance of the X-band signal
loss of S-band signal	9:45:56	11:09:51	4:09:51	Likely disappearance of the S-band signal
End of Ingress	10:08:16	11:32:11	4:32:11	End of Saturn ingress occultation
Behind Saturn				

Figure B.5: Predicted Cassini REV 12 Ingress Radio Occultation Events Timeline. Figure courtesy Essam Marouf (SJSU) and Aseel Anabtawi (JPL).

Behind Saturn				
Start of Egress	11:38:16	13:02:11	6:02:11	Start of Saturn egress occultation
weak S-Band signal	12:07:10	13:31:05	6:31:05	S-Band starts to build up systematically
weak X-band signal	12:08:10	13:32:05	6:32:05	X-Band level starts to build up systematically
weak Ka-band signal	12:09:44	13:33:39	6:33:39	Ka-Band level starts to build up systematically
Troposphere out	12:16:29	13:40:24	6:40:24	Blind pointing error may affect signal level
Ionosphere out	12:26:41	13:50:36	6:50:36	Strong signal level
DSS-55: Enable Monopulse	12:34:12	13:51:00	6:51:00	Impact parameter > 68,000 km
Ring C in	12:34:12	13:58:07	6:58:07	Strong dynamically changing signal level
DSS-55: Disable Monopulse	12:56:34	14:20:29	7:20:29	Monopulse offset used to reinitialize blind
Ring B in	12:57:04	14:20:59	7:20:59	Signal level drops substantially
Ring B out	13:30:30	14:54:25	7:54:25	Signal level is small in Ring B
DSS-55: Enable Monopulse	13:31:00	14:54:55	7:54:55	Monopulse enabled ~ 30 s after exit from Ring B
Ring A in	13:36:28	15:00:23	8:00:23	Signal level comes back up in the Cassini Division
Enke Gap	13:51:46	15:15:41	8:15:41	Clear dynamic signal throughout most of Ring A
Ring A out	13:56:01	15:19:56	8:19:56	Sudden transition to free-space signal level
Ring F	14:01:02	15:24:57	8:24:57	Rings F is only detectable in postprocessing
End of Baseline	14:29:16	15:53:11	8:53:11	End of the rev 10 radio occultation experiment
End LMB	15:07:04	16:30:59	9:30:59	HGA Continues to be Earth pointed
DSS-55: End-of-Track	15:26:05	16:50:00	9:50:00	Gravity Enhancement Observation during DL

Note: Some Ring Edges are known to be noncircular, which will affect event times above
 Enable/Disable monopulse strategy is tentative at this time: may be changed in real-time

Figure B.6: Predicted Cassini REV 12 Egress Radio Occultation Events Timeline. Figure courtesy Essam Marouf (SJSU) and Aseel Anabtawi (JPL).

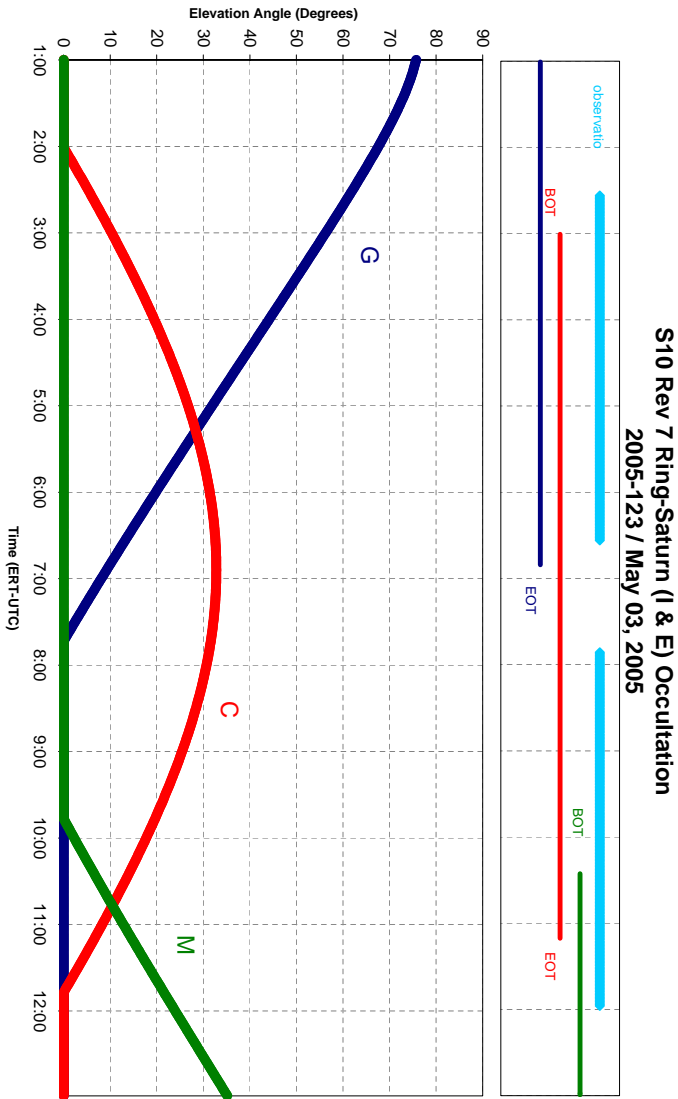


Figure B.7: Cassini REV 7 Local Elevation Angle at DSN Receiving Stations. Figure courtesy Aseel Anabtawi (JPL).

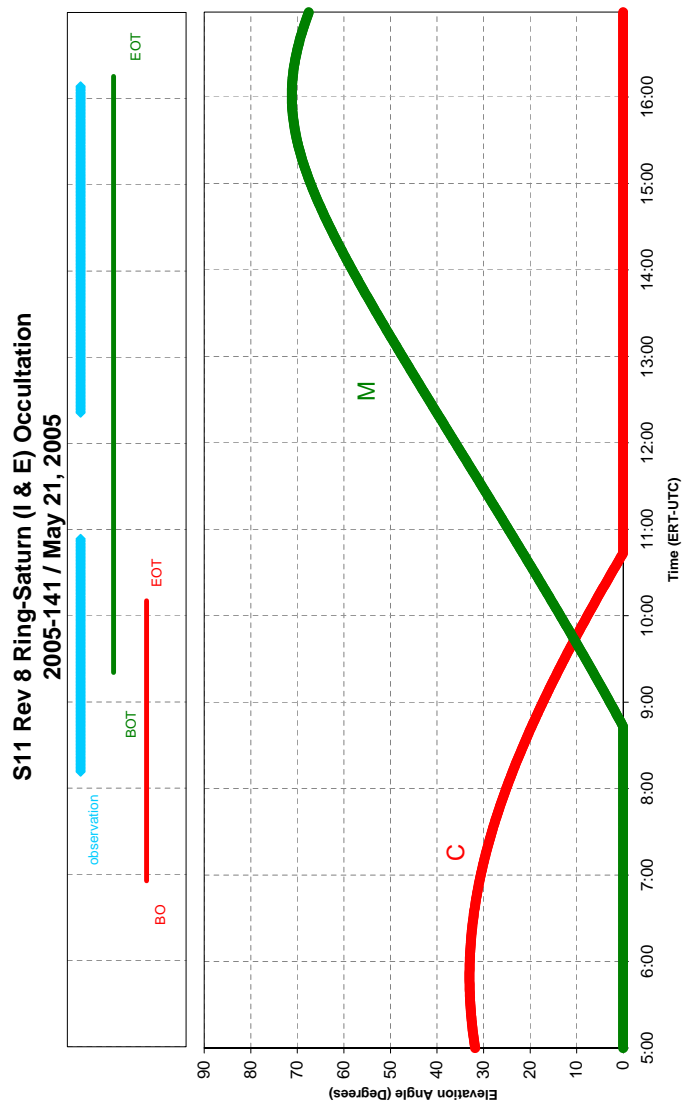


Figure B.8: Cassini REV 8 Local Elevation Angle at DSN Receiving Stations. Figure courtesy Aseel Anabtawi (JPL).

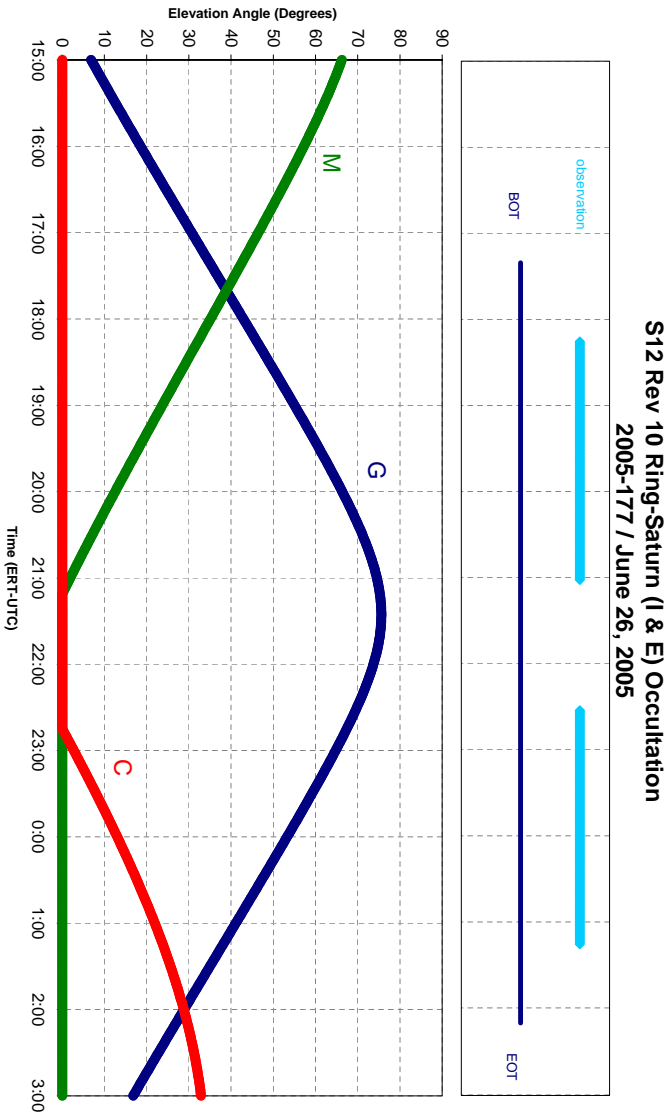


Figure B.9: Cassini REV 10 Local Elevation Angle at DSN Receiving Stations. Figure courtesy Aseel Anabtawi (JPL).

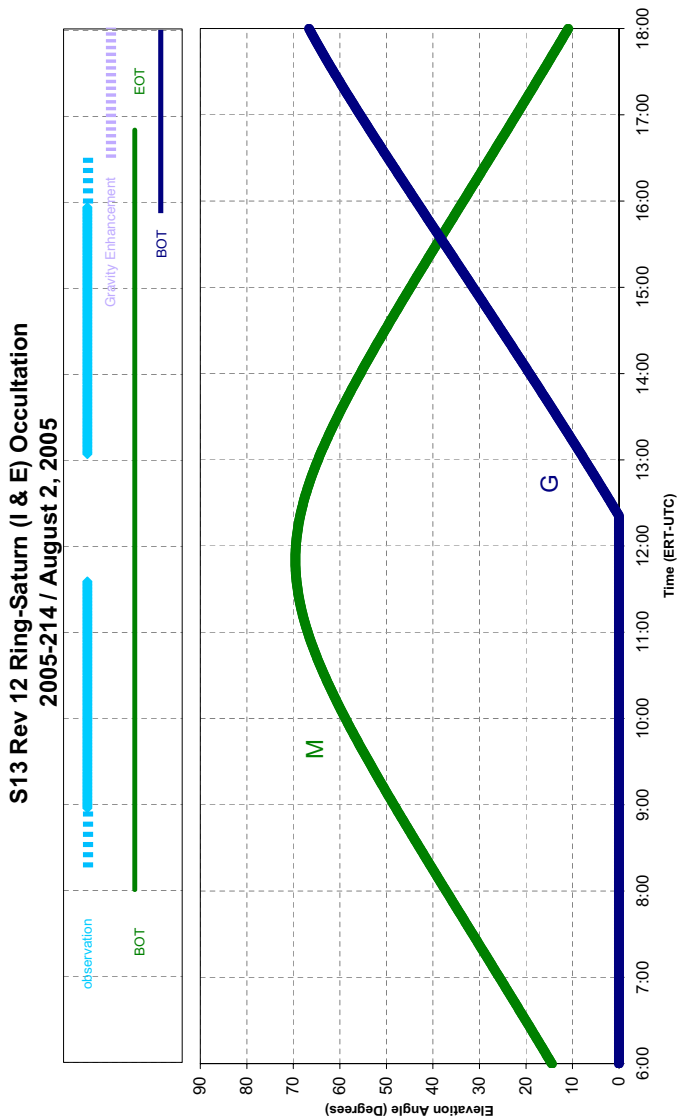


Figure B.10: Cassini REV 12 Local Elevation Angle at DSN Receiving Stations. Figure courtesy Aseel Anabtawi (JPL).

Appendix C

Historically Important Articles on Saturn's Rings

The translated text contained in this appendix is courtesy of Dr. John O'Connor, Mathematical Institute, University of St. Andrews (Scotland). I am very grateful to him for making this material available to me.

C.1 Christiaan Huygens' article on Saturn's Ring

In 1659, Christiaan Huygens published an article on Saturn's Ring in *Systema Saturnium*. The text below is based on a translation from the original latin, completed by J. H. Walden in 1928.

Excerpt from *Systema Saturnium*

When Galileo made use of the telescope, noblest invention of nation of Belgium, for observation of the heavenly bodies, and, before all other men, disclosed to mortals those very celebrated phenomena of the planets, the most wonderful of his discoveries, it would seem, were those relating to the star of Saturn. For all the other phenomena, though justly calling for our wonder and admiration, were still not of a kind to make it necessary to question strongly the causes of their existence. But Saturn's

changing forms showed a new and strange device of nature, the principle of which neither Galileo himself nor, in all the time since, any of the astronomers (with their permission be it said) has succeeded in divining. Galileo had first seen this star shining, not as a single disk, but in what seemed to be a triple form, as two smaller stars in close proximity to, and on opposite sides of, a larger star, in line with its centre. And seeing this form continue for nearly three years with no change, he had become firmly convinced that, just as Jupiter was provided with four satellites, so Saturn was provided with two, which, however, had no motion, and so would always cling to the sides of Saturn in the same position. But when Saturn came forth alone, quite destitute of his former retinue of satellites, Galileo was obliged to change his opinion. Astonished by what he saw, he tried to reach by conjecture the cause of the appearance, and made a few predictions as to the time when the former phase was due to recur. But, it was shown by the event, these predictions were not then fulfilled according to his expectation, nor, it appeared, was Saturn satisfied with having only two aspects. For a succession of other strange and marvellous forms was revealed, which I find first described by Josephus Blancanus and Franciscus Fontana - forms of such unusual appearance that they were considered by many as a mockery of the eyes, shapes adhering to the lenses rather than existing in the heavens; but after the same forms had been seen by more, it became clear that it was no false evidence that revealed them.

And so I was also drawn by an urgent longing to behold these wonders of the heaven. But I had only the ordinary form of telescope, which measured five or six feet in length. I, therefore, set myself to work with all the earnestness and seriousness I could command to learn the art by which glasses are fashioned for these uses, and I did not regret having put my own hand to the task. After overcoming great difficulties (for this art has in reserve more difficulties than it seems to bear on its face), I at last succeeded in making the lenses which have provided me with the material for writing this account. For upon immediately directing my telescope at Saturn, I found that things there had quite a different appearance from that which they had previously been thought by most men to have. For it appeared that the two neighbouring appendages clinging to Saturn were by no means two planets, but rather

something different, while, distinct from these, there was a single planet, at a greater distance from Saturn and revolving around him in sixteen days; and the existence of this planet had been unknown through all the centuries up to that time. Following the wise advice of a distinguished man, one equally conspicuous for his ability and his character, Johannes Capellanus, I three years ago informed astronomers of my new observation. For while I was sojourning at Paris, I told Capellanus, as well as Gassendi and others, of the satellite of Saturn which I had seen, and Capellanus gave me many reasons for believing that I ought not to withhold an announcement that would be so pleasing to all men until I should finish the work on the complete System of Saturn, which I was then engaged upon. And so, on the 5th day of March [later in the article Huygens says it was the twenty-fifth of March, so one of these is a misprint], I in the year 1656, I put forth the result of my observation on the Moon of Saturn (for so I have quite properly named the, new star), and, together with it, an hypothesis containing an explanation of the other phenomena of Saturn; in the case of the latter, however, I confused the order of the letters in which it was written, that it might witness to the fact simply that I was not unacquainted with it at that time, and also that others might be induced in this way to publish the results of their speculations and might not complain that the glory of the discovery had been snatched from them. Afterwards, however, in response to the request of the same distinguished man, I also solved this literary riddle, and set before him in outline the entire hypothesis; whence perhaps my theory about the phases of Saturn has already found its way to the ears of others. But, in any case, the wonderful and unusual creation of nature shown in connection with this planet demands a fuller treatment, and I ought not to expect that either my account of the phenomena or the assumptions I make for explaining them will gain general support unless it is seen that the latter, rest on the principles of reasoning, and the former is backed by the evidence of observation. Therefore, I now propose to fulfil both of these requirements. And, in the first place, I will determine as accurately as possible from my observations the facts which have to do with the motion and the period of revolution of the planet's satellite, and I will construct tables of its motion. Then I will assign the various phases of Saturn himself to their separate causes, that thus we may have a ready means of determining beforehand

what the future phases will be ...

That neither you [Hodierna] nor those distinguished men whose opinions I have previously reviewed have reached the truth of the matter, is not at all to be wondered at or to be imputed to you as a fault, since for the most part false phenomena were reported to you as true, and other phenomena which were observed in connection with Saturn, free from the deception of sight, did not come to your notice at all. If you had been so fortunate as to observe these phenomena with me, it is reasonable to suppose that you would have drawn from them the same conclusions with regard to the real form of the planet that I have. Now I was greatly helped in this matter not only by those more genuine phases, but also by the motion of Saturn's Moon, which I observed from the beginning; indeed it was the revolution of this Moon around Saturn that first caused to dawn upon me the hope of constructing the hypothesis. The nature of this hypothesis I will proceed to explain in what follows.

When, then, I had discovered that the new planet revolved around Saturn in a period of sixteen days, I thought that without any doubt Saturn rotated on his own axis in even less time. For even before this I had always believed that the other primary planets were like our Earth in this respect that each rotated on its own axis, and so the entire surface rejoiced in the light of the Sun, a part at a time; and, more than this, I believe that in general the arrangement with the large bodies of the world was such that those around which smaller bodies revolved, having themselves a central position, had also a shorter period of rotation. Thus the Sun, its spots declare, rotates on its own axis in about twenty-six days; but around the Sun the various planets, among which the Earth is also to be reckoned, complete their courses in times varying as their distances. Again, this Earth rotates in daily course, and around the Earth the Moon circles with monthly motion. Around the planet Jupiter four smaller planets, that is to say Moons, revolve, subject to this same law, under which the velocities increase as the distances diminish. Whence, indeed, we must conclude perhaps that Jupiter rotates in a shorter time than 24 hours, since his nearest Moon requires less than two days. Now having long since learned all these facts, I concluded even then that Saturn must have a similar motion. But it was my observation in regard to his satellite that gave me the information about the velocity

of his motion of rotation. The fact that the satellite completes its orbit in sixteen days leads to the conclusion that Saturn, being in the centre of the satellite's orbit, rotates in much less time. Furthermore, the following conclusion seemed reasonable: that all the celestial matter that lies between Saturn and his satellite is subject to the same motion, in this way that the nearer it is to Saturn, the nearer it approaches Saturn's velocity. Whence, finally, the following resulted: the appendages also, or arms, of Saturn are either joined and attached to the globular body at its middle and go around with it, or, if they are separated by a certain distance, still revolve at a rate not much inferior to that of Saturn.

Furthermore, while I was considering these facts in connection with the motion of the arms, these arms appeared under the aspect which was exhibited at the time of my previous observations of the year 1655. The body of Saturn at its middle was quite round, while the arms extended on either side along the same straight line, as though the planet were pierced through the middle by a kind of axis; although, as indicated in the first figure of all, these arms, as seen through the twelve-foot telescope that I was then using, appeared a little thicker and brighter toward the ends on either side of the planet than they did where they joined the middle of the sphere. When, therefore, the planet continued day after day to present this same aspect, I came to understand that, inasmuch as the circuit of Saturn and the adhering bodies was so short, this could happen under no other condition than that the globe of Saturn were assumed to be surrounded equally on all sides by another body, and that thus a kind of ring encircled it about the middle; for so, with whatever velocity it revolved, it would always present the same aspect to us, if, of course, its axis were perpendicular to the plane of the ring.

And so was established the reason for the phase which continued through that period. Therefore, after that, I began to consider whether the other phases that Saturn was said to have could be accounted for by the same ring. I was not long in coming to a conclusion on this point through noting in frequent observations the obliquity of Saturn's arms to the ecliptic. For when I had discovered that the straight line along which on either side these arms projected did not follow the line of the ecliptic, but cut it at an angle of more than 20 degrees, I concluded that in the same

way the plane of the ring which I had imagined was inclined at about the same angle to the plane of the ecliptic - with a permanent and unchanging inclination, be it understood, as is known to be the case on this Earth of ours with the plane of the equator. From this inclination it necessarily followed that in its different aspects the same ring showed to us at one time a rather broad ellipse, at another time a narrower ellipse, and sometimes even a straight line. As regards the handle-like formations, I understand that this phenomenon was due to the fact that the ring was not attached to the globe of Saturn, but was separated from it the same distance all around. These facts, accordingly, being thus brought into line, and the above-mentioned inclination of the ring being also assumed, all the wonderful appearance of Saturn, I found, could be referred to this source, as will presently be shown. And this is that very hypothesis which, in the year 1656, on the 25th day of March [earlier Huygens says the fifth of March, so one is a misprint], I put forth in confused letters, together with my observation on the Saturnian Moon.

Now the letters were: a a a a a a c c c c c d e e e e e g h i i i i i i I I l l m m n n n n n n n n n n o o o o p p q r r s t t t t t u u u u u, which, being restored to their proper places, signify the following: *Annulo cingitur, tenui, plano, nusquam cohaerente, ad eclipticam inclinato.* ["It is encircled by a ring, thin, plane, nowhere attached, inclined to the ecliptic."] That the width of the space intervening between the ring and the globe of Saturn is equal to the width of the ring itself or even exceeds it, is shown by the figure of Saturn as observed by others. and then more definitely by its figure as seen by myself; that, likewise, the ratio of the greatest diameter of the ring to the diameter of Saturn is about 9 to 4. Thus the true appearance is such as I have indicated in the appended scheme.

I believe that I should digress here to meet the objection of those who will find it exceedingly strange and possibly unreasonable that I should assign to one of the celestial bodies a figure the like of which has up to this time not been found in any one of them, although, on the other hand, it has been believed as certain, and considered as established by natural law, that the spherical form is the only one adapted to them; and that I should place this solid and permanent ring (for such I consider it) about Saturn, without attaching it by any joints or ties, although imagining that

it preserves a uniform distance on every side and revolves in company with Saturn at a very high rate of speed. These men should consider that I do not construct this hypothesis from pure invention and out of my own fancy, as the astronomers do their epicycles, which nowhere appear in the heavens, but that I perceive this ring very plainly with the eyes; with which, obviously, we discern the figures of all other things. And there is, after all, no reason why it should not be possible for some heavenly body to exist having this form, which, if not spherical, is at least round, and is quite as well adapted to the possession of circumcentral motion as the spherical form itself. For it certainly is less surprising that such a body should have assigned to it a shape of this kind than that it should have some absurd and quite unbeautiful shape. Furthermore, since, owing to the great similarity and relationship that exists between Saturn and our Earth, it seems possible to conclude quite conclusively that the former, like the latter, is situated in the middle of its own vortex, and that its centre has a natural tendency to reach toward all that is considered to have weight there, it must also result that the ring in question, pressing with all its parts and with equal force toward the centre, comes by this very fact to a permanent position in such a way that it is equally distant on all sides from that centre. Exactly so some people have imagined that, if it were possible to construct a continuous arch all the way around the Earth, it would sustain itself without any support. Therefore, let them not consider it absurd if a similar thing has happened of itself in the case of Saturn; let them rather regard with awe the power and majesty of Nature, which, by repeatedly bringing to light new specimens of its works, admonishes us that yet more remain.

C.2 Cassini's Paper on his Eponymous Division

In 1730, a paper written by Giovanni Domenico Cassini was posthumously published as *The Discovery of the Division in Saturn's Ring* in Volume X of the *Mémoires de l'Académie Royale des Sciences*. The paper has been translated from its original French.

The Discovery of the Division in Saturn's Ring

After the discoveries which have been made at different times concerning the globe of Saturn, its ring and its satellites, in part by Huygens who discovered one of the satellites which revolves around Saturn in 16 days less 47 minutes, and in part by Cassini who discovered two others of which we will give the history at an early date, it seemed that there was nothing more to discover concerning the planet; however, the latest observations that Cassini has made concerning the body of Saturn and its ring, show that in the Heavens as well as on the Earth, something new to observe always appears.

After the emergence of Saturn from the rays of the Sun as a morning star in the year 1675, the globe of the planet appeared with a dark band, similar to those of Jupiter, extending the length of the ring from East to West, as it is nearly always shown by the 34-foot telescope, and the breadth of the ring was divided by a dark line into two equal parts, of which the interior and nearer one to the globe was very bright, and the exterior part slightly dark. There was about the same difference between the colours of these two parts that there is between dull silver and burnished silver, which had never before been observed but which has since been seen in the same telescope, more clearly at twilight and in moonlight than on a darker night.

This appearance gave an impression of a double ring, of which the inferior ring, being larger and darker, had superposed upon it another that is narrower and brighter, and reminds one that in the year 1671, when the extensions of Saturn were on the verge of disappearing they contracted beforehand, perhaps because the outer part of the ring, which was single and dark, disappeared before the inner part, which was double and brighter.

In the same year, 1671, the shorter diameter of the ring was still less than the diameter of the globe which extended outside the ring on the North and South sides, and this phase lasted until the immersion of Saturn in the rays of the Sun in the year 1676. But after its emersion, which took place last summer, the shorter diameter of the ring exceeded that of the globe. There is an observation by Hevelius in the English Journal, which corresponds to the first of these two phases; but as he has

noted neither the band of Saturn, nor the distinction which can be seen in the ring, one has reason to judge that the telescopes which he uses are much inferior to those of the Royal Observatory.

Appendix D

Limitations on the Use of the Power-Law form of $S_y(f)$ to Compute Allan Variance

An edited version of this appendix was published in the Institute of Electrical and Electronics Engineers (IEEE) journal *Transactions on Ultrasonics, Ferroelectrics, and Frequency Control* [Thomson *et al.*, 2005]. Note that in this appendix only, we abbreviate the term 'phase modulation' as PM. In every other section of this dissertation, PM denotes periodic microstructure.

D.1 Abstract

An exact solution to the well-known integral transform that relates the spectral density of the instantaneous fractional frequency deviation, $S_y(f)$, to the Allan variance, $\sigma_y^2(\tau)$, is presented for the case of a power-law representation of $S_y(f)$. The approximate solution to this integral transform, which is found throughout the literature, is also derived. A graphical convergence analysis is presented, showing the range of applicability of the approximate solution. The results reinforce the utility of the approximate solution, which converges quickly to the exact solution under virtually all reasonable measurement conditions.

D.2 Introduction

The preferred measures of frequency and phase stability are Allan deviation $\sigma_y(\tau)$ (in the time domain) and the one-sided power spectral density measures $S_\phi(f)$ and $S_y(f)$ (in the frequency domain) [Barnes *et al.*, 1971; Rutman, 1978]. In frequency standards, frequency and phase deviations from the oscillator center frequency ν_o are commonly attributed to five separate noise processes, each exhibiting unique frequency-dependent behavior as depicted in Figure D.1. Accordingly, $S_\phi(f)$ and $S_y(f)$ are often modeled as power-law series of these five processes. The time and frequency domain measures of stability are related, and Allan variance—the square of Allan deviation—can be computed directly from either $S_\phi(f)$ or $S_y(f)$ via an integral transform. This integral transform is well-known and documented extensively in the literature [Barnes *et al.*, 1971; Rutman, 1978; Sullivan *et al.*, 1990; IEEE, 1999].

A model of Allan variance $\sigma_y^2(\tau)$, given in terms of the integral transform of a power-law $S_y(f)$, is also well-known and widely documented, as is an approximate solution to this integral transform [Barnes *et al.*, 1971; Rutman, 1978; Sullivan *et al.*, 1990; IEEE, 1999]. However an exact solution of the integral transform for the power-law model has not been published to date. Also absent from the literature is a quantitative analysis that characterizes the range of applicability of the approximate power-law solution.

In order to better understand the origin and applicability of the approximate solution, we have solved the integral transform exactly—term-by-term, for each noise process in the power-law expression of $S_y(f)$. The approximate solution has also been derived, and a graphical convergence analysis between the approximate and exact solutions of the power-law model has been performed in terms of the sampling rate of the measurement system. Our analysis quantifies the differences between the exact and approximate expression of $\sigma_y^2(\tau)$ in terms of a power-law $S_y(f)$, and reinforces the wide-ranging utility of the approximate solution.

D.3 Exact and Approximate Solutions for $\sigma_y^2(\tau)$

The Allan variance $\sigma_y^2(\tau)$ in terms of a power-law form of $S_y(f)$ is expressed as follows [Barnes et al., 1971],

$$\sigma_y^2(\tau) = \frac{2}{(\pi\tau)^2} \sum_{n=-2}^{+2} \left[h_n \int_0^{f_m} \frac{\sin^4(\pi\tau f)}{f^{2-n}} df \right] \quad (\text{D.1})$$

where τ is the integration time, h_n is a constant associated with the n^{th} term in the power-law model [Barnes et al., 1971; Rutman, 1978; Sullivan et al., 1990], and f_m is taken to be the one-sided bandwidth of the frequency source. We proceed with a term-by-term evaluation of (D.1) to determine both the exact and approximate solutions for each term¹, followed by a graphical presentation of the convergence behavior.

D.3.1 Evaluation of the f^{-2} -term

$$\begin{aligned} \frac{2h_{-2}}{(\pi\tau)^2} \int_0^{f_m} \frac{\sin^4(\pi\tau f)}{f^4} df &= -\frac{h_{-2}}{12(\pi\tau)^2 f_m^3} \left(3 + {}_1F_2 \left[\begin{matrix} -1.5 \\ -0.5, 0.5 \end{matrix} ; -4(\pi\tau f_m)^2 \right] \right. \\ &\quad \left. -4 {}_1F_2 \left[\begin{matrix} -1.5 \\ -0.5, 0.5 \end{matrix} ; -(\pi\tau f_m)^2 \right] \right) \end{aligned} \quad (\text{D.2})$$

$$\text{ROC} \in \{\Im m\{\tau\} = 0, f_m > 0\}$$

where ROC specifies the region of convergence of the integral, and

$${}_pF_q \left[\begin{matrix} a_1, a_2, \dots, a_p \\ b_1, b_2, \dots, b_q \end{matrix} ; z \right] \quad (\text{D.3})$$

is the generalized hypergeometric function, which is in turn given by a hypergeometric series,

¹Throughout this paper, the authors make use of the terms “exact” and “approximate” to describe solutions of (D.1). Since (D.1) is itself an approximation based upon a bandlimited power-law model of $S_y(f)$, the reader should bear in mind that an exact solution of (D.1) is still only an approximation of $\sigma_y^2(\tau)$.

$${}_pF_q \left[\begin{matrix} a_1, a_2, \dots, a_p \\ b_1, b_2, \dots, b_q \end{matrix} ; z \right] = \sum_{k=0}^{\infty} \frac{(a_1)_k (a_2)_k \cdots (a_p)_k}{(b_1)_k (b_2)_k \cdots (b_q)_k} \frac{z^k}{k!} \quad (\text{D.4})$$

where $(a)_k$ is the Pochhammer symbol or rising factorial. If we assume that f_m is large, then we can approximate (D.2) by taking the limit as $f_m \rightarrow \infty$, yielding the following,

$$\lim_{f_m \rightarrow \infty} \left[\frac{2h_{-2}}{(\pi\tau)^2} \int_0^{f_m} \frac{\sin^4(\pi\tau f)}{f^4} df \right] = \frac{2}{3} h_{-2} \pi^2 \tau \quad (\text{D.5})$$

$$\text{ROC} \in \{\mathfrak{M}\{\tau\} = 0\}$$

The result given in (D.5) is consistent with corresponding approximate formulations given in the literature (eg. *Barnes et al.* [1971]).

Figure D.2 shows the correspondence between the exact solution (D.2) and the approximate solution (D.5) for the f^{-2} component of the solution of the integral in (D.1). The ratio of the exact solution to the approximate solution is plotted as a function of τ/τ_o , the ratio of the integration time τ to the sampling rate τ_o . For this analysis, we have assumed a Nyquist sampling rate, or $\tau_o = (2f_m)^{-1}$. The dashed lines in Figure D.2 indicate the region within which the ratio of the exact to approximate solution is within 1%.

D.3.2 Evaluation of the f^{-1} -term

$$\begin{aligned} \frac{2h_{-1}}{(\pi\tau)^2} \int_0^{f_m} \frac{\sin^4(\pi\tau f)}{f^3} df &= 2h_{-1} (\text{Ci}[2\pi\tau f_m] - \text{Ci}[4\pi\tau f_m] \\ &\quad + \ln(2) - \sin^3(\pi\tau f_m) \frac{4\pi\tau f_m \cos(\pi\tau f_m) + \sin(\pi\tau f_m)}{2(\pi\tau f_m)^2}) \end{aligned} \quad (\text{D.6})$$

$$\text{ROC} \in \{\text{everywhere}\}$$

where $\text{Ci}[z]$ is the cosine integral function. Adopting the same approach as in Section

D.3.1, we take the limit of (D.6) as $f_m \rightarrow \infty$, yielding the following result,

$$\lim_{f_m \rightarrow \infty} \left[\frac{2h_{-1}}{(\pi\tau)^2} \int_0^{f_m} \frac{\sin^4(\pi\tau f)}{f^3} df \right] = 2h_{-1} \ln(2) \quad (\text{D.7})$$

$$\text{ROC} \in \{\Im m\{\tau\} = 0\}$$

Figure D.3 shows the ratio of the exact solution (D.6) to the approximate solution (D.7) of the f^{-1} term in (D.1) as a function of τ/τ_o .

D.3.3 Evaluation of the f^0 -term

$$\begin{aligned} \frac{2h_0}{(\pi\tau)^2} \int_0^{f_m} \frac{\sin^4(\pi\tau f)}{f^2} df &= -\frac{h_0}{4f_m(\pi\tau)^2} \left(3 + {}_1F_2 \left[\begin{matrix} -0.5 \\ 0.5, 0.5 \end{matrix}; -4(\pi\tau f_m)^2 \right] \right. \\ &\quad \left. - 4 {}_1F_2 \left[\begin{matrix} -0.5 \\ 0.5, 0.5 \end{matrix}; -(\pi\tau f_m)^2 \right] \right) \end{aligned} \quad (\text{D.8})$$

$$\text{ROC} \in \{\Im m\{\tau\} = 0, f_m > 0\}$$

Again, taking the limit as $f_m \rightarrow \infty$ simplifies the expression,

$$\lim_{f_m \rightarrow \infty} \left[\frac{2h_0}{(\pi\tau)^2} \int_0^{f_m} \frac{\sin^4(\pi\tau f)}{f^2} df \right] = \frac{h_0}{2\tau} \quad (\text{D.9})$$

$$\text{ROC} \in \{\Im m\{\tau\} = 0\}$$

Figure D.4 shows the ratio of the exact solution (D.8) to the approximate solution (D.9) of the f^0 term in (D.1) as a function of τ/τ_o .

D.3.4 Evaluation of the f^1 -term

$$\begin{aligned} \frac{2h_1}{(\pi\tau)^2} \int_0^{f_m} \frac{\sin^4(\pi\tau f)}{f} df &= \frac{h_1}{4(\pi\tau)^2} [(3\gamma + 2\ln(2) + 3\ln(\pi)) \\ &\quad + 3\ln(\tau f_m) - 4\text{Ci}[2\pi\tau f_m] + \text{Ci}[4\pi\tau f_m]] \end{aligned} \quad (\text{D.10})$$

$$\text{ROC} \in \{\Im m\{\tau\} = 0, f_m > 0\}$$

where γ is the Euler-Mascheroni constant. Evaluation of the constant terms on the right-hand side of (D.10) affords the following simplification,

$$\begin{aligned} \frac{2h_1}{(\pi\tau)^2} \int_0^{f_m} \frac{\sin^4(\pi\tau f)}{f} df \\ = \frac{h_1}{(2\pi\tau)^2} [6.55213 + 3\ln(\tau f_m) - 4\text{Ci}[2\pi\tau f_m] + \text{Ci}[4\pi\tau f_m]] \end{aligned} \quad (\text{D.11})$$

$$\text{ROC} \in \{\Im m\{\tau\} = 0, f_m > 0\}$$

This differs somewhat from the form of the f^1 -term most commonly found in the literature [*Barnes et al.*, 1971; *Rutman*, 1978; *Sullivan et al.*, 1990],

$$f^1 \text{ term as given in [1]-[3]} = \frac{h_1}{(2\pi\tau)^2} [1.038 + 3\ln(2\pi\tau f_m)] \quad (\text{D.12})$$

A comparison of (D.11) and (D.12) shows that the two converge to within 1% for $\tau/\tau_o > 11.5$. Figure D.5 shows the ratio of the exact solution as presented in (D.11) to the solution (D.12) of the f^1 term as given in the literature [*Barnes et al.*, 1971; *Rutman*, 1978; *Sullivan et al.*, 1990].

D.3.5 Evaluation of the f^2 -term

$$\frac{2h_2}{(\pi\tau)^2} \int_0^{f_m} \sin^4(\pi\tau f) df = \frac{h_2}{16(\pi\tau)^3} [12\pi\tau f_m - 8\sin(2\pi\tau f_m) + \sin(4\pi\tau f_m)] \quad (\text{D.13})$$

$$\text{ROC} \in \{\text{everywhere}\}$$

The first term in (D.13) is proportional to $f_m\tau^{-2}$, while the second and third terms are of fixed envelope, attenuated proportionally to τ^{-3} . Evaluating the integration of (D.13) in the limit as $f_m \rightarrow \infty$ yields the approximate solution,

$$\lim_{f_m \rightarrow \infty} \left[\frac{2h_2}{(\pi\tau)^2} \int_0^{f_m} \sin^4(\pi\tau f) df \right] = \frac{3h_2 f_m}{(2\pi\tau)^2} \quad (\text{D.14})$$

which is consistent with what is published in the literature. Figure D.6 shows the ratio of the exact solution (D.13) to the approximate solution (D.14) of the f^2 term in (D.1) as a function of τ/τ_o .

D.4 Results and Conclusions

It is possible to approximate the frequency response $S_y(f)$ of a frequency source with a 5-term power-law model of $S_y(f)$ that is bandlimited to f_m . The Allan variance of such a modeled frequency source is then given by (D.1). We have shown that the approximate solution of (D.1), which is commonly found in the literature [Barnes *et al.*, 1971; Rutman, 1978; Sullivan *et al.*, 1990; IEEE, 1999], results from allowing $f_m \rightarrow \infty$ in the limit of the integration.² The exact and approximate solutions of each term in (D.1), as well as the conditions under which these two solutions converge to within 1% (for the case of a Nyquist-sampled frequency source) are summarized in Table D.1. The convergence behavior is shown graphically in Figures D.2–D.6.

The results show that the *white FM* (f^0) and *white PM* (f^2) noise terms in the power-law representation of $S_y(f)$ impose the strictest limitations on the minimum ratio τ/τ_o required for convergence, while the *random walk FM* (f^{-2}) noise term imposes the least stringent convergence conditions. The worst-case integration time

²Except in the case of the f^1 term, as discussed in Section D.3.4.

τ must be at least 45 times the sampling rate τ_o to ensure 1% convergence of all exact and approximate terms in the solution of (D.1). Typically, Allan variance is not computed (or specified) for integration times shorter than $\tau = 0.1$ seconds. Taking that as a “worst case” example, a measurement bandwidth of 450 Hz would be required for convergence—a bandwidth easily achieved by modern test equipment, and which is likely much less than the sampling bandwidth that would be chosen in order to satisfy the Nyquist criterion for the frequency source model (bandlimited by f_m , sampled at $2f_m$ in our analysis).

While the results show that convergence is not guaranteed for all values of τ , they nevertheless show fast convergence behavior under reasonable measurement conditions. These results serve to underscore the utility of the approximate solution of (D.1), as presented in the literature [*Barnes et al.*, 1971; *Rutman*, 1978; *Sullivan et al.*, 1990].

Table D.1: One Percent Convergence Conditions for the Exact Solution and the Approximate Solution to Each Term in the Power-Law Formulation of Allan Variance $\left(\sigma_y^2(\tau) = \frac{2}{(\pi\tau)^2} \sum_{\alpha=-2}^{+2} \left[h_\alpha \int_0^{f_m} \frac{\sin^4(\pi\tau f)}{f^{2-\alpha}} df \right] \right)$

Noise Type	$S_y(f)$	Exact Solution of $\sigma_y^2(\tau)$ in (D.1)	Approximate Solution of $\sigma_y^2(\tau)$	1% Convergence
Random Walk FM	$h_{-2}f^{-2}$	$-\frac{h_{-2}}{12(\pi\tau)^2 f_m^3} \left(3 + {}_1F_2 \left[\begin{matrix} -1.5 \\ -0.5, 0.5 \end{matrix} ; -4(\pi\tau f_m)^2 \right] \right. \\ \left. -4 {}_1F_2 \left[\begin{matrix} -1.5 \\ -0.5, 0.5 \end{matrix} ; -(\pi\tau f_m)^2 \right] \right)$	$\frac{2}{3} h_{-2} \pi^2 \tau$	$\tau/\tau_o > 1.3$
Flicker FM	$h_{-1}f^{-1}$	$2h_{-1} (\text{Ci}[2\pi\tau f_m] - \text{Ci}[4\pi\tau f_m] + \ln(2) - \sin^3(\pi\tau f_m) \frac{4\pi\tau f_m \cos(\pi\tau f_m) + \sin(\pi\tau f_m)}{2(\pi\tau f_m)^2})$	$2h_{-1} \ln(2)$	$\tau/\tau_o > 3$
White FM	$h_0 f^0$	$-\frac{h_0}{4f_m(\pi\tau)^2} \left(3 + {}_1F_2 \left[\begin{matrix} -0.5 \\ 0.5, 0.5 \end{matrix} ; -4(\pi\tau f_m)^2 \right] \right. \\ \left. -4 {}_1F_2 \left[\begin{matrix} -0.5 \\ 0.5, 0.5 \end{matrix} ; -(\pi\tau f_m)^2 \right] \right)$	$\frac{h_0}{2\tau}$	$\tau/\tau_o > 31$
Flicker PM	$h_1 f^1$	$\frac{h_1}{(2\pi\tau)^2} [6.55213 + 3\ln(\tau f_m) - 4\text{Ci}[2\pi\tau f_m] + \text{Ci}[4\pi\tau f_m]]$	$\frac{h_1}{(2\pi\tau)^2} [1.038 + 3\ln(2\pi\tau f_m)]$	$\tau/\tau_o > 11.5$
White PM	$h_2 f^2$	$\frac{h_2}{16(\pi\tau)^3} [12\pi\tau f_m - 8\sin(2\pi\tau f_m) + \sin(4\pi\tau f_m)]$	$\frac{3h_2 f_m}{(2\pi\tau)^2}$	$\tau/\tau_o > 45$

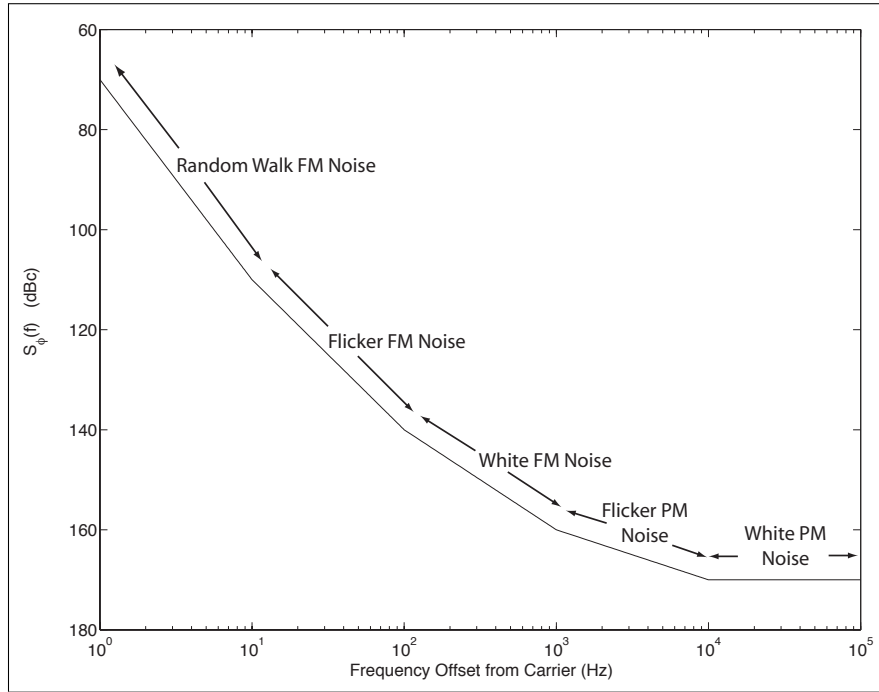


Figure D.1: Characteristic physical noise processes in frequency standards. Frequency dependency is shown with respect to $S_\phi(f)$ (Note: $S_y(f) = \left(\frac{f}{\nu_o}\right)^2 S_\phi(f)$).

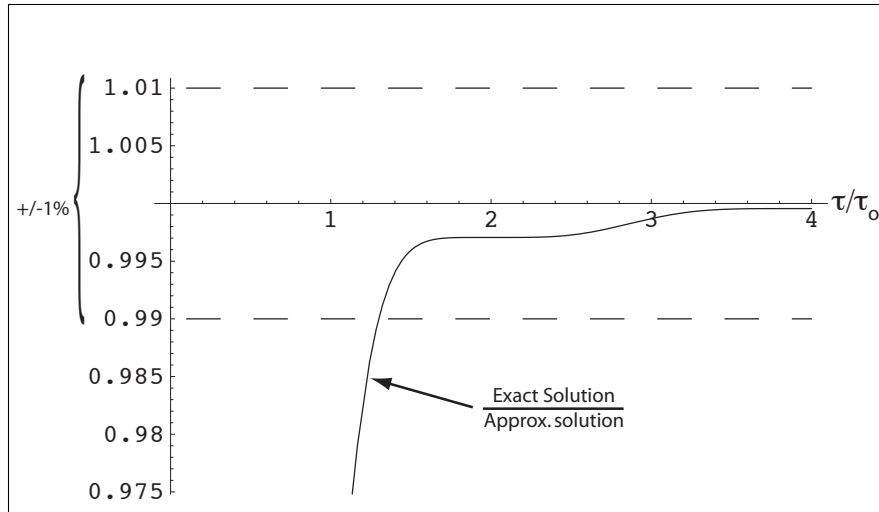


Figure D.2: Ratio of the exact solution (D.2) to the approximate solution (D.5) of the f^{-2} term in (D.1) as a function of the ratio of integration time to sampling rate, τ/τ_o . Convergence to within 1% is achieved for $\tau/\tau_o > 1.3$.

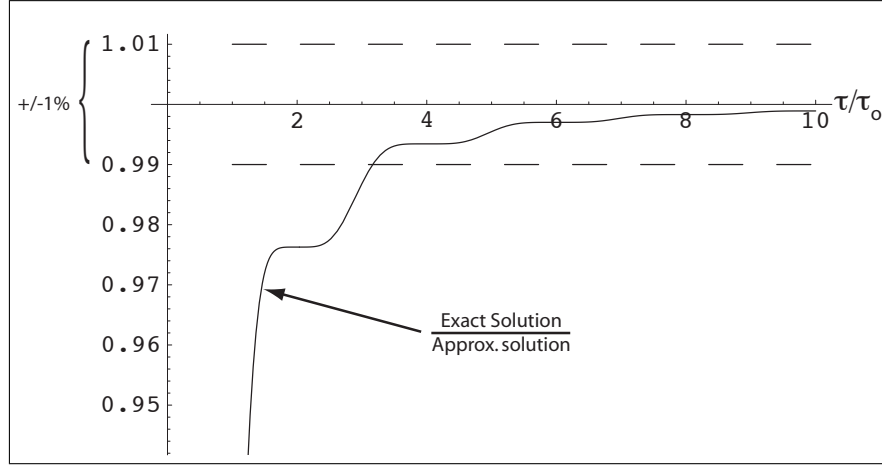


Figure D.3: Ratio of the exact solution (D.6) to the approximate solution (D.7) of the f^{-1} term in (D.1) as a function of the ratio of integration time to sampling rate, τ/τ_o . Convergence to within 1% is achieved for $\tau/\tau_o > 3$.

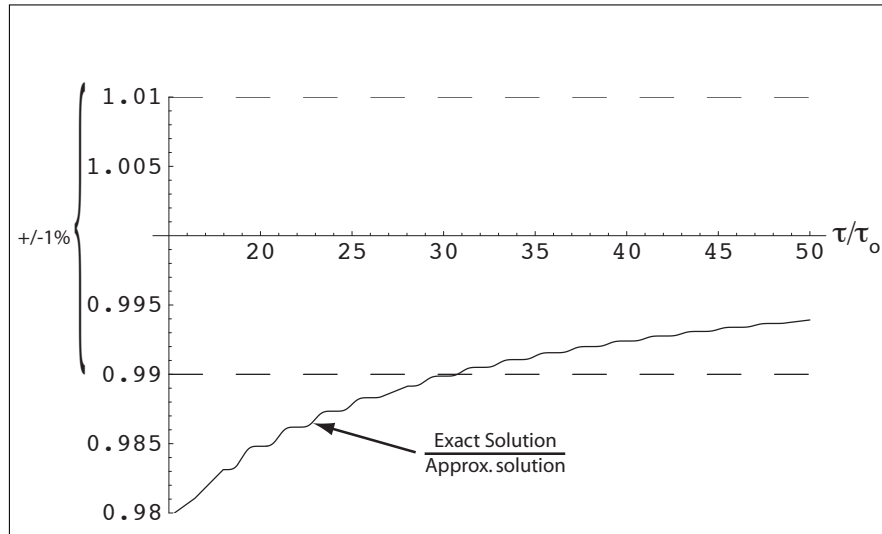


Figure D.4: Ratio of the exact solution (D.8) to the approximate solution (D.9) of the f^0 or DC-term in (D.1) as a function of the ratio of integration time to sampling rate, τ/τ_o . Convergence to within 1% is achieved for $\tau/\tau_o > 31$.

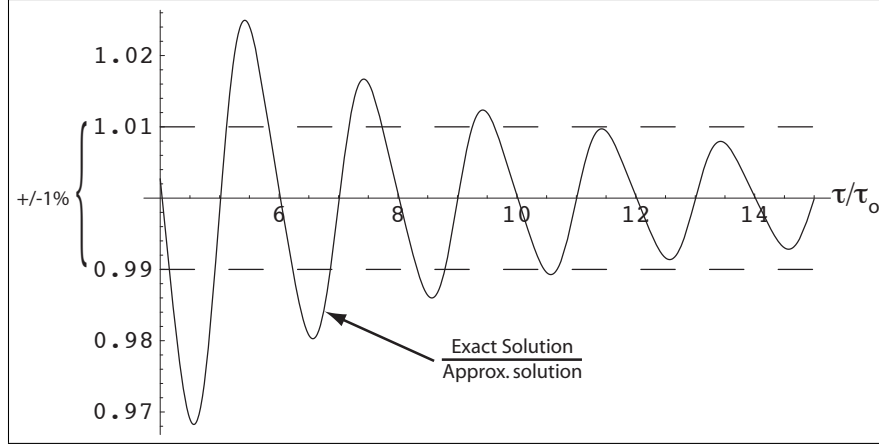


Figure D.5: Ratio of the exact solution (D.11) of the f^1 term in (D.1) to the solution (D.12) commonly given in the literature [1]-[3]. The ratio is given as a function of the ratio of integration time to sampling rate, τ/τ_o . Convergence to within 1% is achieved for $\tau/\tau_o > 11.5$.

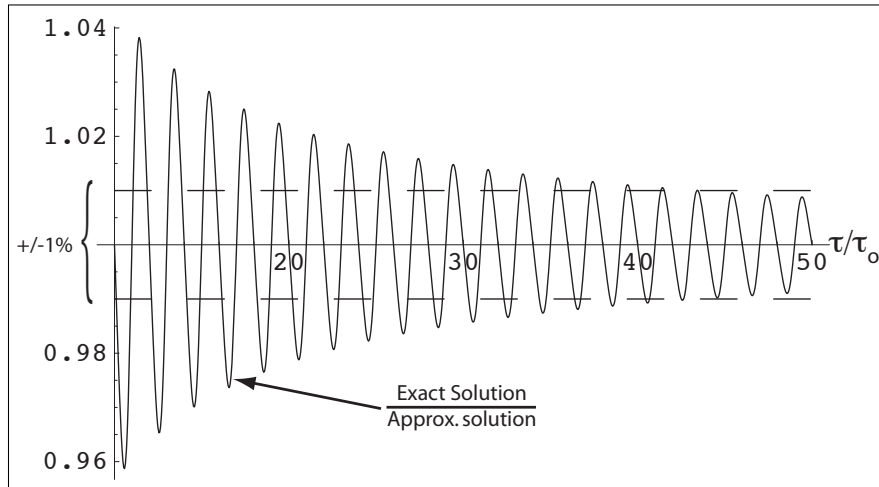


Figure D.6: Ratio of the exact solution (D.13) to the approximate solution (D.14) of the f^2 term in (D.1) as a function of the ratio of integration time to sampling rate, τ/τ_o . Convergence to within 1% is achieved for $\tau/\tau_o > 45$.

Appendix E

Radon and Abel Transform Equivalence in Atmospheric Radio Occultation

An edited version of this appendix was published in the American Geophysical Union (AGU) journal *Radio Science* [Thomson and Tyler, 2007].

E.1 Abstract

The Radon Transform plays a central role in the image reconstruction technique known as computed tomography, used commonly in radio astronomy and medical imaging. Although usually formulated as a projection of a spatial density function along straight ray paths, the Radon Transform kernel also permits curved path projections, providing the path can be defined. Reformulation of the Radon Transform as a path integral for the case of a radio ray refracting in a spherically symmetric atmosphere leads directly to the Abel Transform formulation commonly used in atmospheric radio occultation.

E.2 Introduction

Radio occultation is a technique which, among other applications, is employed to probe planetary atmospheres in search of their physical properties. Considering, for convenience, only the neutral atmosphere, radio waves propagating within the gas are refracted and simultaneously retarded in phase. The degree of bending that occurs depends on the gas refractivity, which is controlled by gas composition and density, and reflects the atmospheric structure that the wave encounters along the propagation path. The refractivity profile $\nu(r)$ of the atmosphere under study is retrieved by processing of radio occultation data, subject to the assumption of local conformance to spherical symmetry. For a known or assumed composition, plus the additional strong assumption of hydrostatic equilibrium, atmospheric pressure and temperature profiles local to the experimental ray path are deduced from the refractivity data. The refractivity profile normally is retrieved from pre-processed occultation data through the use of the Abel Transform. The details of this procedure may be found in *Fjeldbo et al.* [1971]; *Eshleman* [1973]; *Tyler* [1987]; *Karayel and Hinson* [1997]; *Ahmad and Tyler* [1998].

The Radon Transform (RT), broadly employed in computed tomography (CT), is a more general reduction tool than the Abel Transform (AT) since spherical symmetry is not required. The RT is formulated for straight ray paths. In radio occultation, however, the functional argument to the AT is modified to accommodate curved ray paths. When the RT is re-formulated for curved ray paths in a spherically symmetric system, it reduces to the form of the AT familiar in radio occultation studies.

E.3 Atmospheric Radio Occultation

The geometry of an atmospheric radio occultation measurement is shown in Figure E.1. Radio waves from the transmitter, T, which is moving in the frame of the planet with a velocity $\vec{v}_T(t)$, propagate along an initial path defined by \hat{u}_T . The waves arrive along unit vector $-\hat{u}_R$ at the receiver, R, moving with velocity $\vec{v}_R(t)$. Refraction by the neutral atmosphere perturbs the path of radio rays, bending them towards the

center of the refractivity field, as shown in Figure E.1. In actual atmospheres, both positive and negative refractivity can occur, corresponding to the neutral atmospheric gas and the ionosphere, respectively, but the same analysis applies to both. In the ionosphere, the refractivity gradient can be either positive or negative.

The basic observable of radio occultation is the perturbation of signal frequency associated with the Doppler shift that occurs as a result of the refractive bending of a ray linking a moving transmitter and receiver as the ray passes through an intervening atmosphere. Doppler shift $f_D(t)$ is induced in the received signal by the combination of the relative motion of T and R with respect to the center of the planet O , and by the bending of the rays in the planet's atmosphere [Ahmad and Tyler, 1999]. For the classical result,

$$f_D = \frac{f_T}{c} [\vec{v}_T \cdot \hat{u}_T + \vec{v}_R \cdot \hat{u}_R - (\vec{v}_T \cdot \hat{u} - \vec{v}_R \cdot \hat{u})] \quad (\text{E.1})$$

where the time dependence of the quantities in (E.1) is omitted to simplify the notation. The geometric solution of this system is unique under the assumption of spherical symmetry, which constrains the ray to lie in the plane defined by the positions of the transmitter, receiver, and the center of refractive symmetry, which is notionally the center of the planet. With this assumption and knowledge of the positions and velocities of the transmitter and receiver, observation of f_D is sufficient to determine the vectors \hat{u}_T and \hat{u}_R uniquely, and the total bending angle α and ray asymptote closest approach distance a , or impact parameter, found.

An occultation experiment proceeds by measuring the ray parameters α and a at many points throughout the planet or moon's atmosphere—from the top of the sensible atmosphere, where the first bending of the ray is detected, to the point where the ray path intersects the surface of the occulting planet/moon, or is otherwise undetectable due to atmospheric refraction, absorption, or defocusing. A sequence of such measurements yields a profile of the bending angle $\alpha(a)$ spanning the measurable limits of the atmosphere. Temperature and pressure profiles are derived from the measurement of $\alpha(a)$ according to (e.g. Fjeldbo *et al.* [1971]),

$$T(r) = T(r_o) \frac{\nu(r_o)}{\nu(r)} + \frac{\bar{m}}{k\nu(r)} \int_{r'=r}^{r'=r_o} g(r') \nu(r') dr' \quad (\text{E.2})$$

$$p(r) = kn_t(r)T(r) \quad (\text{E.3})$$

where $T(r)$ is temperature, $p(r)$ is atmospheric pressure, \bar{m} is the mean molecular mass, k is Boltzmann's constant, $g(r)$ is the acceleration due to gravity, $n_t(r)$ is the total number density of neutral atoms and molecules, $\nu(r)$ is the refractivity of the atmosphere, and r_o is the closest approach of the ray to the planet's surface, as shown in Figures E.1 and E.2. The refractivity is related to the refractive index $\mu(r)$ according to $\nu(r) = \mu(r) - 1$. The refractive index is retrieved directly from the measured bending angle α via Abelian transformation, as discussed below.

E.4 Applicability of the Abel Transform to the Radio Occultation Technique

Fjeldbo et al. [1971] showed that determination of the refractive index profile $\mu(r)$ from $\alpha(a)$ is a special case of Abelian inversion. Consider the geometry of a radio ray, refracting as it propagates, as depicted in Figure E.2, where the view is in the plane of the ray. The center of the coordinate system is located at the center of the planet under study, which is taken to be the center of symmetry.

Section E.8 shows that the relationship of the bending angle α as a function of the ray asymptote a is given by,

$$\alpha(a) = 2 \int_0^{\frac{\pi}{2}} d\psi = -2a \int_{r=r_o}^{\infty} \frac{d\mu}{\mu dr} \frac{dr}{\sqrt{(\mu r)^2 - a^2}} \quad (\text{E.4})$$

The integral equation (E.4) is equivalent to a standard form of the Abel Transform [*Bracewell*, 2000],

$$f(a) = 2 \int_a^{\infty} \frac{x g(x)}{\sqrt{x^2 - a^2}} dx \quad (\text{E.5})$$

Defining $x = \mu r$, and replacing the function $g(x)$ with

$$g(x) = -\frac{a}{x} \frac{d\mu}{\mu dx} \quad (\text{E.6})$$

yields an alternative form of (E.4),

$$\alpha(a) = -2a \int_{x=a}^{\infty} \frac{d\mu}{\mu dx} \frac{dx}{\sqrt{x^2 - a^2}} \quad (\text{E.7})$$

Fjeldbo et al. [1971] showed that since $\frac{d \ln(\mu)}{dx} = \frac{d\mu}{\mu dx}$, (E.7) can be solved by Abel inversion to find a solution for the refractive index as a function of the impact parameter,

$$\ln(\mu(a)) = \frac{1}{\pi} \int_a^{\infty} \frac{\alpha(x)}{\sqrt{x^2 - a^2}} dx \quad (\text{E.8})$$

E.5 The Radon Transform

The Radon Transform can be thought of as a generalization of the Abel Transform, in instances where the requirement of spherical symmetry is removed. The Radon Transform, $f(R, \theta)$, is defined as the set of all straight line integrals through a spatial function $h(x, y)$ at some perpendicular distance R from the origin of the coordinate system [*Bracewell*, 2000],

$$f(R, \theta) = \int_{-\infty}^{\infty} \int_{-\infty}^{\infty} h(x, y) \delta(R - x \cdot \cos \theta - y \cdot \sin \theta) dx dy \quad (\text{E.9})$$

The argument of the Dirac delta function in the integrand defines a line as illustrated in Figure E.3. The distance from the origin to the intercept P is calculated using the Pythagorean theorem,

$$R^2 = x^2 + y^2 \quad (\text{E.10})$$

The variables x and y can also be expressed in terms of sines and cosines,

$$\cos(\theta) = \frac{x}{R} \quad \sin(\theta) = \frac{y}{R} \quad (\text{E.11})$$

With a slight modification:

$$x \cdot \cos(\theta) = \frac{x^2}{R} \quad y \cdot \sin(\theta) = \frac{y^2}{R} \quad (\text{E.12})$$

we can substitute (E.12) into (E.10) to obtain the equation of the line,

$$R = x \cdot \cos(\theta) + y \cdot \sin(\theta) \quad (\text{E.13})$$

A zero of the argument to $\delta(\cdot)$ in (E.9) occurs when a point (x, y) lies on the line,

$$R - x \cdot \cos(\theta) - y \cdot \sin(\theta) = 0 \quad (\text{E.14})$$

For fixed values of θ and R (θ_1 and R_1 , say), then the integral $f(R_1, \theta_1)$ represents the projection of the density function $h(x, y)$ along the line $L = L_{\theta_1}$. The equation of the scan line L_{θ_1} is sometimes expressed in a more standard $y = mx + b$ form,

$$f(m, b) = \int_{-\infty}^{\infty} \int_{-\infty}^{\infty} h(x, y) \delta(y - (mx + b)) dx dy \quad (\text{E.15})$$

Note that in Figure E.3, the line L has been drawn with a negative slope (i.e. $m \rightarrow -m$).

E.6 Radon and Abel Transform Equivalence for Radio Occultation

In the RT, (E.9) and (E.15) above, the argument of the Dirac delta defines a straight line. Physically, a straight line scan is a mathematical approximation to a thin pencil beam in the CT technique used in imaging, and used by Bracewell to image radio galaxies [Bracewell, 1956].

In medical CT, individual pencil beams are arranged to form a fan of beams that sweeps around a patient. Detectors are placed opposite the fan such that each pencil beam is aligned with an individual detector. The function $h(x, y)$ is a measure of the spatial absorption and/or scattering of the pencil beam energy at the frequency of transmission. Images are reconstructed by applying an inverse RT—most commonly one of several approximations to this inverse—to recover $h(x, y)$ from the data, yielding $f(R, \theta)$.

For the case of ray propagation through a refractive atmosphere, there is some deviation between the actual ray path and a straight line path. In this instance, the argument of the Dirac delta must be reformulated to define the curved path of a ray refracting as it propagates in the atmosphere.

Let us modify the Radon Transform (E.9)—using imprecise language for the moment—to allow for a curved path,

$$f(x, y) = \int_{-\infty}^{\infty} \int_{-\infty}^{\infty} h(x, y) \delta(p(x, y)) dx dy \quad (\text{E.16})$$

where the argument p of the Dirac delta defines a curved path in (x, y) . The variable R is a ray path-related parameter that remains undefined for the moment. Reformulation in polar coordinates gives,

$$f(R, \theta) = \int_0^{\infty} \int_0^{2\pi} h(r, \theta) \delta(p(r, \theta)) r d\theta dr \quad (\text{E.17})$$

Assuming that the field $h(r, \theta)$ is spherically symmetric, $h(r, \theta) \rightarrow h(r)$. With this,

$$f(R) = \int_0^{\infty} \int_0^{2\pi} h(r) \delta(p(r, \theta)) r d\theta dr \quad (\text{E.18})$$

The projection operation performed by the Dirac delta in the integral (E.18) is equivalent to integration along the path defined by $p(r, \theta)$. Thus, in instances for which a differential ray path element dl can be defined, we can re-write (E.18) as follows,

$$f(R) = \int_0^{\infty} \int_0^{2\pi} h(r) \delta(p(r, \theta)) r d\theta dr = \int_{\text{path}} h(r) dl \quad (\text{E.19})$$

where dl is a small element along the path.

An element dl along a curved radio ray path in a refracting atmosphere can be calculated by analysis similar to that of Section E.4. Referring to Figure E.2, the path element dl for the case of a spherically-symmetric refracting medium is given by,

$$dl^2 = (r d\theta)^2 + (dr)^2 \quad (\text{E.20})$$

Substituting $d\theta$ as previously defined in (E.34) into (E.20) and simplifying yields,

$$dl = \frac{\mu r}{\sqrt{(\mu r)^2 - a^2}} dr \quad (\text{E.21})$$

Thus, the θ -dependence of the ray path is removed from the path integral. Incorporating the assumption of a symmetric ray path and the result (E.21) allows (E.19) to be re-written,

$$f(R) = 2 \int_{r_o}^{\infty} h(r) \frac{\mu r}{\sqrt{(\mu r)^2 - a^2}} dr \quad (\text{E.22})$$

In Section E.4, the specific form of $g(x)$ defined in (E.6), combined with the substitution $x = \mu r$ transforms the general form of the AT, (E.5), into specific forms used in atmospheric radio occultation, (E.4), (E.7). Using (E.6) in (E.22) by applying the substitution $h(r) = \mu^{-1}g(r)$, and simplifying yields the following,

$$f(a) = -2a \int_{r_o}^{\infty} \frac{d\mu}{\mu dr} \frac{dr}{\sqrt{(\mu r)^2 - a^2}} \quad (\text{E.23})$$

A comparison of Figures E.1 and E.3 shows that the variable R , which has been defined to this point as a ray-path parameter, is actually the impact parameter. Accordingly, R has been replaced by a in (E.23). Equation (E.23), found by exchanging the Dirac delta kernel of the Radon Transform for the path integral of a refracting ray, is identical to the Abel integral (E.4) which resulted from first principles analysis of refraction in a spherically symmetric medium, where $f(a) = \alpha(a)$.

E.7 Discussion and Conclusion

Ahmad and Tyler [1998] identified the substitution $x = \mu r$ as a transformation between straight and curved ray paths, for the purpose of computing α , μ , and a . *Fjeldbo et al.* [1971] employed this substitution to invert (E.4) via standard Abelian inversion, yielding a closed-form expression for refractive index as a function of impact parameter, (E.8). No approximations are introduced into the procedure as a result of these substitutions. For both the AT and the path integral derived from the RT, a connection to the bending angle formula (E.4) exists via the functions $g(r)$ and

$\mu^{-1}g(r)$, respectively, which transform the Abel and Radon Transform kernels from straight ray to curved ray path formulations.

Normally, the ray path in the RT kernel is a straight line, but use of a refractive path is not precluded by the mathematics. The Dirac delta kernel of the RT performs a sampling operation on the spatial density function $h(r, \theta)$, effectively projecting $h(r, \theta)$ along a path for which the argument of the Dirac delta is zero. In computed tomography, this is the path of a ray propagating through the medium under study. Formulating the RT as a path integral defines a curved ray path in the Radon kernel, with the path element dl prescribed by the geometry of a radio ray propagating in a spherically symmetric refractive medium. The resulting equation, (E.23), is the same as the specific form of the AT, (E.4), commonly used in atmospheric radio occultation.

E.8 Derivation of Eq. (E.4)

Following Fjeldbo *et al.*, suppose that the distance r to a ray changes by the distance dr as the position vector to the ray sweeps through the angle $d\theta$. The local inclination of the ray, ξ , can be expressed in terms of,

$$\tan \xi = \frac{r d\theta}{dr} \quad (\text{E.24})$$

The relationship between a , μ , and r is obtained from *Bouguer's Rule* [Born and Wolf, 1999],

$$a = \mu r \cdot \sin \xi \quad (\text{E.25})$$

where a is the impact parameter discussed above, and depicted in Figure E.1. It is implicit in (E.25) that $\mu = \mu(r)$ and $\xi = \xi(r)$. By inspection, the three angles θ , ξ , and ψ sum to $\frac{\pi}{2}$,

$$\theta + \xi - \psi = \frac{\pi}{2} \quad (\text{E.26})$$

therefore taking the derivative yields,

$$d\theta + d\xi - d\psi = 0 \quad (\text{E.27})$$

or,

$$d\psi = d\theta + d\xi \quad (\text{E.28})$$

We would like to develop expressions for $d\theta$ and $d\xi$ to use in (E.28), thus deriving an expression for $d\psi$ that we can integrate to yield the total bending angle α . We begin this task by differentiating Bouguer's Rule (E.25) with respect to r and solving for $d\xi$,

$$0 = \frac{d\mu}{dr} r \cdot \sin \xi + \mu \cdot \sin \xi + \mu r \cdot \cos \xi \frac{d\xi}{dr} \quad (\text{E.29})$$

$$d\xi = \frac{-\left(\frac{d\mu}{dr} r \cdot \sin \xi + \mu \cdot \sin \xi\right)}{\mu r \cdot \cos \xi} dr \quad (\text{E.30})$$

With the trigonometric substitutions,

$$\sin \xi = \frac{a}{\mu r} \quad \cos \xi = \sqrt{1 - \sin^2 \xi} = \frac{\sqrt{(\mu r)^2 - a^2}}{\mu r} \quad (\text{E.31})$$

equation (E.30) for $d\xi$ becomes,

$$d\xi = -\frac{a \left(\mu + \frac{d\mu}{dr} r\right) dr}{\mu r \sqrt{(\mu r)^2 - a^2}} \quad (\text{E.32})$$

We now turn to the expression (E.24) for $\tan \xi$ and solve for $d\theta$,

$$r \frac{d\theta}{dr} = \tan \xi = \frac{\sin \xi}{\cos \xi} = \frac{\frac{a}{\mu r}}{\frac{\sqrt{(\mu r)^2 - a^2}}{\mu r}} \quad (\text{E.33})$$

Simplifying (E.33) yields,

$$d\theta = \frac{dr}{r} \frac{a}{\sqrt{(\mu r)^2 - a^2}} \quad (\text{E.34})$$

Armed with expressions for $d\theta$ and $d\xi$, we combine (E.32) and (E.34) in (E.28) to obtain an expression for $d\psi$,

$$d\psi = \frac{dr}{r} \frac{a}{\sqrt{(\mu r)^2 - a^2}} - \frac{a \left(\mu + \frac{d\mu}{dr} r\right) dr}{\mu r \sqrt{(\mu r)^2 - a^2}} \quad (\text{E.35})$$

A final simplification of terms gives an expression for $d\psi$ in terms of a , μ , and r ,

$$d\psi = \frac{-a}{\sqrt{(\mu r)^2 - a^2}} \left(\frac{d\mu}{dr} \right) \frac{dr}{\mu} \quad (\text{E.36})$$

Integration of the quantity $d\psi$ along the entire ray path yields the total bending angle α as shown in (E.4). α is conventionally defined as positive for bending towards the center of the planet/moon, as shown in Figure E.1. The impact parameter a is related to the closest approach distance r_o by Bouguer's Rule, (E.25), with $\xi = \pi/2$, thus $a = \mu r_o$ (also see Figure E.2).

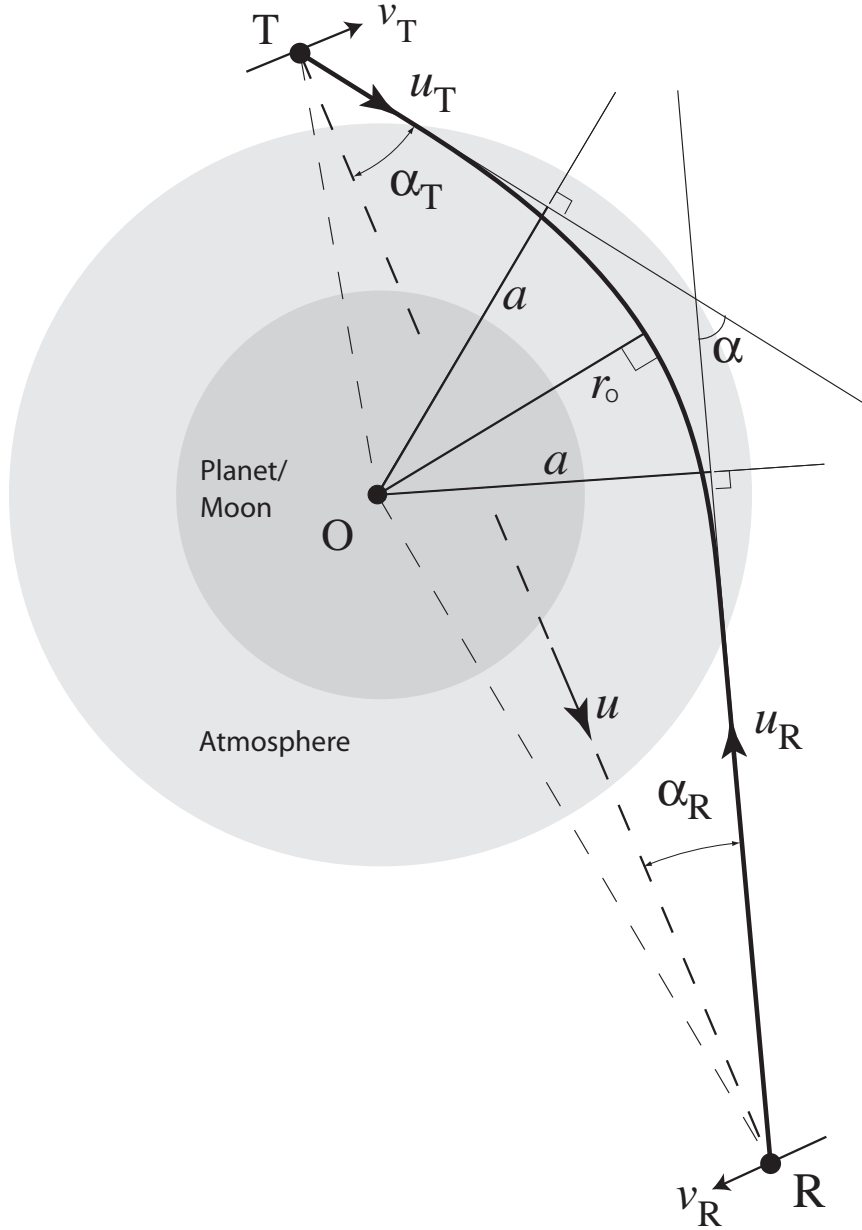


Figure E.1: Geometry of radio occultation measurements. Refraction in a spherically symmetric atmosphere results in a radio ray path that is a mirror image about the radius of closest approach r_o . Note impact parameter a , and bending angle α . The bending angle α is exaggerated, relative to typical cases, for clarity.

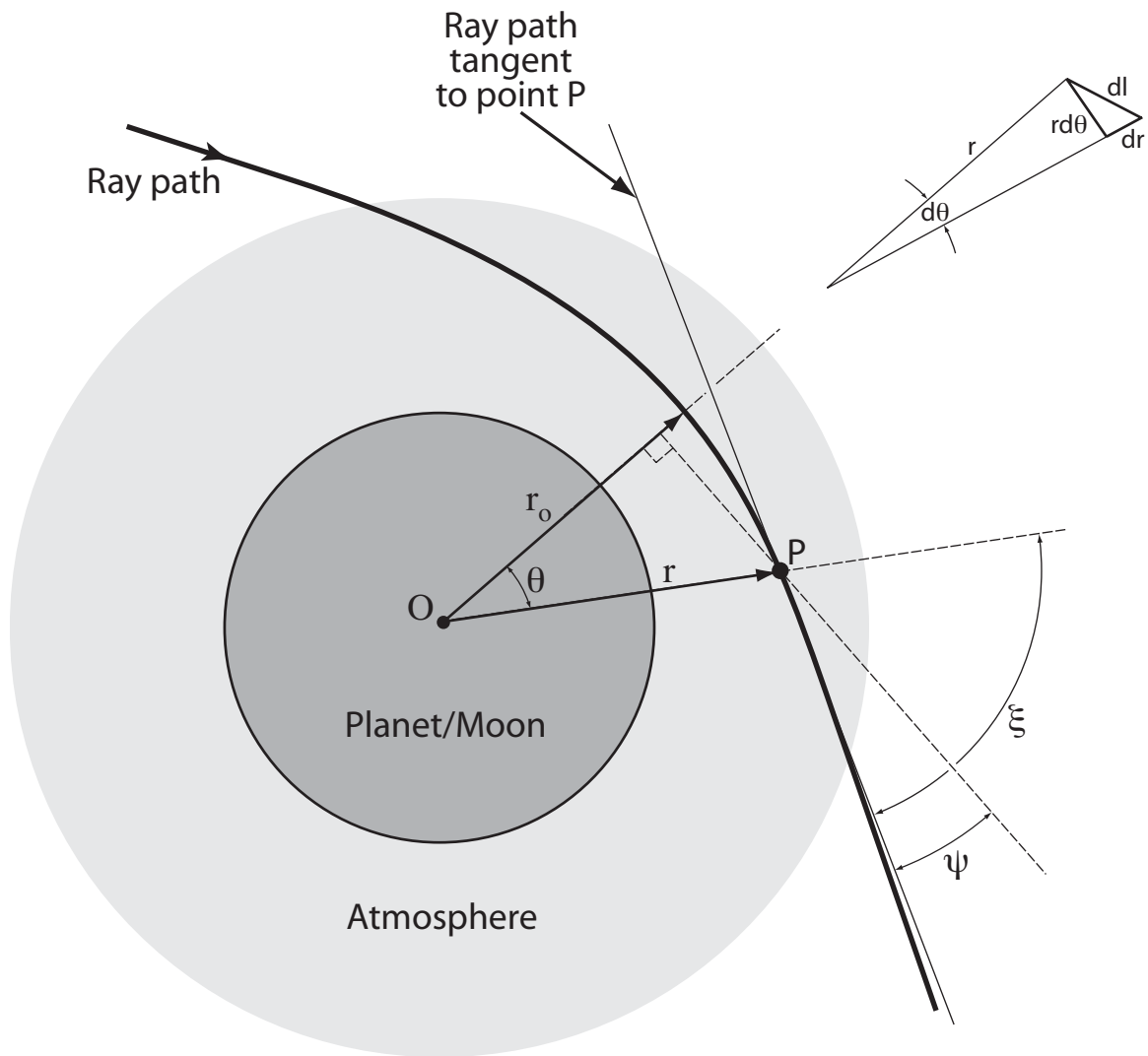


Figure E.2: Geometry for derivation of differential bending angle $d\psi$ and path integral element dl . The actual bending of the ray path depends on the nature of the atmosphere, and can vary greatly.

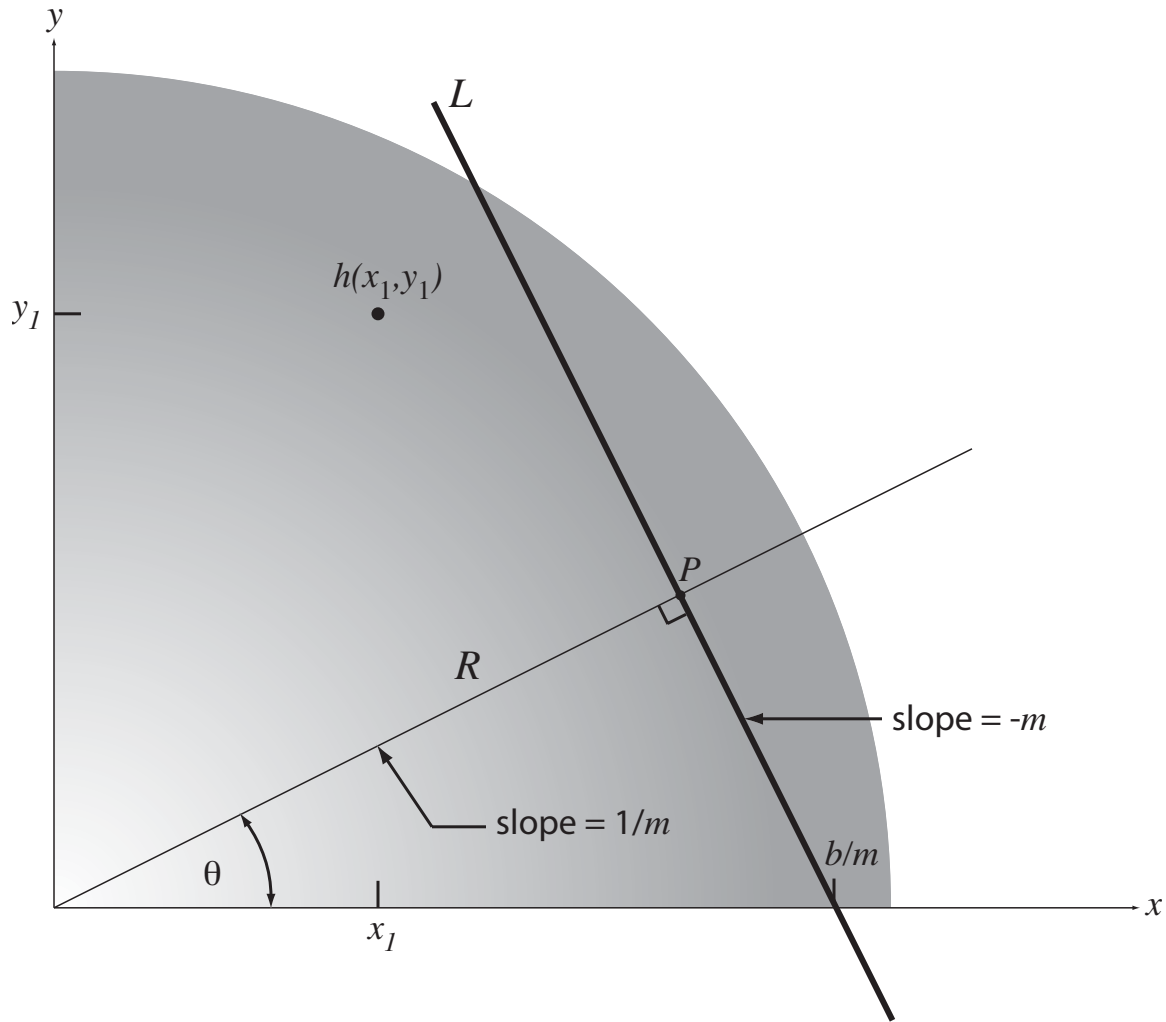


Figure E.3: Radon Transform Geometry. Spatial function $h(x, y)$ in the plane of the figure is integrated along a line L , generating projections of $h(x, y)$ along L . The line L is defined in polar coordinates for a given R and θ as satisfying $R - x \cdot \cos \theta - y \cdot \sin \theta = 0$. In cartesian coordinates, line L satisfies $y + mx - b = 0$. After *Bracewell* [2000].

Bibliography

- Ahmad, B., and G. L. Tyler, The two-dimensional resolution kernel associated with retrieval of ionospheric and atmospheric refractivity profiles by Abelian inversion of radio occultation phase data, *Radio Science*, 33, 129–142, 1998.
- Ahmad, B., and G. L. Tyler, Systematic errors in atmospheric profiles obtained from Abelian inversion of radio occultation data: Effects of large-scale horizontal gradients, *Journal of Geophysical Research*, 104, 3971–3992, 1999.
- Alexander, A. F. O., *The planet Saturn: a history of observation, theory, and discovery*, New York, Macmillan, 1962., 1962.
- Barnes, J. A., et al., Characterization of Frequency Stability, *IEEE Transactions on Instrumentation and Measurement*, 20, 105–120, 1971.
- Bohren, C. F., and D. R. Huffman, *Absorption and Scattering of Light by Small Particles*, John Wiley and Sons, 1998.
- Born, M., and E. Wolf, *Principles of optics: 7th (expanded) edition*, Cambridge University Press, 1999.
- Bracewell, R. N., Strip Integration in Radio Astronomy, *Australian Journal of Physics*, 9, 198–217, 1956.
- Bracewell, R. N., *The Fourier transform and its applications*, 3rd ed., McGraw Hill, 2000.
- Bromwich, T. J., The scattering of plane electric waves by a sphere, *Phil. Trans. Roy. Soc.*, 220, 189–206, 1920.

- Bruning, J. H., and Y. T. Lo, Multiple scattering of EM waves, part I—multiple expansion and ray optical solutions, *IEEE Trans. Antennas Propag.*, pp. 378–390, 1971a.
- Bruning, J. H., and Y. T. Lo, Multiple scattering of EM waves, part II—numerical and experimental results, *IEEE Trans. Antennas Propag.*, pp. 391–400, 1971b.
- Burns, J. A., *The New Solar System (4th ed.)*, chap. Planetary Rings, pp. 221–240, Sky Publishing/Cambridge University Press, 1999.
- Charnoz, S., L. Dones, L. W. Esposito, P. R. Estrada, and M. M. Hedman, Origin and evolution of saturn’s ring system, in *Saturn from Cassini-Huygens*, edited by M. K. Dougherty, L. W. Esposito, and S. M. Krimigis, pp. 537–573, Cambridge University Press, 2009.
- Colwell, J. E., and L. W. Esposito, Density and Bending Waves in Saturn’s Rings from Cassini UVIS Star Occultations, in *Bulletin of the American Astronomical Society*, *Bulletin of the American Astronomical Society*, vol. 38, 2007.
- Colwell, J. E., L. W. Esposito, and M. Sremčević, Self-gravity wakes in Saturn’s A ring measured by stellar occultations from Cassini, *Geophysical Research Letters*, 33, doi:10.1029/2005GL025163, 2006.
- Colwell, J. E., L. W. Esposito, M. Sremčević, G. R. Stewart, and W. E. McClintock, Self-gravity wakes and radial structure of Saturn’s B ring, *Icarus*, 190, 127–144, doi:10.1016/j.icarus.2007.03.018, 2007.
- Colwell, J. E., P. D. Nicholson, M. S. Tiscareno, C. D. Murray, R. G. French, and E. A. Marouf, *Saturn from Cassini-Huygens*, chap. The Structure of Saturn’s rings, pp. 375–412, Cambridge University Press, doi:10.1007/978-1-4020-9217-6, 2009.
- Cuzzi, J., R. Clark, G. Filacchione, R. French, R. Johnson, E. Marouf, and L. Spilker, Ring particle composition and size distribution, in *Saturn from Cassini-Huygens*, edited by M. K. Dougherty, L. W. Esposito, and S. M. Krimigis, pp. 459–509, Cambridge University Press, 2009.

- Cuzzi, J. N., J. J. Lissauer, L. W. Esposito, J. B. Holberg, E. A. Marouf, G. L. Tyler, and A. Boishchot, Saturn's rings - Properties and processes, in *IAU Colloq. 75: Planetary Rings*, edited by R. Greenberg & A. Brahic, pp. 73–199, 1984.
- Cuzzi, J. N., et al., Saturn's Rings: pre-Cassini Status and Mission Goals, *Space Science Reviews*, 104, 209–251, doi:10.1023/A:1023653026641, 2002.
- de Pater, I., and J. J. Lissauer, *Planetary Sciences*, Cambridge University Press, 2001.
- Deau, E., A. Brahic, and C. Porco, Saturn's rings thickness with the shadow hiding, in *37th COSPAR Scientific Assembly, COSPAR, Plenary Meeting*, vol. 37, 2008.
- Dougherty, E. L. W. . K. S. M., M. K., *Saturn from Cassini-Huygens*, Cambridge University Press, doi:10.1007/978-1-4020-9217-6, 2009.
- Dunn, D. E., I. de Pater, and L. A. Molnar, Examining the wake structure in Saturn's rings from microwave observations over varying ring opening angles and wavelengths, *Icarus*, 192, 56–76, doi:10.1016/j.icarus.2007.06.017, 2007.
- Elliot, J. L., E. Dunham, and D. Mink, The rings of Uranus, *Nature*, 267, 328–330, 1977.
- Eshleman, V. R., The radio occultation method for the study of planetary atmospheres, *Planet. Space Sci.*, 21, 1521–1531, 1973.
- Esposito, L. W., M. Ocallaghan, K. E. Simmons, C. W. Hord, R. A. West, A. L. Lane, R. B. Pomphrey, D. L. Coffeen, and M. Sato, Voyager photopolarimeter stellar occultation of Saturn's rings, *J. Geophys. Res.*, 88, 8643–8649, 1983.
- Esposito, L. W., C. C. Harris, and K. E. Simmons, Features in Saturn's rings, *Astronomical Journal*, 63, 749–770, doi:10.1086/191181, 1987.
- Fjeldbo, G., A. J. Kliore, and V. R. Eshleman, The Neutral Atmosphere of Venus as Studied with the Mariner V Radio Occultation Experiments, *Astronomical Journal*, 76, 123–140, 1971.

- French, R. G., and P. D. Nicholson, Saturn's Rings II. Particle sizes inferred from stellar occultation data, *Icarus*, *145*, 502–523, doi:10.1006/icar.2000.6357, 2000.
- French, R. G., H. Salo, C. A. McGhee, and L. Dones, HST observations of azimuthal asymmetry in Saturn's rings, *Icarus*, *189*, 493–522, doi:10.1016/j.icarus.2007.02.019, 2007.
- French, R. G., E. A. Marouf, N. J. Rappaport, and C. A. McGhee, Occultation Observations of Saturn's B Ring and Cassini Division, *Astronomical Journal*, *139*, 1649–1667, doi:10.1088/0004-6256/139/4/1649, 2010.
- Fuller, K. A., Cooperative Electromagnetic Scattering by Ensembles of Spheres, Ph.D. thesis, Texas A&M University, TX, 1987.
- Fuller, K. A., G. W. Kattawar, and R. T. Wang, Electromagnetic scattering from two dielectric spheres: further comparisons between theory and experiment, *Applied Optics*, *25*, 2521–2529, 1986.
- Goodman, J. W., *Introduction to Fourier optics*, McGraw-Hill, 1995.
- Greenberg, R., and A. Brahic (Eds.), *Planetary rings*, University of Arizona Press, 1984.
- Gresh, D. L., Voyager radio occultation by the Uranian rings: Structure, dynamics, and particle sizes, Ph.D. thesis, Stanford University, CA), 1990.
- Gresh, D. L., P. A. Rosen, G. L. Tyler, and J. J. Lissauer, An analysis of bending waves in Saturn's rings using Voyager radio occultation data, *Icarus*, *68*, 481–502, doi:10.1016/0019-1035(86)90052-7, 1986.
- Gresh, D. L., E. A. Marouf, G. L. Tyler, P. A. Rosen, and R. A. Simpson, Voyager radio occultation by Uranus' rings. I - Observational results, *Icarus*, *78*, 131–168, doi:10.1016/0019-1035(89)90074-2, 1989.
- Gudin, M., and W. Gawronski, Low Noise Signal Processing Technique for Monopulse Pointing of DSN 34-meter Diameter Antennas, in *2000 IEEE Aerospace Conference*, 2000.

- Hedman, M. M., et al., Saturn's dynamic D ring, *Icarus*, 188, 89–107, doi:10.1016/j.icarus.2006.11.017, 2007.
- Hillier, J. K., et al., The composition of Saturn's E ring, *Monthly Notices of the Royal Astronomical Society*, 377, 1588–1596, doi:10.1111/j.1365-2966.2007.11710.x, 2007.
- Holberg, J. B., W. T. Forrester, and J. J. Lissauer, Identification of resonance features within the rings of Saturn, *Nature*, 297, 115–120, 1982.
- IEEE, *IEEE Standard Definitions of Physical Quantities for Fundamental Time Metrology*, IEEE Standard No. 1139-1999, 1999.
- Karayel, E. T., and D. P. Hinson, Sub-Fresnel-scale vertical resolution in atmospheric profiles from radio occultation, *Radio Science*, 32, 411–424, doi:10.1029/96RS03212, 1997.
- Keeler, J. E., A Spectroscopic Proof of the Meteoric Constitution of Saturn's Rings, *Astrophysical Journal*, 1, 416–427, doi:10.1086/140074, 1895.
- Kliore, A. J., et al., Cassini Radio Science, *Space Science Reviews*, 115, 1–4, doi:10.1007/s11214-004-1436-y, 2004.
- Latter, H. N., and G. I. Ogilvie, Dense planetary rings and the viscous overstability, *Icarus*, 195, 725–751, doi:10.1016/j.icarus.2008.02.001, 2008.
- Latter, H. N., and G. I. Ogilvie, The viscous overstability, nonlinear wavetrains, and finescale structure in dense planetary rings, *Icarus*, 202, 565–583, doi:10.1016/j.icarus.2009.03.011, 2009.
- Liang, C., and Y. T. Lo, Scattering by two spheres, *Radio Science*, 2, 1481–+, 1967.
- Mahon, B., *The Man Who Changed Everything: The Life of James Clerk Maxwell*, John Wiley and Sons, 2003.
- Marouf, A. E. A. A., The rings of Saturn, analysis of a bistatic-radar experiment, Ph.D. thesis, Stanford University, CA, 1975.

- Marouf, E., Personal communications, 2006–2010.
- Marouf, E., N. Rappaport, R. French, C. McGhee, and A. Anabtawi, Azimuthal variability of radial structure of Saturn's rings observed by Cassini radio occultations, in *36th COSPAR Scientific Assembly*, p. 2806, 2006a.
- Marouf, E., et al., Cassini First Diametric Radio Occultation of Saturn's Rings, *AGU Spring Meeting Abstracts*, pp. A4+, 2005a.
- Marouf, E., et al., Structure of Saturn's Rings from Cassini Diametric Radio Occultations, in *Bulletin of the American Astronomical Society*, p. 763, 2005b.
- Marouf, E. A., Near-Forward Scattering by Packed Particle Clusters, in *Bulletin of the American Astronomical Society*, p. 1108, 1993.
- Marouf, E. A., Stochastic Geometry Models for Diffraction by Planetary Rings, in *Bulletin of the American Astronomical Society*, p. 1150, 1994.
- Marouf, E. A., Comparative Diffraction by Thin and Thick Planetary Ring Models, in *Bulletin of the American Astronomical Society*, p. 1126, 1996.
- Marouf, E. A., Diffraction by Crowded, Clustered, and Anisotropic Planetary Ring Models, in *Bulletin of the American Astronomical Society*, p. 1000, 1997.
- Marouf, E. A., and G. L. Tyler, Microwave edge diffraction by features in Saturn's rings - Observations with Voyager 1, *Science*, *217*, 243–245, doi:10.1126/science.217.4556.243, 1982.
- Marouf, E. A., G. L. Tyler, and V. R. Eshleman, Theory of radio occultation by Saturn's rings, *Icarus*, *49*, 161–193, doi:10.1016/0019-1035(82)90070-7, 1982.
- Marouf, E. A., G. L. Tyler, H. A. Zebker, R. A. Simpson, and V. R. Eshleman, Particle size distributions in Saturn's rings from Voyager 1 radio occultation, *Icarus*, *54*, 189–211, doi:10.1016/0019-1035(83)90192-6, 1983.
- Marouf, E. A., G. L. Tyler, and P. A. Rosen, Profiling Saturn's rings by radio occultation, *Icarus*, *68*, 120–166, doi:10.1016/0019-1035(86)90078-3, 1986.

- Marouf, E. A., R. G. French, N. J. Rappaport, C. A. McGhee, K. Wong, F. S. Thomson, and A. Anabtawi, Structure and Properties of Saturn's Ring B from Cassini Radio Occultations, in *Bulletin of the American Astronomical Society, Bulletin of the American Astronomical Society*, vol. 38, p. 552, 2006b.
- Marouf, E. A., R. G. French, N. J. Rappaport, C. A. McGhee, K. Wong, F. S. Thomson, and A. Anabtawi, Comparative Structure of Saturn's Rings from Cassini Radio Occultation Observations, in *Bulletin of the American Astronomical Society, Bulletin of the American Astronomical Society*, vol. 38, p. 419, 2007a.
- Marouf, E. A., R. G. French, N. J. Rappaprt, C. A. McGhee, F. S. Thomson, K. Wong, and A. Anabtawi, Characterization of Enigmatic Saturn's Ring B by Cassini Radio Occultations, *AGU Fall Meeting Abstracts*, p. 1296, 2007b.
- McGhee, C. A., R. G. French, N. J. Rappaport, E. A. Marouf, R. Dawson, and K. Stack, Cassini Radio Science Observations of Density Waves in Saturn's Rings, in *Progress in Planetary Exploration Missions, IAU Joint Discussion*, vol. 10, 2006.
- Mie, G., Beiträge zue optik trüber medien speziell kolloidaler metallösungen, *Ann. Phys.*, 25, 377–452, 1908.
- Morishima, R., and H. Salo, Simulations of dense planetary rings. IV. Spinning self-gravitating particles with size distribution, *Icarus*, 181, 272–291, doi:10.1016/j.icarus.2005.10.023, 2006.
- Nicholson, J. W., The scattering of light by a large conducting sphere, *Proc. Math. Soc. (London)*, 9, 67–80, 1910.
- Nicholson, J. W., The scattering of light by a large conducting sphere (2nd paper), *Proc. Math. Soc. (London)*, 11, 277–284, 1912.
- Nicholson, P. D., M. L. Cooke, K. Matthews, J. H. Elias, and G. Gilmore, Five stellar occultations by Neptune - Further observations of ring arcs, *Icarus*, 87, 1–39, doi: 10.1016/0019-1035(90)90020-A, 1990.

- Nicholson, P. D., R. G. French, E. Tollestrup, J. N. Cuzzi, J. Harrington, K. Matthews, O. Perkovic, and R. J. Stover, Saturn's rings I. Optical depth profiles from the 28 Sgr occultation, *Icarus*, 145, 474–501, doi:10.1006/icar.2000.6356, 2000.
- Nicholson, P. D., M. M. Hedman, B. D. Wallis, and Cassini-VIMS Team, Cassini-VIMS Observations of Stellar Occultations by Saturn's Rings, in *AAS/Division of Dynamical Astronomy Meeting*, *AAS/Division of Dynamical Astronomy Meeting*, vol. 38, 2007.
- Porco, C. C., et al., Cassini Imaging Science: Initial Results on Saturn's Rings and Small Satellites, *Science*, 307, 1226–1236, doi:10.1126/science.1108056, 2005.
- Rappaport, N., P. Longaretti, E. A. Marouf, R. G. French, and C. A. McGhee, Analysis of Nonlinear Density Waves in Saturn's Rings in the Light of Cassini Radio-science Data, in *Bulletin of the American Astronomical Society*, *Bulletin of the American Astronomical Society*, vol. 38, p. 553, 2006.
- Rappaport, N., P. Longaretti, E. A. Marouf, R. G. French, and C. A. McGhee, Analyses of RSS Optical Depth Occultation Profiles for Several Occultations, in *Bulletin of the American Astronomical Society*, *Bulletin of the American Astronomical Society*, vol. 40, p. 445, 2008.
- Reitsema, H. J., W. B. Hubbard, L. A. Lebofsky, and D. J. Tholen, Occultation by a Possible Third Satellite of Neptune, *Science*, 215(4530), 289–291, doi:10.1126/science.215.4530.289, 1982.
- Rosen, P. A., Processing with the Fresnel Transform: Applications to Inverting Diffraction-Limited Data from the Voyager 1 Radio Occultation Experiment, *Technical Report No. D840-1985-1*. Center for Radar Astronomy, Stanford University, 1985.
- Rosen, P. A., Waves in Saturn's rings probed by radio occultation, Ph.D. thesis, Stanford University, CA, 1989.

- Rosen, P. A., and J. J. Lissauer, The Titan-1:0 nodal bending wave in Saturn's Ring C, *Science*, *241*, 690–694, 1988.
- Rosen, P. A., G. L. Tyler, and E. A. Marouf, Resonance structures in Saturn's rings probed by radio occultation. I - Methods and examples, *Icarus*, *93*, 3–24, doi:10.1016/0019-1035(91)90160-U, 1991a.
- Rosen, P. A., G. L. Tyler, E. A. Marouf, and J. J. Lissauer, Resonance structures in Saturn's rings probed by radio occultation. II - Results and interpretation, *Icarus*, *93*, 25–44, doi:10.1016/0019-1035(91)90161-L, 1991b.
- Rutman, J., Characterization of phase and frequency instabilities in precision frequency sources: fifteen years of progress., *IEEE Proceedings*, *66*, 1048–1075, 1978.
- Sadiku, M. N. O., Refractive index of snow at microwave frequencies, *Applied Optics*, *24*, 572–575, 1985.
- Salo, H., Gravitational wakes in Saturn's rings, *Nature*, *359*, 619–621, doi:10.1038/359619a0, 1992.
- Salo, H., Simulations of dense planetary rings. III. Self-gravitating identical particles., *Icarus*, *117*, 287–312, doi:10.1006/icar.1995.1157, 1995.
- Salo, H., Personal communication, 2006.
- Salo, H., and J. Schmidt, N-body simulations of viscous instability of planetary rings, *Icarus*, doi:10.1016/j.icarus.2009.07.038, 2009.
- Salo, H., J. Schmidt, and F. Spahn, Viscous Overstability in Saturn's B Ring. I. Direct Simulations and Measurement of Transport Coefficients, *Icarus*, *153*, 295–315, doi:10.1006/icar.2001.6680, 2001.
- Salo, H., R. Karjalainen, and R. G. French, Photometric modeling of Saturn's rings. II. Azimuthal asymmetry in reflected and transmitted light, *Icarus*, *170*, 70–90, doi:10.1016/j.icarus.2004.03.012, 2004.

- Sandel, B. R., et al., Extreme ultraviolet observations from the Voyager 2 encounter with Saturn, *Science*, *215*, 548–553, 1982.
- Schmidt, J., H. Salo, F. Spahn, and O. Petzschmann, Viscous Overstability in Saturn's B-Ring. II. Hydrodynamic Theory and Comparison to Simulations, *Icarus*, *153*, 316–331, doi:10.1006/icar.2001.6679, 2001.
- Schmidt, J., K. Ohtsuki, N. Rappaport, H. Salo, and F. Spahn, Dynamics of saturn's dense rings, in *Saturn from Cassini-Huygens*, edited by M. K. Dougherty, L. W. Esposito, and S. M. Krimigis, pp. 413–458, Cambridge University Press, 2009.
- Schmit, U., and W. M. Tscharnuter, A fluid dynamical treatment of the common action of self-gravitation, collisions, and rotation in Saturn's B-ring., *Icarus*, *115*, 304–319, doi:10.1006/icar.1995.1099, 1995.
- Schmit, U., and W. M. Tscharnuter, On the Formation of the Fine-Scale Structure in Saturn's B Ring, *Icarus*, *138*, 173–187, doi:10.1006/icar.1999.6078, 1999.
- Shu, F. H., Waves in planetary rings, in *IAU Colloq. 75: Planetary Rings*, edited by R. Greenberg and A. Brahic, pp. 513–561, 1984.
- Smith, B. A., et al., The Jupiter System Through the Eyes of Voyager 1, *Science*, *204* (4396), 951–972, doi:10.1126/science.204.4396.951, 1979.
- Spilker, L. J., S. Pilorz, A. L. Lane, R. M. Nelson, B. Pollard, and C. T. Russell, Saturn A ring surface mass densities from spiral density wave dispersion behavior, *Icarus*, *171*, 372–390, doi:10.1016/j.icarus.2004.05.016, 2004.
- Sremcevic, M., G. R. Stewart, N. Albers, J. E. Colwell, and L. W. Esposito, Density Waves in Saturn's Rings: Non-linear Dispersion and Moon Libration Effects, in *Bulletin of the American Astronomical Society, Bulletin of the American Astronomical Society*, vol. 40, p. 430, 2008.
- Sremcevic, M., J. E. Colwell, and L. W. Esposito, Small-scale ring structure observed in Cassini UVIS occultations, *AGU Fall Meeting Abstracts*, p. A5, 2009.

- Stratton, J. A., *Electromagnetic Theory*, McGraw-Hill, Inc., 1941.
- Sullivan, D. B., D. W. Allan, D. A. Howe, and F. L. Walls, *Characterization of clocks and oscillators*, 352 pp., U.S. Government Printing Office, Washington, D.C., 1990.
- Theimer, O., G. D. Wassermann, and E. Wolf, On the Foundation of the Scalar Diffraction Theory of Optical Imaging, in *Proceedings of the Royal Society of London. Series A, Mathematical and Physical Sciences*, vol. 212, pp. 426–437, 1952.
- Thomson, F., S. Asmar, and K. Oudrhiri, Limitations on the Use of the Power-Law Form of $S_y(f)$ to Compute Allan Variance, *IEEE Trans. on Ultrasonics, Ferroelectrics, and Freq. Control*, 52, 1468–1472, 2005.
- Thomson, F., E. Marouf, R. French, N. Rappoport, H. Salo, L. Tyler, and A. Anabtawi, Statistical Modeling and Characterization of Microstructure in Saturn's Rings, *AGU Fall Meeting Abstracts*, 2006a.
- Thomson, F. S., and E. A. Marouf, Diffraction theory modeling of near-forward radio wave scattering from particle clusters, *Icarus*, 204, 290–302, doi:10.1016/j.icarus.2009.06.015, 2009.
- Thomson, F. S., and G. L. Tyler, Radon and Abel Transform equivalence in atmospheric radio occultation, *Radio Science*, 42, 2007.
- Thomson, F. S., E. A. Marouf, and G. L. Tyler, Near-Forward Radio Wave Scattering from Particle Aggregate Ring Models, in *AAS/Division for Planetary Sciences Meeting Abstracts*, 2006b.
- Thomson, F. S., E. A. Marouf, G. L. Tyler, R. G. French, and N. J. Rappoport, Periodic microstructure in Saturn's rings A and B, *Geophysical Research Letters*, 34, 2007.
- Tiscareno, M. S., J. A. Burns, M. M. Hedman, and C. C. Porco, The Population of Propellers in Saturn's A Ring, *Astronomical Journal*, 135, 1083–1091, doi:10.1088/0004-6256/135/3/1083, 2008.

- Tiscareno, M. S., R. P. Perrine, D. C. Richardson, M. M. Hedman, J. W. Weiss, C. C. Porco, and J. A. Burns, An analytic parameterization of self-gravity wakes in Saturn's rings, with application to occultations and propellers, *ArXiv e-prints*, 2009.
- Trinks, W., Zur Vielfachstreuung an kleinen Kugeln, *Annalen der Physik*, *414*, 561–590, doi:10.1002/andp.19354140605, 1935.
- Tyler, G. L., Radio propagation experiments in the outer solar system with Voyager, *IEEE Proceedings*, *75*, 1404–1431, 1987.
- Tyler, G. L., E. A. Marouf, and G. E. Wood, Radio occultation of Jupiter's ring - Bounds on optical depth and particle size and a comparison with infrared and optical results, *Journal of Geophysical Research*, *86*, 8699–8703, 1981.
- Tyler, G. L., E. A. Marouf, R. A. Simpson, H. A. Zebker, and V. R. Eshleman, The microwave opacity of Saturn's rings at wavelengths of 3.6 and 13 CM from Voyager 1 radio occultation, *Icarus*, *54*, 160–188, doi:10.1016/0019-1035(83)90191-4, 1983.
- Tyler, G. L., et al., Voyager 2 radio science observations of the Uranian system Atmosphere, rings, and satellites, *Science*, *233*, 79–84, doi:10.1126/science.233.4759.79, 1986.
- Vallado, D. A., *Fundamentals of Astrodynamics and Applications*, 2nd ed., Microcosm Press, 2001.
- van de Hulst, H. C., *Light scattering by small particles*, Dover Publishing, 1981.
- van Helden, A., Saturn and his Anses, *Journal for the History of Astronomy*, *5*, 105–121, 1974.
- van Helden, A., *Planetary Rings*, chap. Rings in astronomy and cosmology, 1600-1900, pp. 12–22, University of Arizona Press, 1984.
- Verbiscer, A. J., M. F. Skrutskie, and D. P. Hamilton, Saturn's largest ring, *Nature*, *461*, 1098–1100, doi:10.1038/nature08515, 2009.

- Wiscombe, W. J., Improved Mie scattering algorithms, *Applied Optics*, *19*, 1505–1509, 1980.
- Xu, Y., Calculation of the Addition Coefficients in Electromagnetic Multisphere-Scattering Theory, *Journal of Computational Physics*, *127*, 285–298, doi:10.1006/jcph.1996.0175, 1996.
- Xu, Y.-L., Electromagnetic scattering by an aggregate of spheres, *Applied Optics*, *34*, 4573–4588, 1995.
- Xu, Y.-L., Electromagnetic scattering by an aggregate of spheres: far field, *Applied Optics*, *36*, 9496–9508, 1997.
- Xu, Y.-L., and B. Å. S. Gustafson, Experimental and theoretical results of light scattering by aggregates of spheres, *Applied Optics*, *36*, 8026–8030, 1997.
- Zebker, H. A., and G. L. Tyler, Thickness of Saturn's rings inferred from Voyager 1 observations of microwave scatter, *Science*, *223*, 396–398, 1984.
- Zebker, H. A., G. L. Tyler, and E. A. Marouf, On obtaining the forward phase functions of Saturn ring features from radio occultation observations, *Icarus*, *56*, 209–228, doi:10.1016/0019-1035(83)90034-9, 1983.
- Zebker, H. A., E. A. Marouf, and G. L. Tyler, Saturn's rings - Particle size distributions for thin layer model, *Icarus*, *64*, 531–548, doi:10.1016/0019-1035(85)90074-0, 1985.